UNIVERSIDAD COMPLUTENSE DE MADRID

FACULTAD DE CIENCIAS FÍSICAS

Departamento de Física Atómica, Molecular y Nuclear

TESIS DOCTORAL

Mejoras en la detección de rayos gamma con cristales centelladores de última generación y aplicaciones

Advances in Gamma-Ray detection with modern scintillators and applications

MEMORIA PARA OPTAR AL GRADO DE DOCTOR

PRESENTADA POR

Esteban Picado Sandi

Directores

José Manuel Udías Moinelo
Luis Mario Fraile Prieto

Madrid, 2013

Universidad Complutense de Madrid
Facultad de Ciencias Físicas
Dpto. de Física Atómica, Molecular y Nuclear

MEJORAS EN LA DETECCION DE RAYOS GAMMA CON CRISTALES CENTELLADORES DE ÚLTIMA GENERACION Y APLICACIONES

ESTEBAN PICADO SANDI

Tesis dirigida por los profesores
Dr. Luis Mario Fraile Prieto
Dr. José Manuel Udías Moinelo

Madrid, 2013

Para las mujeres de mi vida: mi madre, mi Agüe, Tía M, y en especial a mi musa particular: Silvia.

Contents

Agradecimientos

Agradezco a mis tutores José Manuel Udías y Luis Mario Fraile por sus enseñanzas, cooperación y paciencia. Alcanzar su nivel de conocimiento es el reto profesional más elevado al que puedo aspirar.

A todos mis compañeros de estudios y oficinas, mejor dicho, a mis agmigos: Joaquín, Bruno, Jacobo, Pablo, Khaled, Elena, Cris, Laura, Maylin, Paula, Vicky, Vadym, Richi y Esther. Y los que se me quedan por fuera. Siempre tendieron su mano para ayudarme. Gracias por introducirme en el mundo de las simulaciones y reconstrucciones.

A Eduardo Lage y Alejandro Sisniega del Hospital Gregorio Marañón por sus ganas de ayudar y explicar los temas de electrónica.

A mi madre y abuelita por comprarme libros y revistas mes a mes aunque fuera de cosas que no entendían. Gracias por darme siempre confianza para seguir adelante y regalarme sus bendiciones día a día.

Y particularmente a mi esposa Silvia, su paciencia, cariño y comprensión han sido enormes. Su aliento es mi inspiración de cada mañana, su mirada mi eterno deseo por mejorarme.

Thesis Outline

After a brief general introduction in the chapter 1, chapter 2 presents the characterization of an HPGe detector. An empirical expression for the full energy photo-peak efficiency in terms of gamma-ray energy (E) and the vertical distance from the detector surface (d) has been obtained for a high pure germanium detector (HPGe) using a 5% absolutely calibrated ^{152}Eu sources. Through this semiempirical formula the internal activity of scintillator crystals and point-like gamma sources was calibrated.

In chapter 3 we present a complete characterization of a novel LuAG:Pr crystal. Here we report measurements performed using a small crystal cube of 1 cm^3 coupled to a Hamamatsu R5320 photomultiplier tube. We study the energy resolution and linearity, together with the time response at ^{22}Na and ^{60}Co energies. In addition, we estimate the internal activity of ^{176}Lu by gamma ray spectrometry with an HPGe detector and from theoretical estimates.

Chapter 4 contains a complete characterization of a novel inorganic scintillator $CeBr_3$. Several measurements are performed using a $CeBr_3$ cylindrical crystal of 1-inch in height and 1-inch in diameter, at ^{22}Na and ^{60}Co photon energies for timing and ^{137}Cs, ^{152}Eu and ^{133}Ba sources for energy resolution and linearity. Moreover, we estimate the absolutely efficiency of the crystal with absolutely calibrated gamma sources positioned at 5, 15 and 25 cm in front of the entrance face of the detector. Furthermore, we study the radiopurity of the crystal in an ultra-low level underground facility located in LSC, Spanish Pyrenees.

In chapter 5 we study a new phoswich configuration based on two continuous high density inorganic crystals: LYSO and LuAG:Pr. We explore the energy response and pulse shape for several crystal arrangements in order to identify the optimum configuration. We digitize the pulse with a high speed oscilloscope using a Python code developed in the group, with a large commitment from this PhD candidate. In addition, we search the best for Delayed Energy Method parameters to disentangle phoswich layers (delay and layer factors).

At the end of this manuscript we present the general conclusions of this thesis and the scientific communications derived from the work presented here.

1. Introduction

1.1. Introduction

Gamma spectroscopy is a very useful tool, with an established tradition of decades, and with an increasing number of applications. It is based on gamma interaction with matter and the applications range from atomic, molecular, nuclear and high energy physics to medical physics, homeland security, material sciences, cultural heritage studies, geosciences, etc.

There are various materials that can be used to detect gamma to radiation, with specific dosimetric and spectroscopic properties. Some of these, particularly some very recently introduced in the market and that will be reviewed almost for the first time, will be studied in this PhD. work.

In this work we characterize three new gamma ray detectors in order to explore its properties and to try to define their viability as candidates for several measurements scenarios. In addition, we will characterize a standard HPGe and lead cage, which will be employed for low activity gamma measurements such as to estimate internal activity of scintillator crystals and also calibrated point-like gamma sources.

1.2. Gamma Ray Spectroscopy

1.2.1. Approach

Many nuclear reactions, radioactive decays, and particle interactions result in the emission of gamma (γ) rays, the highest-energy electromagnetic waves (or photons). Their energies range from thousands of electron volts (keV) to millions of electron volts (MeV) and their wavelengths are very short ($l0^{-11}$ to 10^{-l3} m) [Jevremovic, 2005]. These high-energy particles have found application in several scenarios like medical treatment or diagnostic, industrial sterilization, archeometry, border security protocols, etc.

In order to detect these particles, we need to study how these particles interact with the media. We first consider energy loss when gamma radiation passes through different media. This energy provides information about the electromagnetic beam. How these gamma rays, massless and neutral particles deposits energy in different media can be found in [Attix, 1986].

Indeed, the behaviour of photons in matter (whether gamma or X-rays) is dramatically different from that of charged particles. In particular, the photon lack of electric charge makes impossible the inelastic collisions with atomic electrons characteristic of charged particles interaction with media [Leo, 1994].

Although a large number of interaction mechanisms are known for gamma rays in matter, only three types play a major role in radiation measurements: photoelectric absorption, Compton scattering and pair production. All these processes lead to partial or complete

transfer of the gamma-ray photon energy to electrons (and positrons). They result in sudden and abrupt changes in the gamma-ray photon history, in that the photon either disappears entirely or is scattered through a significant angle. This behaviour contrasts to charged particles which slow down gradually through continuous, simultaneous interactions with many absorber atoms [Knoll, 2000].

1.2.2. Photoelectric Effect

In this case gamma-ray interacts with a strongly bound electron in an absorber atom and is completely absorbed, producing a fast electron. Most often, the gamma-ray will interact with the innermost or K-shell of the atom, provided that it is energetic enough to ionise the K-shell. The photoelectron is emitted with the energy of the gamma-ray energy minus the binding energy of the electron in the shell:

$$E_e = E_\gamma - E_K$$

Since this process leaves a vacancy for an electron in the K-shell, it may be filled by an electron from an outer shell, resulting in one or more fluorescence X-rays. An alternative mode of de-excitation, more likely in low Z absorbers, is the emission of Auger electrons instead of the X-ray. In this process the excitation energy is transferred directly to one of the outer electrons, which is then emitted with energy equal to the excitation energy less its own binding energy [Knoll, 2000].

The photoelectric effect is stronger for lower energy gamma-rays and for absorber materials of high atomic number. The probability of the photoelectric interaction occurring is roughly proportional to:

$$Z^n / E_\gamma^3$$

Where n varies between 4 and 5. For this reason high atomic number materials are better for shielding purposes and for detection of gamma-rays, especially where energy measurements are to be made [Cooper, 2011].

1.2.3. Compton Effect

Unlike photoelectric effect, which mostly occurs on strongly bound electrons, Compton scattering is an interaction between gamma-rays or X-rays and free or weakly bound electrons. The gamma-ray transfers only part of its energy to the electron and a resulting scattered gamma ray at a lower energy results in the process, besides the electron. In the figure 1.1 the Compton scatter is depicted and the angles of scatter of the electron and gamma-ray are defined for use in the following equations [Leo, 1994]. The energy of the scattered gamma-rays as a function of the angle of scatter θ is:

$$E_\gamma^{'} = \frac{E_\gamma}{1 + \frac{E_\gamma}{m_0 c^2} \cdot (1 - \cos\theta)}$$

Where m_0c^2 is the rest mass energy equivalent of the electron, 511 keV.

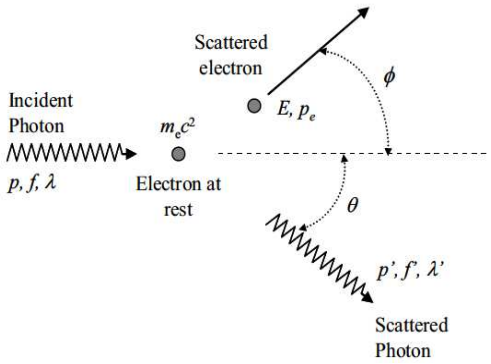

Fig. 1.1: *Compton Effect Representation* [Jevremovic, 2005].

Except for very low incident energies, the angular distribution of the scattered gamma-ray is strongly forward peaked. Two extreme values are important in Compton scattering. The first is the minimum energy of the scattered gamma-ray that occurs at a scattering angle of 180º. This minimum energy gamma-ray is often called the backscattered gamma-ray and its energy, obtained by putting $cos\theta = -1$ in equation NN, is given by [Cooper, 2011]:

$$E'_{BS} = \frac{E_\gamma}{1+\frac{2E_\gamma}{m_0c^2}}$$

From which it can be seen that the energy of the backscattered gamma-ray cannot exceed 0.255 MeV even for very high energy incident gamma-rays.

The second extreme value of interest is the energy of the electron recoiling at $\phi=0^o$, often termed the Compton edge energy. This forward scattered electron accompanies the 180º backscattered gamma-ray since there can be no transverse component of momentum in this case and its energy is easily found from conservation energy to be:

$$E'_{eCE} = \frac{E_\gamma}{1+\frac{m_0c^2}{2E_\gamma}}$$

From this equation it can be seen that the Compton edge energy is always less than the incident gamma-ray energy and for gamma ray energies in the region of 1 MeV the difference is about 0.4 MeV [Knoll, 2000].

The probability of Compton scattering depends upon the number of available (i.e. weakly bound) electrons as well as on the cross-section and so it increases with both atomic number of scatterer and incident gamma-ray energy. Whereas the probability of Compton scattering for a carbon atom (Z=6) is almost exactly six times that for a hydrogen atom over a wide energy range, the probability for lead (Z=82) is 26.3 times the one of hydrogen at 0.01 MeV, 69.7 times at 0.1 MeV and 81.5 times at 1 MeV [Cooper, 2011].

1.2.4. Pair Production

This reaction, which results in the production of a positron and an electron, is only energetically possible provided that the gamma-ray energy exceeds twice the rest mass energy equivalent of the electron or 1.022 MeV/c^2. This process has a very low probability until the gamma-ray energy exceeds this value by large and so it is mainly observed for higher energy gamma-radiation. This interaction has to take place in the field of a nucleus, the gamma-ray completely disappears and an electron-positron pair is created, the two particles sharing the available energy of E – 1.022 MeV. Just as for positrons released in radioactive decay, the positron will, after being slowed down to rest, annihilate with the nearest available electron and soon releases two gamma-ray of 0.511 MeV each (See figure 1.2)

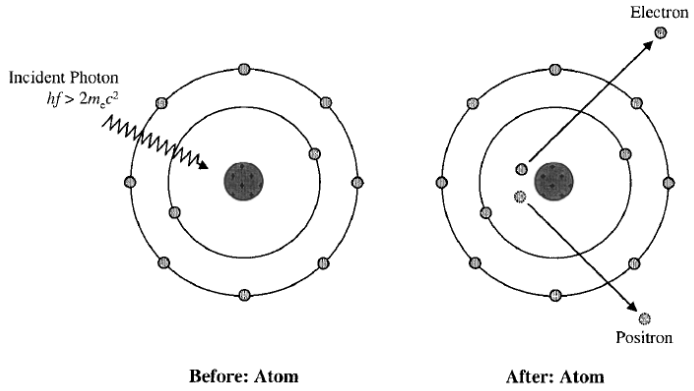

Fig. 1.2: *Pair Production Representation* [Jevremovic, 2005].

Photon interactions are summarized in Table 5-9 and show that photoelectric absorption and Compton scattering are limited to the orbital electrons of the absorber. These interactions are probable for incident photon energies less than or not significantly higher than the energy equivalent of the rest mass for two electrons (1.022 MeV/c^2). Pair production dominates in the energy range well above this threshold.

Interaction with:	Absorption	Elastic Scattering	Inelastic Scattering
Electrons in atoms	Photoelectric Effect	Rayleigh Scattering	Compton Scattering
Electromagnetic field of a nucleus or electron	Pair Production		

Table 1.1: *Types of Photons Interactions*

1.2.5. Gamma-ray Attenuation

The total probability for a photon interaction in matter is the sum of the individual cross sections outlined above. In other words, this is simply the probability per unit path length that the gamma-ray photon is removed from the beam. If we calculate the cross-section per atom, this yields [Leo, 1994]:

$$\sigma = \phi_{photoelectric} + Z\sigma_{Compton} + \tau_{pair}$$

Where we have multiplied the Compton cross-section by Z to take into account the Z electrons per atom. If we multiple σ by the density of atoms, N, we then obtain the probability per unit length for an interaction,

$$\mu = N\sigma = \sigma\left(\frac{N_a \rho}{A}\right)$$

With N_a: Avogadro's number; ρ: density of the material; and A: molecular weight.

This is more known as the Total Absorption Coefficient and is just the inverse of the mean free path of the photon. Then, the fraction of photons surviving a distance x is then:

$$I / I_0 = \exp(-\mu x)$$

Where I_0 is the incident intensity.

One has to take into account that these formulae for the absorption coefficient refers to photon that are either disappeared from the initial photon beam because they were absorbed, or that were scattered outside the initial direction of the beam.

For compounds and mixtures, the total absorption coefficient may be calculated using Bragg's rule:

$$\left(\frac{\mu}{\rho}\right)_{TOTAL} = w_1 \frac{\mu_1}{\rho_1} + w_2 \frac{\mu_2}{\rho_2} + \ldots = \sum_{i=1}^{N} w_i \frac{\mu_i}{\rho_i}$$

1.3. Main parameters of interest for materials employed in the detection of gamma rays

We will introduce some basic definitions of detectors properties, such as efficiency and energy resolution, together with some general modes of operation and methods of recording data that will be helpful in categorizing detectors applications.

1.3.1. Sensitivity

The capability of producing a useable signal for a given type of radiation and energy is the sensitivity of a detector. No detector can be sensitive to all types of radiation at all energies. Instead, they are designed to be sensitive to certain types of radiation in a given energy range. Going outside this region usually results in an unusable signal or greatly decreased efficiency [Leo, 1994].

Detector sensitivity to a given type of radiation of a given energy depends on several factors like: cross section for ionizing reactions in the detector, the inherent detector noise, the mass of the detector and the protective material surrounding the sensitive volume of the detector [Cooper, 2011].

1.3.2. Detector Energy Response

As well as detecting the presence of radiation, most detectors are also capable of providing information about the radiation: energy, time, etc. This follow since the amount of ionization produced by radiation in a detector is proportional to the energy it loses in the sensitive volume. If the detector is sufficiently large such that the radiation is completely absorbed, then this ionization gives a measure of the energy of the radiation. Depending on the design of the detector, this information may or may not be preserved as the signal is processed, however [Leo, 1994].

Besides some detectors operate in a continuous mode in which the signal is a continuous current or voltage, the output signal of electrical detectors is usually a current pulse type. The amount of ionization is then reflected in the electrical charge contained in this signal [Knoll, 2000].

- Energy Resolution

For detectors which are designed to measure the energy of incident radiation, the most important factor is the *energy resolution*. This is the extent to which the detector can distinguish two close lying energies. In general, the resolution can be measured by sending a monoenergetic beam of radiation into the detector and observing the resulting spectrum. The resolution is usually given in terms of the full width at half maximum of the peak (FWHM). Energies which are closer than this interval are usually considered irresolvable. Energy deposition in a detector is a stochastical process and thus it is bound to statistical fluctuations. A main limitation to energy resolution is the number of elementary processes for which charge is deposited (ionization, particle-hole creation, fluorescence excitations and subsequent emission of light) and the efficiency of these further processes. These statistical fluctuations thus should be in relative terms reduced with increasing energy, approximately as: $1/\sqrt{E}$

- Energy Linearity

Linearity of the response of the detectors is a very desirable property. That is, that the output signal of the detector is proportional to the energy deposited on it. A detector may lose linearity at the high extreme of energies (saturation) or may be nonlinear in the low end.

- Detection Efficiency

All radiation detectors will, in principle, give rise to an output pulse for each quantum of radiation that interacts within its active volume. For neutral radiation such as gamma rays or neutrons, they must first undergo a significant interaction in the detector before detection is possible. Because gamma radiations can travel large distances between interactions, detectors of finite size are often less than 100% efficient. It then become necessary to have a precise figure for the detector efficiency in order to relate the number of pulses counted to the number of neutrons or photons incident on the detector [Leo, 1994].

It is convenient to subdivide counting efficiencies into two classes: absolute and intrinsic. The Absolute or Total detection efficiencies are defined as the fraction of pulses recorded and the number of radiation quanta emitted by the source and it depends not only on detector properties but also on the details of the counter-source geometry.

The intrinsic efficiency is the ratio of number of pulses recorded and the number of radiation quanta actually incident on detector and no longer depends on the solid angle subtended by the detector as an implicit factor [Knoll, 2000].

1.3.3. Detector Time Response

- Time resolution

Time resolution is the ability of a detector or experimental set up to being used to determine the precise instant that an event happened in the detector

Time resolution is expressed in FWHM (Full Width Half Maximum) terms in the time measurements. Time histograms are usually obtained by coincidence measurements of one detector against another one employed as a reference.

- Time Jitter and Energy Walk Effects

These two effects are important sources of inaccuracy in timing measurements.

The first one applies to pulse independently on the amplitude and it is a source of time inaccuracy even if every pulse is of the same amplitude Time jitter arises because timing fluctuations, caused by noise and statistical fluctuations in the original detector signal, are always present. Because of these random fluctuations, two identical signals will not always trigger at the same point, giving a time variation independent on the amplitude of the fluctuations.

The second effect, Energy Walk, also called *Time Slewing*, is associated to the variable amplitudes of input pulse. For example, consider two signals of differing pulse height but exactly coincident in time. Suppose we introduce both signals into a discriminator with some fixed threshold and the pass over threshold is employed as time mark. Because of the difference in amplitude, one signal will appears before than the other, in spite of both arriving at the same time to the detector, one is recorded as previous to the other. This dependency of the time mark on amplitude can be reduced using improved trigger strategies.

- Decay Time

The decay time characterises the prompt scintillation yield of a material and its time of recovery before the material returns to its unexcited state and can undergo another scintillation event [Knoll, 2000].

- Dead Time

Dead Time is the minimum amount of time that must separate two events in order that they are recorded as two separate pulses. In other words, it is the finite time required by the detector to process an event which is usually related to the duration of the pulse signal. Depending on the type, a detector may or may not remain sensitive to other events during these periods. In some cases the limiting time may be set by process in the detector itself, and in other cases the limit may arise in the associated electronics [Knoll, 2000].

Because of the random nature of radioactive decay, there is always some probability that a true event will be lost because it occurs too quickly following a preceding event. These losses affect the observed count rates and distort the time distribution between the arrivals of events. To avoid large dead time effects, the counting rate of the detector must be kept sufficiently low such that the probability of a second event occurring during a dead time period is small. The remaining effect can then be corrected.

1.3.4. Radiopurity

It can be the case that the materials that the detector is made of, contain trace amounts of radioactive material. In everyday life, the effects of these radiation levels are unnoticeable. Potassium-40, uranium-238, and thorium-232 are the usual suspects when it comes to building materials. However, when you are dealing with detectors, the internal activity or the radiopurity level is a parameter that has to be determined in order to subtract its effect from the measurements. Even for inorganic crystals this feature could be a very restrictive condition for certain applications.

1.4. Most used gamma ray detectors and comparison among them

When ionising radiations pass through any material, gaseous, liquid or solid, ionisations are created as energy is lost. Solid materials have the advantage of high density and hence high materials have the advantage of high density and hence high stopping power, especially compared with gases, and so offers the prospect of a compact and high efficiency detector [Leo, 1994].

If a high electric field can be sustained across the solid then the charge released by the ionisation can be collected and the presence of ionising radiation so recorded. It is essential that the current flow through the detector in the absence of ionising radiations is negligible in order that the small quantity of charge that is produced by the ionising event can be observed, and so metals are totally unsuitable [Cooper, 2011].

1.4.1. Semiconductos

The ionisation process in crystalline solids consists of raising electrons from the valence band to the conduction band, a process that leaves an equal number of positive holes in the valence band. Materials with a small band gap such as germanium (0.7 eV) and silicon (1.1 eV) require an average of 3.0 eV and 3.6 eV, respectively, to be expended in creating a hole-electron pair, and so the amount of primary charge released is about ten times that in a gas-filled detectors [Cooper, 2011].

a. HPGe

For gamma-ray detection, germanium is preferred over silicon because of its much higher atomic number (Z(Si)=14, Z(Ge)=32). The photoelectric cross section is thus about 60 times greater in Ge than Si. Germanium, however, must be operated at low temperatures because of its smaller band gap. This inconvenience is offset, however, by its greater efficiency. Germanium may also be used for charged-particle detection however, apart from its larger stopping power, it offers no advantages over silicon and, in fact, becomes disadvantageous

because of its need for cooling.

Because of the small band gap (0.7 eV), room-temperature operation of germanium detectors of any type is impossible because of the large thermally-induced leakage current that would results. Instead, germanium detectors must be cooled to reduce the leakage current to the point that the associated noise does not spoil their excellent energy resolution. Normally, the temperature is reduced to 77 K through the use of an insulated Dewar in which a reservoir of liquid nitrogen is kept in thermal contact with the detector.

The principal application of germanium detectors is gamma ray spectroscopy. At present, germanium detectors offer the highest resolution available for gamma-rays energies from a few keV up to 10 MeV. In this work HPGe detectors will be characterised and then employ to measure the intrinsic activity and other properties of the other detectors considered in this thesis.

1.4.2. Scintillator Detectors

A scintillator detector is comprised of two main components: firstly, a scintillator that absorbs incident radiation and converts the energy deposited by ionisation into a fast pulse of light and, secondly, a photodetector that transform the visible light received into an electric signal. Indeed, this second component is very often an electron photomultiplier (PMT) which converts the light pulse into a pulse of electrons and also amplifies the electron pulse by a very large factor by means of a sequence of secondary emission stages. Further external amplification is generally necessary before the pulse can be processed or recorded [Cooper, 2011].

In general, the scintillator signal is capable of providing a variety of information. Among its most outstanding features are [Leo, 1994]:

- *Sensitivity to Energy*: Above a certain minimum energy, most scintillators behave in a near linear fashion with respect to the energy deposited. Since the photomultiplier is usually a linear device, the amplitude of the final electrical signal will also be proportional to this energy. This makes the scintillators suitable as an energy spectrometer although it is not the ideal instrument for this purpose.
- *Fast Time Response*: Scintillation detectors are fast instruments in the sense that their response and recovery times are short relative to other types of detectors. This faster response allows timing information. This and its fast recovery time also allow scintillation detectors to accept higher count rates since the dead time.
- *Pulse Shape Discrimination*: With certain scintillators, it is possible to distinguish between different types of particles by analyzing the shape of the emitted light pulses. This is due to the excitation of different fluorescence mechanism by particles of different ionizing power. The technique is known as pulse-shape discrimination.

While many scintillating materials exist, not all are suitable as detectors. In general, a good detector scintillator should satisfy the following requirements: high efficiency for conversion of exciting energy to fluorescence radiation, transparency to its fluorescent radiation so as to allow transmission of the light, emission in a spectral range consistent with the spectral response of existing photomultipliers, and a short decay constant [Leo, 1994; Cooper, 2011].

At present, six types of scintillator materials are in use: organic crystals, organic liquids, plastics, inorganic crystals, gasses and glasses. For our purpose we only will comment the inorganic scintillators [Knoll, 2000].

1.4.2.1 Inorganic Crystals

The inorganic scintillators are mainly crystals of alkali halides containing a small activator impurity. By far, the most commonly used is NaI(Tl), where Thallium (Tl) is the impurity activator. Other crystals include CsF2, CsI(Tl), CsI(Na), KI(Tl) and LiI(Eu). Among the non-alkali materials are BGO, BaF2, ZnO(Ga), CdWO4 among others [Leo, 1994].

In general the inorganic scintillators are 2-3 orders of magnitude slower (~500 ns) in response than organic scintillators due to phosphorescence. A major disadvantage of certain inorganic crystals is hygroscopicity. To protect it from moisture in the air, it must be housed in an air tight protective enclosure. Other hygroscopic crystals are CsF, KI:Tl. On the other hand, BGO and BaF2 are non-hygroscopic and can be handled without protection, while CsI:Tl is only slightly hygroscopic but can generally be handled without protection.

The advantage of inorganic crystals lies in their greater stopping power due to their higher density and higher atomic number. Among all the scintillators, they also have some of the highest light outputs, which results in better energy resolution. This makes them extremely suitable for the detection of gamma-rays and high-energy electrons and positrons.

Scintillation spectrometers are widely used in detection and spectroscopy of energetic photons (X-rays and γ-rays) at room temperature. These detectors are commonly used in nuclear and particle physics research, medical imaging, diffraction, non-destructive testing, nuclear treaty verification and safeguards, nuclear non-proliferation monitoring, and geological explorations [Shah, 2005].

In this work we are going to focus in explore the properties of two novel scintillators crystal: $CeBr_3$ and LuAG:Pr. As well we going to use the faster inorganic crystal in order to perform the time response characterization: BaF_2. In the next table we compare the main properties of the detectors that we will characterize or use in this thesis work:

	Detector				
Feature	HPGe	LYSO:Ce	LuAG:Pr	$CeBr_3$	BaF_2
Detector type	Semiconductor	Scintillator			
Density (g/cm^3)	5.32	7.2	6.7	5.1	4.9
Resolution at 662 keV	<0.5%	~9%	~7%	~5%	~9%
Operating Temperature (ºC)	-178	Environmental (no cooling needed)			
Peak Emission (nm)	N-A	420	310	370	210-310
Internal Activity	Negligible for standard purposes	Yes, mainly from ^{176}Lu.		Negligible for standard purposes	
Hygroscopicity	Encapsulated	No		Yes	Slightly

Table 1.2: *General comparison of the detectors used in this work.*

Although the HPGe is the best detector for gamma-ray spectroscopy, it is also the most expensive and it is not easy to transport. Inorganic scintillators are relatively cheaper than HPGe and can be coupled to any photomultiplier with wide sensitivity. Semiconductors are slow detectors compared to scintillators. Because its fast response, scintillators are widely used under high fluence scenarios like medical imaging or nuclear reactors. Instead of the more expensive and delicate semiconductors, many applications are based on scintillator detectors because of their portability and detector design flexibility.

The scintillators previously mentioned, with the exception of BaF_2, belong to the new generation of inorganic scintillators. In the last years almost all the companies which grow and sell this kind of crystal have developed new formulas in order to improve time and energy responses. For instance, $CeBr_3$ substitutes NaI:Tl with much improved features: very good energy resolution, fast response and small intrinsic radioactive background As NaI:Tl, $CeBr_3$ is hygroscopic and it needs to be encapsulated. Another new scintillator, LuAG:Pr has also very good parameters, as for instance an stopping power almost similar to BGO, but with a much better energy resolution and a much faster time response. It has, however, a sizeable internal activity. LuAG:Pr is almost not hygroscopic and it is easy to handle and to explore configurations as phoswich or arrays of several crystals.

1.5. Scope of this thesis

In this thesis we will study several devices employed for gamma spectroscopy. Beginning with an HPGe detector that will be used as energy reference, to measure internal activity and to compare efficiency, with the other detectors studied in this thesis. Further, two new inorganic materials recently introduced in the market, a high-Z lutetium based scintillator, and a halide one, CeBr3, similar to LaBr3:Ce, will be studied for efficiency, energy resolution and timing properties.

Finally, we would assess the possibility of combining two dissimilar scintillators optically coupled to a single photomultiplier, either SiPM or PMT, what is often called a phoswich detector. The crystals for the phoswich detectors are chosen to have different decay times so that the shape of the output pulse depends on the relative contribution of scintillation light from the two scintillators [Knoll, 2000]. Most applications involve the use of this pulse shape difference to distinguish events that have occurred in only one scintillator from those that occur in both, or events that take place in one layer against events that take place in another.

1.6. Goals of this thesis

The Nuclear Physics Group of Complutense University (GFN-UCM) is actively engaged in the development of new gamma detectors, with improved energy resolution, timing properties, stopping power or all of them altogether. These are needed on one side due to the commitment of the group to the development of FATIMA (Fast Timing Array, (http://nuclear.fis.ucm.es/fasttiming), coordinated by Luis Mario Fraile and funded within NUPNET. The goal of FATIMA is to design a new modular high-efficiency FAst TIMing array designed for measurements with the ultra fast timing method using fast response scintillation detectors, to measure level lifetimes in the range from a few picoseconds to several nanoseconds [Mach, H., *et al.*, 1989, Mach, H., *et al.*, 1991]. Thus a large part of the activity presented in this thesis are aimed toward the test of new scintillator and

photodetectors that can be used for fast timing with improved in the existing ones, either in price, performance or both. To this end, the recently available $CeBr_3$ scintillator was tested and fully characterised [Fraile, L.M., *et al.*, 2013 (1), Fraile, L.M., *et al.*, 2013 (2), Fraile, L.M., *et al.*, 2011, Corzo, P.M.G., *et al.*, 2010, Vaquero, J.J., *et al.*, 2010]. Also related to the fast timing measurements agenda of the GFN-UCM were the characterization for timing, efficiency and energy resolution of the very newly introduced LuAG:Pr scintillator. Not only this scintillator has a high stopping power, similar to BGO, but its energy resolution is very interesting and, further and not so well established in the literature previous to our work, its timing properties make this scintillator a very promising alternative for fast timing measurements where the internal activity is not a drawback.

The GFN-UCM is also heavily involved in the development of new detectors for Positron Emission Tomography imaging [PhD thesis: Vicente, E., 2012; Abushap, K., 2012, España, S., 2009 and papers: Fraile, L.M., *et al.,* 2012, Corzo, P.M.G., *et al.*, 2010]. This includes the evaluation of new scintillators with improved timing capabilities for their use as PET detectors with time of flight capabilities, a technology which enables PET images of quality (spatial resolution, quantification properties, signal to noise ratio) not achievable in common PET scanners. For this application, the LuAG:Pr scintillator may prove very useful, depending on the results of its characterization. Thus, a second part of this thesis work pertains the evaluation of LuAG:Pr and to assess its suitability for PET applications, including its suitability to be mounted in phoswich arrangements.

2. HPGe Characterization

Abstract: We report on a characterization and optimization of a gamma spectroscopy system based on an N-type HPGe detector. In order to set the best perfom of this semiconductor detector, we have explored not only the physical properties of the crystal itself but the electronic parameters associated to the signal processing like shaping time, bias supply, dead time, peaking time, etc. Furthermore, we have obtained the full energy photo-peak efficiency for this detector at several distances. These values were fitted by a semi-empirical expression and then used to calibrate point-like gamma sources and to estimate the internal activity of a scintillator crystal. Finally, we have performed a cooling system to refill periodically the Deward with LN2.

2.1. Introduction

Hyper-pure germanium (HPGe) detectors are essential instruments in high-resolution gamma spectroscopy applications. In this chapter we characterize a semiconductor detector based on hyper-pure germanium (HPGe) with the aim of obtain the absolute efficiency in function of distance and energy as well to fit a semi-empirical formula to interpolate energy values in a range from 30 to 1408 keV. The precise knowledge of the absolute full energy peak efficiency at several distances makes it possible to use the detector for several applications. In particular, in the following sections, we are going to calibrate a set of exempt radiosources and to determine the internal activity of a sample of scintillators crystals.

In order to study low-level gamma sources and internal activity of scintillators, a detector with a high energy resolution and a good efficiency for low energy gammas and X-rays should be used. Under these conditions, high purity germanium detectors are the best suited for this purpose. In particular, current N-type models provide several improvements such as increased energy window (including low energies gamma and X-rays), which allows identifying gamma lines at very low energy (near to 10 keV), and enhanced geometric efficiency (nowadays it can reach bigger sizes). In more recent years, advances in semiconductor growth technology have allowed the fabrication of very high purity germanium (HPGe) with impurity concentrations of less than 10^{10} atoms/cm^3 [Leo, 1994, Van Cleef, 2009].

The HPGe detectors operate as reverse-biased semiconductor diodes. When the incoming radiation passes through the semiconductor crystal, it produces electron-hole pairs. These released charges are collected at electrodes in the surfaces of the crystal due to the electrostatic field applied to the junction. The number of electron-hole pairs created, and magnitude of the resulting electrical signal, is proportional to the amount of energy deposited in the detector by the incoming radiation [Boson, 2008]. A reverse-biased semiconductor representation is shown in the figure 2.1.

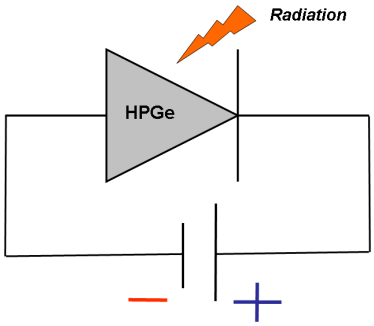

Fig. 2.1: *Representation of HPGe as reverse biased semiconductor diode.*

In this thesis we have used a LOAX 60450-30P-CW model provided by ORTEC. It is a N-type semiconductor detector based on high purity germanium (HPGe). This kind of detectors is optimized to measure X-rays and low-energy gammas (down to 10 keV or even below) because the aluminium capsule has a thin carbon entrance window, which lets low energy photons through. Furthermore, the N-type allows using a very thin external contact (ion implanted contact) that reduces the stopping power or collimation of incident radiation [ORTEC, 2012].

In addition, in order to keep the detector and the surrounding electronics cool, the detector is housed inside an aluminium capsule together with several electronic elements, such as the preamplifier, a high voltage filter, an impurity filter, voltage contacts, carbon fiber, etc. The aluminium capsule is a so-called PopTop model by ORTEC, which has its own vacuum and makes it possible to move it and install it in any suitable cyrsotat. A scheme of our detector is shown in the figure 2.2.

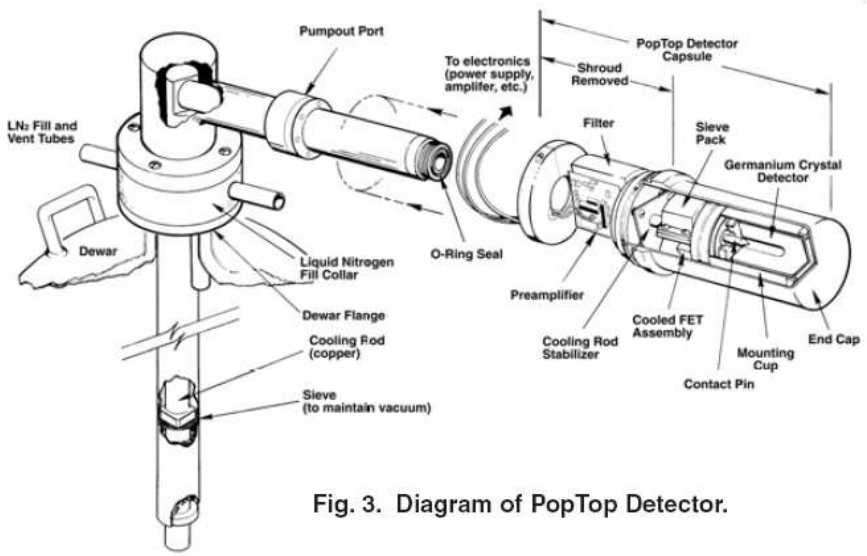

Fig. 2.2: *Scheme of PopTop Detector and Diagram of a PopTop Detector* [ORTEC, 2012].

In the following we first describe the optimization of several parameters of the HPGe detector in order to get the best HPGe performance. Consequently we made several tests over different variables of the spectroscopic processing; especially we have focused on digitization parameters like shaping time, peaking time, dead time and energy resolution. Afterwards the photopeak efficiency is obtained and a semiempirical formula is used to describe its dependence with energy.

2.2. Experimental set-up

2.2.1. The LOAX 60450-30P-CW HPGe detector

Inside the PopTop capsule there is an N-type crystal of High Purity Germanium (HPGe). This kind of detector works as a semiconductor diode, this means that its operation is based on the electronic band structure in crystalline material with a valence band in which electrons cannot move, and a conduction band in which the electrons can move. For HPGe the forbidden energy gap is around 0.7 eV [Leo, 1994, Tacetti, 1997].

When the incoming radiation interacts with the detector, some electron-hole pairs are produced inside the semiconductor. The released charges can travel through the crystal until are collected by the electrodes at the surfaces of the detector. Even, before they are catched, the charges release more charges because are accelerated by the applied electric field. Finally, the number of electron-hole pairs created, and magnitude of the resulting electrical signal, is proportional to the amount of energy originally deposited in the detector [Ljungvall, 2005, Sze, 1985].

For semiconductor diode detectors, a reverse bias is applied over a p-n junction. This bias should be large enough to completely deplete the detector and to saturate the drift velocity of electrons and the holes [Knoll, 2000]. If the germanium crystal has an N-type configuration, then the contact material can be reversed, that is, the thin contact (*minus terminal*) can be put on the outside of the crystal while the thick contact (*plus terminal*) on the inside, as shown in Fig. 2.3. This configuration still maintains the junction near the inner contact. Furthermore, the low energy efficiency increases due to the reduced thickness of the dead layer [Keyser, 2004].

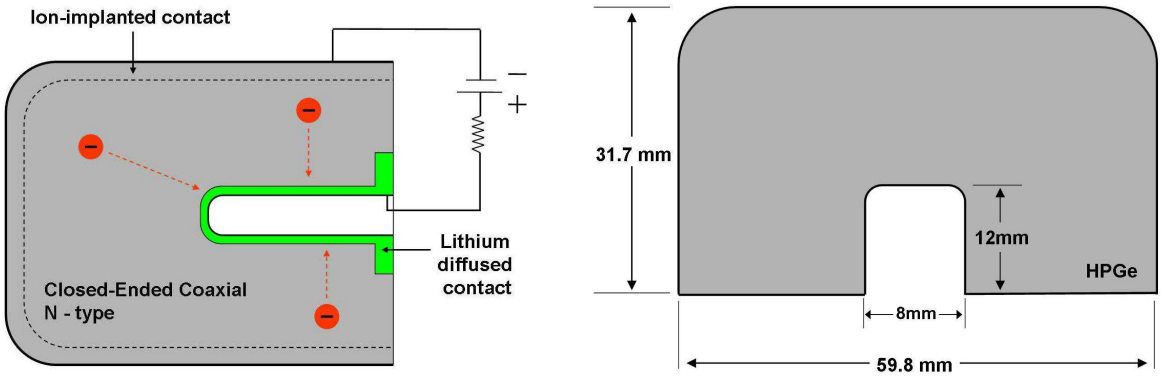

Fig. 2.3: *Left, closed-ended coaxial HPGe in N-type configuration. Right, dimensions of the HPGe crystal in our LOAX 60450-30P-CW, as provided by ORTEC.*

Another important feature of our HPGe is its geometry. The detector belongs to the closed-ended type of coaxial detectors [ORTEC, 2012]. This means that this detector provides some advantages regarding to typical "true coaxial" geometry. First, it allows overcoming the leakage current problem at the front. Second, it allows the transmission of low energy radiation through the front surface, only if it is made with a thin contact. Additionally, our detector has a bulletized geometry, that is, the corners of the front surface were rounded in order to remove weak electric fields close to the corners of the crystal. In this way the net electric field is more homogenous inside the crystal (see figure 2.3) [Knoll, 2000].

2.2.2. Cooling the HPGe: Liquid Nitrogen, Dewar and extraction

The high energy resolution of the HPGe is due to the small value of the forbidden energy gap (for Ge 0.7 eV). However, the resolution is strongly dependent of the temperature. If the temperature of the HPGe is not low enough, the resolution deteriorates due to the increase of the forbidden energy gap, the thermal noise and the leakage current. It is only at sufficiently low temperature (usually liquid nitrogen temperature) that thermal generation of intrinsic carriers (electrons and holes) in the germanium crystal becomes negligible, the forbidden energy gap is optimized and the leakage current decreases to the low value that is required for good performance [Taccetti, C., *et al.*, 1997, Vénos, C., *et al.*, 2000]. For this reason is imperative keeping the germanium cooled. The customary procedure to achieve the needed cooling is the use of liquid nitrogen, although alternatives using electrical cooling are commercially available.

The detector must be housed in a vacuum-tight cryostat to reduce potential condensation of impurity gases on the detector surface and to inhibit thermal conductivity between the crystal and the surroundings [Knoll, 2000]. In order to cool the detector, the cryostat is usually mounted on a liquid nitrogen Dewar. In this configuration the cryostat is cooled by thermal conductivity achieved by a thermal finger in contact with the deposit of liquid nitrogen (See figure 2.4). There are several geometries for cryostat; in our case the model ORTEC **CFG-LP-SH** is a horizontal extension coupled to 30 litters Dewar [ORTEC, 2012].

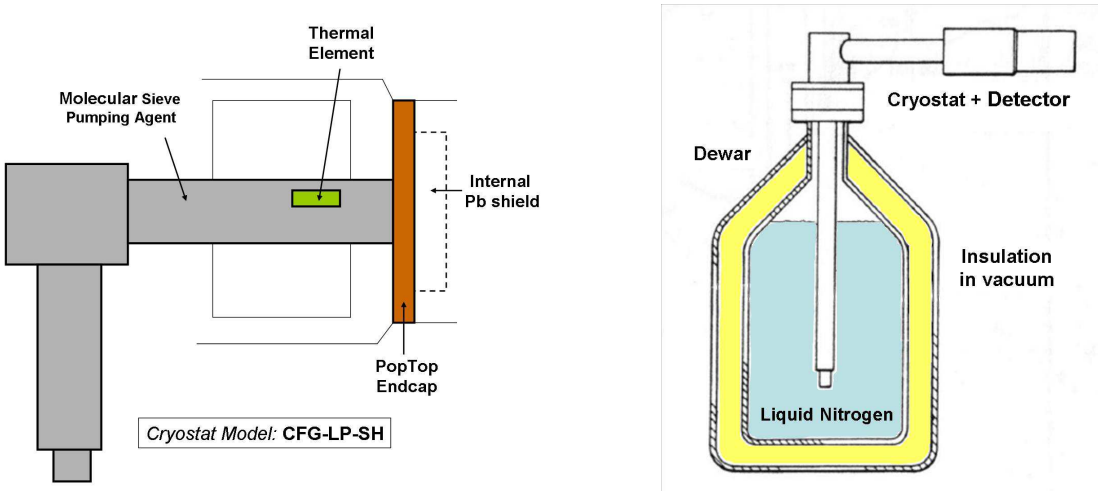

Fig. 2.4: *Left, cryostat model CFG-LP-SH provided by ORTEC (coupled to PopTop detector). There are versions with Pb shielding in the back, but in this model it is not included it. Right, scheme of the coupling between cryostat, thermal finger and liquid nitrogen deposit.*

Often there is a molecular sieve or charcoal trap in the cryostat to help establish high vacuum conditions. These filters are effective only at liquid nitrogen temperatures, thus it may be advisable to maintain germanium detectors constantly at liquid nitrogen temperature as a precaution and to help ensure a longer lifetime [Taccetti et al., 1997]. In fact, to prevent serious damage, high voltage can be applied to the diode only when the crystal temperature is sufficiently low to make reverse current negligible [Leo, 1994]. For all these reasons, we have devised a "boiling system" to transfer nitrogen from a portable Dewar into a fixed Dewar reservoir (See figure 2.5). This system is an extension of a similar system developped for a positronium laboratory [From J. del Río, 2010 (internal communication)].

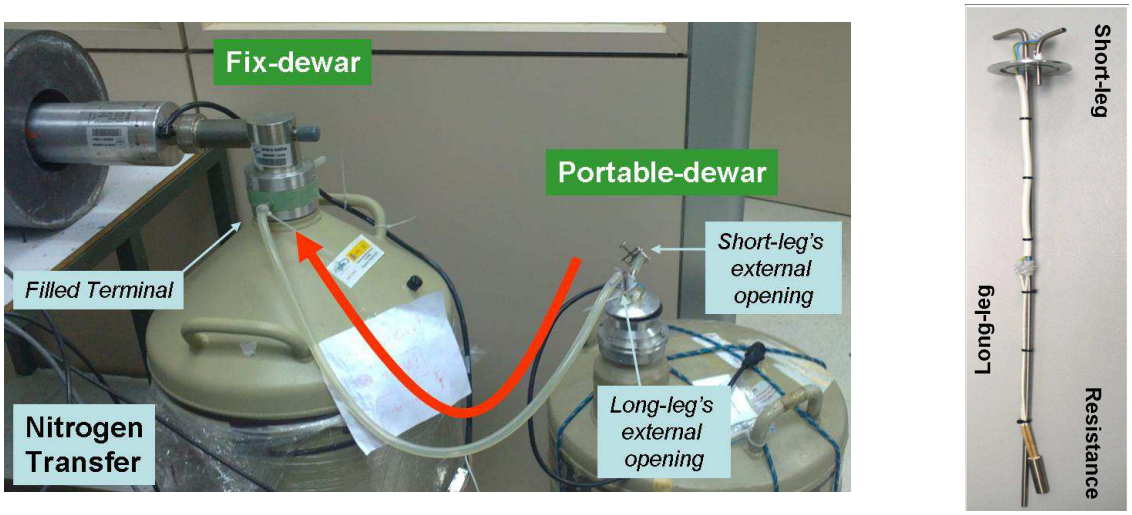

Fig. 2.5: *Left, nitrogen transfer from a portable-Dewar to fix-Dewar. Right, stick to extract LN2.*

Our "boiling system" consists basically in an aluminium stick with two legs and one resistance coupled to longest leg (See figure 2.5). Each leg is a hollow aluminium cylinder of diameter 5 mm to let the liquid nitrogen go through it. Likewise a dissipative resistance is used to boil the liquid nitrogen, which is chose to dissipate 100W at 100 V.

In order to refill the fixed Dewar, a pressure gradient between Dewars is created just to pull out the LN2 from one (Portable-Dewar) and drive it to another (Fix-Dewar). This is the procedure: First, the stick is introduced into the portable-Dewar. Second, while the external opening of the short-leg is closed, the external opening of the long-leg is connected to the filled terminal (know as fill tubes, too) by a plastic hose. Third, 100V are applied to the resistance in order to boil the LN2, so some liquid nitrogen (LN2) begins to become into gas nitrogen (Ni_2). Fourth, the remains LN2 is pushed by the gas pressure to goes though the long-leg and the hose toward the Fix-Dewar. Thus, the LN2 is diverted from one container to another because a pressure gradient was established between Dewars (See figure 2.6).

When the fix-Dewar is overflowing, the external opening of the short-leg has to be open and the voltage must to be removed, thus the gaseous nitrogen can escape and the pressure over the LN2 is reduced. After few minutes the hose could be disconnected and the external opening of the short-leg is closed again in order to reduce nitrogen losses. (See figure 2.6)

Because the large volume of the Dewar used (30L) and the system is required to be cool while is working, the fix-Dewar was refilled one time per week during the campaign of measurements. Despite small losses of nitrogen during each boiling process, this method is inexpensive and faster compared with integrated vacuum systems or conventional suction pump devices.

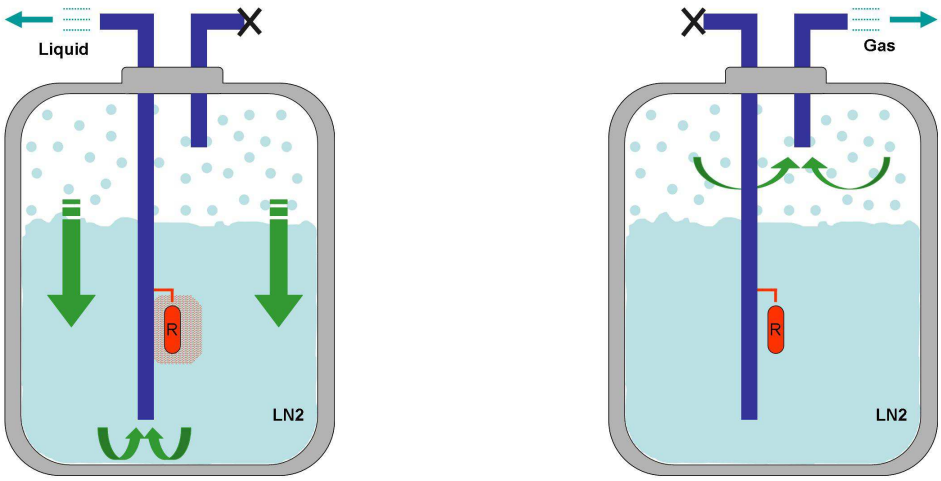

Fig. 2.6: *Left, the system is operating and the LN2 is pulling out through the stick. Right, the longest leg of the stick is closed, the voltage is off and the nitrogen vapour goes out though the short leg.*

2.2.3. Carbon Window

In order to reduce attenuation of gamma rays before they interact with the detector, a thin end window is located close to the detector. This window increases the transmission of lower energy gammas than normal aluminium housing [Knoll, 2000]. Usually for HPGe this end cap consists of a beryllium or carbon filter because both have a smaller Z compared to the aluminium [Mauring, 2012]. In the figure 2.7 is shown a comparison of transmission and intrinsic efficiency to low energy gammas and X-ray through Be and C windows.

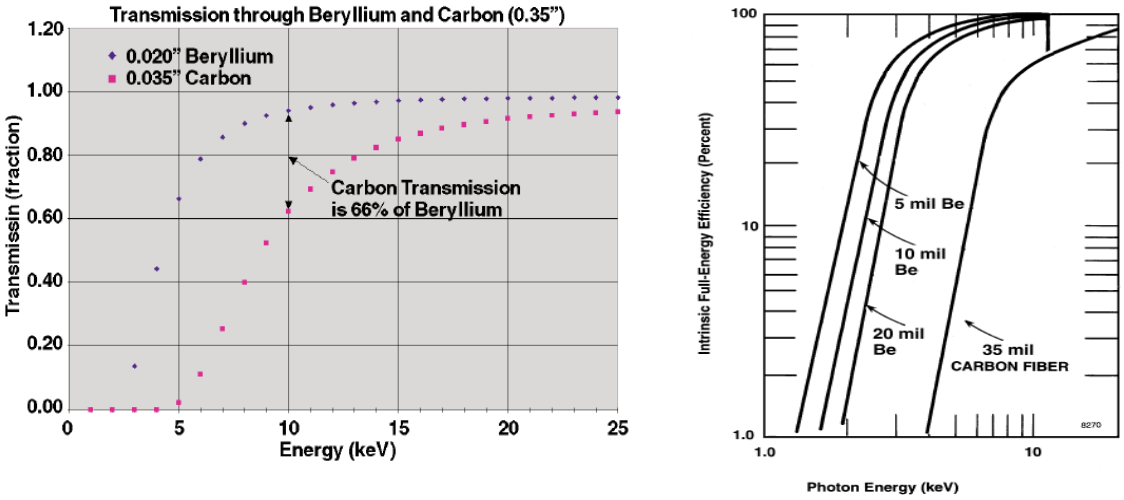

Fig. 2.7: *Left, low energy gamma and X-ray transmission through B and C windows. Right, intrinsic full-energy efficiency according with energy and window thickness.*

The lower Z of these windows allow to reduce the MDA (Lower Minimum Detectable) for a specific counting time, which provides another step in increasing sample throughput in low background counting applications. Moreover, these fibers provide a low-energy window without the additional background found in most alloys. [ORTEC, 2012, Mauring, 2012]

The carbon window lets in gammas and X-rays over 5 keV, although the provider recommends use for energies higher than 8 keV because the intrinsic efficiency is upper than

40% from this value. Furthermore, the carbon window is cheapest and less toxic than beryllium [ORTEC, 2012].

For the model **LOAX 60450-30P-CW** there is a carbon fiber window. In the figure 2.8 the crystal and carbon windows are drawn using the sizes reported by the provider.

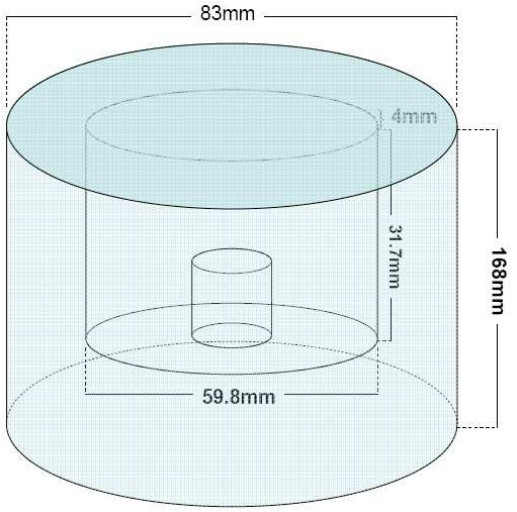

Fig. 2.8: *Scheme of detector (internal cylinder) and carbon window (darker circle). The draw is not a scale but the sizes were reported by the provider.*

2.2.4. Lead Shielding

In order to reduce the gamma background contribution, the detector should to be surrounded by thick shielding material. Usually the shielding is made of materials with a high atomic number such as lead, steel or concrete [Leo, 1994]. Among all the conventional low-background shields the lead (Pb) is the most widely used because of its high density, malleability and large atomic number [Knoll, 2000].

Because the PopTop detector has a cylindrical shape, a cylindrical shielding of Pb was used to remove gamma rays coming from natural and artificial sources, and so to reduce the gamma background. In the figure 2.9 the set-up is shown. The shielding covers the detector region and let some space to put the sample to characterize. The back of the Poptop no needs to be covered because just contains electronic.

Fig. 2.9: *Lead shielding. Left, how the shielding covers the PopTop and the end cap. Right, the space to put material is appreciated.*

On the other hand, some X-rays are released by the lead because some cosmic rays and gammas coming from the samples interact with the shielding. These X-rays could enter to the detector and increase the background. For this reason this effect has to be taken into account during the analysis, this means the contributions of X-rays from Pb have to be subtracted from the spectra. In the next chart (see figure 2.10) the X-ray coming from lead are listed according to National Nuclear Data Centre [Martin, 2007].

XR	Energy (keV)	Intensity (%)
l	10.6	2.8 % *12*
kα2	72.805	2.0 % *6.*
kα1	74.969	3.4 % *9.*
kβ3	84.45	0.4 % *11*
kβ1	84.938	0.8 % *22*
kβ2	87.3	0.3 % *8.*

Fig.2.10: *List of X-ray from lead taken from NNDC.*

2.2.5. Electronic Devices

Because signal processing plays an extremely important role in extracting useful information from detectors, there is important to characterize all the electronic devices that shape the spectrometric system. Besides the Low-Energy Photon Detector (LOAX) manufactured by ORTEC, we should to study and to optimize the parameters in the charge-sensitive preamplifier, HV power supply, amplifier, wave generator oscilloscope, and multichannel analyzer (MCA). In the figure 2.11 a schematic of the set-up is shown.

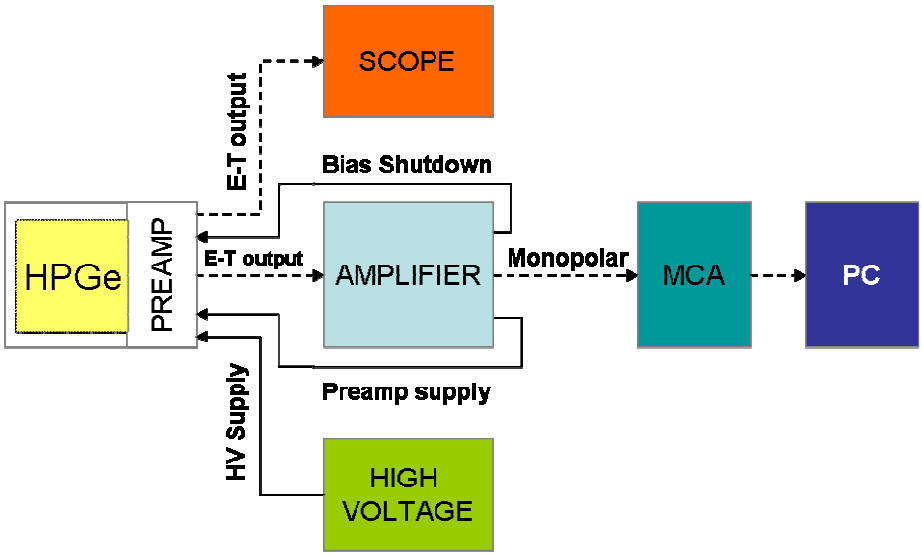

Fig.2.11*: Schematic representation of the set-up.*

2.2.5.1 Preamplifier

The signal pulse produced as a result of passage of radiation through an HPGe detector usually has a very narrow width, short duration, noise and small amplitude, thus it can not be directly digitized or even counted. For these reason a preamplification stage is necessary before any further treatment of the signal [Naeem, 2007]. Thereby, the main purposes of the preamplifier are: provide an optimum coupling between the detector and the rest of the electronic system, shape to the pulse, minimize the noise by filtering, and increase the amplitude of the pulses [Tsoulfanidis, 1995].

In order to reduce the electronic noise and to optimize the coupling between devices, the preamplifier must to deal with changes in the capacitance of the detector and from cables. Thus, to reduce the capacitance effect from wires, the preamplifier has to be mounted as close as possible to the detector. For high resolution operation at low temperatures, such as with HPGe, a direct coupling is made for the minimum in input capacitance. In fact, a direct coupling also allows monitoring of the leakage current [Leo, 1994]. Besides, to compensate changes in capacitance of the detector by unfix temperature, the preamplifier has to be insensitive to change in capacitance and also must to act as an integrator of charge, which means, a charge-sensitive preamplifier is needed [Tsoulfanidis, 1995]. This device, instead of directly amplifying the voltage or converting the current to voltage, integrates the accumulated charge on the detector capacitance in another capacitor [Naeem, 2007].

Inside the PopTop there is, almost touching the detector, a charge-sensitive preamplifier model A259 provided by AMPTEK (see figure 2.12). This preamplifier belongs to the A250 series, which, in order to reduce the noise, a low capacitance capacitor is put just in the output of the detector. Likewise, a FET is incorporated to control the conductivity between preamplifier and detector (See Figure 2.12). Both devices can resist very low temperatures without create noise or deform the signal [AMPTEK, 2012], this imply, the system is able to ensure the proportionality between the output voltage and the total collected charge in the detector [Knoll, 2000]. Even, the signal-to-noise ratio can also be increased without be affected by pile-up effects [Leo, 1994].

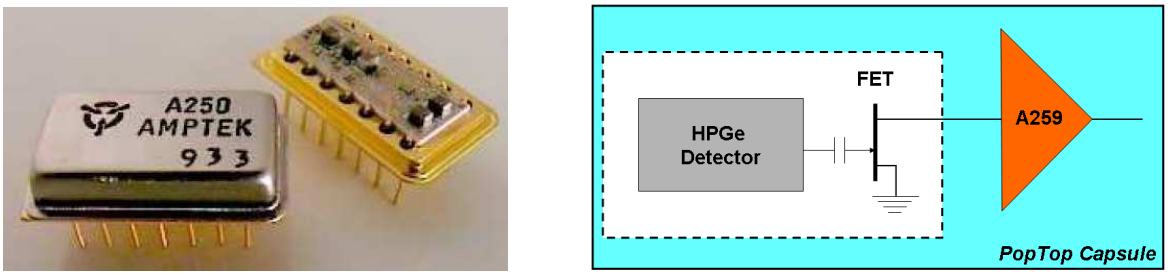

Figure 2.12: *Left, exemplary of A250 preamplifier. Right, Scheme of preamplifier, FET and capacitor inside the PopTop capsule.*

2.2.5.2 Amplifier

From the PopTop comes out two duplicated preamplified signals, called Energy and Time signals. Before the pulses are registered in the MCA, one of the signals must be connected into the amplifier, while the other has to be ended with a 50Ω resistance. In fact, the main functions of the amplifier are: fix the gain of the signals (increase the amplitude), restore the

baseline, filter the noise, provide a (near-) Gaussian shaping and cancel the pole-zero [Knoll, 2000].

In our case, the amplifier is a Nuclear Instrument Module (NIM) model 2022 provided by Canberra, which have a 6-steps shaping time selector (times in μs: 0.5, 1, 2, 4, 8 y 12), a 6-steps course gain selector (with factors of: 10, 30, 100, 300, 1K, 300K), a continuous fine gain selector (with factors from 0.3-1.3), a input polarity (positive and negative), a multi-turn screwdriver adjustable pole/zero, an automatical base-line restorer, a standard Amphenol (type 17-10070) bias to preamplifiers in the rear panel, and several BNC connectors to input and output signals (see figure 2.13).

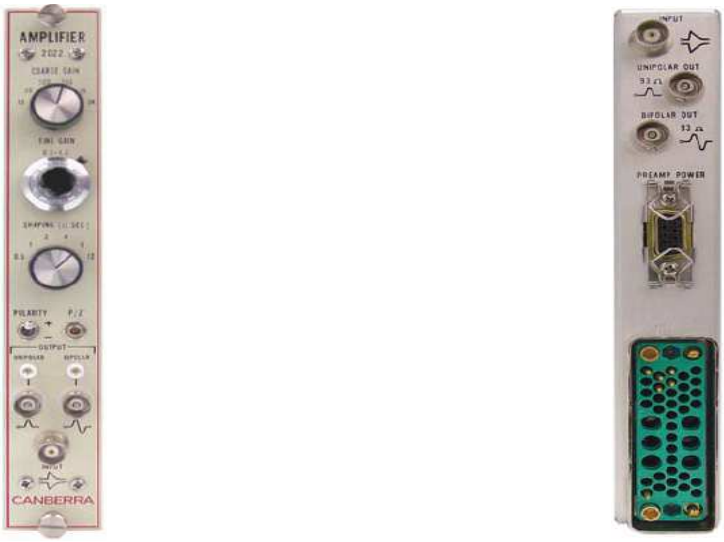

Fig. 2.13: *Canberra Amplifier model 2022. Left, frontal panel. Right, Rear panel.*

From the amplifier there are two output signals. One of them is unipolar with a positive lobe, while the other is bipolar with a positive lobe leading. Usually the first one is used to gamma spectroscopy, this means, it is carried to the MCA whereas the other is used to timing or gating applications. In all cases, both signals have linear amplitude until 10V, that is, the integral is proportional to the amplitude of the preamplified signal.

Finally, an ideal spectroscopy amplifier should have a constant amplification for pulses of all amplitudes without distorting any of them. Unfortunately, some pulse distortion is always present because of electronic noise, gain drift due to temperature, pulse pile-up, and limitations on the linearity of the amplifier [Tsoulfanidis, 1995]. For these reason we have to explore the best configuration of parameters in order to optimize the spectroscopy information obtained from the detector.

2.2.5.3 HV power supply

Because the bias voltage determines not only the thickness of the depletion layer but the capacitance of the detector, its value have to be controlled in order to set a stable coupling between devices and to reduce the thermal noise [Leo, 1995].

The number of fully stopped radiation and the pulse height depends of the applied voltage. When the bias voltage and electric field are low, the collection of charge carriers is

incomplete because of trapping or recombination along the track of the incident particle. The fraction that escape to the collection will decrease as the electric field is increased. Once the electric field or high voltage is sufficiently high, charge collection becomes complete and the pulse height no longer change with further increases in the detector bias voltage. This region normally is called the saturation region or true saturation region [Schmitt, 1975].

If radiation of a single energy and type are involved, it is sometimes possible to operate the detector at a bias voltage that is shorter than true saturation without significant deterioration in the energy resolution; in someway the fraction of charge lost for each event at this voltage is likely to be nearly constant. Now, if the radiation have diverse energy, then it is quite important to ensure that the detector is operating in the region of true saturation to avoid significant deterioration in the energy resolution [Knoll, 2000].

In our case, the high voltage is biased by an ORTEC NIM model 459 (see figure 2.14), which is optimized for HPGe detectors, this means, it afford a stable power supply and give the bias for remote shutdown. This module has an internal switch to select the voltage polarization. In the front panel there is a continuous selector to set the wished value of voltage and some screen to control the magnitude. Also, it have a switch to activate the high voltage, otherwise the supply is suspended. In the rear panel there are three SHV connectors, both of them are to provide two different range of voltage (0-500 V and 0-5kV). The spare connector is to provide the supply for the remote shutdown.

The voltage supply should be applied only when the HPGe is cooled at LN2 temperature. The ratio of increasing has to be slow, starting from 0V until get to the saturation region (in our case the provider suggests -3500V). The ratio can be estimated following the behaviour of the baseline of one signal that coming from the preamplifier. Often an exempt gamma source is used to get pulses and to visualize the signal in an oscilloscope. The PopTop accepts only small increments of the voltage; otherwise the baseline and pulses are missed in the screen. In that case it is recommended to wait until the baseline and pulses come back to the equilibrium state, then the supply process can be continued until arrive to the right voltage value.

Fig. 2.14: *Power Supply model 459 provided by ORTEC.*

2.2.5.4 Multichannel Analyzer (MCA)

The Multichannel Analyzer (MCA) is a device which sort out incoming pulses according to pulse height and keep count of the number at each height in a multichannel memory. The contents of each channel can then be displayed on a screen or printed out to give a pulse height histogram [Leo, 1994].

The MCA digitize the amplitude of the incoming pulses through of an analog-to-digital converter (ADC), which associates a value according to the pulse height. The MCA takes this value and looks for the memory channel whose value is proportional to the digitized value and then increments in one the number of events stored. In this way incoming pulses are sorted out according to its height and located in the right memory channel [Knoll, 2000]. Furthermore, the total number of channels settles the grid into which the voltage range going to be digitized. This grid is known as *conversion gain* and determines the resolution of the MCA. Nowadays most of the commercial MCA offer conversion gain upper 128 until 8 or 16K [Tsoulfanidis, 1995]. The nominal value of the resolution depends on the number of bits provided by the ADC, and is specified as the maximum number of addressable channels [Knoll, 2000].

In our case the unipolar signal goes to MCA (MCA8K-01) manufactured by Atomki and is known as PalmTop. This device is optimized to collect signals from nuclear radiation detectors such as HPGe, Si or CZT. It accepts positive going unipolar or bipolar semi-Gaussian shaped pulses with shaping time constant >100 ns. A dual sliding scale ADC is incorporated in order to provide good values of nonlinearity. Also, it includes a dead-time and pile-up correction circuitry to assures stability even at high counting rate and to remove pile-up events from the spectrum. Moreover, this MCA is a portable instrument because have a small size and operates without external power supply or batteries, just needs a PC with USB ports [Atomki, 2009].

The PalmTop have three female lemo terminals, two works as gates for coincidences or anticoincidence events, and the other is to connect the input signal from amplifier. Also, have a 3-step selector to fix the voltage range allowed (0-2.5V, 0-5V and 0-10V). Furthermore, there have a USB port to link with the PC to send info and to be biased (see figure 2.15).

Fig. 2.15: *PalmTop MCA of Atomki.*

On the other hand, the MCA has a digital interface (named *PalmTop MCA version 2.6*) to deal with the spectral info and to control several functions of the MCA. This software runs on windows environment and allows controlling several variables like the number of channels, threshold level, pile-up filters and peaking time. In the figure 2.16 is shown the hardware setup panel.

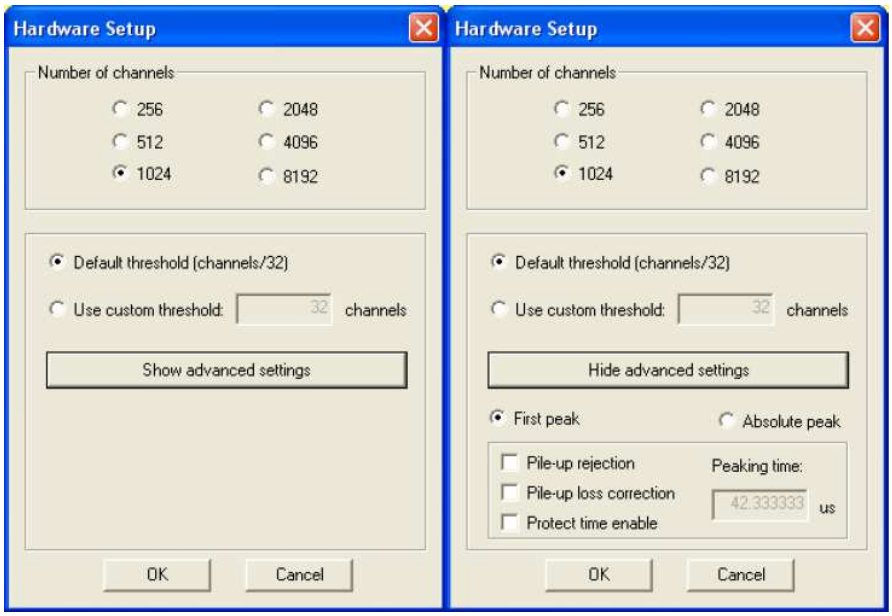

Fig. 2.16: *Hardware Setup control in the software.*

The digital data coming from ADC is stored in two types of files. The first one have a *.mcd* extension (is exclusively readable by the software) and the other has a *.mca* extension, which is readable in different programs because is written in ASCII format.

In order to facilitate the treatment of the data, the PalmTop software opens these files in a friendly interface where plots histograms awaiting for the user to calibrate in energy; to declare Regions Of Interest (ROIs); to define the acquisition mode and to set the time mode (real or live time) as well as the interval of acquisition. In the figure 2.17 a spectrum is plotting in the screen by PalmTop MCA software.

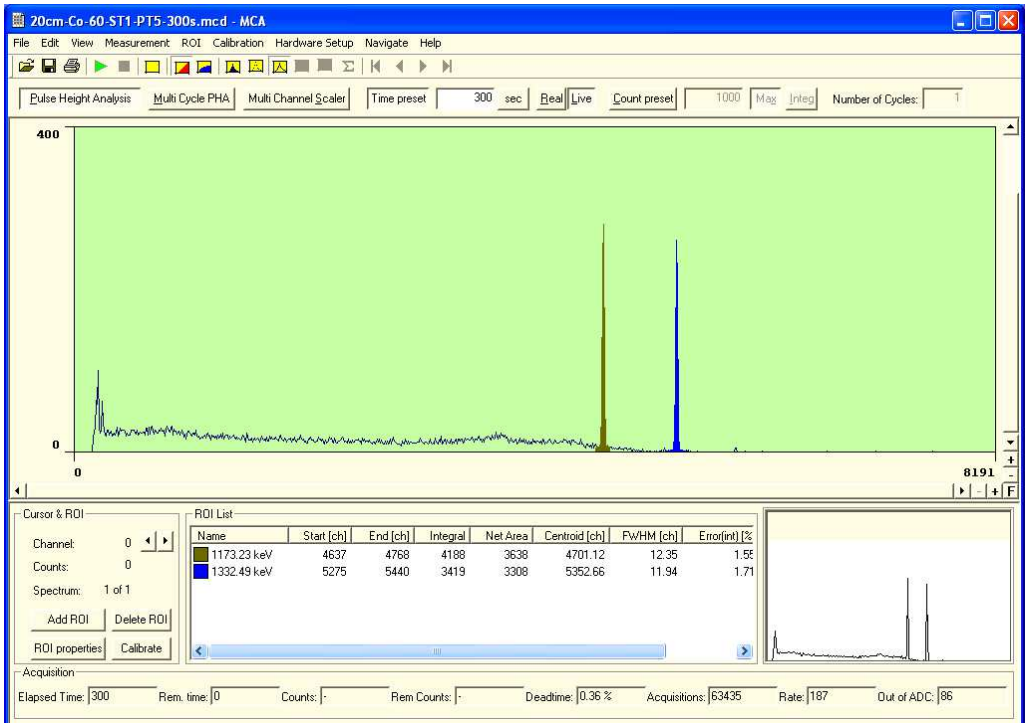

Fig. 2.17: *A ^{60}Co spectrum taken with the HPGe and digitized through the PalmTop MCA.*

2.2.5.5 Oscilloscope

In order to visualize signals from preamplifier and amplifier, we have used a digital oscilloscope (model *DS06104A*) provided by Agilent. This 4-channel scope has the traditional form but with a longer depth that is stackable. Its bandwidth is of 1 GHz, the sample rate can reach 4 GSa/s and the depth memory is 8 Mpts. Also, it accepts signals until ±75V and is able to change the impedance in two values: 50Ω or 1MΩ. Furthermore, provides some advantages like different types of filtering, several ways of digitization, and allows changing the trigger mode.

Because we ought to corroborate that preamplification and amplification stages are working adequately, one of the energy-time signals from preamplifier and the bipolar signal from amplifier are carriers to the oscilloscope during measurements. Our goal is just to corroborate the shape of the pulses and level of the baseline. Through this method, is possible to check also that there is no parasitic current, pile-up or electronic noise in the signal, in other words, this method allow us to assure the correct behaviour of the electronic system.

Furthermore, when the detector will turn on or turn off, the baseline of the energy-time signal must to be followed carefully. During the rise and fall of the voltage, the baseline level of the signal have to be controlled just to prevent excessive increase or decrease of the bias over the detector, which could damage the detector and affect its quality of operation.

Fig. 2.18: *Agilent Oscilloscope model DSO6104A. Left, front panel; Right, Rear panel.*

2.2.6. Calibration sources

A set of four exempt gamma sources was used to estimate the absolute efficiency in scintillator crystals, as we going to see in the next section. However, the activities of these point-like sources were reported with 10% of uncertainty. Thus, in order to reduce the uncertainty, we use a 5% absolutely calibrated Eu-152 source like pattern or reference to the others.

Each exempt gammas source was positioned in the same position than Eu-152 source in front of the HPGe (*5, 10, 15, 20 and 25cm*), thus the fluence would directly be compared. However, before any comparison, we need to set a semi-empirical efficiency formula to estimate the activity related to the energy and the position of the sources [Croft, S. and Russ, W., 2005]. In our case, we want o calibrate a set of four standard gamma sources (*Co-60, Cs-137, Na-22 and Ba-133*) by comparison with the efficiency of the Eu-152 source recorded in the HPGe at different distance in front of the detector [Knoll, 2000].

Finally, we have to remind that these commercial sources can be considered as point-like sources because consist of tiny deposits fixed on a thin backing material (usually lead or iron for gammas). This feature reduces to negligible the self-absorption effect over the emitting gamma radiation [Knoll, 2000].

2.3. Methods and Analysis

2.3.1. Prelimary parameters

In order to optimize the conversion in the MCA, we must find the best parameters values of shaping time and peaking time. The first one ought to be fixed in the Amplifier (selecting the right value) while the second can be fixed in the display of the PalmTop software (is a digital test).

The amplifier must accept the pulse shapes provided by output of the preamplifier and change them into the pulse shapes suitable for optimum energy spectroscopy, in our case semi-Gaussian shape. The output for each pulse consists of a rapidly rising step, followed by a slow exponential decay. Its amplitude represents the energy of the incident radiation [ORTEC, 2012]. Thus, before amplification, the amplifier must replace the long decay time of the preamplifier output pulse with a much shorter decay time. Otherwise, the acceptable counting rate would be seriously restricted. The energy information represented by the

amplitudes of the steps from the preamplifier output has been preserved, and the pulses return to baseline before the next pulse arrives. This makes it possible for a peak sensing ADC to determine the correct energy by measuring the pulse amplitude with respect to the baseline. Even, if the shorter pulse widths are reached in the amplifier output, then much higher counting rates can be tolerated before the pile-up cause significant "distortion" in the survey [Knoll, 2000].

For semiconductor detectors like HPGe or Si, the electronic noise at the preamplifier input makes a clear contribution to the energy resolution. This noise contribution can be minimized by choosing the appropriate amplifier shaping time constant. At short shaping time constants, the *series noise* component of the preamplifier is dominant. This noise is typically caused by thermal noise in the channel of the field-effect transistor, which is the first amplifying stage in the preamplifier. At long shaping time constants the *parallel noise* component at the preamplifier input dominates. This component arises from noise sources that are effectively in parallel with the detector at the preamplifier input (e.g., detector leakage current, thermal noise in the preamplifier feedback resistor) [Leo, 1994; Knoll, 2005]. The total noise at any shaping time constant is the square root of the sum of the squares of the series and parallel noise contributions. Consequently, the total noise has a minimum value at the shaping time constant where the series noise is equal to the parallel noise. This time constant is called the *noise corner time constant*. The time constant for minimum noise will depend on the characteristics of the detector, the preamplifier, and the amplifier pulse shaping network [Tsoulfanidis, 1995].

The contribution of series noise as a fraction of the signal increases the detector capacitance, while the relative contribution of parallel noise to the signals remains independent of this capacitance. For this reason, the optimum shaping time among similar types of detectors tends to shift toward longer times for those with large capacitance. An experimental optimization of the shaping time is an important procedure the user should carry out as part of the initial set up of the detector system if electronic noise contribution is to be kept to a minimum [Knoll, 2005; Karabidak, 2011].

On the other hand, in order to reduce count losses and pile-up effects in quantitative and qualitative analysis, the proper peaking time have to be fixed. The *peaking time* is the time interval taken for the signal leading edge to raise from baseline until reach the maximum of the amplitude. If peaking time is shorter than collection time (signal duration), the pulse amplitude going to be reduced (this effect is called signal loss) or directly discarded by the MCA because in lower than the threshold level. If the peaking time is too long (longer than collection time), then the pile-up effect is increased and the energy resolution getting worst [Karabidak, 2011].

The peaking time is deeply linked to the MCA dead time. Usually the amplifiers contain an internal live time corrector which statistically corrects counting losses of the amplifier, pile-up rejecter, and ADC by extending the counting time by one "*mean-pulse-spacing interval*" for each event loss. The inaccuracy of the correction depends on the system dead time and the input count rate [Tsoulfanidis, 1995]. Hence the effect of minimising the dead time due to peaking time is to minimise the counting losses.

Related with the peaking time, the PalmTop software provides three functions to improve the quality of the pulses that going to be processed in the MCA. The first function is the *pile-up rejection*, this function rejects those inputs signals whose peaking time is longer than the

value set in the peaking time window (see figure 2.16). The second function is *Pile-up loss correction*, this function basically reject those events that were sorted incorrectly because were shifted by another pulse (reducing pile-up effect). Finally, the *Protect Time Enable* function, which extend the dead time due to the analog input signal length by adding a "protect time" immediately after the analog signal has fallen bellow the signal recognition level (threshold). The length of the protect time is equal to the value set for the Peaking time. This function is useful just when the dead-time is too high (more than 90%) for too long pulses (longer than the time in the comparator) and for signal has a significant undershoot after returning to the baseline. The signal recognition comparator will falsely detect that the signal has ended but a subsequent signal may get measured lower or – if small enough – may not get recognized at all [Atomki, 2009].

2.3.2. Area Calculation and Peak shape

In first order any full-energy peaks of gamma-rays with enough statistics have (semi-) Gaussian shape. However, it is usual to find these peaks superimposed on a continuum or appearing mixed with others peaks. Even, could be deformed by a tail. For these reason the estimation of the area under any full-energy is no a quite simple task. Different approaches have been presented to solve this problem, some of them use modifications of a Gaussian distribution [Sanderson, *et al.*, 1976] and others use discrete methods [Osae, *et al.*, 1999] in order to preserve the area and then determine the real contribution from the gammas through net area estimation.

The continuum, background and nearby peaks are effects which could affect the estimation of the area. For this reason it is mandatory to analyze carefully peak-by-peak in order to reject any problem or at least reduce the error that coming for them. Likewise others effects, for instance tailing, can arise from several physical effects, including imperfect charge collection in some regions of the detector, or due to secondary electron and bremsstrahlung escape from the active volume [Knoll, 2000].

In our case, the PalmTop-MCA software allows us to define the Region of Interest (ROI) around the peak of interest. The software automatically integrates the total area, subtracts the background and provides the net area of the peak. The background contribution is subtracted assuming a simple linear behaviour. This approach is particularly poor to solve scenarios where the peak is over the Compton edge or to separate nearby peaks. For instance, from a ^{60}Co source the 1173.2 keV peak is over the Compton edge of the 1332.5 keV, this imply that subtraction can not be assumed as linear, but must be polynomial. Thus, some peaks require a deep treatment in order to separate mixed peaks or solve the contribution from the tail.

The PalmTop software calculates the areas using the next two formulas for a ROI which starts in channel A and finish in B [Atomki, 2009]:

$$ROI\ Area = \sum_{i=A}^{i=B} C_i \qquad (2.1)$$

$$Peak\ Area = \sum_{i=A}^{i=B} C_i - (B-C)\frac{C_A + C_B}{2} \qquad (2.2)$$

In order to calculate the error in the estimation of the peak's net area we use the error propagation:

$$\Delta A_{\mathrm{p}}{}^2 = \Delta A_I{}^2 + \Delta A_B{}^2 \tag{2.3}$$

$$\Delta A_{\mathrm{p}} = \left[\left(\sqrt{A_I} \right)^2 + \left(\sqrt{A_B} \right)^2 \right]^{1/2} \tag{2.4}$$

$$\Delta A_{\mathrm{p}} = \left[\left(\sqrt{A_I} \right)^2 + \left(\sqrt{A_I - A_P} \right)^2 \right]^{1/2} \tag{2.5}$$

Where: A_p is area of peak, A_I is the integral of the ROI and A_B is the background subtracted to A_I to obtain A_p.

Additionally the centroid could be calculated as a weighted average of channels under the peak after subtracting the background through:

$$Centroid = \frac{\sum_{i=A}^{i=B} i \cdot C_i}{\sum_{i=A}^{i=B} C_i} \tag{2.6}$$

Where C_i equals the counts in channel i after background subtraction was performed.

2.3.3. Energy Calibration

In gamma-ray spectroscopy with germanium detectors, the pulse height scale must be calibrated in terms of absolute gamma-ray energy. To calibrate any gamma spectrum is necessary to identified properly the centroid of some known energy peaks, and then a calibration curve can be performed to pass from channels to energy units. In our case we have used a set of standard calibration sources which supply gammas with known energies from 10 to 1408 keV.

Once the energy calibration points have been established over the entire energy range of interest, a calibration curve relating energy to channel number is normally derived. Common techniques involve the least-square fitting of a polynomial of the form:

$$E_i = \sum_{n=0}^{N} a_n \cdot C_i^n \tag{2.7}$$

Where E_i is the energy corresponding to the channel number C_i. Usually the calibration curve for a standard HPGe is linear, however there are some cases where the nonlinearity forces to use a polynomial of order greater than 3 or 4 [Knoll, 2000]. In our case the degree of nonlinearity is negligible, so the calibration curve could be fitted by a linear function.

2.3.4. Experimental Efficiency

Any measurement of absolute emission rates of gamma rays requires knowledge of the detector efficiency. The emission rate for a point source can then be calculated measuring the full-energy peak area over a fixed time and by determining the detector solid angle from its dimensions and the source-detector spacing [Leo, 1995]. However, the dimensions of these detectors are not standardized to any degree, and it is very difficult to determine precisely their active volume. Although efficiencies of germanium detectors can be estimated from published measurements or calculations for detectors of similar size, the accuracy of results based on these values will not be much better than 10-20% [Knoll, 2000]. Furthermore, there is long-term change in charge collection efficiency and/or window thickness can lead to drifts in the detector efficiency over periods of time [Castro, R., *et al.*, 2005].

For these reasons, users will normally carry out their own periodic efficiency calibrations of their germanium detectors using sources calibrated by some other means. Hence, any error in assumed detector dimensions will then apply both to the calibration and actual measurements and will not affect the accuracy of activity measurements. Nonetheless, the source-detector distances still must be accurately measured and reproduced to avoid errors in the relative solid angle [Knoll, 2000].

The efficiency calibration is usually reported as an assortment of gamma-ray energies covering the range of interest to allow construction of an empirical efficiency versus energy curve. Experimentally, the full energy peak efficiency for a particular sample-to-detector geometry is obtained by measuring the net counts under the photopeak energy of interest and using the equation [Nair, C., *et al.*, 2005]:

$$\varepsilon = \frac{N_\gamma}{N_S} = \frac{N_\gamma}{t_\gamma \cdot P \cdot A_0 \cdot e^{-\lambda \Delta t}} \qquad (2.8)$$

Where: N_γ is number of counts in the photopeak, corrected for dead-time and pile-up losses and N_s is number of photons emitted from the source. The other terms describe themselves as ΔT is time elapsed since calibration up to measurement, A_0 is activity of the source on the reference date, P is branching ratio corresponding to the energy E_γ, λ is the decay constant, and t_γ denotes the real time taken for the data run.

The uncertainties can be calculated by the propagation of error equation and assuming the time t_γ is known precisely [Longoria, L., *et al.*, 1996]:

$$(\Delta\varepsilon)^2 = \left[\left(\frac{\partial \varepsilon}{\partial N_\gamma} \right)^2 (\Delta N_\gamma)^2 + \left(\frac{\partial \varepsilon}{\partial A_0} \right)^2 (\Delta A)^2 + \left(\frac{\partial \varepsilon}{\partial P} \right)^2 (\Delta P)^2 + \left(\frac{\partial \varepsilon}{\partial \lambda} \right)^2 (\Delta \lambda)^2 \right] \qquad (2.9)$$

Thus,

$$\Delta\varepsilon = \left(\frac{N_\gamma}{t_\gamma \cdot P \cdot A_0 \cdot e^{-\lambda \Delta t}} \right) \left[\left(\frac{\Delta N_\gamma}{N_\gamma} \right)^2 + \left(\frac{-\Delta A}{A_0} \right)^2 + \left(\frac{-\Delta P}{P} \right)^2 + (\Delta t \cdot \Delta \lambda)^2 \right] \qquad (2.10)$$

Finally, we have to note that N_γ is the same than ΔA_p (see subsection 2.3.2). For this reason we must included the results from equation 2.5 in the previous equations (2.10) to estimate correctly its errors.

2.3.5. Efficiency function vs energy

Once the efficiency of a detector has been measured at several energies using calibrated sources, it is useful to fit a curve to these points in order to describe the efficiency over the entire energy range. Thus, interpolation could be done for any value of energy within the total energy range.

Several empirical formulas to estimate the efficiency of an HPGe have been described in the literature and incorporated into software packages used for gamma-ray spectrum analysis. However, these fitting are optimized for one type of HPGe detector, whether planar or coaxial geometries. However, it is recommended to fit our own efficiency curve for each particular detector [Leo, 1996].

A small number of parameters can be sufficient if the energy range is limited. Formulas with more parameters are generally required to cover wider energy ranges, but are also more prone to the possible appearance of nonphysical oscillations in the fitted function if the data points are widely spaced. In some cases, the energy is subdivided into two or more sections, and separate fits carried out for each range. For covering wide energy ranges, one commonly-used formula is a linear function relating the logarithm of the efficiency to the logarithm of the energy. The full energy peak (ε) of a high purity germanium (HPGe) detector may be expressed in the form of a polynomial with respect to the gamma-ray energy (E) as [Sanderson, P., *et al.*, 1976; Osae, L., *et al.*, 1999]:

$$\ln(\varepsilon) = \sum_{i=1}^{N} a_i \left(\ln E\right)^{i-1} \qquad (2.11)$$

Where E is the energy and a_i are the coefficients of the polynomial for different source-to-detector distances (z). When a few data points are available or all are concentrated in a small region of energy, the value of N might be limited to as few as 2 or 3 terms to yield a stable solution free of oscillations [Knoll, 2000].

These coefficients, a_i, may be obtained for each z distance by fitting to the experimentally measured efficiency values for that particular z distance. Assuming that the coefficients, a_i, can also be expressed in a polynomial form involving, z, then we may write:

$$a_i \equiv a_i(z) = \sum_{j=0}^{M} a_{ij} z^j \qquad (2.12)$$

Where a_{ij} are the polynomial coefficients. These coefficients, a_{ij} may also be obtained by fitting the graphs of $a_i(z)$ versus z. Thus by combining equations (2.11) and (2.12) a general equation for the efficiency may be expressed as:

$$\ln(\varepsilon) = \sum_{i=1}^{N}\sum_{j=0}^{M} a_{ij} z^{j} \left(\ln E\right)^{i-1} \qquad (2.13)$$

In our case we are going to divide the full energy range in two intervals. First one will be called "*Low Energy*" which covers energies from 30 to 245 keV. For this interval we are going to use a value of N=3, what corresponds to a quadratic approximation. While for the other interval, named "*High Energy*", the fitting will be performed through a linear approximation (setting N=2).

2.3.6. Estimation of Activity from Efficiency

Because we only have one absolutely calibrated source (^{152}Eu at 5%), we need to calibrate the others point-like sources through the absolute efficiency fitting of our detector for different distances. Originally our set of gamma sources was provided with a calibrated activity of around 10%, thus our aim is to reduce this uncertainty through a precise absolute efficiency fitting. And thus can use this set as reference for different applications.

Basically we start from the same expression (2.8), only instead to estimate the efficiency; we are in pursuit of the activity in function of the energy. Thus, the activity can be estimated as function of the energy:

$$A(t_{survey}) = \frac{N_\gamma}{t_\gamma \cdot P \cdot \varepsilon(E)} \qquad (2.14)$$

Where: N_γ is number of counts in the photopeak, corrected for dead-time and pile-up losses and N_s is number of photons emitted from the source. The other terms describe themselves as ε is the efficiency related to some particular energy, P is branching ratio corresponding to the energy E_γ, and t_γ denotes the real time taken for the data recording.

The uncertainties for activity can be calculated by the propagation of error equation. Also, if we assume that time t_γ is known precisely, we obtain:

$$(\Delta A)^2 = \left[\left(\frac{\partial A}{\partial N_\gamma}\right)^2 (\Delta N_\gamma)^2 + \left(\frac{\partial A\varepsilon}{\partial \varepsilon}\right)^2 (\Delta\varepsilon)^2 + \left(\frac{\partial A}{\partial P}\right)^2 (\Delta P)^2\right] \qquad (2.15)$$

Thus,

$$\Delta A = \left(\frac{N_\gamma}{t_\gamma \cdot P \cdot \varepsilon(E)}\right)\left[\left(\frac{\Delta N_\gamma}{N_\gamma}\right)^2 + \left(\frac{-\Delta\varepsilon}{\varepsilon}\right)^2 + \left(\frac{-\Delta P}{P}\right)^2\right] \qquad (2.16)$$

Finally, in order to set the right value of the activity for each source, we have to estimate the average between every different gamma peaks which are provided from the source. In the same way the error associated to each activity can be calculated by means of averaging the errors of each gamma peak emitted for a specific gamma source.

2.4. Results

2.4.1. Preliminary parameters: Peaking, Shaping and Dead Time

In order to test the relation between three processing parameters: peaking time, dead time and shaping time; several gamma spectra were taken with a uniform and stable radiation field. This field was provided by a monochromatic gamma source (^{137}Cs) fixed at 15 cm in front of the HPGe. Any change in the spectra comes of the variation of the parameters, thus all the results were plotted just to use it like criteria to set the best values during the survey.

2.4.1.1. Dead-Time criteria

At the same radiation fluence field, several gamma spectra were taken for eight different values of peaking time (in μs: 2, 3, 4, 5, 10, 30, 50 and 70) in the MCA at three different shaping time values (in μs: 0.5, 1 and 2) in the Amplifier. For each case the dead-time was recorded and plotted in the figure NN. Any other parameters, like voltage, were fixed.

As we can see in the figure 2.19, the dead-time is always highest when the shaping time is fixed in 2 μs and even the MCA could not take data from 5 μs of peaking time. However, for 0.5 and 1 μs the dead-time presents a similar behaviour. For values lower than 5 μs of peaking time, the associated dead-time was lower to 2%. Thus, in order to reduce the dead-time during measurements, the shaping time must be set in 0.5 or 1 μs.

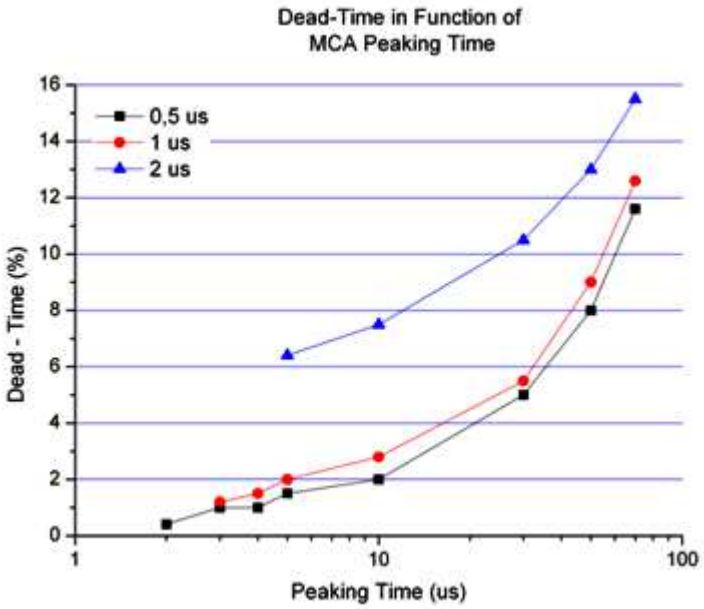

Fig. 2.19: *Dead-Time in function of MCA peaking time at different shaping time values.*

2.4.1.2. FWHM criteria

Below the same previous conditions, several spectra were taken in order to explore the FWHM of the 662 keV peak while change the value of peaking time (in μs: 2, 3, 4, 5, 10, 30, 50 and 70) in the MCA and shaping time (in μs: 0.5, 1 and 2) in the Amplifier. For each case the FHWM was recorded in channel scale and plotted in the figure 2.20. Any other

parameters, like voltage, were fixed. Furthermore, to compare if the FWHM dependents of the time clock mode, we acquired the data in two scenarios: real-time and live-time.

As we can see in the figure 2.20, the FWHM is almost not dependent of the peaking time or the time clock mode, but is strongly related to the shaping time. When the shaping time is fixed in 0.5 μs, the FWHM is roughly the double than the others. Difference between 1 and 2 μs of shaping time is around 1-1.5 channel, this imply that the value of energy resolution between this values will be really close. For these reason, any of both can be considered that optimized the FWHM.

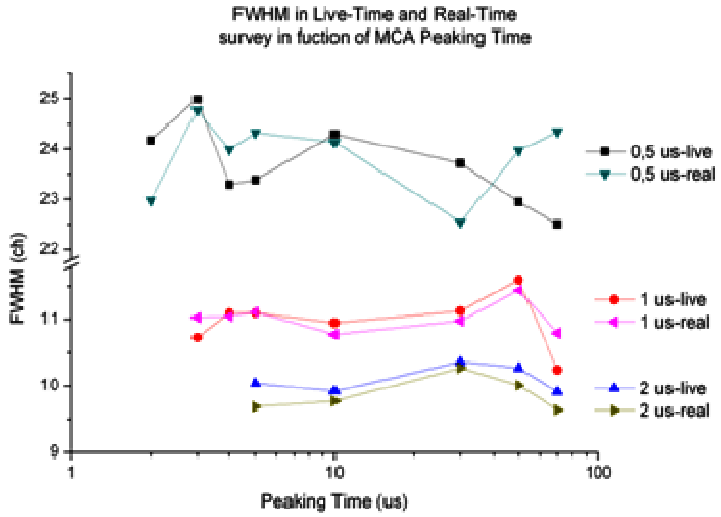

Fig. 2.20: *FWHM of the 662 keV peak in function of the peaking time and shaping time.*

2.4.1.3. Live-time and Real-time

Dead time is the time interval that detection system required to process two consecutive events. If an event arrives to ADC while it is busy, then this event is rejected or simply not recorded in the memory. Thus there is a fraction of pulses detected which are not counted due to the Dead Time, this is caused by the time spent for the ADC to process a previous event.

In other words, the total number of particles which deposits energy in the detector (N_{TOT}) is equivalent to the sum of particles which are converted to counts (N_{ACQ}) and the fraction of lost counts because the dead time (N_{LOST}). Thus we can express the total number of particles as follow:

$$N_{TOT} = N_{ACQ} + N_{LOST} \rightarrow N_{LOST} = N_{TOT} - N_{ACQ} \qquad (2.17)$$

The ratio of particles which are not recorded over the total number of particles which interact with the detector, define the Ratio or Fraction of Dead Time:

$$\tau = \frac{N_{LOST}}{N_{TOT}} = \frac{N_{TOT} - N_{ACQ}}{N_{TOT}} = 1 - \frac{N_{ACQ}}{N_{TOT}} \rightarrow \boxed{N_{TOT} = \frac{N_{ACQ}}{1-\tau}} \qquad (2.18)$$

Also, the Dead Time Fraction is related with the total real time of survey (T) and the number of processed time (k) by this formula:

$$\tau` = \frac{k\,\tau}{T} \qquad (2.19)$$

This concept is used by the MCA Palm Top to correct the measurements by Dead Time, this acquisition mode is called "Live Time".

In the figure 2.21 is shown the behaviour of the MCA PalmTop for high rates of events per second (more than 5000 cps). The measurements were recorded in Real Time (blue) and Live Time (black) modes. Additionally, the acquisitions taken in Real Time mode were corrected by the equation 2.18 and plotted in 2.21 with red circles. As can see this correction provides data in good agreement with the Live Time mode reported by the MCA.

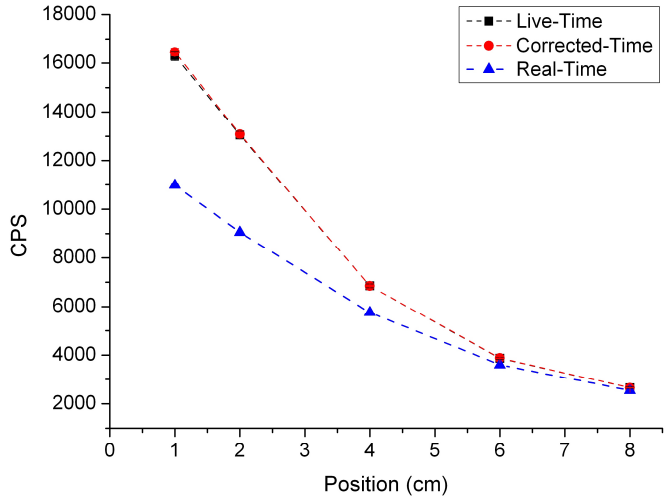

Fig. 2.21: *Comparison of the Live-Time and Real-Time corrected by Dead-time.*

In order to set different fluencies in the HPGe, a ^{137}Cs gamma source was positioned in front of the detector at 5 positions (1, 2, 4, 6 and 8 cm). Then for each position of the source two spectra were recorded. First one was acquired in Real Time mode (with no correction for dead time) while the other was obtained in Live Time Mode (with the Dead Time correction activated). In the figure 2.21 we also show how our adjustment fits quite well what allow us not only to understand how the MCA estimates the correction for Live Time but to perform our own correction for different scenarios. In general, our adjustment for Dead Time is in agreement with the correction elaborated in MCA Palmtop.

Because the previous correction depends strongly of the fraction of Dead Time, a study about the Dead Time has to be performed. In the figure 2.22 are shown the fraction of Dead Time in function of the counts per second (cps) and one quadratic fitting. Both the data taken in Live Time mode and the percentage of Dead Time were provided by the MCA itself. The fluence was supplied by a monochromatic gamma source (^{137}Cs) which was positioned in several places in front of the detector. The fitting have a quadratic form ($DT(\%)=Ax^2+Bx+C$), its parameters are listed in the next table (Table 2.1), where C=0 because there is not Dead Time for a zero rate of counts recorded in the detector.

Parameter		Error
A	1.50×10^{-7}	9.89×10^{-9}
B	1.53×10^{-3}	1.21×10^{-4}
C	0	0

***Table 2.1**: Parameters of a quadratic fitting to obtain the Dead Time Fraction.*

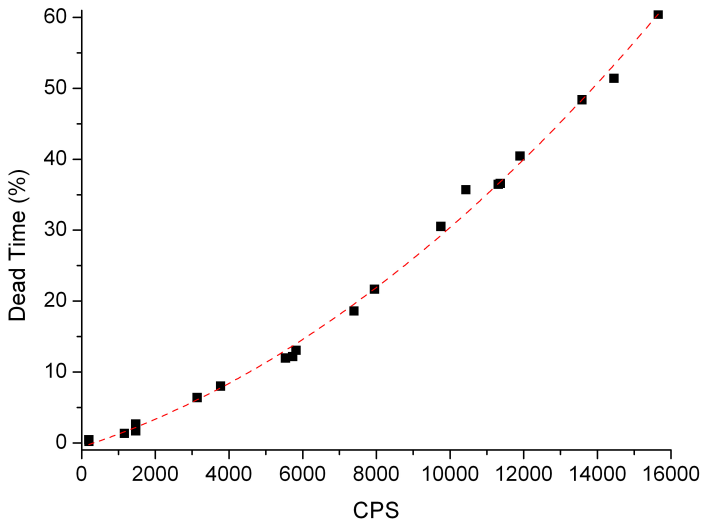

***Fig. 2.22:** Counts per second recorded by the MCA in Real Time mode and the fraction of Dead Time reported for the same measurement. Also, a quadratic fitting to estimate*

2.4.2. Effect of the shielding

For one hand, the lead castle shields from radiation which coming from the surroundings. In the figure 2.23 are shown two spectra taken during 1000 seconds in Live Time mode with the detector inside (black) and outside (red) of the shielding. In the red spectrum we can see typical peaks that coming from natural radioactivity chains: Radium (from ^{238}U), Thorium (from ^{234}Th) and Actinides (from ^{235}U) series. Outside the shielding the HPGe can reach around 85 cps, while inside the lead castle the rate is reduced to less than 15 cps. Now, because we want to perform low level survey is necessary to use the detector inside the shielding.

However, if we are dealing with radioactive gamma sources we must be careful because the lead can be excited by the gammas and so release fluorescence X-ray which can be included in the spectrum. In the figure 2.24 we can see the effect of these Pb X-rays. In a “low energy regime”, in our case from 10 to 130 keV, the fluorescence X-rays appear in the middle of the scale. If we remove the shielding and take again the measurement, then we can see how these X-rays disappear.

Thereby, the use of the shielding depends of what we are looking to do. If we pretend measurements with low contribution from the background, the shielding is mandatory. However, if we want to explore a region which contains X-rays from the shielding (70-80 keV), the best way if remove the shielding and take measurements directly from the sample.

Now, if the shielding is rejected, the subtraction of the background turns compulsory because the number of counts will be considerable in the spectrum and can deform structures.

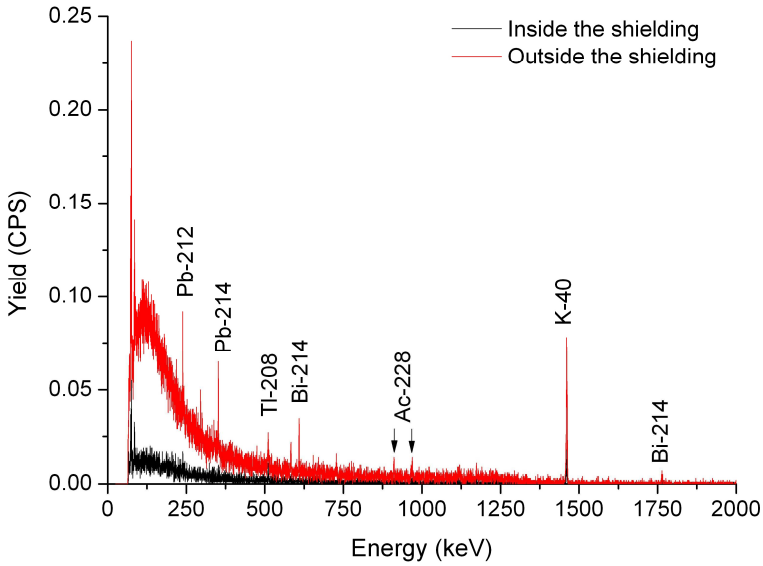

Fig. 2.23: *Background spectra. Red one is without the shielding while the black was taken inside a lead castle. Both were recorded during 1000s.*

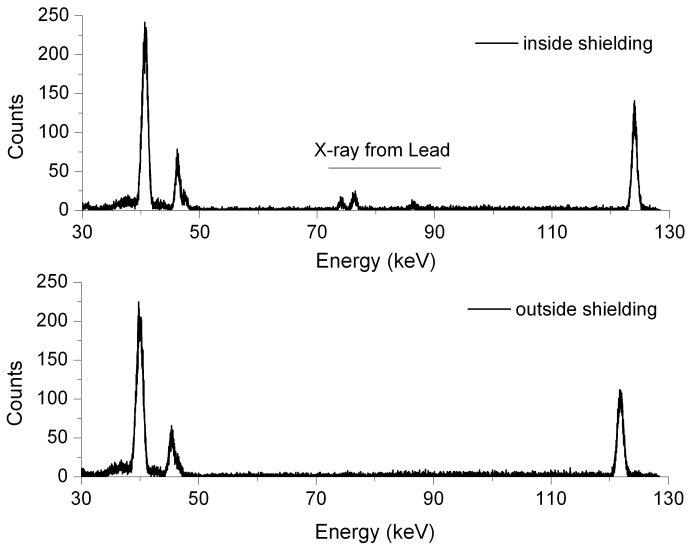

Fig. 2.24: *Two ^{152}Eu spectra for an energy window from 30 to 130 keV. Top spectrum shows the typical x-ray fluorescence peaks from the lead in the shielding. In the bottom is the same scenario but with the detector outside the shielding.*

2.4.3. Histogram and Energy Spectra

In order to take advantage of the properties of the detector and the electronic, two regimen of energy were used to take the measurements and estimate the efficiency of the HPGe. The first one starts around 65 keV until 1600 keV, this interval is called "*High Energy*". The other goes from 10 keV to 130 keV, and is called "*Low Energy*". In the figure 2.25 is shown a ^{152}Eu

spectrum in logarithmic scale for "High Energy" regime. Two energy windows are detailed in order to show the behaviour of the detector at the beginning and the ends of the range. In the green square we can see some peaks which coming from the ^{152}Eu source but we also see the 1460 keV peaks from the ^{40}K, this means that we need to subtract de background from the spectra in order to get clean the spectrum. In the cyan square there are some X-rays from lead, so this effect has to taking in account in order to avoid false estimations or deformation of the peaks shape.

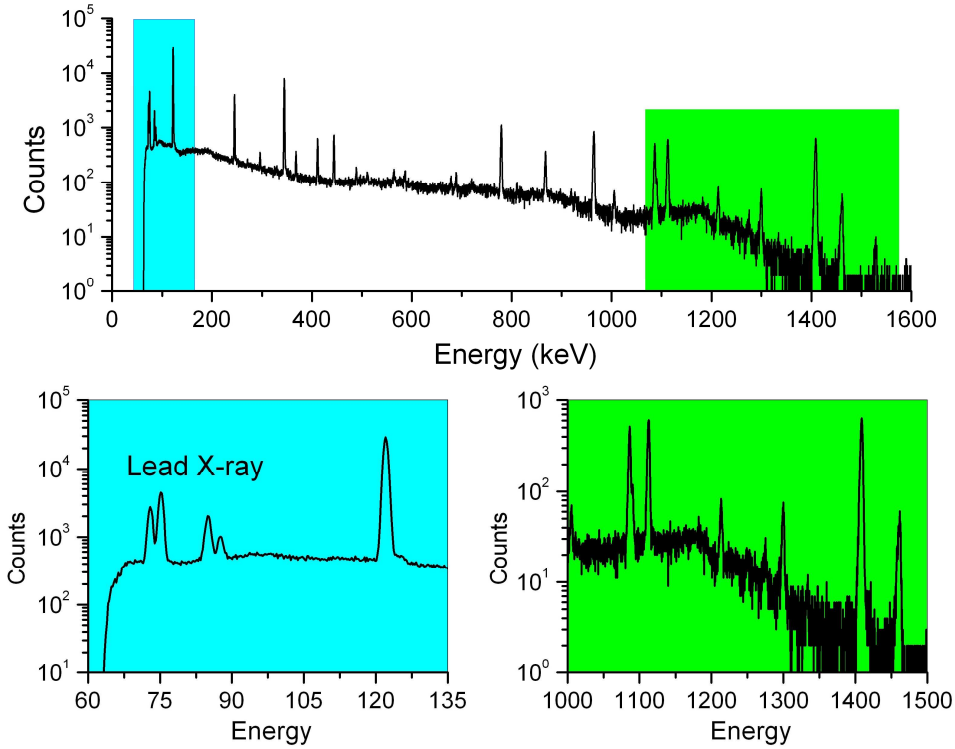

Fig. 2.25: *A ^{152}Eu spectrum in log-scale. In the green square, the last peak corresponds to 1460 keV from ^{40}K, which implies that the background contribution has to be subtracted. In the cyan square we can see the X-rays from the Lead in the shielding.*

In the figure 2.26 are shown the spectra from ^{152}Eu and the background which should has to be subtracted. Both were taken in the same conditions and identical live time (5000 s). The energy calibration used was: *E (keV) = 0.244 ·channel + 24.810*. The number of channel is the same in order to subtract the background without problems of binning.

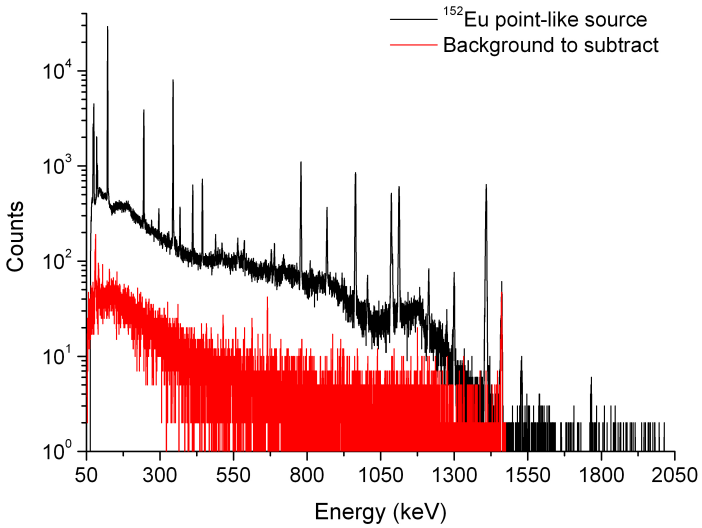

Fig. 2.26: *Comparison of the Live-Time and Real-Time corrected by Dead-time.*

In the table 2.2 are listed the parameters used in every spectra in function of the regimes used. The power supply, amplifier and MCA devices were the same for both survey modes.

Parameter	LOW ENERGY	HIGH ENERGY
Energy window	10 – 130	65 - 1700
Voltage	-3500 V	- 3500 V
Coarse Gain	300	30
Fine Gain	1.14	0.73
Total Gain	342	21.9
Shaping Time (μs)	1	1
Peaking Time (μs)	5	5
Linear Energy Calibration - *E (keV) = A + B*ch* -	A=0.0015 B=1.6109	A=0.244 B=24.810

Table 2.2*: Parameters fixed to get the spectra.*

2.4.4. Resolution in function of energy

The energy resolution of the HPGe is quite linear. In the figure 2.26 is plotted the Full Width at Half Maximum (FWHM) in energy units (keV) against the energy of the incident gammas. While there are a lot of representations of the energy resolution, the FWHM provide the information of the width of the peaks directly, which can be related with the number of channel. If we remember that the relation between energy and channel is a linear relation, then this information is easily translatable. To plot the linear curve fitting, we has to reject some peaks because are double peaks (with contribution of two nearby gammas) or peaks with not enough statists (which show a semi-Gaussian shape).

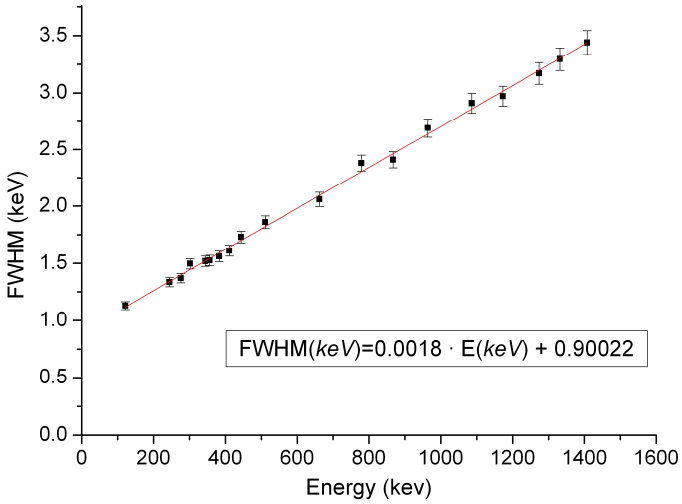

Fig. 2.26: *FWHM in energy units (keV) versus Energy (keV). The data were fitted with a linear curve and its equation is remarked in the same plot.*

2.4.5. Efficiency Measurements

The results of the absolute efficiency calibration for our HPGe are shown in the figure 2.27. In a log-log plot we can see the response of our detector in function of the incident gammas energies. In these points the errors are already included. In general, the curves have the typical shape of HPGe efficiency curves. The maximum is around 80 keV, similar to low level detector from Canberra [Gültekin, A., *et al*., 2006]. The values after the maximum, for energies over 100 keV, presents a linear slope, at least for the interval explored here (until 1408 keV). And for the energies below 100 keV there is also a linear but can be fitted by a quadratic expression in order to cover the maximum and some "linked" points (points which connect both fittings).

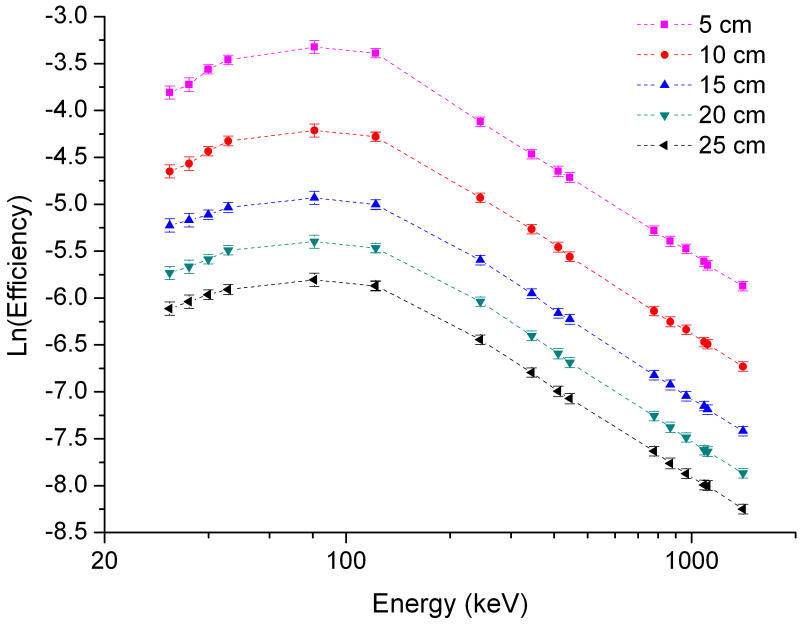

Fig. 2.27: *Absolute Efficiency in logarithmic scale in function of the energy (keV) at five positions in front of the detector. Here the data is just linked through dashed lines.*

It is important to note how the effect of the distance plays a key role in the determination of the absolute efficiency. The separation between curves increase in function of the distance, instead of a simple inverse square of the distance, the separation shows also the change of the geometric efficiency with the distance source-to-detector.

These curves were plotted by put together data of two scenarios. From one side, we use the information from a High Energy range, and the other from Low Energy range. In both cases we explore the net contribution from the sources, this means subtracting the background. For the first range we only use a ^{152}Eu source, while for the other scenario we use the same ^{152}Eu source and a ^{133}Ba source which were previously calibrated through efficiency obtained in the previous range.

The empirical results are listed in the table 2.3. It is important to note that no efficiency have an error upper than 10%. The maximum error 7.3% was provided by the ^{133}Ba which is a tertiary calibrated source. The ^{133}Ba source was calibrated with the results of the High Energy range, and later we used to fit the Low Energy interval. The lower error values were obtained with the ^{152}Eu because was traced in a secondary laboratory at 5%. However, by the estimation of the area and others sources of error this value increase a little, but never more than 5.7%.

Energy (keV)	Eff at 5 cm	Error %	Eff at 10 cm	Error %	Eff at 15 cm	Error %	Eff at 20 cm	Error %	Eff at 25 cm	Error %
30.8	2.22E-02	7.0	9.57E-03	7.0	5.38E-03	7.0	3.24E-03	7.0	2.21E-03	7.0
35.1	2.41E-02	7.3	1.04E-02	7.2	5.69E-03	7.2	3.46E-03	7.1	2.39E-03	7.1
39.9	2.84E-02	5.0	1.19E-02	5.1	6.02E-03	5.1	3.75E-03	5.1	2.57E-03	5.1
45.6	3.14E-02	5.1	1.32E-02	5.2	6.51E-03	5.4	4.13E-03	5.2	2.72E-03	5.3
80.9	3.60E-02	7.0	1.48E-02	7.1	7.22E-03	7.1	4.53E-03	7.0	3.01E-03	7.1
121.8	3.37E-02	5.0	1.38E-02	5.1	6.72E-03	5.2	4.22E-03	5.1	2.82E-03	5.1
121.8	3.37E-02	5.0	1.38E-02	5.0	6.72E-03	5.0	4.23E-03	5.0	2.83E-03	5.0
244.7	1.62E-02	5.0	7.21E-03	5.0	3.71E-03	5.0	2.39E-03	5.1	1.59E-03	5.1
344.3	1.15E-02	5.0	5.17E-03	5.0	2.60E-03	5.0	1.66E-03	5.0	1.12E-03	5.0
411.1	9.57E-03	5.5	4.27E-03	5.4	2.11E-03	5.3	1.37E-03	5.5	9.17E-04	5.7
443.9	8.97E-03	5.3	3.85E-03	5.3	1.97E-03	5.2	1.25E-03	5.3	8.49E-04	5.5
778.9	5.09E-03	5.1	2.16E-03	5.1	1.09E-03	5.1	7.05E-04	5.1	4.85E-04	5.1
867.4	4.54E-03	5.6	1.92E-03	5.5	9.82E-04	5.4	6.26E-04	5.6	4.25E-04	5.7
964.1	4.18E-03	5.1	1.77E-03	5.1	8.71E-04	5.1	5.61E-04	5.1	3.81E-04	5.1
1086.4	3.66E-03	5.1	1.55E-03	5.1	7.84E-04	5.1	4.90E-04	5.1	3.38E-04	5.2
1112.1	3.52E-03	5.1	1.52E-03	5.1	7.55E-04	5.1	4.83E-04	5.1	3.36E-04	5.2
1408	2.81E-03	5.1	1.19E-03	5.1	6.00E-04	5.0	3.83E-04	5.1	2.61E-04	5.1

Table 2.3*: List of results of absolute efficiency for our HPGe at five different distances.*

2.4.6. Fittings

In order to yield a stable solution free of oscillations, the absolute efficiency data were separated in two regions: Low and High energy. As is shown in the figure 2.28 the Low Energy interval can be fitted be a quadratic expression (N=3) and the High Energy interval

with a linear function (N=2). The fittings were obtained through the ORIGIN program and corroborated with the Gnuplot software. The results in both cases took in account the weight of the error. For instance, in the figure 2.28, the fitting for a ^{152}Eu positioned at 25 cm in front of the crystal.

For the Low Energy interval we use a quadratic fitting (N=3):

$$\ln(\varepsilon) = \sum_{i=1}^{N=3} a_i \left(\ln E\right)^{i-1} \rightarrow \ln(\varepsilon) = a_1 + a_2 \cdot (\ln E) + a_3 \cdot (\ln E)^2 \qquad (2.20)$$

And for the High Energy interval we use a simple linear fitting (N=2):

$$\ln(\varepsilon) = \sum_{i=1}^{N=2} a_i \left(\ln E\right)^{i-1} \rightarrow \ln(\varepsilon) = a_1 + a_2 \cdot (\ln E) \qquad (2.21)$$

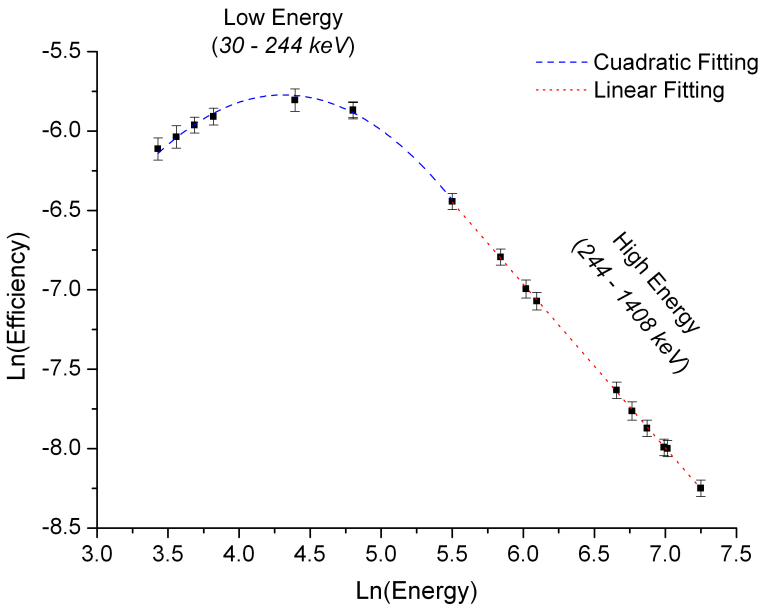

Fig. 2.28: *Fitting the efficiency by two separated ranges. A quadratic fitting for a Low Energy (30 – 244 keV) and a linear fitting for a High Energy interval (244 – 1408keV).*

In the table 2.4 are listed the parameters for the fittings in according with the interval and distance source-detector.

Position (cm)	Low Energy (*30 – 244.7 keV*) $\ln(\varepsilon) = A\cdot(\ln E)^2 + B\cdot(\ln E) + C$			High Energy (*244.7 – 1408 keV*) $\ln(\varepsilon) = A\cdot(\ln E) + B$		
	Parameter		Error	Parameter		Error
5	A	-0.6445	0.0227	A	1.3765	0.0318
	B	5.6192	0.2021	B	-0.9994	0.0049
	C	-15.5242	0.4404			
10	A	-0.5747	0.0182	A	0.7615	0.0438
	B	5.0061	0.1621	B	-1.0345	0.0067
	C	-15.0762	0.3532			
15	A	-0.4792	0.0248	A	0.1401	0.0375
	B	4.1293	0.2213	B	-1.0444	0.0057
	C	-13.7991	0.4822			
20	A	-0.4836	0.0170	A	-0.2781	0.0341
	B	4.1874	0.1509	B	-1.0488	0.0052
	C	-14.4348	0.3289			
25	A	-0.4705	0.0197	A	-0.7756	0.0337
	B	4.0598	0.1758	B	-1.0315	0.0052
	C	-14.5300	0.3830			

***Table 2.4**: Parameters to fit the efficiency data..*

2.4.3 Estimation of Activity for point-like gammas sources

Our set of gamma sources count with a ^{22}Na, ^{60}Co, ^{137}Cs and ^{133}Ba point-like sources. Only the ^{152}Eu was calibrated in a secondary laboratory SPECTECH in June 21, 2012. Its stated activity was the weighted average of the measured gamma lines with an estimated uncertainty of 5%. Through this information we performed the measurements to set absolute efficiency curve for our HPGe and so to calibrate the others gamma sources.

Usually a set of gamma sources, like ours, is provided with an uncertainty of around 10%. Because this value can be bigger, we sent one source to be calibrated. We choose the ^{152}Eu because supply several gamma to cover all the energy range of interest, from 39 to 1408 keV. Thereby, our main purpose is improving the calibrations in order to obtain the activity of the remaining sources with an uncertainty lower than 10%.

Firstly we estimated the activity through the formula 2.14, using the information of the efficiency for a specific energy. Thus, the activity is obtained as a function of the energy peak:

$$A(t_{survey}) = \frac{N_\gamma}{t_\gamma \cdot P \cdot \varepsilon(E)} \qquad (2.14)$$

The next step is set the right value for the uncertainty through the expression 2.16, which assume the time interval and the branching ratio are known precisely. Thus,

$$\Delta A = \left(\frac{N_\gamma}{t_\gamma \cdot P \cdot \varepsilon(E)}\right)\left[\left(\frac{\Delta N_\gamma}{N_\gamma}\right)^2 + \left(\frac{-\Delta\varepsilon}{\varepsilon}\right)^2 + \left(\frac{-\Delta P}{P}\right)^2\right] \qquad (2.16)$$

Finally, in order to set the right value of the activity for each source, we have to estimate the average between every different gamma peaks which are provided from the source. In the same way the error associated to each activity can be calculated by means of averaging the errors of each gamma peak emitted for a specific gamma source. The results are listed in the Table 2.5.

Source	Activity		Error
	Bq	μCi	(%)
^{133}Ba	41540.7	1.12	7.00
^{22}Na	32518.0	0.88	6.00
^{60}Co	26983.3	0.73	5.00
^{137}Cs	9440.2	0.26	9.00

***Table 2.54**: New activity estimated for a set of point-like gamma sources.*

All errors have been estimated lower than 10%. Only the ^{137}Cs sources have only one gamma peak. Although the backscatter peak could be used to get information from two peaks in the same spectrum, the treatment of the data not was optimized to this type of pseudo-peak. Also, these peaks depend strongly of the surrounding. For instance, if the source is shielded the intensity can be increase and so drives to false estimation of the area.

These same protocol or strategy will be follow in the next chapter to determine the internal activity of a scintillator crystal, which is made of lutetium and counts with an important contribution for an instable isotope.

2.5. Conclusions

In this chapter we have characterized a hyper-pure Germanium detector (HPGe) model LOAX 60450-30P-CW marketed by ORTEC. Firstly we have studied the main properties of this semiconductor crystal and its Aluminium housing and carbon filter window. Moreover, we have explored the electronic devices which make up the processing system. In particular, we explore the properties of the preamplifier (inside the PopTop Detector capsule), Amplifier (Canberra 2022), Power supply, Oscilloscope and the multichannel analyzer (MCA-PalmTop) provided by Atomki.

We also have made and explained a system to refill the Dewar with LN2. Basically a boiling system was created in order to drive the LN2 from a portable-Dewar to Fix-Dewar where is located the HPGe. The system has proved be a cheap and efficient method with almost not losses.

Furthermore, preliminary time parameters were optimized. The Shaping, Peaking and Dead Time were studied to take advantage of the features of the HPGe and its processing system. The Shaping Time was fixed at 1 μs in the amplifier and the Peaking Time was set at 5 μs seconds for the MCA. The Dead Time was associated to a function to correct the results taken in Live Time mode and to suggest different corrections if is necessary.

The HPGe shows a very good linear response to energy in the range explored. The resolution and linearity presents a quite linear behaviour. Both quantities were related to linear expression to do interpolations and control the well operation of the system.

Furthermore, the effect of the lead shielding over the measurements was explored. For one hand, the Lead castle reduces the rate of counts from the background. However, in the other hand, if the sample emits gammas with enough energy to excite the Lead, then the shielding could release some X-rays. As consequence of this effect some extra peaks appears in the spectra. Thus, for instance, if one studied wants to characterize something in the range of 70-80 keV have to be careful and consider this fluorescence effect from the shielding. Also, the backscatter will be increased due to nearness of the sample to the Lead.

Absolute efficiency was calculated for our HPGe. An absolute calibrated point-like source was positioned in five positions in front of the detector. In order to avoid oscillations in the fitting, we have divided the range in two intervals. At low energy a quadratic curve was used to fit the data from 30 to 244.7 keV and for the High Energy interval we have used a linear fitting from 244.7 to 1408 keV. Both functions fit quite good for the overlapping values and shows continuity.

Finally, through the absolute efficiency fitting we were estimated the activity for a set of point-like sources. The results are good because we have satisfied the condition of reduce the error a values lower than 10%. In fact, the calibration was made only with the fitting curves from the High Energy interval, later we used the ^{133}Ba to fit the Low Energy interval.

2.6. References

AMPTEK. Charge-sensitive Preamplifiers A250. (2012) URL: http://www.amptek.com/a250.html

Atomki. Palmtop Multi Channel Analyzator and Scaler. User's Manual. (2009).

Boson, J. Improving accuracy of in situ gamma-ray spectrometry. Sweden: Print & Media, 2008. ISBN 978-91-7264-621-6

Canberra. Spectroscopy Amplifier. Model 2022.

Castro, R., Vanin, V., Maidana, N., Pascholati, P., Dias, M. Koskinas, M. Efficiency Loss in HPGe Detectors due to Beta and Gammas Sum Coincidence. Brazilian Journal of Physics. Vol. 35. Number 3B. September 2005.

Croft, S. and Russ, W. A semi-empirical formula for representing the full energy peak efficiencies of planar Ge detectors. The 10th International Conference on Environmental Remediation and Radioactive Waste Management. September 4-8, 2005, Scottish Exhibition & Conference Centre, Glasgow, Scotland.

Gültekin, A., Kaynak, G., Gürler, O. Determination of full energy peak efficiency of HPGe detector from 59.5 to 1332.5 keV. Indian Journal of Pure & Applied Physics. Vol. 44, pp. 281-286. April 2006.

Jurado, M., Cornejo, N. and Pérez, D. Efficiency transfer in the calibration of a coaxial p-type HPGe detector using the Monte Carlo method. Applied Radiation and Isotopes 58 (2003) p. 707-712.

Karabıdak, S.M. et al. Determination of proper peaking time for Ultra-LEGe detector. Radiation Measurements 46 (2011) 446-450.

Keyser, R.M. and Twomey, T.R. Efficiency for Close Geometries and Extended Sources of a P-type Germanium Detector with Low-energy Sensitivity. Modern Trends in Activation Analysis - 11, June 2004, Guildford, England.

Knoll, Glen. Radiation Detection and Measurement. Third Edition. New Jersey: John Wiley & Sons, Inc., 2000.

Leo, W.R. Techniques for Nuclear and Particles Physics Experiments. A How-to Approach. Second Revised Edition. Berlin: Springer-Verlag, 1994.

Ljungvall, J. Characterisation of the Neutron Wall and of Neutron Interactions in Germanium-Detector System. Acta Universitatis Upsaliensis. Digital Comprehensive Summaries of Uppsala Dissertations from the Faculty of Science and Technology 66. viii+65pp. ISBN 91-554-6283-9 (2005).

Longoria, L. and Benitez, J. Full Energy Peak Efficiency of a Ge Detector as a Function of Energy and Distance. Appl. Radit. Isot. Vol 47. No. 3, pp. 339-343, 1996.

Martin, M.J. Nuclear Data Sheets 108, 1583 (2007).

Mauring, A. and Drefvelin, J. Simplified Methods for coincidence summing corrections in HPGe efficiency calibration. Applied Radiation and Isotopes 70 (2012) 2161–2163.

MCFarland, R. Behavior of Several Germanium Detector Full-Energy-Peak Efficiency Curve Fitting Functions. From the Counting Room, Vol 2. No. 4, 1991.

Naeem, S. Physics and Engineering of Radiation Detection. First Edition. USA: Academic Press Inc. Published by Elsevier, 2007

Nair, C. Junghans, A., et al. Absolute Efficiency Calibration of HPGe Detectors for Photoactivation Experiments. Pag. 41. FZD Annual Report, 2005.

Nix, D., Scott, N. Detection Efficiency Calibration for Radiological Monitoring of Nuclear Plants, Radioelement Analysis: Progress and Problems Proc. of the 23er Conf. on Analytical Chemistry in Energy and Technology, Gatlingburg, Tennessee, 1976.

Sanderson, C. Comparison of Ge(Li) Well and N-Type Coaxial Detectors for Low-Energy Gamma-Ray Analysis of Environmental Samples, Radioelement Analysis: Progress and Problems Proc. of the 23er Conf. on Analytical Chemistry in Energy and Technology, Gatlingburg, Tennessee, 1976.

Schmitt, H.W. et al. Proceedings of the IAEA Conference on The Physics and Chemistry of Fission, Salzburg, 197 5 (531).

Sudarshan, M. Joseph, J. and Singh, R. Full energy peak efficiency of NaI(Tl) gamma detectors and its analytical and semi-empirical representations. J. Phys. D: Phys. 25 (1992) 1561-1567.

Sze, S.M. Semiconductor devices. Physics and technology, John Wiley & Sons, 1985.

ORTEC. LO-AX Low Energy Photon Detector. Product Configuration Guide. (2012) URL: http://www.ortec-online.com/Solutions/RadiationDetectors/semiconductor-photon-detectors.aspx

ORTEC. Dual 5-kV Bias supply. Model 660 (2012) URL: www.ortec-online.com/download/**660**.pdf

Osae, E. et al. An empirical expression for the full energy peak efficiency o fan N-type high purity germanium detector. Journal of Radioanalytical and Nuclear Chemistry, Vol. 242, Number 3 (1999) 617-622.

Taccetti, F. et al. Temperature and vacuum measurements on the commercial assembly of a large-volume Ge detector. Nuclear Instruments and Methods in Physics Research A 398 (1997) 238-248.

Tsoulfanidis, N. Measurement and Detection of Radiation. Second Edition. USA: Taylor & Francis, 1995.

Van Cleef, D.J. High-fidelity decision making using portable HPGe instrumentation. J Radioanal Nucl Chem (2009) 282:837–840. DOI 10.1007/s10967-009-0140-5

Vénos, D et al. The behavior of HPGe detectors operating at temperatures below 77 K. Nuclear Instruments and Methods in Physics Research A 454 (2000) 403-408.

3. LuAG:Pr characterization of a novel scintillator crystal

Abstract: The recently developed praseodymium-doped lutetium aluminum garnet, LuAG:Pr, holds a strong potential for enhancing the properties of the the well-know lutetium-based scintillators crystals. These properties increase the range of possible applications for this crystal such as nuclear structure studies or medical imaging. In this chapter we report on measurements performed using a small crystal cube of 1 cm^3 coupled to a Hamamatsu R5320 photomultiplier tube. We have studied the energy resolution and linearity, together with the time response at ^{22}Na and ^{60}Co energies. Also, we estimate the internal activity of ^{176}Lu through of gamma ray spectrometry with an HPGe.

3.1. Introduction

During the last decade new types of scintillators have been produced and tested in order to increase the potential for applications requiring high gamma detection efficiency and fast response to radiation. Indeed, research and development of new high density fast scintillators have been mainly triggered by the growing needs of high energy physics and modern medical imaging [Chewpraditkul, W. *et al*., 2009]. For example in medical imaging the main interest on this type of scintillators has been reactivated by the renewed interest in time-of-flight for positron emission tomography (TOF-PET), where the present generation of scanners, based on a LSO and LYSO scintillators, are characterized by a time resolution of the order of 0.5 ns [Lewellen, T., 2008]. That value could be improved if instead of the aforementioned detectors a modern inorganic scintillator is used in the detector system [Yoshikawa, A., *et al*., 2010]. The purpose of this quest is to develop different types of scintillator crystals that provide better properties such as energy resolution, increase the efficiency and offer a faster time response, and, of course, can be manufactured by a cheaper known method. In this chapter we are going to expose a study of the main properties of particular scintillator crystal: LuAG:Pr.

The interest around LuAG:Pr ($Lu_3Al_5O_{12}:Pr^{3+}$) garnet is rapidly increasing due to their excellent scintillation properties attractive for hard X-ray and gamma-ray detection in various applications [Derdzyan, M.V., *et al.*, 2012]. The reported light yield of LuAG:Pr is 16,000–20,000 ph/MeV, fast scintillation decay component of the order of 20 ns, and the energy resolution is 5–7% at 511 keV; and good yield non-proportionality of 8% up to 1275 keV [Drozdowski *et al.*, 2008]. The time resolution for 511 keV photons is reported by Conti and coauthors [Conti *et al.*, 2009] to be 285 ± 15 ps for very small 0.005 cm^3 LuAG:Pr cubes. The emission is due to the 5d–4f transition of Pr^{3+} ion and lies in the range of 310–380 nm. The highest value of the light yield is attained in moderately doped single crystals containing 0.2–0.25 at % of Pr^{3+} [Yanagida *et al.*, 2012]. Thus, all these features have turned the LuAG:Pr crystal into a very promising candidate for several applications due to its high Z and density, fast rise time and high light output.

A possible drawback of the LuAG:Pr crystal is the presence of internal activity. A fraction of 2.59% of the natural Lutetium corresponds to ^{176}Lu, which is an unstable isotope with a very long half life (~$3.76x10^{10}$ y) [Yao, R., *et al.*, 2007]. Because the LuAG:Pr contains Lutetium is expected to have some selfactivity from this beta-decaying isotope. In fact,

previous studies found a relatively high intrinsic count rate of 210 Bq/cm^3 [Drozdowski *et al.*, 2008]. However, all these studies were accomplished using crystals based on old crystal growth procedure. Recently the provider, Furukawa, has changed the manufacturing for the LuAG:Pr in order to improve its properties, which means that a new estimation of the intrinsic concentration of ^{176}Lu is needed. For this reason, in this chapter, we are going to describe our estimation of the internal activity for a new formula sample of LuAG:Pr through gamma spectrometry via an absolutely calibrated HPGe detector.

Furthermore, because the crystal composition has slightly changed, some of the energy and time parameters may have changed too. Thus, in this chapter we will report on new measurements of the energy resolution, linearity and time response for a 1-cm^3 cube of LuAG:Pr crystal at different energies. For time measurements we have used ^{22}Na and ^{60}Co photon energies, while for energy we have include a ^{133}Ba, ^{137}Cs and ^{152}Eu. For the energetic measures a standard MCA module was used, while for timing measurements we have used time-delayed coincidences based on the fast timing method, where the time interval is precisely measured between events reaching two scintillator gamma detectors and NIM electronic devices to process the signals.

3.2. Description of measurements

3.2.1. Study of the Internal Activity

3.2.1.1. Low-level Gamma Spectra

In order to measure the internal activity of the LuAG:Pr crystal, we have employed an HPGe detector absolutely calibrated in efficiency for gamma energies to 5% precision with a ^{152}Eu source. During the measurements the HPGe was shielded from the surrounding background activity by lead blocks. The gamma intensities from natural lutetium were corrected for self absorption in the crystal. For comparison the spectrum of the intrinsic activity of the LuAG:Pr + R5320 detector combination has also been recorded.

All the gamma spectra were taken with an HPGe inside a lead shielding (see figure 3.1). The HPGe is LOAX 60450-30P-CW model provided by ORTEC, and was supply with -3.5 kV. The output signal was amplified by a 2022 Canberra amplifier, with coarse gain of 30, fine gain of 8 and shaping time of 0.5 μs. Finally, the signal was processed in a multichannel analyzer model PalmTop provided by ATOMKI.

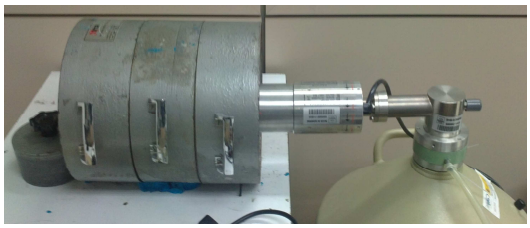

Fig. 3.1: *HPGe detector and lead shielding.*

Both calibrated ^{152}Eu source and LuAG:Pr crystal were putted at 5 and 10 cm in front of HPGe detector inside the lead castle. The spectra were taken for 8000s in order to get enough statistics. Also, a background spectrum was taken for 8000s to subtract the surrounded

contribution. We expect to record at least three different gammas coming from beta-transition of the ^{176}Lu. In the figure 3.2 a simplified decay scheme of ^{176}Lu is shown. The intensity of each gamma emission is in relative to decay of ^{176}Lu.

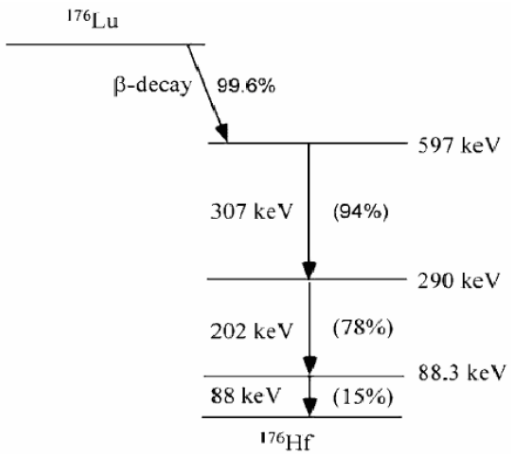

Fig. 3.2: *Simplified decay scheme of Lu-176.*

For the activity estimation we chose the NuDat information reported to energies and intensities for ^{176}Lu transitions (See Table 3.1), which is based on the A=170 evaluation by [Basunia, 2006].

Energy (keV)	Absolute Intensity (%)
88.34	14.5 (6)
201.82	78.0 (25)
307	93.6 (-)

Table 3.1: *Energies and intensities for main β-decay of Lu-176.*

Because we already have the efficiency calibrated for the HPGe, we need to estimate the activity from the source using an analogous procedure than the described in section 2.3.5. First, we need to estimate the activity in the moment of measure,

$$A(Bq) = \frac{N_\gamma}{t_r \cdot P \cdot \varepsilon_E}$$

where N_γ is number of net counts in the photopeak (area of the peak), corrected for dead-time and pile-up losses. P is branching ratio corresponding to the energy E_γ, t_γ denotes live-time elapsed for the measurement, ε_γ is the efficiency at a given energy for the HPGe at some particular distance from detector, A is the activity estimated for each specific energy in Becquerel.

The uncertainties can be calculated by error propagation equation for several variables, assuming time t is precisely known and neglecting the error in the branching ratio [Longoria, L., 1996]:

$$(\Delta A)^2 = \left[\left(\frac{\partial A}{\partial N_\gamma} \right)^2 (\Delta N_\gamma)^2 + \left(\frac{\partial A}{\partial \varepsilon_E} \right)^2 (\Delta \varepsilon)^2 + \left(\frac{\partial A}{\partial P} \right)^2 (\Delta P)^2 + \left(\frac{\partial A}{\partial t} \right)^2 (\Delta t)^2 \right]$$

$$(\Delta A)^2 = \left(\frac{N_\gamma}{t_r \cdot P \cdot \varepsilon_E} \right)^2 \cdot \left[\left(\frac{\Delta N_\gamma}{N_\gamma} \right)^2 + \left(\frac{\Delta \varepsilon_E}{\varepsilon_E} \right)^2 \right]$$

Finally,

$$\frac{\Delta A}{A} = \left[\left(\frac{\Delta N_\gamma}{N_\gamma} \right)^2 + \left(\frac{\Delta \varepsilon_E}{\varepsilon_E} \right)^2 \right]^{1/2}$$

Now, some fraction of the gamma rays is auto-absorbed by the crystal itself. These gammas are not released from the crystal volume and therefore they can not be recorded in the HPGe detector. In order to estimate the fraction of gammas which do not exit the crystal, we must determine the energy-absorption fraction.

3.2.1.2. Estimation of Energy-Absorption Fraction

The Absorbed Fraction (AF) is a quantity to estimate the γ–ray dose at an internal point in an intermediate-sized radioactive object, and could be define as:

$$AF = \frac{\gamma - \text{ energy absorbed in target}}{\gamma - \text{ energy produced by the source}}$$

In other words, the AF helps to estimate the fraction of gammas that are auto-absorbed in the crystal. Because these gammas are absorbed in the crystal, they cannot be recorded in the HPGe detector. So AF gives us the fraction of counts that we had missed during a gamma measurement. In other way, the AF is a factor to correct the estimation of intrinsic activity.

In order to get an expression to estimate the AF factor, we going to follow the derivation suggested in [Attix, F., 2004]. First we have to consider a simple scenario, which is represented in the figure 3.3. Suppose a radioactive object with a volume V. This object is filled by a homogeneous medium and a uniformly distributed γ–ray source. It may be surrounded either by an infinite homogeneous medium identical to that in V, but nonradioactive, or and infinite vacuum. In the first case a γ–ray escaping from V may be scattered back in; in the second case it will be irrevocably lost. The first case simulates more closely an organ in the body; the second an object surrounded by air, which is more similar to our cubic crystal [Attix, F., 2004].

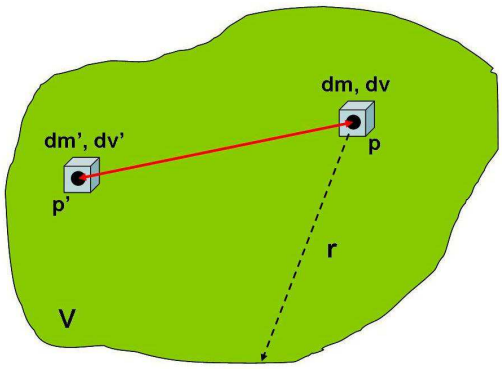

Fig. 3.3: *Schematic relation to the Absorbed Fraction*

If $\overline{R}_{dv}$ is the expectation value of the γ–ray radiant energy emitted by the source in dv and $\overline{\varepsilon}_{dv,V}$ the part of that energy that is spent in V, then the absorbed fraction with respect to source dv and target V is:

$$AF_{dv,V} = \frac{\overline{\varepsilon}_{dv,V}}{\overline{R}_{dv}}$$

Assuming to $\overline{\mu}'$ be the mean effective attenuation coefficient for γ–ray energy fluence transmission through a distance r of the medium, the fraction escaping from V in the direction of r from point P is $e^{-\overline{\mu}'r}$. In terms of the polar coordinates, with P at the origin, the value of the absorbed fraction is:

$$AF_{dv,V} = \frac{1}{4\pi}\int_{\theta=0}^{\pi}\int_{\beta=0}^{2\pi}(1-e^{-\overline{\mu}'r})\sin\theta d\theta d\beta$$

For the scenario two, for which the volume V is surrounded by vacuum, it is possible to obtain a crude estimate of the dose at some point **P** within a uniformly γ–active homogenous object, it may suffice to obtain the average distance r from the point to the surface of the object, either by inspection or using:

$$\overline{r} = \frac{1}{4\pi}\int_{\theta=0}^{\pi}\int_{\beta=0}^{2\pi} r\sin\theta d\theta d\beta$$

Now, in order to determine $\overline{r}$, we have used simple geometrical considerations about the 1cm-side cube crystal. Basically we estimate the maximum distance from one point P to the edge, in this $\overline{r}$ correspond to the diagonal from the geometrical center of the cube until the border of the crystal. This method is usually used to approximate the distance because it allows to over-estimate the fraction without many change in the ratio [Attix, F., 2004]. In our case, as is shown in the figure 3.4, the mean distance is $\overline{r} = 0.866\,cm$.

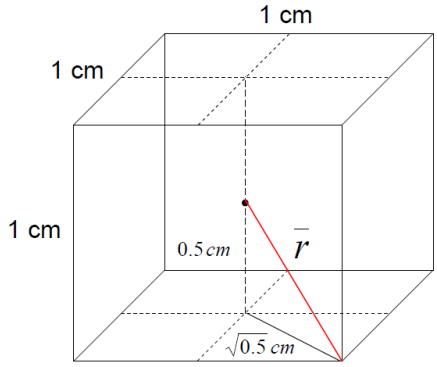

Fig. 3.4: *Estimation of $\bar{r}$ to a cube LuAG:Pr crystal.*

Now, if in the scenario two the Radiation Equilibrium (RE) conditions are satisfied: the atomic composition of the medium and its density are homogenous, the radioactive source is uniformly distributed and there are not electric or magnetic fields; then, one may employ $\mu_{en} \cong \overline{\mu'}$ in the straight-ahead approximation to obtain [Sugano, K., 2009]:

$$AF_{dv,V} \cong 1 - e^{-\mu_{en}\bar{r}}$$

Thus, this expression approximates roughly the ratio of γ–rays which are auto-absorbed in the crystal.

Finally, in order to estimate AF we have to obtain the μ_{en} term for the crystal. Because the LuAG:Pr is a mixture of elements - $(Pr_{0.025}Lu_{0.975})_3Al_5O_{12}$ -, we can use the *Bragg Rule* to estimate the Mass Energy-Absorption Coefficient. Remembering that this approximation is valid only when radiative losses are assuming small [Attix, F., 2004]. The Bragg Rule to mixtures is given by:

$$\left(\frac{\mu_{en}}{\rho}\right)_{mix} = \left(\frac{\mu_{en}}{\rho}\right)_{Pr} f_{Pr} + \left(\frac{\mu_{en}}{\rho}\right)_{Lu} f_{Lu} + \left(\frac{\mu_{en}}{\rho}\right)_{Al} f_{Al} + \left(\frac{\mu_{en}}{\rho}\right)_{0} f_{0}$$

The energy attenuation coefficients will be obtained from [NIST, 2012], and atomic mass fraction will be estimated for mass contribution of the crystal.

3.2.2. Experimental set-up for time-delayed measurements

3.2.2.1. Set up

Timing methods in Nuclear Particle Physics are used for the measured of small time intervals. In Nuclear Physics important insight on the nuclear structure can be gained by the measurement of nuclear level lifetimes. Timing spectroscopy can be performed by electronic methods, directly measuring the time interval between two correlated events.

Nuclear lifetime measurements in the micro and nanosecond range are normally performed by delayed coincidences with planar HPGe detectors. In the case of lifetimes in the range of nanoseconds down to tens of picoseconds, measurements can be done employing the

ultra Fast Timing Methods [Mach, H., *et al.*, 1989, Moszinski, M., *et al.*, 1989]. The original method consists on triple β-γ-γ coincidences. Timing information is obtained by the delayed coincidence between two fast detectors (a beta plastic scintillator and an inorganic scintillator crystal), while the energy branch is selected by a coincident γ–ray in an HPGe detector.

In addition, inorganic scintillators are extensively used in medical imaging techniques than profit from the detection of gamma rays. In particular, Positron Emission Tomography (PET) is a powerful functional imaging method that makes use of inorganic scintillators to detect collinearly photons produced in an annihilation process after β^+-decay. Timing information is relevant in Time Of Flight PET, due to the fact that time information is used for improving the precision in determining the annihilation point. Therefore new materials play a key role in these fields as well.

In this work we have used time-delayed coincidences based on the fast timing method, where the time interval is precisely measured between events reaching two scintillator gamma detectors. The set-up consisted of a reference detector with ultra-fast time response, a BaF_2 in this case, and the scintillator detector (Crystal and PMT combination) under test. The measurements of time resolution were performed with ^{60}Co and ^{22}Na γ-sources in a close geometry, with the detectors about 7 mm apart and the source positioned in between them. Both signals from detectors were coupled to standard NIM front-end electronics (See Figure 3.5). More details of technique in [Mach *et al.*, 1991] and [Fraile, L.M., *et al.*, 2012].

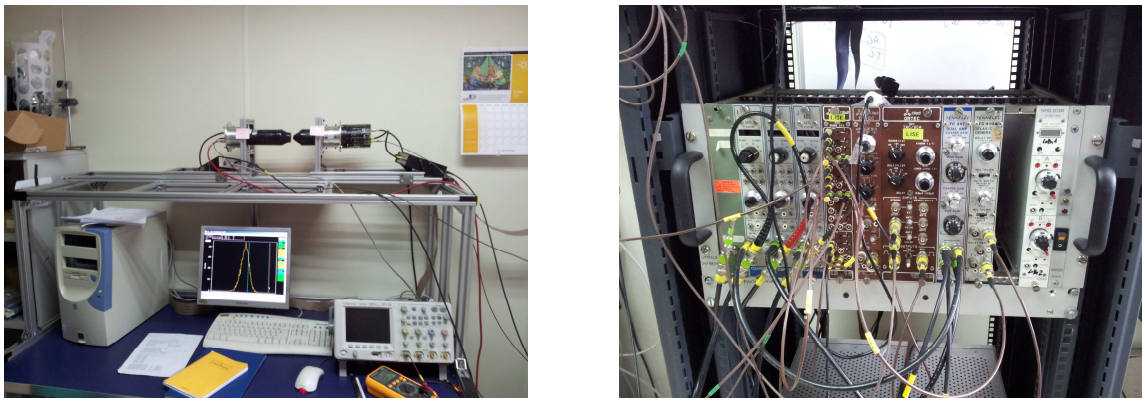

Fig. 3.5: *Left: Laboratory set up, Right: Front-End modules used to process the signals.*

Anode signals, which are used for estimate timing response, are taken from the photomultiplier tubes (PMTs) directly fed to ORTEC 935 Constant Fraction Discriminators (CFDs). The CFDs were individually optimized for delay and walk effects, and their output signals were taken to an ORTEC 567 TAC. The TAC amplitude signal, providing the time difference between two detector signals, was digitized in an ADC.

Dynode signals, which are used for energy response, are processed via a slow electronic branch for energy measurements. Each energy signal should be preamplified and amplified before fed to the ADCs, in our case we have used an ORTEC 113 preamplifier and Tennelec TC247 spectroscopic amplifier. A logic signal generated for each valid TAC event was sent to the Gate and Delay Generator (GG) in order to provide gating signal to open the ADCs. Listmode coincidence data from the three ADCs were stored on a disk and analyzed off-line (See Figure 3.5).

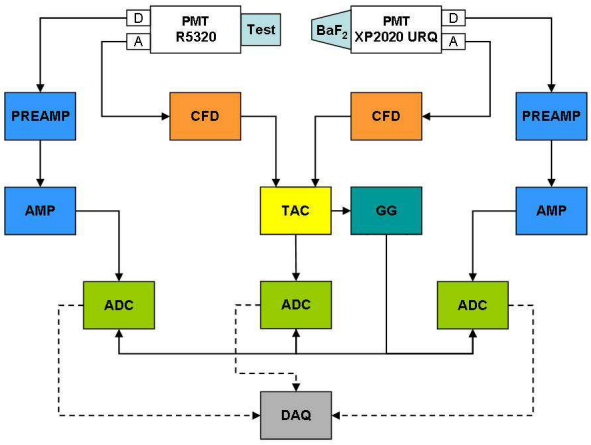

***Fig. 3.6**: Schematics of the time-delayed setup used to measure time response of the LuAG:Pr crystal versus the ultra-fast reference BaF_2 detector.*

Also, in order to study the shape of the pulses, the anode signal (time signal) was driven to a 4 GSa/s digitizer to explore the rise and falling time and to determine if there is or not noise presence. In our case the digitizer is an oscilloscope of Agilent model DSO6104A of 1 GHz of bandwidth and sampling of until 8000 channels. The time interval between two consecutive channels or points of sampling was fixed in 250 ps.

3.2.2.2. Crystal and coupling of the LuAG:Pr

The LuAG:Pr 1 cm^3-cube crystal was commercially produced and kindly provided to us by Furukawa [Furukawa]. The crystal, with all faces polished, was wrapped in teflon and optically coupled to a Hamamatsu R5320 PMT by means of Viscasil 60000 cSt, a standard industrial silicon grease [Klamra et al., 1987].

The R5320 is a 1-inch PMT with quartz window, suited for the photoemission of LuAG:Pr, which peaks around 310 nm, but tails below 300 nm. It is a fast PMT with a gain of the order of $6x10^6$, a rise time with typical anode pulse rise time of 0.7 ns and FWHM Transit Time Spread of 160 ps, as reported by the manufacturer [Hamamatsu Photonis, 2009]. The R5320 PMT was incorporated in the assembly H6610, with serial number BA0222. Its cathode luminous sensitivity is 88 μA/lm, anode luminous sensitivity 576 A/lm and anode dark current 6.50 nA. The cathode blue sensitivity index was 9.9 (See figure 3.7).

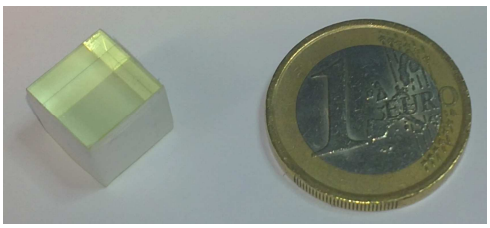

***Fig. 3.7**: Left, LuAG:Pr scintillator crystal by side of a one- euro coin. Right, photo of a R5320 PMT.*

We have set the high voltage of the PMT to provide anode output signals of approximately 1V amplitude for 1 MeV photons. This is our standard procedure for setting up fast scintillator detectors for fast-timing measurements in nuclear structure experiments. The

typical operation voltage for the R5320 PMT in our measurements was -1940 V. Nevertheless the dependence of the FWHM time resolution on the high voltage applied the phototube has been studied in this work, too.

3.2.2.3. BaF_2 as Reference crystal

A small truncated cone BaF_2 crystal was used as fast-response reference detector. This crystal is usually used as reference in timing experiments because its scintillation light has a very fast component [Knoll, 2000]. In fact, BaF_2 crystal still is the fastest commercial scintillator crystal available nowadays (*0.6-0.7 ns*) [SCIONIX, 2012]. Although the attainable energy resolution (*of the order of 10%, it can be down to 9% in the best cases, at 662 keV*) is considerably poor and the light yield in the fast component is quite small (*1.8 photons/keV*), its high density (*4.88 g/cm*^{3}) and atomic number have made it the scintillation material for several timing applications [Moszynski *et al.*, 1989]. Also, because the BaF_2 is only slightly hygroscopic material, there is no need to be encapsulated.

The reference crystal was coupled to the Photonis XP2020-URQ PMT, which has a quartz window that increases the ultraviolet sensitivity to use the fast component of the BaF_2. To increase the internal reflectivity avoiding photons lose, the crystal were carefully covered by Teflon tape before coupled to a PMT. In order to determine the time response of the reference detector, a system of three identical BaF_2 crystals coupled to XP2020-URQ photomultipliers with similar parameters was set up and operated at 2300V.

From the combined FWHM time resolution at ^{60}Co and ^{22}Na energies of the three pairs of detectors the individual time resolution of each of them was obtained. For instance, the deconvoluted value of time resolution for our reference BaF_2 detector was 79±2 ps for ^{60}Co full energy peaks and 120±2 ps for photons of 511 keV from ^{22}Na source.

3.2.2.4. Time Resolution and Optimization of timing

Time resolution is the ability of a detector or experimental set up to measure two events that happened within a time interval. The greater the time resolution of a detector, the closer events that can be detected [Knoll, 2000]. Over a time spectrum the coincidence events usually takes a (semi-)Gaussian shape. Time resolution is expressed in FWHM (Full Width at Half Maximum) terms. Calibration to pass from channels to base-time is provided by the TAC. Further, when the measure system is made of two detectors, timing info can be obtained directly by a deconvolution between the FWHM obtained and the time response of the reference crystal. The expression to obtain the time resolution for the test crystal:

$$FWHM_{\text{LuAG:Pr}} = \sqrt{\left(FWHM_{\text{Total}}\right)^2 - \left(FWHM_{\text{BaF}_2}\right)^2}$$

The measurements of time resolution were performed with ^{60}Co and ^{22}Na-sources. In the case of ^{60}Co there are two full energy peaks at 1173 and 1332 keV recorded in each detector. Thus the time resolution represents an average value for two possible combinations of the peaks selected in the pair of detectors. In the first step, the full energy peak at 1332 keV was selected in one of the detectors (BaF_2) and the coincident 1173 keV peak was selected in the other one (LuAG:Pr). The energy gates were set roughly at the Full Width at Tenth Maximum (FWTM) of the energy peaks. Data corresponding to the selected energy events were sorted out and projected into a time spectrum (e.g. BaF_2[1332 keV]-LuAG:Pr[1173 keV]). The

sorting included the instability corrections. In the next step, the energy gates were reversed in the two detectors and a second time spectrum (BaF_2[1173] - LuAG:Pr [1332]) was created. Both time spectra have typically shown an approximately Gaussian symmetric shape, except when extreme parameters were set in the CFD, in which case the time spectra showed a small asymmetry on one side of the peak. Finally, the last time resolution FWHM was given for the summed spectrum.

In general the FWHM resolutions for the (1332-1173) and (1173-1332) time spectra are different, reflecting the fact that the time resolution for the LuAG:Pr are significantly worse than for the reference crystals. In addition the time resolution depends on energy and deteriorates for lower energies. In the case of ^{22}Na only one time spectrum, (BaF_2[511]-LuAG:Pr[511]), was sorted out by selecting the energy events on the peak at 511 keV.

In the other hand, in order to find the optimum time resolution of test detector LuAG:Pr coupled to the fast-response PMTs we have measured the time resolution as a function of high voltage applied to the tube and two parameters of the CFD: the external delay and the walk adjustment (Z). The internal delay jumper on the ORTEC 935 CFD, W1, was removed throughout our measurements. According to the ORTEC user manual this setting corresponds to an internal delay of about -1 ns. The optimization process was iterative, by first finding a preliminary set of optimal parameters and then optimizing again using high precision measurements.

3.3. Results for LuAG:Pr

3.3.1. LuAG:Pr Internal Activity

3.3.1.1 Theoretical estimation of concentration of activity

Assuming the chemical composition of LuAG:Pr - $(Pr_{0:025}Lu_{0:975})_3Al_5O_{12}$, where 2.5% of the Lu is replaced by Pr, as described in [Kamada et al., 2012], the quantity of Lu in the crystal can be readily obtained. Because 2.599% of the natural Lu corresponds to radioactive ^{176}Lu, with $T_{1/2}$ = 3.76 (7) x 10^{10} years β-decaying to ^{176}Hf, we are able to estimate *theoretically* the activity per unit volume in the crystal.

First, we can estimate the crystal mass through volume of the crystal (cube of a 1cm per side) and density of 6.73 g/cm^3 ratio, and so: m=6.73g.

Because we also can calculate the total molar mass (MM = 848.06 g) of the mixture, the number of lutetium atom is easily computable:

$$6.73\,g \cdot \frac{1\,mol\ LuAG}{848.06\,g} \cdot \frac{6.022\times10^{23}\ molecules\ LuAG}{1\ mol\ LuAG} \cdot \frac{2.975\,atoms\ Lu}{1 molecules\ LuAG} = 1.42\times10^{22}\ atoms\ Lu$$

Thus, the fraction atoms of ^{176}Lu (2.599%) which are in the crystal is approximately $N_0 = 3.68\times10^{20}$. By this value the concentration of activity for the LuAG:Pr would be roughly calculated of the order of 215±20 Bq/cm^3.

3.3.1.2 Empirical estimation of the concentration of activity

First measurement in order to understand the internal activity in the LuAG:Pr was a energy spectrum with the crystal coupled to the R5320 PMT operated at -1940 V during 10 ks. This energy spectrum is plotted in the figure 3.8 and shows the beta spectrum of the β- transitions from ^{176}Lu to ^{176}Hf shifted by the contributions of auto-absorbed X-rays and gamma-rays of the decay and some X-rays from Hafnium. Only the peak at 1460 keV is not related with the transition and must be came from natural ^{40}K in the surrounding environment (please check again the figure 3.2 to see the decay schema).

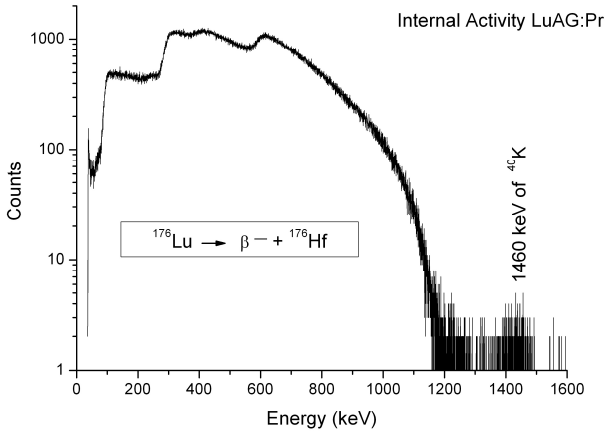

Fig. 3.8: *Energy spectrum of LuAG:Pr internal activity coupled to R5320 PMT during 1000 s.*

Now, in order to estimate the absolute intrinsic activity of ^{176}Lu, the gamma spectrum of the 1 cm^3 LuAG:Pr crystal has been measured with a HPGe detector (ORTEC LOAX 60450-30P-CW), absolutely calibrated for efficiency with a ^{152}Eu source, whose intensity is known to better than 5%. The measurements were taken at a distance of 5 cm from the HPGe end cap. Spectra were taken during 2000 s, and the room background was subtracted. The most intense gamma transitions of 201.8 and 306.8 keV were considered for the subsequent analysis. The self absorption fraction for gammas of these energies in the crystal were estimated via the Bragg Rule for the $(Pr_{0.025}Lu_{0.975})_3Al_5O_{12}$ compound, where an uniform distribution of ^{176}Lu is assumed and the radiation attenuation distance is estimated as half of the diagonal of the cube.

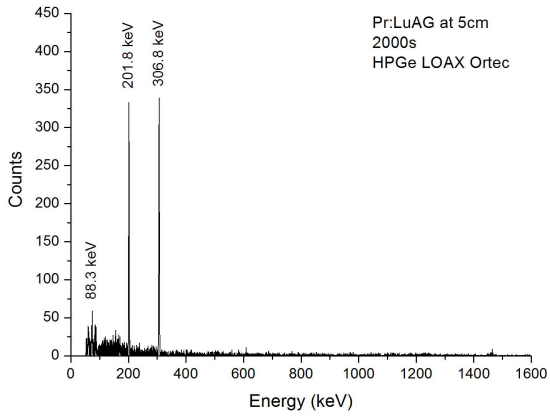

Fig. 3.9: *Gamma spectrum of LuAG:Pr internal activity took by HPGe at 5cm during 2000s with background subtracted.*

Because we already have the absolute efficiency for the HPGe at 5 and 10 cm, it is possible to estimate a local efficiency around the region of interest that includes 201.8 and 306.8 keV gammas of ^{176}Lu. Now, by a linear local approximation of the efficiency for the region which contains the 201.8 and 306.8 keV of ^{176}Lu (See figure 3.9), we obtain:

Distance	Time	Energy (keV)	ε_E	ε_{error}
5 cm	2000	201.83	1.98E-02	9.89E-04
		306.78	1.32E-02	6.88E-04
10 cm	8000	201.83	8.44E-03	4.30E-04
		306.78	5.49E-03	2.96E-04

Table 3.2: *Efficiencies values in function of energy and distance for ^{176}Lu gammas*

From the spectra data we obtained the net area for each energy peak and from these efficiency values, now we are able to use the activity equation in order to calculate the internal activity related to the energy before the auto-absorption fraction correction be applied. So it is obtained:

Position (cm)	Interval (s)	Peaks E (keV)	A_{source} (Bq)	Error (%)
5	2000	201.83	122.3	8.5
	2000	306.78	157.8	7.6
10	8000	201.83	115.2	8.1
	8000	306.78	153.3	7.2

Table 3.3: *Estimation of ^{176}Lu activity without applied the auto-absorption fraction correction.*

However, the activities differences between energies are due to auto-absorption fraction (AF) which depends of the energy and how the crystal is made of. Hence, we have to explore the correction factor for auto-absorption.

First, from the NIST X-ray attenuation databases we extract the values of the mass attenuation coefficient, μ/ρ, and the mass energy-absorption coefficient, μ_{en}/ρ, as a function of photon energy, for elemental media. So, by analytical interpolation, we obtain the μ_{en} term for the crystal in order to estimate the Absorption Fraction (AF) (See figure 3.10) [NIST, 2012].

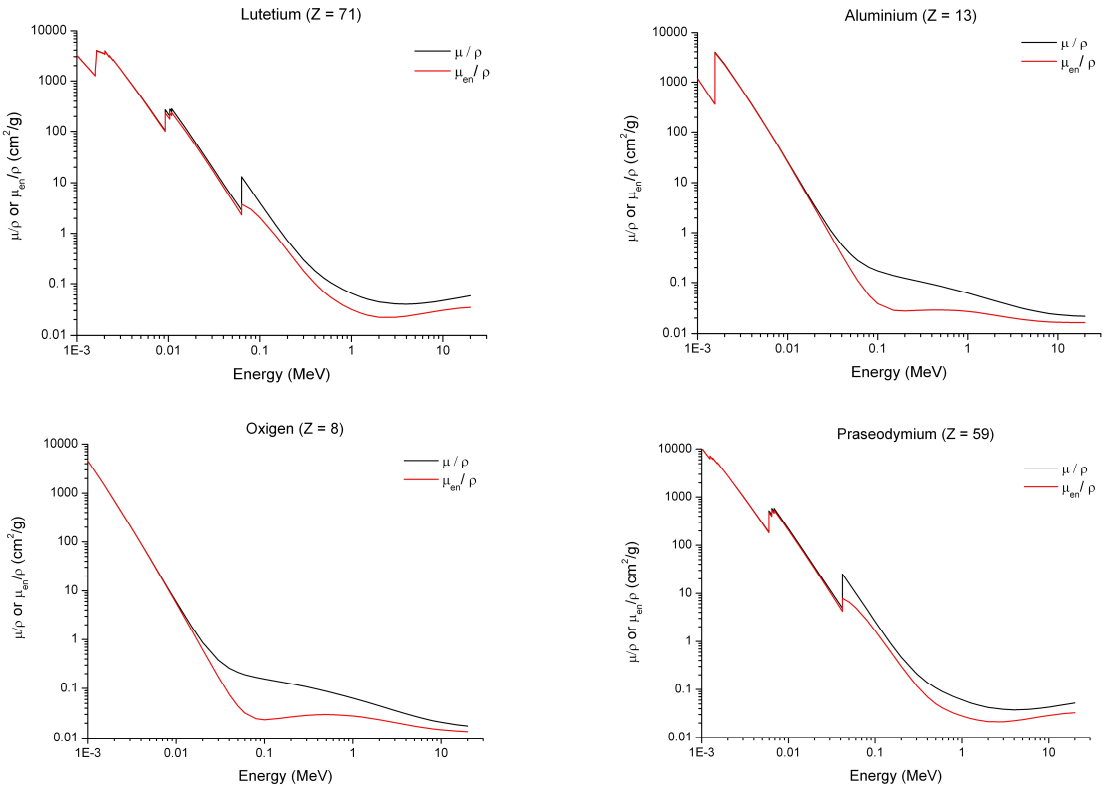

Fig. 3.10: *Mass attenuation (μ/ρ)-black line- and mass energy-absorption (μ_{en}/ρ) – red line-coefficients as a function of photon energy for LuAG:Pr elements: Lu, Pr, Al and O.*

Because NIST allows downloading the values to reproduces the previous plots, we can interpolate in order to estimate the right values of energy-absorption for LuAG:Pr energies. Interpolation was made following a simple polynomial fitting. In the figure 3.11 the interpolation techniques is exposed for the lutetium case.

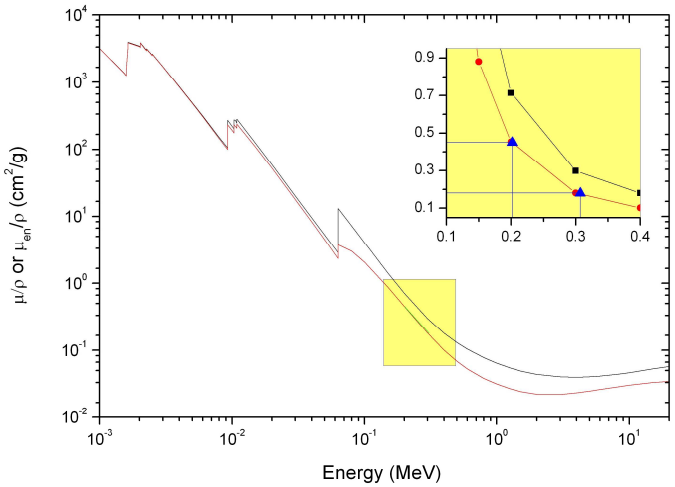

Fig. 3.11: *Representation of how the interpolation technique works for the 201.8 and 306.8 keV energies (blue triangles in the small box).*

For this technique we obtain the coefficients for all the elements (See Table 3.4):

	Lu	Al	O	Pr
Energy (keV)	**μ_{en}/ρ (cm^2/g)**	**μ_{en}/ρ (cm^2/g)**	**μ_{en}/ρ (cm^2/g)**	**μ_{en}/ρ (cm^2/g)**
202	6.91E-01	1.22E-01	1.23E-01	4.55E-01
307	3.20E-01	1.04E-01	1.06E-01	2.27E-01

Table 3.4: *Estimation of mass energy-absorption coefficient for LuAG:Pr elements.*

Also we need to calculate the atomic mass fraction (F_i) from the mass contribution of each element in the crystal (see Table 3.5) using the new formula - $(Pr_{0:025}Lu_{0:975})_3Al_5O_{12}$ -:

Element	Moles in formula	Atomic Mass (g/mol)	Molar Mass (g)	Mass Factor F_i
Lu	2.925	174.97	511.79	60.3%
Pr	0.075	140.91	10.57	1.2%
Al	5	26.98	134.90	15.9%
O	12	15.9	190.80	22.5%
Total Molar Mass			**848.06**	

Table 3.5: *Stoichiometry for the LuAG:Pr crystal and estimation of the mass factor (F_i)*

Now, we estimate the energy attenuation coefficient for mixture as function of the gamma energy by:

$$\left(\frac{\mu_{en}}{\rho}\right)_{mix} = \left(\frac{\mu_{en}}{\rho}\right)_{\Pr} f_{\Pr} + \left(\frac{\mu_{en}}{\rho}\right)_{Lu} f_{Lu} + \left(\frac{\mu_{en}}{\rho}\right)_{Al} f_{Al} + \left(\frac{\mu_{en}}{\rho}\right)_{0} f_{0}$$

Then, we obtain:

	Lu		Al		O		Pr		Mixture
Energy (keV)	**μ_{en}/ρ (cm^2/g)**	**F_{Lu}**	**μ_E/ρ (cm^2/g)**	**F_{Al}**	**μ_E/ρ (cm^2/g)**	**F_O**	**μ_E/ρ (cm^2/g)**	**F_{Pr}**	**$(\mu_E/\rho)_{mix}$ (cm^2/g)**
202	6.91E-01	0.60	1.22E-01	0.16	1.23E-01	0.16	4.55E-01	0.01	4.62E-01
307	3.20E-01	0.60	1.04E-01	0.16	1.06E-01	0.16	2.27E-01	0.01	2.29E-01

Table 3.6: *Information used to estimate the energy attenuation coefficient of the mixture.*

Finally, AF value can be calculated assuming r = 0.866 cm (derivate in section 3.2.1.2.) and the previous estimation of μ_{en}/ρ. Correction factor for 202 keV rounds 33% and for 307 keV is close to 18%. Therefore we can approximate the total internal activity concentration of the LuAG:Pr in 171 ± 30 Bq/cm^3.

Hence these measurements yield an activity of ^{176}Lu in the crystal of 171 ± 30 Bq/cm^3. This result is consistent with the estimate of 215 ± 20 Bq/cm^3 using the amount of ^{176}Lu in the LuAG:Pr crystal, and it is in agreement with the value of 210 Bq/cm^3 reported by [Drozdowski et al., 2008]. Therefore the LuAG:Pr crystal has the drawback of high intrinsic activity, yielding a high background that can hamper low level counting experiments. However, this value is low comparing with other crystals which are lutetium activated too. For example, the LSO crystal shows 300 Bq/cm^3 [Knoll, 2000], the LYSO have 277 Bq/cm^3 [Saint-Gobain, 2013] and LuAP presents 285 Bq/cm^3 [Owens, A, 2007].

3.3.2. Energy Resolution and Linearity

In order to explore the energy resolution and linearity of the LuAG:Pr crystal coupled to R5320 photomultiplier, the detector was irradiated with standard gammas sources of ^{137}Cs, ^{22}Na, ^{60}Co and ^{152}Eu during 1000s. Measurements were taken at room temperature with the PMT biased at -1940 V and maintaining the amplification constant. Energy spectra are shown in the figures 3.12 and 3.13.

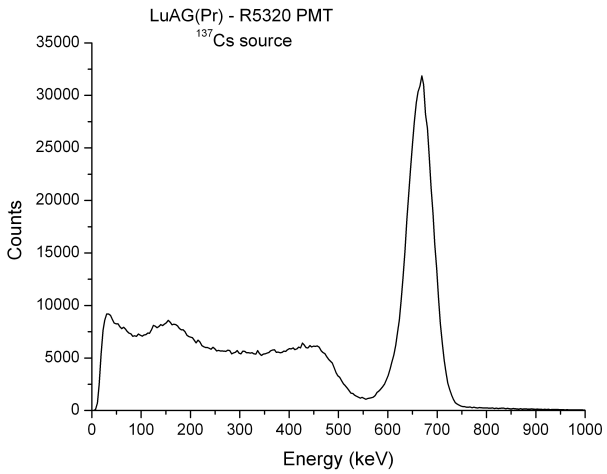

Fig. 3.12: *Energy spectrum for an exempt gamma source of ^{137}Cs.*

The measured energy resolution for 662 keV is 6.0%. This value is significantly higher than 4.6% quoted by the manufacturer in [Kamada et al., 2012]. This might be explained by the use of the R5320 PMT, optimized for fast-response (although without screening grid) with very good TTS, but with not so high quantum efficiency [Szczesniak et al., 2009].

In the figure 3.13 the ^{22}Na spectrum is in semi-log scale in order to shows summing effect between 511 and 1274 keV gammas from ^{22}Na source. This effect, caused by the high rates and the accidental coincidences between two gammas-rays, in this case is useful because shows the good energetic response of the detector to gamma energies over 1.5 MeV and good linearity for wider range of calibration. In the right side of the same figure, gammas from ^{60}Co can be easily separated which is really useful properties for several applications that requiring detectors with high resolution to solve consecutive peaks.

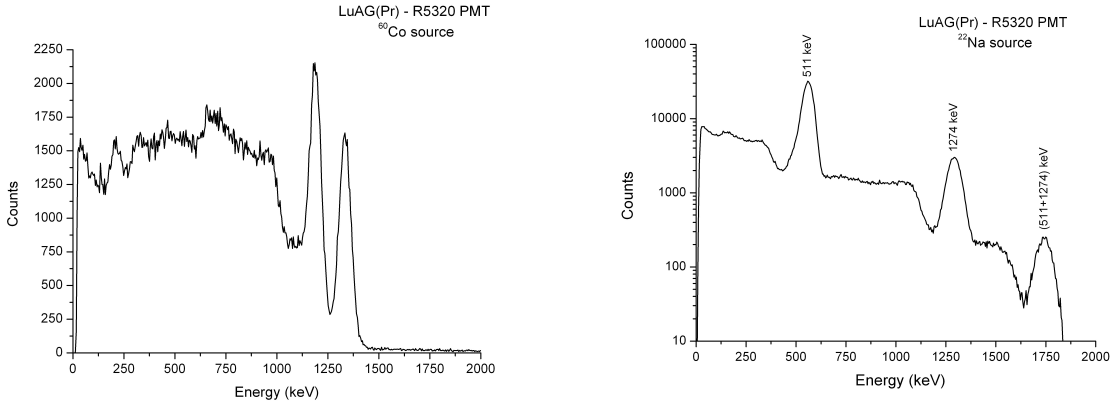

Fig. 3.13: *Energy spectrum for an exempt gamma source of ^{60}Co (left) and ^{22}Na (right).*

We have also explored the energy linearity as a function of the voltage applied. Several values of HV were used to study the linearity, one was at the optimum bias (-1940 V) and others around this value (-1700, -1800 and -2000 V). Because an exempt ^{152}Eu source was included in the study, the energy range of interest was extended from 122 to 1408 keV. The results plotted in fig. 3.14 show very linear energy behaviour for the whole range of voltages applied in these tests, including the 1900 - 2000 V range, where the best time resolution is achieved.

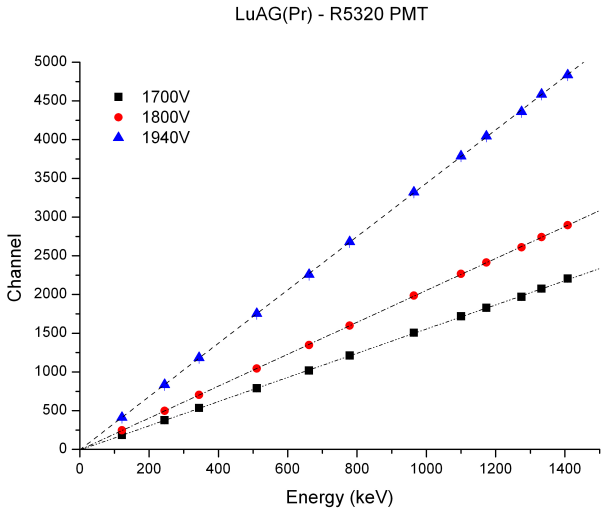

Fig. 3.14: *Energy linearity plots for the LuAG:Pr and Hamamatsu detector.*

3.3.3. Time Resolution for LuAG:Pr

In order to find the optimum time response of the LuAG:Pr detector we have measured the resolution as a function of the applied high voltage to the PMT and two parameters of the CFD: the external cable delay and the walk adjustment (Z). Also, we have digitized several pulses in order to explore the rise and falling time of an average pulse. Finally, all time resolution results in this and next sections are deconvoluted values, that is, they are given for a single detector involving LuAG:Pr and the Hamamatsu R5320 phototube.

3.3.3.1. Rise and Fall time

Firstly the fast negative anode pulses were driven to a 4 GSa/s oscilloscope in order digitized it in a grid of 250 ps between consecutive samples or channels. Then, by a simple code they where normalized and summed to obtain an average pulse. In the figure 3.15 is shown the sum of several inverted anode pulses.

To estimate the rise time we can use a standard (10-90%) or the CFD (20-100%) methods because provide similar results around 3 ns. However, we chose the CFD method which provides the output signal at a constant fraction of 20% of the maximum input amplitude, and then the rise time can be estimated of the order of 3 ns. The small box inside the left side of the figure 3.15 amplifies the rise region of the pulse. The red points indicate the 20 and 100 percent of the amplitude, thus we can estimate the rise time.

To estimate the falling time we can fit the decay region of the pulse to an expression with two or three terms [Moszynski, M., *et al.*, 1996]. In our case we chose to use only two exponential terms, one associated to fast decay and other with the slow decay. Our polynomial fitting is:

$$y = y_0 + A_1 e^{-t/\tau_{fast}} + A_2 e^{-t/\tau_{slow}}$$

In the right side of the figure 3.15 the fitting curve is drawing with a red line and its coefficients shows clearly two components, one fast of the order of 25 ns and the other slow of the order of 500 ns.

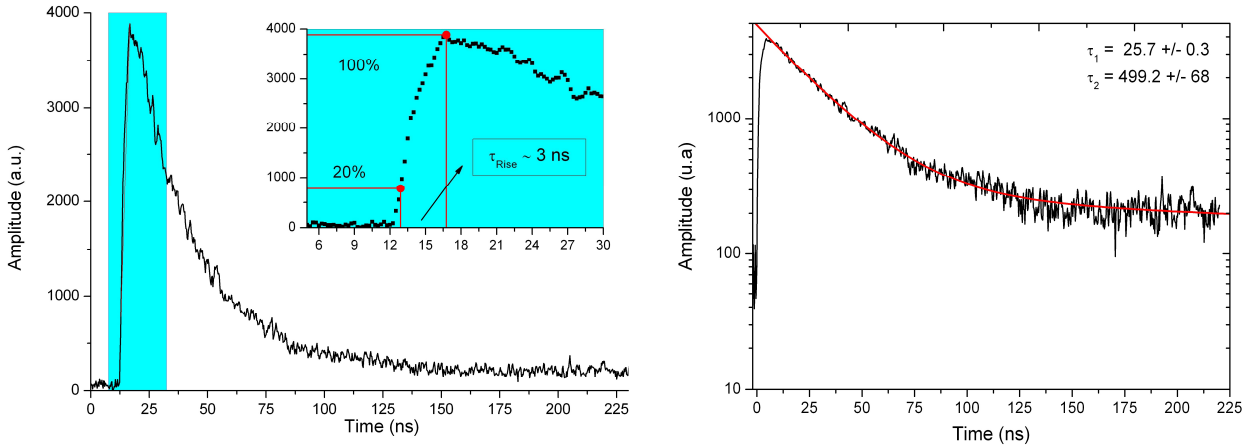

Fig.3.15: *Inverted and added fast negative anode pulses for LuAG:Pr coupled to Hamamatsu R5320 PMT. Left, the rise time or the order of 3 ns following the CFD methods. Right, the decay curve (black line)) and its two exponential terms fitting (red line).*

3.3.3.2. Optimization of External delay for test signal in the CFD.

The internal delay jumper on the ORTEC 935 CFD, W1, was removed throughout our measurements, which according to the manufacturer sets the internal delay to approximately -1 ns. The optimization process was iterative, by first finding a preliminary set of optimal parameters and then optimizing again using high precision measurements.

In order to optimize the time resolution, we have to explore the external delay applied to the signal of the LuAG:Pr in the CFD. From 0.5 to 30 ns of external delay were tested in the CFD for the ^{60}Co and ^{22}Na energies. Both cases show some similar results. In the figure 3.16 the results for ^{60}Co are shown. The minimum of time resolution is reached in a sharp minimum at short delays at 0.8 ns (see zoomed region in figure 3.16). Based on this result we have selected an external CFD delay of 0.8 ns for further tests. We should note that the walk has then been optimized by setting the Zero crossing of the CFD, but only a negligible effect has been observed.

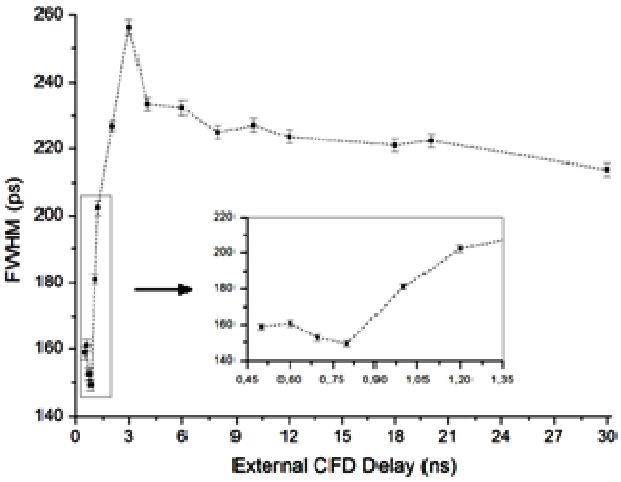

Fig. 3.16: *The dependence of time resolution FWHM in ps as a function of the external delay in ns for an individual LuAG:Pr coupled to Hamamatsu R5320 PMT. These results were obtained using ^{60}Co but are identical for ^{22}Na.*

3.3.3.3. Optimization of the HV.

We also have explored the influence of the applied high voltage on the time resolution. Since we are dealing with a scintillator where the photon yield is not very large, around of 20000ph/MeV, we expect a steady improvement of the resolution, until space charge effects take place at large high voltage values. However, after test several voltage values we found that resolution improves up to about -1900V and remains almost constant until -200V. In other words, around the -1940V we did not find operative changes in the time resolution.

After all these optimization test, we obtain the time spectra for our LuAG:Pr detector against the reference detector (BaF_2). In the figure 3.17 are shown the results for ^{22}Na (511 keV) and ^{60}Co (1173-1333 keV). From the reference crystal we had a time resolution of 120 ± 2 ps at 511 keV and 79 ± 2 ps at 1173-1332 for ^{60}Co. Hence we can deconvolute the time resolution for our crystal at any energy tested.

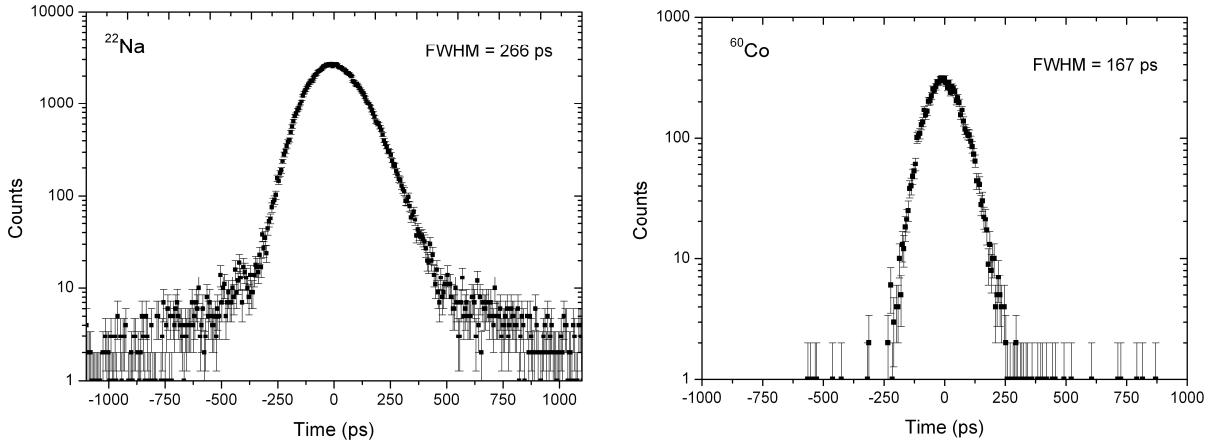

Fig. 3.17: *Time spectra for the LuAG:Pr crystal coupled to R5320 PMT against the reference detector (BaF_2) at two scenarios. Right, time spectrum for 511 keV. The total time resolution is 266 ± 2 ps. Left, Time spectrum for 1173-1333 keV. The total FWHM obtained is 167 ± 2 ps.*

Therefore the FWHM time resolution measured for the LuAG:Pr crystal with the R5320 phototube after full optimization is 147 ± 2 ps at ^{60}Co and 238 ± 2 ps for 511 keV photons from ^{22}Na. Finally, last value can be compared with a previous work published by [Conti *et al.*, 2009], whose reported an intrinsic time resolution of 285 ± 15 ps at ^{22}Na. However, their sample was a smaller LuAG:Pr crystal of 0.005 cm^3. Although better timing properties should be expected from a much smaller crystal, the 15% worse time resolution could be explained by the use of a Photonis XP2020Q photomultiplier, with slower response.

3.4. Conclusions

In this chapter we have studied the benefits of a 1 cm^3-cube of LuAG:Pr crystal, commercially available from Furukawa, coupled to a R5320 Hamamatsu photomultiplier.

We have estimated the internal activity of LuAG:Pr crystal by two methods. First, assuming the chemical composition of LuAG:Pr - $(Pr_{0:025}Lu_{0:975})_3Al_5O_{12}$ -, we obtained a theoretical roughly estimation of 215±20 Bq/cm^3. Later, by a low-level gamma spectrometry with HPGe, the internal activity was calculated in 171 ± 30 Bq/cm^3 which was corrected by the auto-absorption fraction for the crystal geometry. Also, we took an internal energy spectrum of the crystal coupled to the aforementioned PMT in order to study the energy information of β-decay transition from ^{176}Lu to ^{176}Hf, for which we identified the main gamma and beta contributors.

The energy resolution and linearity were studied with distinct exempt gamma sources at different high voltages. The LuAG:Pr shows a very good linear response to energy in the range of 122 to 1408 keV. In particular, for the optimum operation voltage the response of the LuAG:Pr was very linear and the energy resolution was preserved.

Also, we have measured the time resolution as a function of the applied high voltage to the PMT and the external cable delay of the CFD. The best resolution is found for an external delay of 0.8 ns. The time resolution improves with the applied HV up to -1900 V, and then stays basically constant. A good resolution of 147 ± 2 ps was obtained at ^{60}Co energies for the LuAG:Pr + Hamamatsu detector operated at HV = -1940 V. The best value obtained for ^{22}Na

511 keV photons is 238 ± 2 ps.

These results for the new formula would make LuAG:Pr a promising candidate for use as fast timing scintillator, but nonetheless its strong internal activity due to lutetium may hamper its use in low count rate experiments. However, for high activity scenarios like PET, this crystal would be useful not only as direct detector (to form arrays), but as phoswich constituent.

3.5. References

Attix, F. *Introduction to Radiological Physics and Radiation Dosimetry*. United States of America: John Wiley & Sons, Inc, 2004.

Basunia, M., Nuclear Data Sheets 107(4), 791 (2006)

Bauer, F., Aykac, M., Loope, M., Williams, C.W., Eriksson, L., Schmand, M., IEEE Transactions on Nuclear Science 54(3), 422 (2007)

Billnert, R., Oberstedt, S., Andreotti, E., Hult, M., Marissens, G., Oberstedt, A., Nuclear Instruments and Methods in Physics Research A 647, 94 (2011)

Chewpraditkul, W., Swiderski, L., Moszynski, M., Szczesniak, T., Syntfeld-Kazuch, A., Wanarak, C., Limsuwan, P. IEEE Transactions on Nuclear Science, 56 (6), Dec. (2009)

Conti, M., Eriksson, L., Rothfuss, H., Melcher, C.L., Member, S., The, A., T.o.f. Tof, IEEE Transactions on Nuclear Science 56(3), 926 (2009)

Derdzyan, M.V., Ovanesyan, K., Petrosyan, A., Belsky, A. Dujardin, C., Pedrini, C., Auffray, E., Lecoq, P., Lucchini, M., Pauwels, K. Journal of Crystal Growth 361 (2012) 212–216

Drozdowski, W., Dorenbos, P., Bos, A., Bizarri, G., Owens, A., Quarati, F., IEEE Transactions on Nuclear Science 55(3), 1391 (2008)

Drozdowski, W., Dorenbos, P., Haas, J.T.M.D., Drozdowska, R., Owens, A., Kamada, K., Tsutsumi, K., Usuki, Y., Yanagida, T., Yoshikawa, A., IEEE Transactions on Nuclear Science 55(4), 2420 (2008)

Ekstroem, L.P. and Firestone, R.B. WWW Table of Radioactive Isotopes (2004): Online: http://ie.lbl.gov/toi

Glodo, J. , Moses, W.W., Higgins, W.M., Van Loef, E.V., Wong, P., Derenzo, S.E, Weber, M.J., Shah, K.S., IEEE Transactions on Nuclear Science 52(5), 1805 (2005)

Guss, P., Reed, M., Yuan, D., Reed, A., Mukhopadhyay, S., Nuclear Instruments and Methods in Physics Research, A 608(2), 297 (2009)

Hamamatsu Photonics, Photomultiplier Tube R9779 Specifications (2009)

Hamamatsu Photonics, Photomultiplier Tube R5320 Specifications (2009)

Higgins, W., Churilov, A., Van Loef, E., Glodo, J., Squillante, M., Shah, K., Journal of Crystal Growth 310, 2085 (2008)

Kamada, K., Yanagida, T., Endo, T., Tsutumi, K., Yoshino, M., Journal of Crystal Growth pp. 1–4 (2012)

Klamra, W., Lindblad, T., Moszynski, M., Norlin, L., Nuclear Instruments and Methods in Physics Research A 254(1), 85 (1987)

Knoll, Glen. Radiation Detection and Measurement. Third Edition. New Jersey: John Wiley & Sons, Inc., 2000.

Fraile, L.M., Mach, H., Vedia, V., Olaizola, B., Picado, E., Paziy, V.,Udías, J.M., Nuclear Instruments and Methods in Physics Research A submitted (2012)

Fraile, L.M., Mach, H., Olaizola, B., Paziy, V., Picado, E., Sanchez, J.J., Udías, J.M., Vaquero, J.J., Vedia, V., in Nuclear Science Symposium Conference Record, 2011. NSS '11. IEEE (2011), pp. 72 -74

FURUKAWA CO., LTD. URL: www.furukawakk.co.jp (2012)

Lewellen, T.K., Physics in Medicine and Biology 53(17), R287 (2008). URL: http://stacks.iop.org/0031-9155/53/i=17/a=R01

Mach, H., Gill, R.L., Moszynski, M., Nuclear Instruments and Methods in Physics Research A 280, 49 (1989)

Mach, H., Wohn, F., Molnar, G., Sistemich, K., Hill, J.C., Moszynski, M., Gill, R., Krips, W., Brenner, D. Nuclear Physics A 523, 197 (1991)

Mach, H., Instructions for the program SORTM. (Internal Report. Universidad Complutense, 2012)

NIST. URL: http://physics.nist.gov/PhysRefData/XrayMassCoef/tab3.html (2012), which values are based on the previous work of: Seltzer, Stephen in Radiation Research **136,** 147 (1993)

Moszynski, M., Mach, H., Nuclear Instruments and Methods in Physics Research A 277, 407 (1989)

Moszynski, M., Gierlik, M., Kapusta, M., Nassalki, A., Szczesniak, T., Fonatine, M., Lavoute, P.,

Nuclear Instruments and Methods in Physics Research A 567, 31 (2006)
Moszyriski, M. Wolski, D., Ludziejewski, T., Kapustab, M., Lempicki, A., Brecher, C., Wisniewski, D., Wojtowiczc, A.J. Nuclear Instruments and Methods in Physics Research A 385 (1997) 123-131
Owens, Alan. IEEE Transactions on Nuclear Science 55 (3), 1430-1436 (2008) DOI: 10.1109/TNS.2008.921936
Saint-Gobain. Prelude420. URL: http://www.detectors.saint-gobain.com/PreLude420.aspx (2013)
SCIONIX Holland BV. URL: www.scionix.nl (2013)
Sugano, Kiyohiko. Chem-Bio Informatics Journal, Vol 9, pp. 75-93 (2009)
Shah, K.S., Glodo, J., Higgins, W., Van Loef, E.V., Moses, W.W., Derenzo, S.E., Weber, M.J., IEEE Transactions on Nuclear Science 52(6), 3157 (2005)
Szczesniak, T., Moszynski, M., Swiderski, L., Nassalski, A., Lavoute, P., Kapusta, M., IEEE Transactions on Nuclear Science 56(1), 173 (2009)
Yoshikawa, A., Yanagida, T, Kamada, K., Yokota, Y., Pejchal, J., Yamaji, A., Usuki, Y, Yamamoto, S., Miyake, M. Kumagai, K., Sasaki, K., T.R. dos Santos, T.R., Baba, M, Ito, M., Takeda, M., Ohuchi, N., Nikl, M. Optical Materials 32, 1294–1297 (2010)
Van Loef, E.V., Dorenbos, P., Van Ejik, C.W.E., Krammer, K., Gudel, H.U., Nuclear Instruments and Methods in Physics Research A 486, 254 (2002)
White, E.R., Mach, H., Fraile, L.M., Koster, U., Arndt, O., Blazhev, A., Boelaert, N., Borge, M.J.G., Boutami, R., Bradley, H., Braun, N., Dlouhy, Z., Fransen, C., Fynbo, H.O.U, Hinke, C., Hoff, P., Joinet, A., Jokinen, A., Physical Review C 057303, 7 (2007)
Wiener, R.I., Kaul, M., Surti, S., Karp, J.S., in Nuclear Science Symposium Conference Record, 2010. NSS '10. IEEE, pp. 1991-1995 (2010)
Yao, R., Ma, T., Shao, Y. IEEE Nuclear Science Symposium. 4497-4502. Nov. (2007)

4. Characterization of a $CeBr_3$ crystal

Abstract: We report on a complete characterization of a novel inorganic scintillator $CeBr_3$. Measurements were performed using a $CeBr_3$ cylindrical crystal of 1-inch in height and 1-inch in diameter at ^{22}Na and ^{60}Co photon energies for timing and include ^{137}Cs, ^{152}Eu and ^{133}Ba for energy resolution and linearity. The time response was measured against a fast reference BaF_2 detector. Hamamatsu R9779 and Photonis XP20D0 fast photomultipliers were used. The full width at half maximum (FWHM) time resolution for an individual $CeBr_3$ crystal coupled to Hamamatsu PMT is reported to be as low as 119 ps at ^{60}Co energies, which is comparable to the resolution of 107 ps reported for $LaBr_3$. Furthermore, we have estimated the absolutely efficiency of the crystal through a absolutely calibrated gamma sources positioned at 5, 15 and 25 cm in front of the entrance face of the detector. Finally, we have studied the radiopurity of a 30x30mm cylindrical crystal of $CeBr_3$ in LSC underground facility through ultra-low level laboratory.

4.1. Introduction

Inorganic scintillators crystals are widely used in detection and spectroscopy of energetic photons (X-rays and γ-rays) at room temperature and began to increase the interest for extreme environment applications [Billnert, 2011]. These detectors are commonly used in nuclear and particle physics research, medical imaging, diffraction, non-destructive testing, nuclear treaty verification and safeguards, nuclear non-proliferation monitoring, and geological exploration [Shah, K., *et al.*, 2005]. Recently the main requirements for these crystals include high light output, high stopping power, good efficiency, fast response, good proportionality, low cost and availability in large volume [Knoll, 2000]. All of these requirements cannot be simultaneously met by any of the commercially available scintillators. As a result, there is a continued interest in search for new scintillators with enhanced performance.

Lately, a major breakthrough occurred with the introduction of the $LaBr_3$:Ce scintillator [Van Loef *et al.*, 2002], which unites very good time response with energy resolution of the order of 3% at 662 keV, much superior to 9% for BaF_2 or 5.9% for NaI:Tl crystals. Better energy resolution provides an advantage in fast timing and spectroscopic measurements where one has to disentangle complex decay schemes in which many transitions have similar, and thus overlapping energies. Furthermore, a better energy resolution gives a higher ratio between the full-energy peak and the Compton continuum underneath, and thus results in smaller time corrections due to Compton background under the full-energy peaks [Mach *et al.*, 1991]. The time resolution of $LaBr_3$:Ce crystals are worse by about 10-15% than for BaF_2 crystals of the same size and shape. However, it has been reported that the time resolution of $LaBr_3$:Ce crystals depend on the amount of Ce doping [Glodo *et al.*, 2005] and improve with higher doping. Standard crystals commercially available at present have only 5% doping.

Since $LaBr_3$:Ce is an expensive crystal, there is a strong interest in cheaper alternatives. A viable alternative requires excellent time resolution and very good energy resolution matching $LaBr_3$:Ce properties. The recently developed $CeBr_3$ scintillator is a very promising candidate due to its fast rise time of 0.7 ns, decay constant of 17 ns and high photon yield of about 68000 photons / MeV [Guss *et al,* 2009, Billnert *et al.*, 2011, Mach, 2012]. Its peak emission wavelength is at 380 nm [Mach, H. *et al.*, 2012]. Importantly, at present this crystal is

significantly less expensive. A good energy resolution, of the order of 4.3% at ^{137}Cs energy has been reported [Scionix, 2012] for a 1-inch cylindrical $CeBr_3$ crystal but a poor time resolution of only 326 ps FWHM was measured for energies above 1050 keV. Another important advantage of this crystal over BaF_2 or $LaBr_3$:Ce is that it does not possess internal activity.

In this chapter we perform a complete characterization of a $CeBr_3$ crystal. Previous studies about $CeBr_3$ crystals were made with small samples (less than 1cm^3), while in our research we have performed several studies with one of the largest crystals manufactured commercially (1"x1") by [Scionix, 2012]. We report on energy and time response as well as absolute efficiency and linearity for a $CeBr_3$ cylindrical crystal of 1-inch in height and 1-inch in diameter. For time measurements we have used the well-known Delay Timing γγ-coincidence Method [Mach *et al.,* 1989; Moszynski, *et al.*, 1989]. The time response was measured against a fast reference BaF_2 detector at ^{22}Na and ^{60}Co photon energies. For energy and efficiency measurements we have linked directly dynode signal to a multipurpose MCA and then explored the response of the crystal at different energies through exempt gamma sources like ^{22}Na, ^{60}Co, ^{133}Ba, ^{137}Cs and ^{152}Eu. A summary of this study has been published in [Fraile, L.M., *et al.*, 2012] and partial results are presented in Victoria Vedia Bachelor Dissertation (in Spanish TAD). Furthermore, we have coupled the $CeBr_3$ crystal to two different fast photomultipliers (Hamamatsu R9779 and Photonis XP20D0) in order to compare the features of both PMTs for a high light yield crystal. Finally, we have explored the radiopurity of the crystal in an ultra-low radioactivity facility located at an 850 m deep under the Mount Tobazo at Laboratorio Subterráneo de Canfranc (LSC).

4.2. Description of measurements

4.2.1. Energy Resolution and Non-Linearity

For energy resolution, linearity and efficiency we have used a system based on a simple peak-sensing "MCA Box" multichannel analyzer by Leybold Didactic GmbH, controlled by a general purpose measurement program "CASSY". We have observed that this device yields better energy resolution than the NIM modules described in chapter 2, which were mainly designed for the HPGe detectors having signals with much longer decay times. Consequently, during the energy and efficiency measurements and the determination of linearity, the dynode output of the $CeBr_3$ detector was directly sent to the MCA Box (see Fig. 4.1). The use of preamplifiers did not provide any improvement, and therefore was skipped. However, for timing measurements, we have used a different data acquisition for the energy signal (dynode) which is described in section 4.2.4.

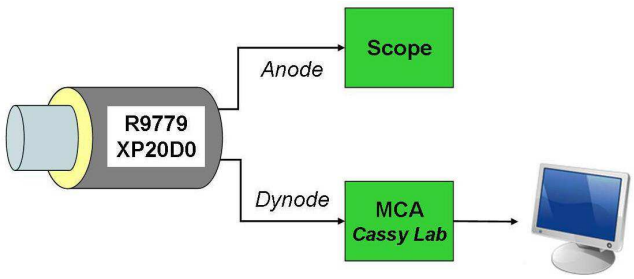

Fig. 4.1: *Set-up for energy resolution and linearity of the $CeBr_3$ coupled to R9779 and XP20D0 PMT.*

When the energy resolution is determined for crystals with high light output, like $LaBr_3$:Ce or $CeBr_3$, care must be taken to account for the energy non-linearity caused by the space-charge effect in the photomultiplier tube and by the scintillator non-proportionality. For $CeBr_3$ the reported non proportionality is 4% in the range from 122 to 1275 keV [Shah *et al.*, 2005]. However, in this work we have not tested the non-linearity but only the energy resolution using γ-ray energies from five exempt gamma sources: ^{137}Cs, ^{60}Co, ^{22}Na, ^{133}Ba and ^{152}Eu.

The procedure, which is described below, involves the determination of the non-linear functional relation between peak position (channel position) and γ-ray energy. Firstly, the energy resolution, *ER*, is determined from the ratio of the peak width (FWHM) in units of energy, here labelled ΔE, and the energy of the γ-ray peak, E_0:

$$ER = \frac{\Delta E}{E_0} \qquad (4.1)$$

the parameters determined from the measured spectrum for the γ-ray of energy E_0 are the Δp (FWHM) and peak position, p_0, both expressed in ADC channels. Hence, an apparent energy resolution would be define as: $\Delta p/p_0$. An energy E_i is then given by a function $f(p)$ at the corresponding position p_i, $E_i = f(p_i)$. Assuming that to first order the jacobian transformation between energy and position is locally linear, the energy resolution can be derived from the relation:

$$ER = \frac{\Delta p}{E_0} \times \left.\frac{df}{dp}\right|_{p=p_0} \qquad (4.2)$$

Where the derivative is calculated at the point $p=p_0$. The function $f(p)$ describes the energy fit to a series of positions of the of full energy peaks of known energies obtained by using a few different radioactive sources. In our work the energy determination we have used γ-sources of ^{137}Cs (662 keV), ^{60}Co (1173 and 1332 keV), ^{22}Na (511 keV), ^{152}Eu and ^{133}Ba where the γ-ray energies ranged from 122 to 1408 keV.

For a relatively small non-linearity, the energy relation $f(p)$ can be expressed by a second order polynomial, $f(p) = a + bp + cp^2$ [Billnert, R., *et al.*, 2011]. By substituting this function into previous *ER* expression it is obtained:

$$ER = \frac{b + 2cp_0}{a + bp_0 + cp_0^{\,2}}\Delta p \qquad (4.3)$$

A perfectly linear energy relation can be recovered by setting a zero offset and neglecting quadratic term, thus a = c = 0. Then the energy resolution becomes:

$$ER = \frac{\Delta E}{E_0} = \frac{\Delta p}{p_0} \qquad (4.4)$$

and in this case the apparent resolution coincides with the energy resolution (ER).

In fact the second equality in Eq. 4.4 is seldom true. For example, for the case of $CeBr_3$ with XP20D0 at 1000 V, taken from the measurements discussed further below, the coefficients for a quadratic fit are: $a = 10.24$, $b = 1.37$ and $c = 0.00059$. Then the correct energy resolution at $E_0 = 662\ keV$ is $ER = 5.0\%$, while the apparent energy resolution given by $\Delta p/p_0$ is 4.4%. In the table 4.1 we list more fitting and its parameters.

	Parameters			FWHM at
HV	a	b	c	662 keV
851	121.09	1.769	1.61×10^{-3}	6.15%
1000	10.24	1.369	5.94×10^{-4}	4.98%
1101	48.96	0.970	1.43×10^{-3}	5.21%
1200	16.18	0.753	1.07×10^{-3}	5.10%
1249	62.00	0.626	2.19×10^{-3}	5.48%
1300	39.31	0.695	2.12×10^{-3}	5.43%

Table 4.1: *Parameters of fitting for $CeBr_3$ coupled to XP20D0 at several voltages.*

We have also examined the energy linearity as a function of the applied high voltage for the $CeBr_3$ crystal coupled to the Hamamatsu and the Photonis photomultipliers. The γ-ray energy range was from 122 to 1408 keV, while the high voltage range was from 1050 to 1400 V for the Hamamatsu PMT and 850 to 1300 V for the Photonis phototube.

4.2.2. Empirical estimation of the Efficiency

The detection efficiency of the $CeBr_3$ detector was determined through five exempt calibrated gamma sources. A 5% absolutely calibrated gamma source of ^{152}Eu was used to calibrate the activity of the other sources. These other four sources were calibrated according to the procedure described in the chapter 2. The sources were positioned in front of the $CeBr_3$ crystal at 5, 15 and 25 cm (See figure 4.2).

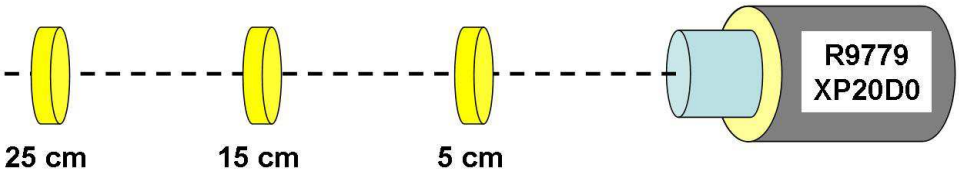

Fig. 4.2: *Set-up for energy resolution and linearity of the LuAG:Pr + R5320 PMT.*

The energy spectra have been acquired with the MCA system described above during real time intervals related to the distance. As growing the distance, the interval increase from 800s, 2000s and 3000s. For all the cases a background spectrum were taken and subtracted to the others.

The full energy peak efficiency for a particular sample-to-detector geometry is obtained by measuring the net counts under the photopeak energy of interest and using the standard formula for efficiency:

$$\varepsilon_E = \frac{N_\gamma}{t_\gamma \cdot P \cdot A} \qquad (4.5)$$

In the above expression N_γ is the number of net counts in the photopeak (area of the peak). P is branching ratio corresponding to the energy E_γ, t_γ denotes live-time elapsed for the measurement; A is the activity (in Becquerel) estimated for each source in the moment of survey, and ε_E is efficiency related to a specific full energy peak evaluated.

The aforementioned net area refers to the net area of full energy peaks (FEP), i.e. this area only takes into account the gammas that were totally absorbed in the crystal. This definition of area defines the *photopeak efficiency*. However, if instead of this area, we integrate over all the gammas which deposit energy in the crystal, this is, peak and its Compton, then we are defining the *absolute total detection efficiency* for a specific energy.

$$\varepsilon_{photopeak} = \frac{\#\text{ of gammas under the photopeak}}{\#\text{ of gamma emitted by source}} \qquad \varepsilon_{Absolute} = \frac{\text{total }\#\text{ of gammas detected}}{\#\text{ of gamma emitted by source}}$$

In our case, we going to estimate the absolute total detection efficiency for the ^{137}Cs source, we will use the 661.7 keV photopeak and its Compton continuum.

Associated uncertainties can be calculated by the propagation of error equation:

$$(\Delta\varepsilon)^2 = \left[\left(\frac{\partial\varepsilon}{\partial N_\gamma}\right)^2(\Delta N_\gamma)^2 + \left(\frac{\partial\varepsilon}{\partial A}\right)^2(\Delta A)^2 + \left(\frac{\partial\varepsilon}{\partial P}\right)^2(\Delta P)^2 + \left(\frac{\partial\varepsilon}{\partial t_\gamma}\right)^2(\Delta t_\gamma)^2\right] \tag{4.6}$$

Assuming time t_γ is known precisely and the branching is a constant with a negligible error, the efficiency error can be calculated as:

$$(\Delta\varepsilon_E)^2 = \left(\frac{N_\gamma}{t_r \cdot P \cdot A}\right)^2 \cdot \left[\left(\frac{\Delta N_\gamma}{N_\gamma}\right)^2 + \left(\frac{\Delta A}{A}\right)^2\right] \tag{4.7}$$

Also, we must propagate this energy efficiency error with the positioning error (Δr). Thus, an expression for the total efficiency error is obtained:

$$\Delta\varepsilon_{TOTAL}(x,E) = \left[\left(\frac{\Delta r}{r}\right)^2 + (\Delta\varepsilon_E)^2\right]^{1/2} \tag{4.8}$$

In all the cases the error in the efficiency as a function of the energy was less than 10% for the range of energy from 30 to 1408 keV.

4.2.3. Radiopurity of the $CeBr_3$

It is expected that $CeBr_3$ presents much less internal activity than others lanthanum halides crystals. However, a high precise study of its internal activity has to be done in order to assess whether this detector could be useful for “extreme scenarios” like spectral prompt fission

gamma ray or low-level environmental gamma spectroscopy searches [Lutter, *et al.*, 2011]. To explore the radiopurity of the $CeBr_3$ crystal, we have measured internal activity of the crystal through an ultra-low level radioactivity technique at LSC in Canfranc, Spanish Pyrenees [LSC, 2013].

The "Laboratorio Subterráneo de Canfranc" (LSC) is a facility for Underground Science which is located under the Pyrenees Mountain El Tobazo, the rock overburden at the site provides 850 maximum meters shielding from cosmic rays, around 2450 m.w.e (the cosmic muon flux is about five orders lower than at sea-level surface) and offers a low background environment for high-precise experiments [Bettini, A., 2011]. In other words, LSC is a laboratory intended to perform experiments based on precise measurements at ultra-low background conditions. In order to elaborate optimized set-ups with very low or negligible internal activity, a careful selection of radiopure material must be done [Billnert, *et al.*, 2012]. In the figure 4.3 are shown the auxiliary entrance to the tunnel (left) and main entrance of the LSC (right) opened by one of the researchers.

Fig. 4.3: *Left, secondary or auxiliary entrance to the tunnel. Right, main entrance to the LSC and one of the researchers.*

The LSC offers a *Radiopurity Service* to measure ultra-low level radioactivity in materials using germanium detectors for gamma ray spectroscopy at the Hall C [LSC, 2013]. Inside the Radiopurity Service Lab there are at six HPGe detectors, for this study we have used GeTobazo which is a p-type close-end coaxial HPGe produced by Canberra France with 100-110% relative efficiencies and a FWHM energy resolution of ~2 keV at 1332 keV from ^{60}Co gamma source. The active volume of the detector is 420 cm^3 and the cryostat is made of ultra-low background aluminium. Each detector has a shield consisting of 5 cm of oxygen-free copper and 20 cm of very low activity lead having <30 mBq/kg of ^{210}Pb; nitrogen gas is flushed inside a methacrylate box to avoid airborne radon intrusion (see figure 4.4) [Álvarez, V., *et al.*, 2013].

The background spectrum for each detector inside its shielding is determined by taking data with no sample for long periods of time of at least one month, due to the low counting rates. For GeTobazo, with detector mass of 2.185 kg, the background rate is 708±3 counts per day per kilogram of HPGe in the energy windows from 100 to 2700 keV. The main isotopes which contribute to the background are ^{214}Bi, ^{208}Tl and ^{40}K. Besides, the radon concentration in air is between 50 and 80 Bq/m^3 in the underground halls [Álvarez, V., *et al.*, 2013].

Fig. 4.4: *Ultra-low level for gamma spectroscopy in Hall C at LSC.*

In order to estimate the detector efficiency, Monte Carlo simulations based on the Geant4 [Geant4 collaboration, 2003] code have been performed by Iulian Bandac (LSC) for our $CeBr_3$ crystal, accounting for intrinsic efficiency, the geometric factor and self-absorption at the sample. Validation of the simulation has been made by comparing the efficiency curve of the detectors measured with a ^{152}Eu reference source of known activity located at 25 cm from the detector with the simulated one [Álvarez, V., *et al.*, 2013].

For the estimation of the activity and its errors we will follow what was written in the section 3.2.1 in the previous chapter. With the differences that we going to use an absolute estimation of efficiency obtained by a simulation and the activity will be reported for each radionuclide as an average of the main peaks detected weighted by its branching ratio and the experimental error. Moreover, we have positioned the $CeBr_3$ just in front of the filter of the HPGe detector in order to improve the geometric efficiency and increase the statistics.

4.2.4. Experimental set-up for time-delayed measurements

The experimental set-up for timing measurements is identical to the method used in the previous chapter to characterize the LuAG:Pr. The study of the reference crystal (BaF_2), the procedure to obtain the time resolution and its optimization are detailed described in the section 3.2.2.

The only one difference is that when we study again the reference crystal to characeterize the $CeBr_3$, this shows a slightly change in comparison with the values reported for the LuAG:Pr. The combined time resolution FWHM at ^{60}Co energies for the set of two identical BaF_2 detectors was found to be 117 ± 2 ps. Thereby, after deconvolution, by assuming a Gaussian and identical time response for both detectors, the time resolution of an individual unit was 83 ± 2 ps. Analogously the individual time resolution was 125 ± 2 ps at 511 keV from a ^{22}Na source (See figure 4.5).

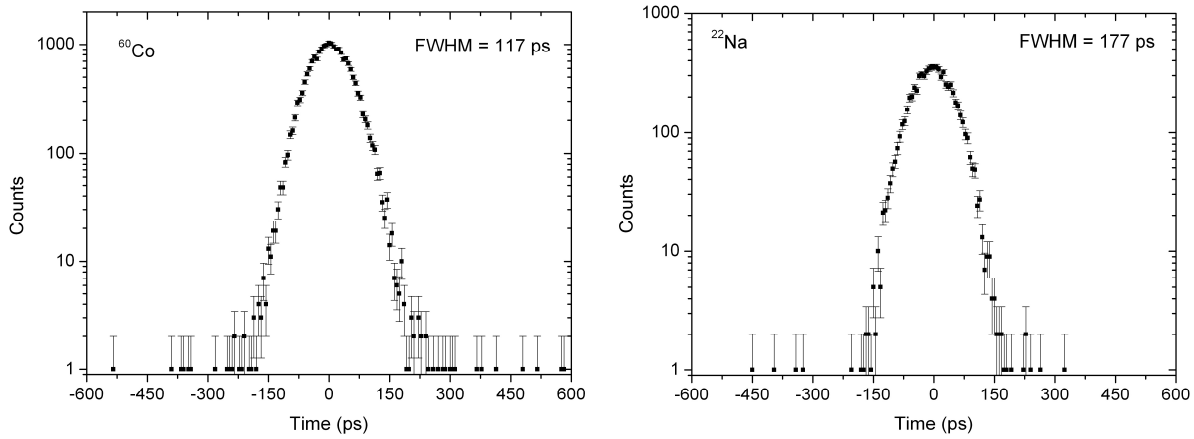

Fig. 4.5: *Time spectrum for ^{60}Co (left) and ^{22}Na (right) generated by selecting full energy peak of γ-rays detected in a pair of reference BaF_2 detectors. The time calibration is 6.0 ps/ch. The FWHM in the plots is the total resolution (not deconvoluted).*

The performance and reproducibility of the time resolution of the reference BaF_2 detector was carefully monitored throughout the whole period of measurements which lasted a few months. Over this period a few timing checks were performed on the reference set of detectors. The monitoring measurements yielded time resolution for a single detector ranging from 81.5 ± 1.5 ps at the beginning of the measurements to 84.4 ± 1.5 ps for ^{60}Co at the end of them.

4.2.4.1. $CeBr_3$ Detector

The $CeBr_3$ crystal, with serial number SEW840, was produced by Scionix [Scionix, 2012]. The cylindrical crystal of 1 inch in diameter and 1 inch in height was surrounded by reflector material and hermetically sealed at the factory with a quartz window in an aluminium case. The crystal was optically coupled by the use of Viscasil silicon grease [Klamra *et al.*, 1987] to the Hamamatsu or Photonis photomultiplier tubes (See figure 4.6). However, for the radiopurity measurements we were used a 30x30 mm cylindrical crystal provided by the same company and with the same housing and reflector.

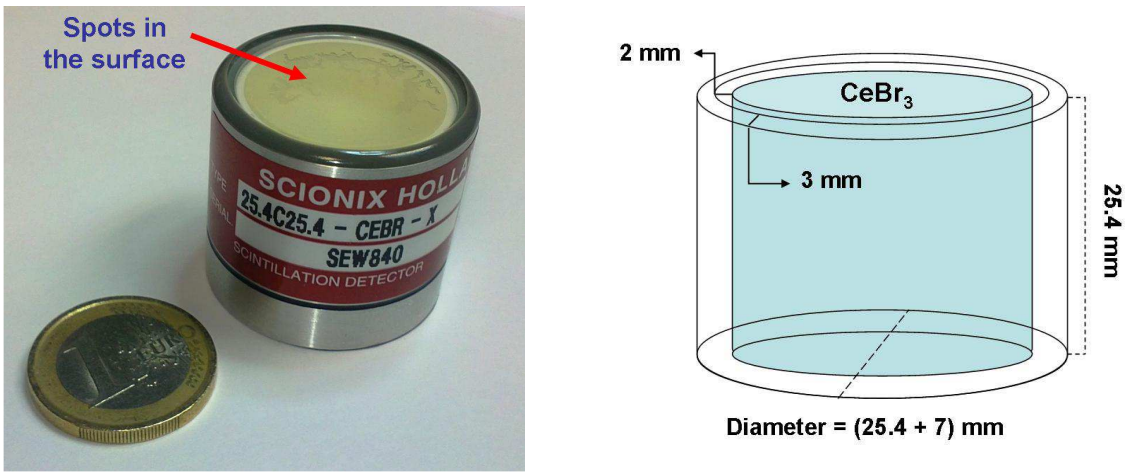

Fig. 4.6*: Left, SEW840 $CeBr_3$ scintillator crystal. Right, Bubbles and spots in the damaged crystal.*

A pre-delivery test at Scionix has shown the energy resolution of 4.2% at ^{137}Cs energy when coupled to Hamamatsu R6231 phototube operated at 880 V. Upon delivery the front

surface of the sealed crystal was smooth. However, a visual inspection after a few weeks of use has shown several spots, which looked like small bubbles formed between the crystal and the sealing optical glass. These spots covered about 5% of the crystal optical window after three weeks after delivery, but then increased to 7% over a few months period. If all the light reaching these spots were absorbed, then up to 7% of light collection from the crystal would be blocked. This evolution is shown in the figure 4.7.

***Fig. 4.7**: Evolution of the spots on our 1'x1' $CeBr_3$ crystal.*

4.2.3.5. Photomultipliers

XP20D0 is the fast-response 8-dynode phototube designed by Photonis to match the $LaBr_3$:Ce crystals having a high yield of about 74000ph/MeV [Glodo, J., *et al.*, 2005]. The front end does not follow the optimized design used in the XP2020-UR PMT, but instead used a simplified one. To improve the time resolution, these tubes are equipped with a double anode. The XP20D0 has a typical rise time of 1.6 ns and a Transit Time Spread (TTS) of 520 ± 30 ps FWHM [Moszynski, M., *et al.*, 2006]. These are worse parameters than 1.4 ns and 350 ps, respectively, for the 12-stage XP2020-URQ phototubes that were used in fast timing measurements with BaF_2 (but have a much lower light yield). Two XP20D0/B tubes, with the serial numbers 2029 and 2156, were used in the tests. They were characterized by cathode blue sensitivity of 12.0 and 11.6 μA/lmF and dark current of 2.3 and 1.13 nA, respectively. Their main properties are summarized in Table 4.1.

The Hamamatsu R9779 photomultiplier was incorporated in to the assembly H10570MOD with the serial number FA0472. This 52 mm 8-stage PMT was also designed for LaBr3:Ce, and a typical anode pulse rise time of 1.8 ns and TTS of 250ps FWHM were reported by the manufacturer [Hamamatsu, 2009]. The PMT properties are also summarized in Table 4.1.

PMT	Serial Number	τ_{rise} (ns)	FWHM TTS (ps)	Blue sensitivity (μA/lmF)	Dark current (nA)
XP20D0	2029	1.6	520 ± 30*	12.0	2.3
XP20D0	2156	1.6	520 ± 30*	11.6	1.13
R9779	FA0472	1.8	250**	9.55	1.40

Table 4.1: *Main properties of the photomultiplier tubes used to coupling the $CeBr_3$ crystal.*
** These were extracted from the σ values by[Moszynski, M., et al., 2006] and ** [Hamamatsu, 2009]*

In this study of the high photon-yield crystals, the high voltage on the photomultipliers was set to provide anode output signals of 1V in amplitude for 1MeV photons. Consequently the typical operation voltage was 1200V for the XP20D0 and 1260V for the R9779.

4.3. Results for $CeBr_3$

4.3.1. Energy Resolution and Linearity

An energy spectrum for the ^{137}Cs source obtained with the $CeBr_3$ crystal coupled to the XP20D0 photomultiplier operated at 1200 V is plotted in Fig. 4.8. The FWHM value was corrected for non-linearity. The measured energy resolution at 662 keV is 5.0%. A similar value of 5.2% is obtained for the $CeBr_3$-Hamamatsu detector operated at 1400V. (See figure 4.8). These values are higher than 4.2% quoted by the manufacturer from the pre-delivery test at Scionix, but they use Hamamatsu R6312, optimized for energy resolution. Fast-response phototubes have a special design, optimized for the time efficient collection of photoelectrons to arrive almost at the same time to the first dynode, in order to generate the output anode signals with the smallest TTS [Szczesniak *et al.*, 2009]. In particular, the XP20D0 PMT includes a screening grid at the anode [Moszynski *et al.*, 2006] whereas the R9779 PMT has an acceleration ring at the front-end [Hamamatsu-R9779, 2009]. This would explain the slightly worse energy resolution obtained in our measurements. Another possible effect would be the presence of bubbles in the crystal which could worsen the light collection and then affecting the energy resolution. However, we see no effect in the timing measurements.

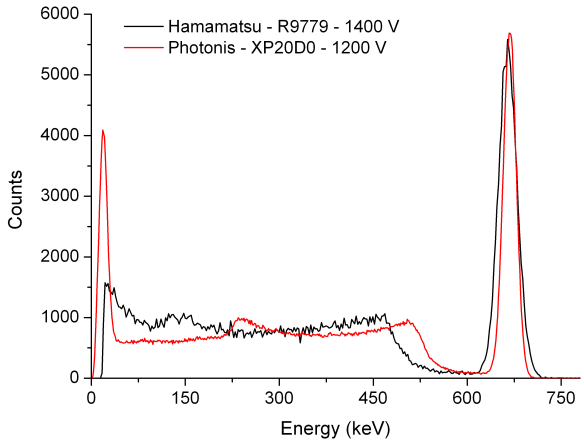

Fig. 4.8: *Comparison of 137Cs energy spectra for CeBr3 crystal coupled to Hamamatsu-R9779 PMT at Energy spectrum of $CeBr_3$ coupled to the Photonis XP20D0 PMT operated at HV = 1200 V for the ^{137}Cs source. The FWHM value was corrected for non-linearity.*

It is expected that the PMT design will have an effect on the linearity as well. We have measured the energy linearity for the $CeBr_3$ crystal and the PMT combination as a function of high voltage applied to the photomultiplier. The results plotted in Fig. 4.9 and 4.10, show a very different behaviour for the tubes. The contribution from the non-proportionality in light yield of $CeBr_3$ is small. As stated above it has been measured [Shah *et al.*, 2005] to be 4% in the range from 122 to 1275 keV and it is better than for other scintillators, specially $LaBr_3$:Ce.

The R9779 PMT shows an almost linear energy relation over the whole energy range and for all high voltages applied in these tests. Particularly important is its good linearity at the voltage range from about 1150 to 1350 V where the best time resolution is achieved (see subsection 4.3.2.).

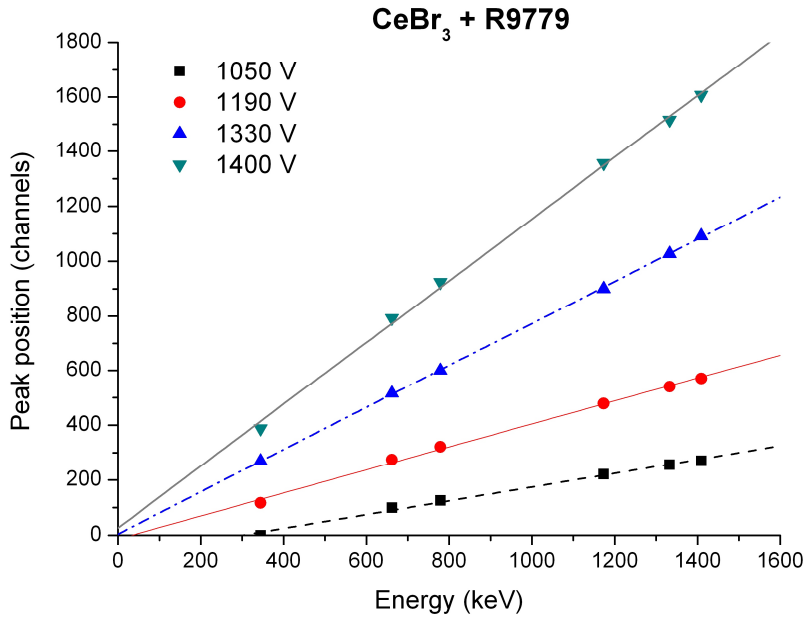

Fig. 4.9: *Energy linearity for $CeBr_3$ crystal coupled to the R9779 PMT. Linear fit is shown together with experimental points.*

There is a strong energy non-linearity observed for the $CeBr_3$ coupled to the XP20D0 PMT for the range of high voltages from 850 to 1400 V. The non-linearity is very strong at the standard operation voltage of 1200 V and increases with the applied voltage. This is shown in Fig. 4.10 by the departure from the linear fit, which was defined by the three lowest energies in the XP20D0 plot. Moreover, although the energy resolution at 662 keV is consistently 5.0% below 1200 V, it strongly deteriorates as the high voltage is further increased. In particular at 1800 V the pair of full energy peaks at 1173 and 1332 keV for ^{60}Co cannot be resolved anymore.

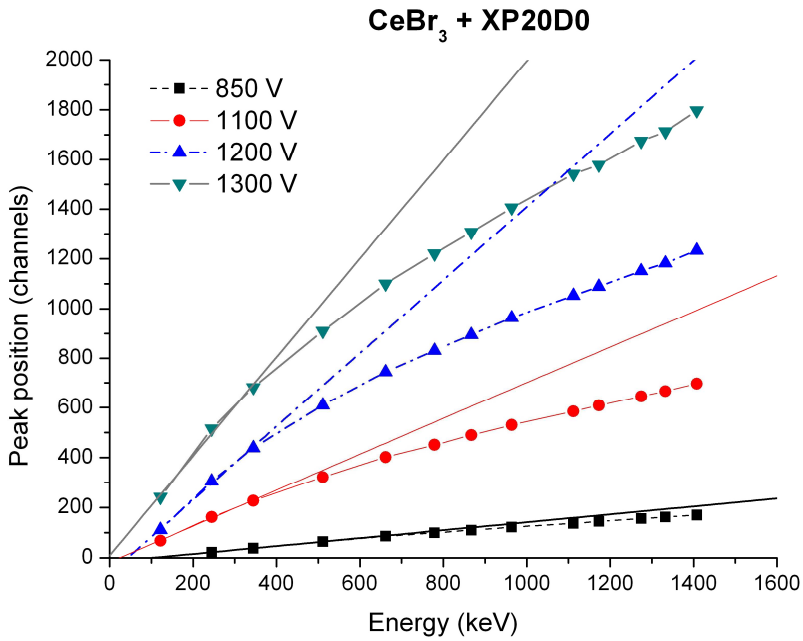

Fig. 4.10: *Energy linearity for $CeBr_3$ crystal coupled to the XP20D0 PMT. Linear fits were performed for the points below 400 keV and then extrapolated to higher energies.*

To illustrate the difference in energy nonlinearity between the detector assemblies we are plotting in the Figure 4.11 the deviation from linearity for $CeBr_3$-Hamamatsu and $CeBr_3$-Photonis combinations, where a linear behaviour is assumed for 344 keV and 662 keV energies. The red line represents the ideal fit (with zero deviation), black line shows a good linearity for R9779 (less than 2% of deviation over 1400 keV) and blue line presents the non-linearity for XP20D0, the deviation could almost reach until 18%.

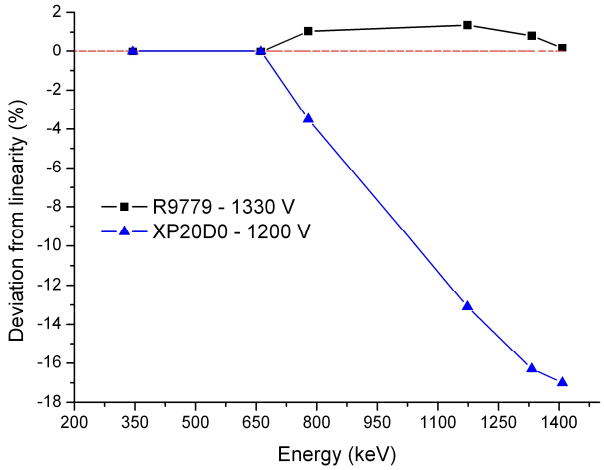

Fig. 4.11: *Energy linearity plots for the $CeBr_3$ crystal coupled to the R9779 PMT (full squares) and XP20D0 PMT (triangles).*

The Relative Energy Resolution (*R(%)*) was calculated from the same data obtained in the measurements. In the figure 4.12 are shown all data points with their uncertainties for $CeBr_3$ crystal coupled to XP20D0 PMT. While the final results were similar to the obtained with R9779, the information provided from XP20D0 had to be corrected by linearity. To estimate the energy resolution we had to convert the FWHM from channel to energy scale, and this process required linearity correction.

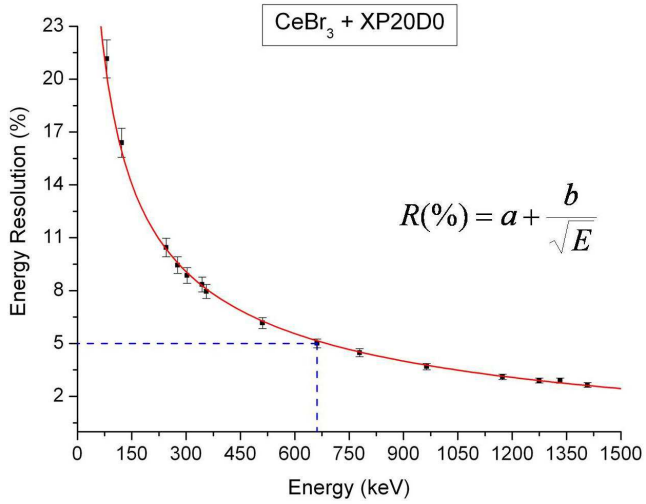

Fig. 4.12: *Relative Energy Resolution of a $CeBr_3$ (1"x1") coupled to XP20D0 PMT at 1200V.*

In order to get enough statistics about energy resolution in a range from 80 to 1408 keV, we have used five gamma sources: ^{22}Na (*511 and 1274 keV*), ^{133}Ba (*80.9, 276.4, 302.8 and 356 keV*), ^{60}Co (*1173.2 and 1332.5 keV*) and ^{152}Eu (*121.8, 244.7, 344.3, 778.9, 964.1 and 1408 keV*). With these 14 peaks we obtained the enough information to plot energy resolution against energy. As we comment at the begging of this section the energy resolution at 662 keV is 5.0% which is higher than 4.2% quoted by the manufacturer from the pre-delivery test at Scionix. The uncertainty of the energy resolution was estimated to be of the order of 5% for the ^{137}Cs full energy peak.

A polynomial function was used to fit the dependence of the relative resolution with the energy. We have used an expression that relates relative resolution with the inverse square root of the energy [Ciemala, 2009]:

$$R(\%) = a + \frac{b}{\sqrt{E}} \qquad (4.10)$$

In our case, the fitting was optimized for a = *-2.927 (0.095)* and b = *207.902 (2.738)* with R^2 = *0.99758* for the energy ranges from 122 to 1408 keV (See figure 4.12).

4.3.2. Empirical estimation of Efficiency

In order to estimate the experimental absolute efficiency for the $CeBr_3$, it was coupled to the XP20D0 PMT and was exposed to five standard point-like gamma sources (See Table 4.2). The measurements were performed at three different distances from the source to the detector entrance face. The sources were positioned at 50, 150 and 250 mm with estimated error of 2.5 mm. This error arises from the distance to the entrance of the crystal measured in a test bench calibrated to 1 mm precission, the estimate of the tilting angle of the source towards the surface of the detector and the uncertainty of the position of radioactive deposit the within the thickness of the source itself . Furthermore, each source was calibrated with an absolutely calibrated HPGe, the uncertainties were less than 10% in its activities (This process was detailed described in the chapter 2).

Gamma Source	γ-peaks provided (keV)	Activity (μCi)		Comments
		Measured *(3/13/2012)*	Quoted to 10%	
^{152}Eu	41*, 121.8, 244.7, 344.3, 778.9, 964.1, 1100.9* and 1408	1.10	1.0 (jan-06)	1. All the sources were calibrated with the 5% absolutely calibrated reference ^{152}Eu source with the HPGe. 2. The ^{152}Eu source used for efficiency measurements has more activity than was reported by the provider. Our estimate is almost double than it was quoted.
^{133}Ba	31.6*, 80.9, 276.4, 302.8 and 356	0.72	1.0 (jan-06)	
^{22}Na	511 and 1274	0.37	1.0 (jan-08)	
^{137}Cs	661.7	3.74	5.0 (sep-00)	
^{60}Co	1173.2 and 1332.5	0.78	1.0 (oct-00)	

Table 4.2: *Main gammas used to estimate the efficiency and the activity when the measurements were taken. The starred values are weigthened average of unresolved gammas.*

To estimate the net peak area the background and continuum contributions are subtracted in the spectrum. Because background gamma spectra were recorded using the same gain and during the same time, the subtraction was quite simple. However, to remove the unwanted counts from continuum as Compton events or background contributions, we have to estimate a baseline (pedestal) between consecutive peaks and even using not linear apprximations.

In almost all gamma spectra taken with a scintillator, the energy peaks contain the "blurring" effects due to the finite energy resolution of the detector (see figure 4.13). The most striking difference is the fact that all peaks now have some finite width rather than appearing as narrow or sharp lines [Knoll, 2000]. Also, for two near peaks (with closed energies) is normal to get some overlap. All these effects turn more difficult to estimate the baseline and so subtract the continuum contribution to the peak.

In the figure 4.13 an example of multipeak fitting is shown. Through a statistic mathematical program called ORIGIN, we could solve consecutive peaks assuming a Gaussian shape for each peak. The baseline level can be fixed related to each case. However, there are some peaks whose baseline is not a straight line, it is necessary to use a polynomial fitting. In all the cases the program permits to manage the baseline shape in order to improve the fitting.

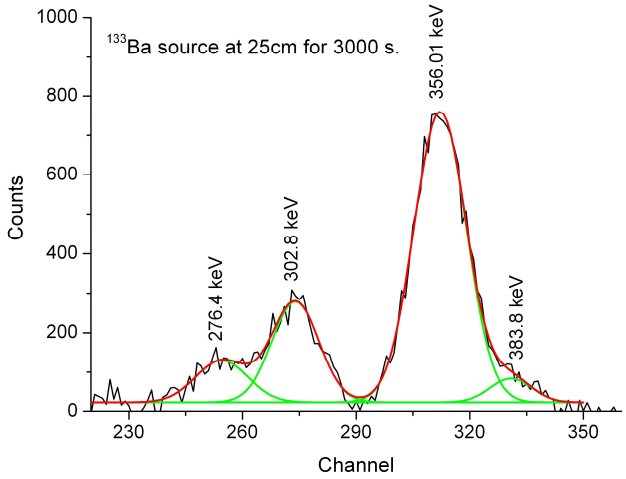

Fig. 4.13: *Example of multi-peak fitting for a ^{133}Ba gamma energies before energy calibration through ORIGIN program.*

The results for photopeak efficiency are shown in the figure 4.13. These three curves show similar shape with the maximum efficiency around 100 keV. Each value is plotted with its error bar. In all the cases the error bar was lower than 10%. The difference between curves is caused by a distance effect (change in the soild angle and $1/r^2$ effect) and the number of counts per second which are arriving to the detector as expected.

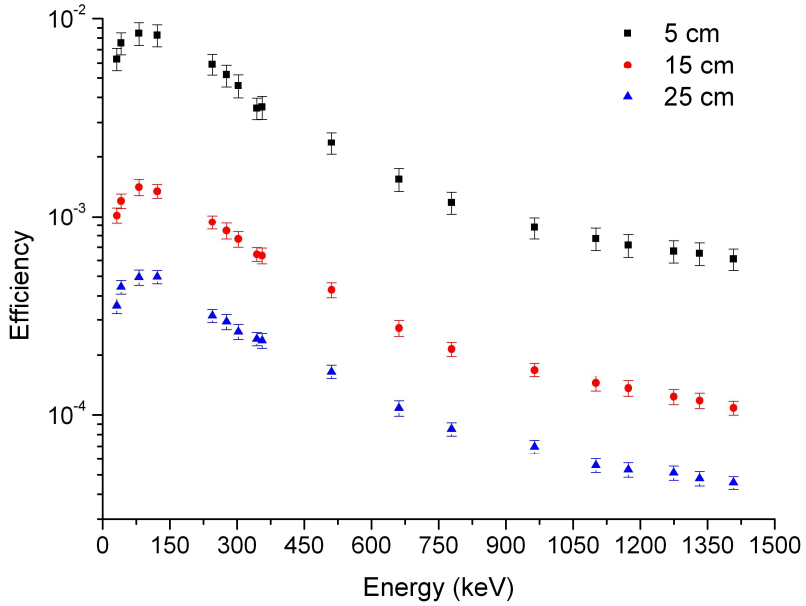

Fig. 4.13: *Photopeak Absolute Efficiency for a $CeBr_3$ coupled to XP20D0 PMT with calibrated gamma source at three distances in front of the detector.*

The error analysis includes errors for net area estimation, activity of the source and fitting. Furthermore, we have added the error in the positioning of the source due to height, distance to entrance face of the detector and finite thickness of the source housing. For the furthest distances (150 and 250 mm) the error did not reach 10%, however for 50 mm error is around 13%.

The previous measurements provide the *Absolute Photopeak Efficiency* at several

distances, in particular for the 662keV energy (from ^{137}Cs). In addition we have calculated the *Total Detection Efficiency* for this source. In order to estimate both efficiencies, first we have to estimate the branching ratio of the gammas that contribute to the making of the spectra. Thus, we can explore all the transition intensities for our ^{137}Cs source:

Transition	Energy (keV)	Intensity (%)
XR l	4.47	0.91 % 4
XR kα_2	31.82	1.99 % 5
XR kα_1	32.19	3.64 % 10
XR kβ_3	36.30	0.348 % 9
XR kβ_1	36.38	0.672 % 18
XR kβ_2	37.26	0.213 % 6
	661.66 3	85.10 % 20

Table 4.3: *Main branching ratio and gamma energies for ^{137}Cs source [Browne, E., Tuli, J.K., 2007]. With intensities above 0.2%.*

In this way the fraction of gammas which are emitted per transition is almost 92% and for gammas with 661.7 keV is 85.1%. Because we want to explore the contribution of a monoenergetic source, we have only considered values over 50 keV. Through this values and using the data from ^{137}Cs spectra (peak area and total integration of counts), we have obtained the results which showed in the table 4.4. In this table the values show good agreement between then. We have to remember that all the areas and efficiency almost reach 10% of error for 150 and 250 mm and 13% for 50 mm, which means, our ratio values between efficiencies are acceptable. It is important to note that this is the first time that the absolute efficiency for a $CeBr_3$ is reported.

Distance (mm)	Experimental Efficiency (%)		Ratio (N_γ/N_{Tot})
	$\varepsilon_{photopeak}$	$\varepsilon_{absolute}$	
50	0.154 ± 0.020	0.44 ± 0.06	0.35 ± 0.004
150	0.027 ± 0.0024	0.078 ± 0.007	0.34 ± 0.004
250	0.011 ± 0.0010	0.034 ± 0.003	0.33 ± 0.005

Table 4.4: *Absolute Total Efficiency and Absolute Photopeak Efficiency for ^{137}Cs at three distances in front of the $CeBr_3$ detector. The ratio between efficiency shows good homogeneity.*

4.3.3. Radiopurity of $CeBr_3$

4.3.3.1 Background in GeTobazo

In order to get enough sadistic for a background gamma spectrum, the GeTobazo detector was recording during 1342 hours (55.9 days) inside the special shielding in the Hall C at LSC. Figure 4.14 shows the background spectrum. The main gamma contributions come from ^{40}K, ^{208}Tl and ^{214}Bi isotopes, the last two belongs to the ^{238}U and ^{232}Th radioactive chains.

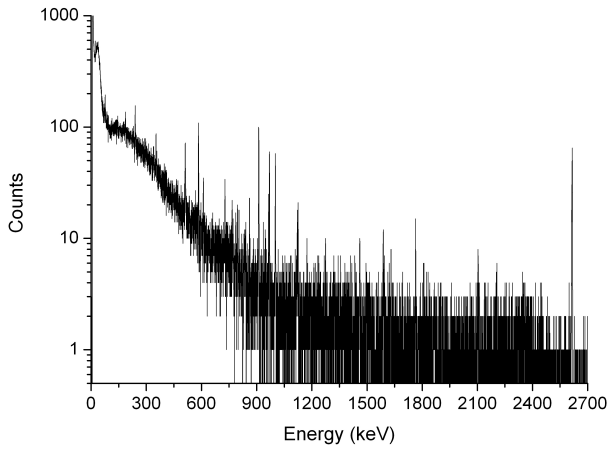

Fig. 4.14: *Background gamma spectrum obtained with GeTobazo during 55.9 days.*

The energy calibration could be done by calibration point-like sources (^{152}Eu and ^{60}Co) or through an internal calibration according to some references gamma peaks. For the previous figure we have used three references peaks (186.2 keV from ^{226}Ra, 1460.8 keV from ^{40}K and 2616.63 keV from ^{208}Tl) to set the next energy calibration equation:

$$E(keV) = 0.35213 \cdot ch + 1.798 \qquad (4.11)$$

4.3.3.2 Measurement of $CeBr_3$

The $CeBr_3$ crystal was positioned just in front of the HPGe entrance face. The gamma spectrum was recording during 831 hours (34.6 days) inside the special shielding in the Hall C at LSC. In order to set the same conditions than background, we have used an internal calibration. In the figure 4.15 both spectra are shown with its energy calibration.

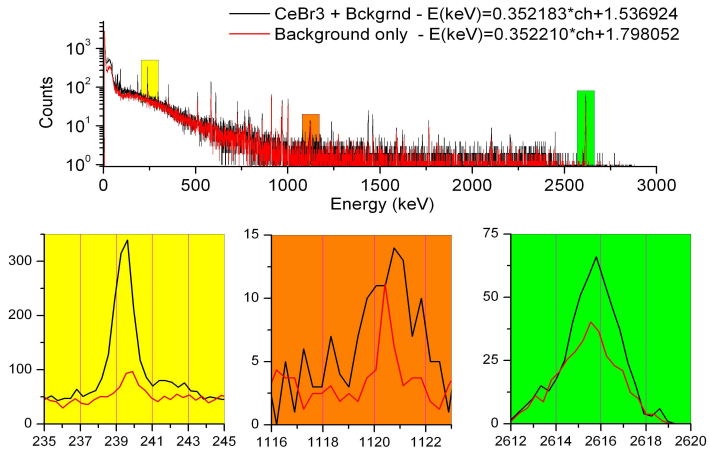

Fig. 4.15: *Gamma ray Spectra of background and $CeBr_3$ were superimposed. Each one were calibrated through an own internal calibration curve.*

Both spectra seem to have a good agreement by their internal calibration, however we could not directly substrate the background to the $CeBr_3$ spectrum because they are distribute

in different bining scale. For this reason both spectra were rebined in a convenient calibration factor of 0.5keV/ch. This method allows us to subtract the background and thus to estimate the presence of main peaks in a clean $CeBr_3$ gamma spectrum.

In the figure 4.16 we have overlapped the background and $CeBr_3$ spectra in four energy windows with the aim of showing the relation between peaks which arise from the laboratory background and peaks coming from $CeBr_3$ and its Aluminium housing. The total energy windows recorded goes from 20 to 2700 keV, but we have divided in four regions or windows in order to highlight the main peaks: 20-200, 200-500, 500-1000 and 1000-2700 keV. The region before 20keV glues the accumulation of counts from low energy Compton effects and X-rays with electronic noise.

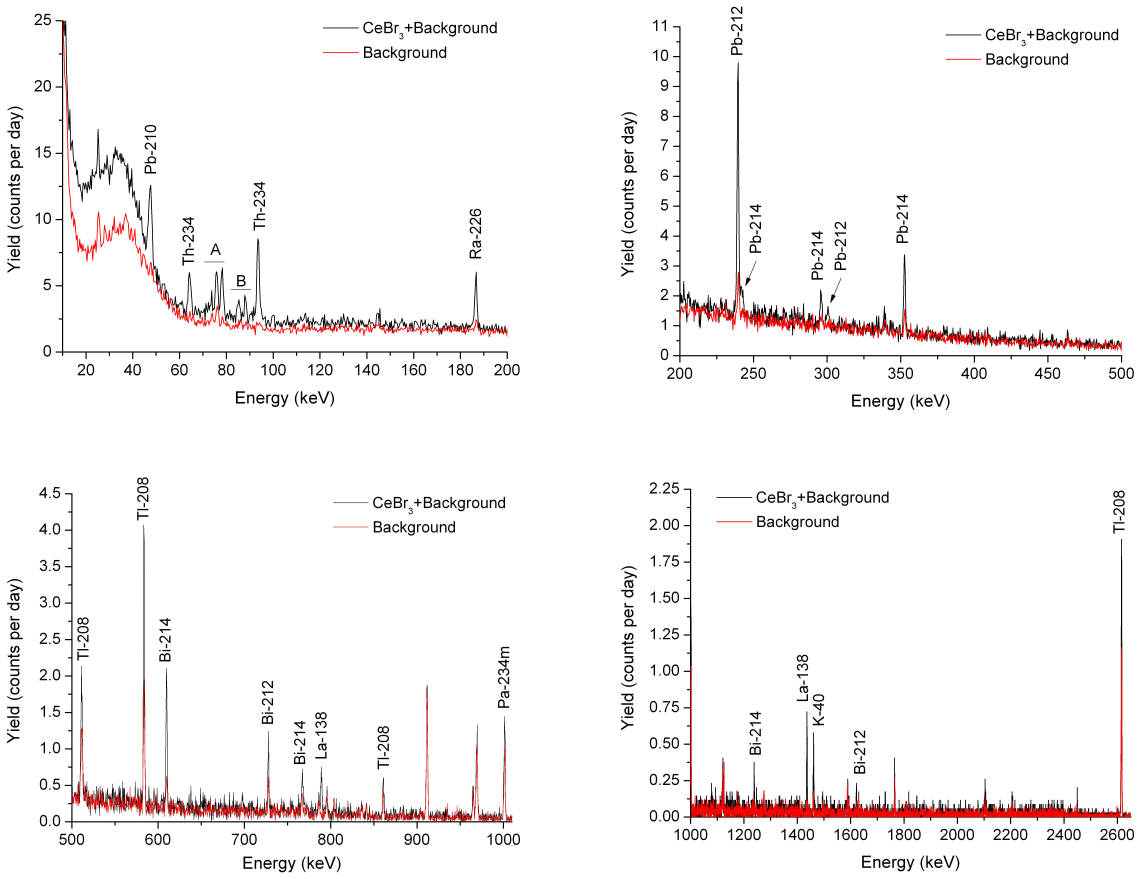

Fig. 4.16: *Identification of net gamma peaks coming from the $CeBr_3$ and its comparison with the background contribution. In the lower energy we have used a letter to denote two regions with several peaks which are listed in the table 4.5.*

In the lower energy windows (in the figure 4.16 above left) we find several peaks which probably contribute to same energy region. Because they are a lot of peaks in a small region, we listed them in the table 4.5. Most of them are Lead X-rays, and also are a couple of peaks from ^{208}Tl. In the same plot we use two capital letters to denote these regions.

Notation	Approximate energy (keV)	Possible gammas which contribute to these peaks. Energy in keV
A	72.81	^{208}Tl (72.81)
	74.9	^{214}Pb (74.82 -XR) ^{212}Pb (74.82 -XR) ^{208}Tl (74.97)
	77.1	^{214}Pb (77.11 -XR) ^{212}Pb (74.82 -XR)
B	87.1	^{214}Pb (86.83 -XR and 87.35 -XR) ^{212}Pb (86.83 -XR and 87.35 -XR)
	89.9	^{214}Pb (89.78 -XR) ^{212}Pb (89.78 -XR)

Table 4.5: *Possible gammas which contribute to the peaks highlighted as A and B in the figure 4.18.*

Before the $CeBr_3$ spectrum was cleaned, we had to normalize the number of counts of the background because it was recorded during a larger interval of time. After the normalization of the background was done and both spectra were internally calibrated, then we could subtract the contribution from the background to the $CeBr_3$ spectra. From the resulting spectrum, which could be called as clean spectrum of $CeBr_3$, we choose the peaks which have enough statistics to be identified and associated to emissions from the $CeBr_3$ crystal or its housing. In the table 4.6 these peaks are listed together with their radionuclide, chain and intensity in counts per day.

Energy Peak (*keV*)	**Radionuclide**	**Chain**	**Intensity (*counts per day*)**	**Yield (*counts per day per kg*)**
46.54	^{210}Pb	^{238}U	17.4 ± 2.6	160.9 ± 24
63.29	^{234}Th	^{238}U	10.1 ± 1.6	93.4 ± 14.8
92.59	^{234}Th	^{238}U	17.6 ± 1.8	162.7 ± 16.6
186.21	^{226}Ra	^{238}U	9.1 ± 1.4	84.1 ± 12.9
238.63	^{212}Pb	^{232}Th	21.2 ± 1.7	196 ± 15.7
241.99	^{214}Pb	^{238}U	1.5 ± 1.2	13.9 ± 11.1
295.22	^{214}Pb	^{238}U	2.1 ± 1.2	19.4 ± 11.1
300.09	^{212}Pb	^{232}Th	1.4 ± 1.1	12.9 ± 10.2
351.93	^{214}Pb	^{238}U	7.7 ± 1.1	71.2 ± 10.2
510.77	^{208}Tl	^{232}Th	3.8 ± 1.0	35.1 ± 9.2
583.19	^{208}Tl	^{232}Th	10.3 ± 1	95.2 ± 9.2
609.32	^{214}Bi	^{238}U	6.7 ± 0.8	62 ± 7.4
727.33	^{212}Bi	^{232}Th	1.7 ± 0.6	15.7 ± 5.5
768.36	^{214}Bi	^{238}U	1.0 ± 0.6	9.2 ± 5.5
788.74	^{138}La	Ce affinity	2.0 ± 0.5	18.5 ± 4.6
860.56	^{208}Tl	^{232}Th	1.5 ± 0.4	13.9 ± 3.7
1001.03	^{234m}Pa	^{238}U	1.8 ± 0.6	16.6 ± 5.5
1238.12	^{214}Bi	^{238}U	0.6 ± 0.3	5.5 ± 2.8
1435.8	^{138}La	Ce affinity	3.3 ± 0.4	30.5 ± 3.7
1460.82	^{40}K	-	2.1 ± 0.4	19.4 ± 3.7
1620.5	^{212}Bi	^{232}Th	0.3 ± 0.2	2.8 ± 1.8
2614.51	^{208}Tl	^{232}Th	4.6 ± 0.8	42.5 ± 7.4

Table 4.6: *Peaks provides by the $CeBr_3$ crystal and its aluminium housing.*

The number of counts for the 510.77 keV peak shows a minor increase due to presence of ^{222}Rn gas in the air. Despite the laboratory is equipped with an outgassing system to reduce the concentration of radon in the air, we estimate that radon contribute with around 20% of

the counts. In a similar way, between 238.63 keV ^{212}Pb and 241.99 keV ^{214}Pb peaks there is a weak contribution from ^{224}Ra. This contribution is lower because the radium decays to radon and this is removed by the air circulation system. The ^{224}Ra is not in secular equilibrium with ^{212}Pb and is almost not perceptible in the clear spectrum.

In order to estimate the absolute efficiency, a simulation with Geant4 was made. In the figure 4.17 are shown the resulting absolute efficiency at different energies (left) and a reconstruction of the geometry simulated (right).

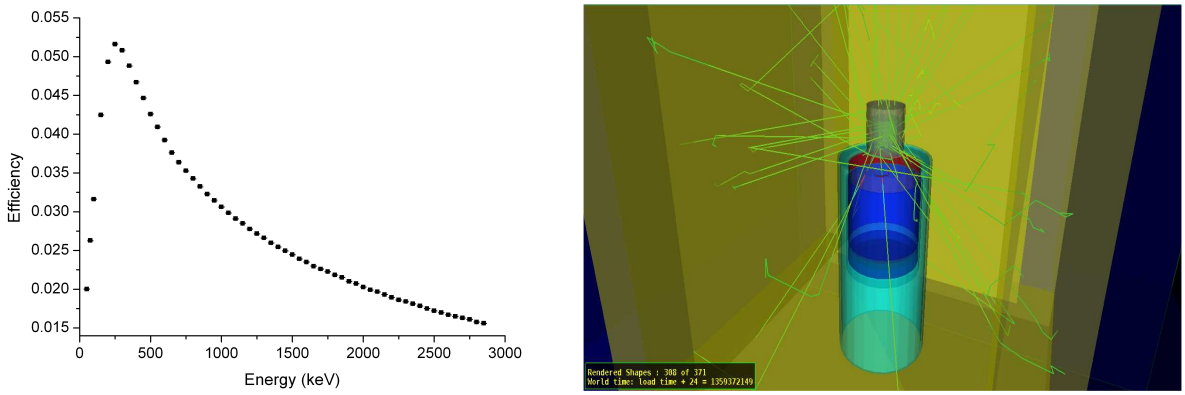

Fig. 4.17: *Left, Absolute Efficiency simulated for a range of energies from 50 to 3000 keV. Right, a frame of the rendering made to the geometry simulated in Geant4.*

First, by interpolation of the efficiency values and using the yield values listed in the table 4.6, we can estimate the activity (mBq) per peak. Later, we estimate the activity for each radionuclide averaging the activity of each gamma and weighting for its branching ratio and error. The results are listed in the table 4.7.

Radionuclide	**Activity (*mBq*)**
^{212}Bi	8.5 ± 8.2
^{214}Bi	5.3 ± 3.9
^{40}K	9.2 ± 1.8
^{138}La	2.1 ± 0.6
^{234m}Pa	82.3 ± 26.9
^{210}Pb	244.9 ± 37.3
^{212}Pb	10.1 ± 8.3
^{214}Pb	4.1 ± 4.0
^{226}Ra	60.2 ± 9.5
^{234}Th	148.2 ± 27.7
^{208}Tl	3.9 ± 1.7

Table 4.7: *Estimation of the internal activity present in a 1"x1" sample of $CeBr_3$ and its housing.*

Through these results we can obtain three conclusions:

First, there are isotopes in the $CeBr_3$ that belong to two natural radioactive chains. The main contribution comes from Radium chain (^{238}U) and weakly from the Thorium chain (^{232}Th). Spite in the background there is radionuclides from Actinides chains, we didn't find presence in the crystal or its housing. Second, unlike other studies [Billnert, R., *et al.*, 2011 and Lutter, G., *et al.*, 2012] we have not found neutron activation products as ^{82}Br or ^{139}Ce.

This is explained because LSC has a lower neutron flux. In this case, it is good that these "missing" products are not appeared. Third, we have found some traces of ^{138}La which is a contamination in the crystal produced by the chemical affinity between lanthanum and cerium. Finally, we have to remember that these results were obtained for the $ceBr_3$ and its aluminium housing. In a close future another study could be performed in order to characterize both parts separately.

4.3.4. Time Resolution for $CeBr_3$

In order to find the optimum time resolution for $CeBr_3$ coupled to the fast-response photomultiplier tubes, we have measured the resolution as a function of the external delay in the CFD and of applied high voltage to the tube. Also we have digitized pulses in order to compare the response of each PMT.

4.3.3.1 Pulse digitizing

We have examined the shapes of the fast negative anode pulses on a 4 GSa/s oscilloscope (Agilent DSO6104A) and determined the time it takes from 20% of the pulse to the maximum, which is suggested in the ORTEC CFD user manual to use as the initial time delay for the CFD. For $CeBr_3$ coupled to the Photonis XP20D0 tube this time was about 8 ns, while for the crystal coupled to the Hamamatsu tube the pulse was much faster with the time difference of only 5 ns. Sample traces from the oscilloscope are plotted in figure. 4.18.

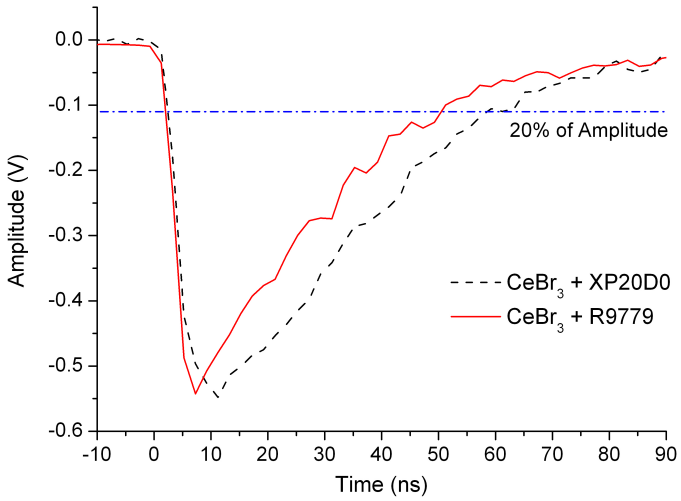

Fig. 4.18: *Example of fast negative anode pulse for $CeBr_3$ coupled to Hamamatsu R9779 PMT and Photonis XP20D0.*

4.3.3.2 CFD and optimization of external delay

We have measured the time resolution as a function of the external delay applied to the $CeBr_3$ CFD. Firstly, according to the manual the CFD have an internal dealy of -1ns. This fact has been checked by exploring the behaviour of the CFD threshold. However, for our measurements the internal delay jumper on the ORTEC 935 CFD was removed in order to test only the external delay under test.

The time resolution given in this section is for a single detector involving $CeBr_3$ and the Hamamatsu or Photonis phototubes, that is, the time response of the BaF_2 + XP2020URQ detector combination has been de-convoluted from the total time peak obtained.

The figure 4.19 shows the results for both phototubes. In the case of the Hamamatsu tube the minimum time resolution was found at only 1.5 ns. A sharp minimum is clearly seen at the ^{60}Co energies as well as at the energy of 511 keV for the ^{22}Na source. The dependence for the Photonis tube is much weaker and the minimum is almost at about 5.5 to 6.0 ns. Based on these results we have selected the external CFD delays of 1.5 ns and 6.0 ns for further tests with the Hamamatsu and Photonis tubes, respectively.

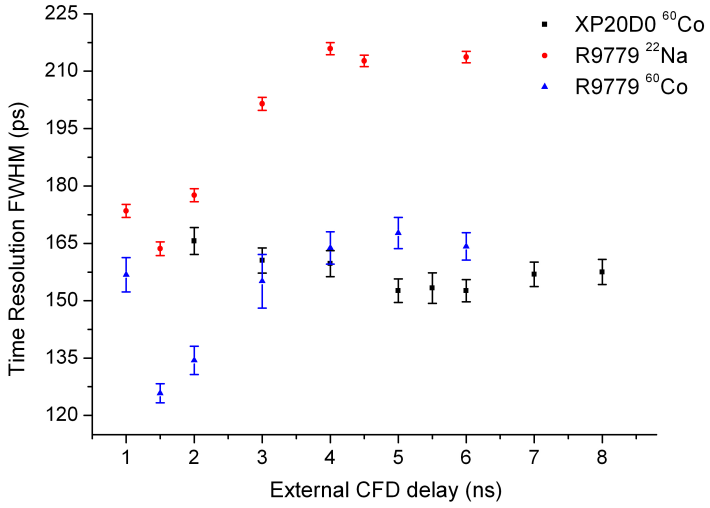

Fig. 4.19: *Dependence of time resolution FWHM in ps as a function of the external delay in ns for an individual detector: $CeBr_3$ coupled to Hamamatsu R9779 PMT and to Photonis XP20D0. The internal delay jumper on the ORTEC 935 CFD was removed. The results were obtained using sources of ^{60}Co with γ-ray energies of 1173 and 1332 keV and from ^{22}Na source the 511 keV peak.*

4.3.3.3 HV optimization

First, the effect of the CFD zero crossing threshold (walk) was investigated. Several Z-values ranging from -4 to 4 mV were evaluated. Beside the effect always was below to 2 ps, we have chosen the value of Z = 2.0 mV.

We have also examined the influence of applied high voltage on the time resolution. The results are plotted in figure 4.20. For the Hamamatsu tube (R9779) the time resolution steadily improves up to the voltage of 1300 V and then it remains rather steady with the minimum value of 119 ps at 1330 V. Operating the tube at higher voltages does not improve the performance for $CeBr_3$.

In contrast, the time resolution for the Photonis tube steadily improves with an increased high voltage until it saturates at very high voltages, of the order of 1700 V, in a regime where the photomultiplier is no longer usable due to its extremely bad energy resolution and drastic non-linearity. In any case, the Photonis tube does not reach the excellent time resolution

provided by the Hamamatsu tube. In the operational region for the Photonis tube, from 850 to 1200 V, even with strong non-linearity, its best time resolution is only 146-160 ps, thus well above the best value for Hamamatsu of 119 ps (See figure 4.20). These results prove that the Hamamatsu R9779 is better suited to perform time measurements for CeBr3 crystals, while the XP20D0 is usefull but not provide the excellent properties required for timing.

Furthermore, our original expectation was that with the increased high voltage the time resolution will first improve and then, when the gain will increase too much, space-charge effects will degrade the shape of the pulses. For a photomultiplier best suited for the application of $CeBr_3$ crystal to the timing spectroscopy, the minimum time resolution should occur at the same high voltage range where the energy resolution and linearity are at least acceptable. In the figure 4.20 we can see how both effects are presented: first, time resolution is improved with the voltage but is impared by saturation.

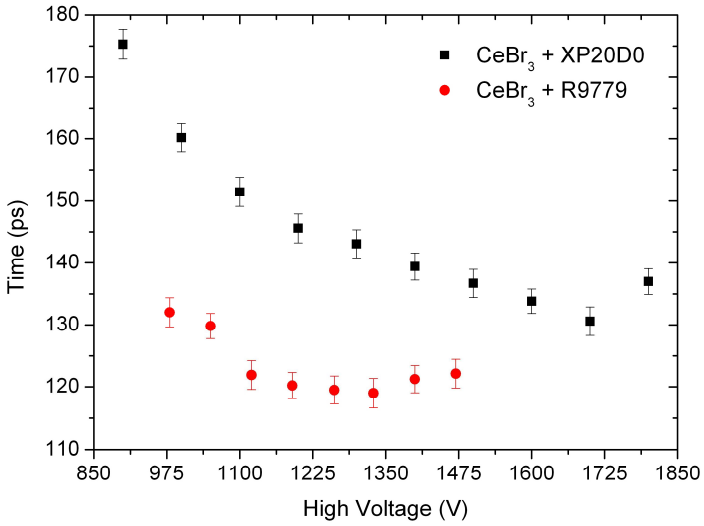

Fig. 4.20: *Dependence of the FWHM time resolution in ps obtained for the $CeBr_3$ crystal coupled to the Hamamatsu R9779 and Photonis XP20D0 PMTs as a function of the applied high voltage. Results are given for an individual detector.*

The FWHM time resolutions measured for the $CeBr_3$ crystal with both photomultipliers are summarized in Table 4.8. For the full energy peaks at ^{60}Co the resolution is 119 ± 2 ps for the $CeBr_3$ and R9779 combination at HV = 1330 V, whereas it is only 146 ± 2 ps for the crystal coupled to the XP20D0 at HV = 1200 V (at the highest bias voltage for which the energy non-linearity can be still acceptable in some applications). Although a better time resolution of 131 ± 2 ps is obtained for the latter detector at 1700 V, at that energy it does not provide any useful energy resolution nor linearity. For 511 keV photons from the ^{22}Na source the time resolution is 164 ± 2 ps for the $CeBr_3$ and Hamamatsu tube at 1330 V, and 210 ± 2 ps for the $CeBr_3$ and XP20D0 at HV = 1200 V.

Detector	**^{60}Co** ***(1173/1332 keV)***	**^{22}Na** ***(511 keV)***
$CeBr_3$ – XP20D0	146 ± 2 ps	210 ± 2 ps
$CeBr_3$ – R9779	119 ± 2 ps	164 ± 2 ps

Table 4.8: *Summary of FWHM time resolution for the $CeBr_3$-Hamamatsu detector at 1330 V and $CeBr_3$-Photonis detector at 1200 V using ^{60}Co and ^{22}Na sources.*

Using a similar 1-inch $CeBr_3$ crystal coupled to a 10-stage Photonis XP6242B01 photomultiplier, an intrinsic FWHM time resolution of 326 ± 7 ps at ^{60}Co was reported in [Billnert *et al.*, 2011]. It is not clear to us why the former time resolution is almost three times worse than our result. On the other hand, an excellent FWHM time resolution of only 59 ps using the ^{22}Na source was reported [Wiener *et al.*, 2010] for a tiny 4x4x5 mm^3 $CeBr_3$ crystal coupled to a Hamamatsu R4998 PMT, which is consistent with our data, since much improved time resolution is generally observed for smaller-size crystals. The crystal used in [Wiener *et al.*, 2010] has about 160 times smaller volume than the one used in our work. In the same work FWHM time resolutions at 511 keV of 173 ps and 210 ps were measured for a small 4x4x30 mm^3 $CeBr_3$ crystal coupled to a Hamamatsu R4998 PMT, and a Photonis XP20D0, respectively.

4.4. Conclusions

We have measured the relative energy resolution in function of the energy, and fit it with a polynomial expression (related with energy through $E^{-1/2}$). The plot shows good agreement between measurements and fitting.

We have also measured the photopeak efficiency with standard point-like sources at three different distances in front of the entrance face of detector. Our range of energy was extended to cover value from 31.61 keV (weigthened average of several unresolved gammas of ^{152}Eu) until 1408 keV.

The radiopurity of the $CeBr_3$ crystal was studied in an underground facility. Our research was performed for a 30x30mm cylindrical crystal and its housing. The main results evidence the presence of Radium and Thorium chains but not from Actinides chains. Also, we found contamination traces of ^{138}La due to chemical affinity but not neutron activation products as ^{82}Br or ^{139}Ce.

We have studied the time response of a $CeBr_3$ crystal of 1 inch in diameter and 1 inch in height, commercially available from Scionix, with two 2-inch fast-response photomultipliers. The best results were obtained with the R9779 Hamamatsu phototube. Very good time resolutions of 119 ± 2 ps and 164 ± 2 ps were obtained at ^{60}Co energies and for 511 keV photons from a ^{22}Na source, respectively, for the $CeBr_3$-Hamamatsu detector operated at HV = 1330 V. The time resolution stays constant over the high voltage range from 1100 to 1450 V. At the operational voltage the response of the $CeBr_3$-Hamamatsu detector was very linear in energy, and good energy resolution was preserved. Based on our measurements it can be concluded that the Hamamatsu R9779 PMT is very well suited for this novel scintillator.

Measurements of the $CeBr_3$ crystal coupled to the Photonis XP20D0 photomultiplier have revealed a strong energy non-linearity and much worse time resolution. In the tests we have used two Photonis XP20D0 tubes, which have shown a similar behaviour. The XP20D0 phototubes have been shown to work very well with $LaBr_3$:Ce crystals. In particular, an excellent time resolution of 107 ± 4 ps was reported [Moszynski *et al.*, 2006] for a $LaBr_3$:Ce cylindrical crystal of identical dimensions to the $CeBr_3$ studied here, and coupled to the XP20D0 photomultiplier.

In the present tests the XP20D0 and R9779 tubes have shown different time characteristics when coupled to the $CeBr_3$ crystal. This demonstrates how important it is to match individually the type of a photomultiplier to a specific class of fast high-yield crystals. The present results also prove that the novel $CeBr_3$ crystal is a strong competitor to $LaBr_3$:Ce in fast timing applications. With similar energy and time resolution to $LaBr_3$:Ce, the $CeBr_3$ crystal, having no internal activity, is more suitable than $LaBr_3$:Ce in applications where very low background activity is required, as for example in the fast timing nuclear spectroscopic studies of very exotic decays.

In conclusion we have proven that $CeBr_3$ is a very promising candidate for a range of applications. The energy resolution is among the best for inorganic scintillators, with 5% measured with fast PMTs. The efficiency is good and comparable to the $LaBr_3$:Ce. The time response is extremely good. Lastly, the radiopurity of the crystal makes it competitives for low counting requiring. Even, the radiopurity can be further improved by requiring radiopure aluminium housing.

4.5. References

Alvarez, V., Bandac, I., Bettini, A., *et al*. Radiopurity control in the NEXT-100 double beta decay experiment: procedures and initial measurements. Doi: 10.1088/1748-0221/8/01/T01002

Basunia, M., Nuclear Data Sheets 107(4), 791 (2006)

Bauer, F., Aykac, M., Loope, M., Williams, C.W., Eriksson, L., Schmand, M., IEEE Transactions on Nuclear Science 54(3), 422 (2007)

Bettini, A. Underground laboratories, Nucl. Instrum. Meth. A 626-627 (2011) S64

Billnert, R., Oberstedt, S., Andreotti, E., Hult, M., Marissens, G., Oberstedt, A., Nuclear Instruments and Methods in Physics Research A 647, 94 (2011)

Browne, E. and Tuli, J.K. Nuclear Data Sheets 108, 2173 (2007)

Ciemala, M., Balabanski, D., Csatlos, M., Daugas, J.M., Georgiev, G., Gulyas, J., Kmiecik, M., Krasznahorkay, A., Lalkovski, S., Lefebvre-Schuhl, A., Lozeva, R., Maja, A., Vitez, A. Nuclear Instruments and Methods in Physics Research A 608 (2009) 76–79

Conti, M., Eriksson, L., Rothfuss, H., Melcher, C.L., Member, S., The, A., T.o.f. Tof, IEEE Transactions on Nuclear Science 56(3), 926 (2009)

Drozdowski, W., Dorenbos, P., Bos, A., Bizarri, G., Owens, A., Quarati, F., IEEE Transactions on Nuclear Science 55(3), 1391 (2008)

Drozdowski, W., Dorenbos, P., Haas, J.T.M.D., Drozdowska, R., Owens, A., Kamada, K., Tsutsumi, K., Usuki, Y., Yanagida, T., Yoshikawa, A., IEEE Transactions on Nuclear Science 55(4), 2420 (2008)

GEANT4 collaboration, S. Agostinelli et al., GEANT4: A Simulation toolkit, Nucl. Instrum. Meth. A 506 (2003) 250 [INSPIRE]

Glodo, J. , Moses, W.W., Higgins, W.M., Van Loef, E.V., Wong, P., Derenzo, S.E, Weber, M.J., Shah, K.S., IEEE Transactions on Nuclear Science 52(5), 1805 (2005)

Guss, P., Reed, M., Yuan, D., Reed, A., Mukhopadhyay, S., Nuclear Instruments and Methods in Physics Research, A 608(2), 297 (2009)

Hamamatsu Photonics, Photomultiplier Tube R9779 Specifications (2009)

Hamamatsu Photonics, Photomultiplier Tube R5320 Specifications (2009)

Higgins, W., Churilov, A., Van Loef, E., Glodo, J., Squillante, M., Shah, K., Journal of Crystal Growth 310, 2085 (2008)

Kamada, K., Yanagida, T., Endo, T., Tsutumi, K., Yoshino, M., Journal of Crystal Growth pp. 1–4 (2012)

Klamra, W., Lindblad, T., Moszynski, M., Norlin, L., Nuclear Instruments and Methods in Physics Research A 254(1), 85 (1987)

Knoll, Glen. Radiation Detection and Measurement. Third Edition. New Jersey: John Wiley & Sons, Inc., 2000.

Fraile, L.M., Mach, H., Vedia, V., Olaizola, B., Picado, E., Paziy, V.,Udías, J.M., Nuclear Instruments and Methods in Physics Research A submitted (2012)

Fraile, L.M., Mach, H., Olaizola, B., Paziy, V., Picado, E., Sanchez, J.J., Udías, J.M., Vaquero, J.J., Vedia, V., in Nuclear Science Symposium Conference Record, 2011. NSS '11. IEEE (2011), pp. 72 -74

FURUKAWA CO., LTD. URL: www.furukawakk.co.jp (2012)

Lewellen, T.K., Physics in Medicine and Biology 53(17), R287 (2008). URL: http://stacks.iop.org/0031-9155/53/i=17/a=R01

Laboratorio Subterraneo de Canfranc (LSC). URL: http://www.lsc-canfranc.es/en/index.html (2013)

Mach, H., Fraile, L.M., Hyperfine Interactions in press (2012). DOI 10.1007/s10751-012-0613-8

Mach, H., Gill, R.L., Moszynski, M., Nuclear Instruments and Methods in Physics Research A 280, 49 (1989)

Mach, H., Wohn, F., Molnar, G., Sistemich, K., Hill, J.C., Moszynski, M., Gill, R., Krips, W., Brenner, D. Nuclear Physics A 523, 197 (1991)

Mach, H., Instructions for the program SORTM. (Internal Report. Universidad Complutense, 2012)

Moszynski, M., Mach, H., Nuclear Instruments and Methods in Physics Research A 277, 407 (1989)

Moszynski, M., Gierlik, M., Kapusta, M., Nassalki, A., Szczesniak, T., Fonatine, M., Lavoute, P., Nuclear Instruments and Methods in Physics Research A 567, 31 (2006)

SCIONIX Holland BV. URL: www.scionix.nl (2012)

Shah, K.S., Glodo, J., Higgins, W., Van Loef, E.V., Moses, W.W., Derenzo, S.E., Weber, M.J., IEEE Transactions on Nuclear Science 52(6), 3157 (2005)

Szczesniak, T., Moszynski, M., Swiderski, L., Nassalski, A., Lavoute, P., Kapusta, M., IEEE Transactions on Nuclear Science 56(1), 173 (2009)

Van Loef, E.V., Dorenbos, P., Van Ejik, C.W.E., Krammer, K., Gudel, H.U., Nuclear Instruments and Methods in Physics Research A 486, 254 (2002)

White, E.R., Mach, H., Fraile, L.M., Koster, U., Arndt, O., Blazhev, A., Boelaert, N., Borge, M.J.G., Boutami, R., Bradley, H., Braun, N., Dlouhy, Z., Fransen, C., Fynbo, H.O.U, Hinke, C., Hoff, P., Joinet, A., Jokinen, A., Physical Review C 057303, 7 (2007)

Wiener, R.I., Kaul, M., Surti, S., Karp, J.S., in Nuclear Science Symposium Conference Record, 2010. NSS '10. IEEE, pp. 1991-1995 (2010)

5. A new Phoswich proposal

Abstract: A phoswich based on two high density inorganic crystals have been characterized. The configuration LuAG:Pr+LYSO provides good energy response and allows to disentangle crystal layers both when coupled to SiPM or PMT. We also have determined the best parameters of the Delayed Energy Method (DEM) to disentangle the phoswich layer (delay and layer factors). We have developed a python code to control an oscilloscope which is used as digitizer to acquire the pulse shapes. From these digitations, an off-line analysis is made with a Fortran code that includes the DEM algorithm and permit to test several parameters in order to find the optimum.

5.1. Introduction

The combination of two dissimilar scintillators optically coupled to a single photomultiplier, either SiPM or PMT, is often called *phoswich* detector. The crystals are chosen to have different shape (most often different decay times) so that the shape of the output pulse from the photodetector depends on the relative contribution of scintillation light coming from each scintillator. Most applications involve the use of this pulse shape difference to distinguish the specific layer on which events take place, or if they took place on both layers [Knoll, 2000].

There are several combinations of scintillators depending on the application. For instance, a phoswich made of two scintillators with high yield (photons/MeV) like $LaBr_3$:Ce+$LaCl_3$:Ce is useful for high energy gamma-ray and proton identification [Tengblad, O., *et al.*, 2013]. Other example of phoswich widely used is NaI+CsI because their decay times are quite different, the first one is much slower compared with the second [Knoll, 2000]. Another example is a combination of two very fast scintillators: one plastic (NE102A) and one inorganic (BaF_2) in order to separate high energy charged particles from photons [Novotny, R., 1996]. In general, there are many examples like BGO+CsI, CsI(Na)+GSO, BGO+GSO and YSO+LYSO [Leo, 1994]. In PET scanners, phoswich detectors have been employed, of GSO+LYSO [Seidel, 1999]. There is continued interest in search for new combination of scintillator with enhanced performance.

Also there are several strategies to separate the signals from each scintillator. Pulse shape discrimination is employed. For our purpose we will use the Delayed Energy Method [Seidel, 1999]. Phoswich detectors in PET were implemented first with BGO+GSO combinations, and later, after the availability of LSO and LYSO scintillator, by means of LYSO+GSO combinations. The GSO scintillator has less stopping power, less light yield and slower fall time than LYSO, and thus the LYSO+GSO combination degrades energy resolution, sensitivity and count-rate performance compared to an equivalent single-scintillator LYSO detector. Here we explore the properties of a novel phoswich made of two inorganic crystals LuAG:Pr and LYSO. LuAG:Pr overcomes all the limitations of GSO crystal, and it has even better properties than LYSO. A LuAG:Pr+LYSO combination would improve the performance of existing phoswich based PET scanners. We will assess if phoswich separation is possible when using Silicon Photomultiplier (SiPM) and Photomultiplier Tube (PMT). The signal from the photosensors will be digitized in a digital oscilloscope. Lastly, the data will be processed off-line which allows to change the integration and delay parameters many times Figure 5.1 shows the three main steps to characterize a phoswich which we are going to follow.

Fig. 5.1: *Scheme of the stages to characterize a phoswich: first chose the right set up, then use an appropriate digitizing system and lastly explore pulse processing strategies.*

5.2. Description of the set up

5.2.1. Set-up to test the phoswich crystal

Our set-up is made of a couple of scintillator crystals, two photomultiplier devices (SiPM and PMT), a Multichannel Analyzer (MCA), an oscilloscope-digitizer, and a system to process the pulses (PC). In this section we are going to talk only about the devices involved in the first step of the procedure: scintillators, photosensors, MCA and digitizers.

5.2.1.1 Crystals in the phoswich

For our phoswich we will use a pair of inorganic high density scintillators: LYSO ($(Lu,Y)_2SiO_5:Ce$) and LuAG:Pr ($Lu_3Al_5O_{12}:Pr^{3+}$). Both crystals are cubes of 1 cm^3 (see figure 5.2) and are not hygroscopic which allows easy manipulation. A previous study [Kato, T., *et al.*, 2011] reported the properties of a phoswich with these same crystals, however they used matrices and now we pretend to characterize a continuous relatively large crystal and with an improved formula for the LuAG:Pr (see the description in chapter 3). Further, we study the SiPM phoswich possibility.

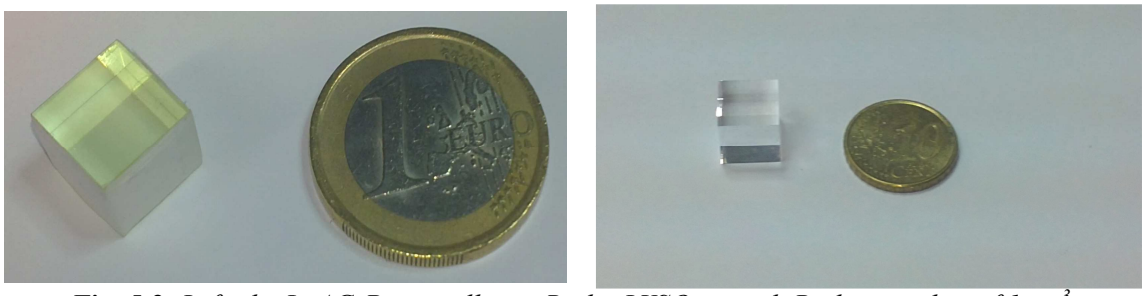

Fig. 5.2: *Left, the LuAG:Pr scintillator. Right, LYSO crystal. Both are cubes of 1 cm^3.*

Both crystals provide excellent scintillation properties (see table 5.1).The medical imaging community, especially TOF-PET researchers, has been interested in exploring these scintillators as possible substitutes of the classic wide-ranging scintillators such as BGO, GSO, NaI:Tl, etc. [Derdzyan, M.V.; *et al.*, 2012; Lewellen, T., 2008; Chewpraditkul, W. *et al.*, 2009].

Features	$CeBr_3$	LuAG:Pr	LYSO
Light Yield (NaI:Tl) Photons/keV	68	20*	30**
Decay Time (ns)	17	25	40
Peak Emission (nm)	371	310	420
Density (g/cm^3)	5.2	6.7	7.2
Intrinsic Radioactivity	NO	Yes (^{176}Lu)	Yes (^{176}Lu)
Hygroscopic	Yes	No	No
$E_{resolution}$ at 662 keV	4.5%	6%	10%

Table 5.1: *Comparison of properties between inorganic scintillator crystals [Scionix, 2012] and [EPIC, 2012]. * in [Mares, J., et al., 2004] and ** in [Hass, J., et al., 2008].*

Another important feature of these crystals is their internal activity. Both scintillators are based in Lutetium which contains a fraction of 2.59% of ^{176}Lu. The concentration of this unstable isotope in both crystals is similar and rounds 200 Bq/cm^3 [Fraile, LM, *et al.*, 2012; Yao, R., *et al.*, 2007; Drozdowski *et al.*, 2008; and see again the chapter 3 of this thesis]. However, this effect is negligible for our purpose because we will expose the phoswich to fluencies upper than 2000 cps of gammas. As we will see in the next sections, the gamma peaks can be resolved without problems.

5.2.1.2 Photosensors

One of the main purposes is compare the response of the phoswich coupled to two different photosensors. On one hand, we will use a photomultiplier tube (PMT) model R5320 provided by Hamamatsu. Its main properties are listed in the table 5.2. From this device we get two signals: the anode signal will be used to characterize the time, pulse shape and integration strategies. And the other signal is taken from the dynode and is used to explore the energy resolution and linearity. Finally, this device is in an assembly together with a base and magnetic shielding which was called by Hamamatsu as H6610.

Feature	Value
Tube Size	25 mm diameter
Size of the Photocathode Area	20 mm diameter
Photocathode Material	Bialkali
Window Material	Quartz
Wavelength Peak	420 nm
Dynode Stages	10
Anode to Cathode Supply Voltage	2250V
Average Anode Current (maximum)	0.1 mA
Typical Gain	5.7 x 106
Typical Dark Current (after 30 min.)	100 nA
Typical Rise Time	0.7 ns
Typical Transit Time	10 ns

Table 5.2: *Technical specifications for the Hamamatsu R5320 PMT [Hamamatsu, 2012].*

In the other hand, we also use a Silicon Photomultiplier (SiPM) model S10985-050C provided by Hamamatsu. This type of devices is a compact and high performance semiconductor photodetector which is insensitivy to magnetic fields, offers good time resolution and have compactness. In addition, if it is operated in Geiger-mode, its gain may be almost comparable to that of PMTs at up to the 10^5-10^6 level [Kato, T., *et al.*, 2013]. Also,

this SiPM is a 2x2 channels array with active areas of 3x3 mm each, and can be used as 6x6mm large-area Multi-Pixel Photon Counter (MPPC). In the table 5.3 are listed the some properties.

Feature	Value
Number of channels	4 (2x2)
Effective active area/channel	3x3
Number of pixels/channel	3600
Pixel Size	50x50
Fill Factor	61.5
Spectral response range	320 to 900 nm
Peak sensitivity wavelength	440
Operating voltage range	70±10
Dark count/channel	6000
Terminal capacitance/channel	320
Temperature coef. of reverse voltage	56
Gain	$7.5x10^5$

Table 5.3: *Technical specifications for the Hamamatsu S10985-50C PMT. [Hamamatsu, 2010].*

Because the SiPM provides four output signals, a circuit board to sum the signal and to obtain an integral or added signal was built. This signal will be used for time, pulse shape, linearity, etc.

5.2.1.3 Multichannel Analyzer (MCA)

Both dynode signal from the PMT and sum signal from the SiPM are driven toward a simple peak-sensing "*MCA Box*" multichannel analyzer by Leybold Didactic GmbH which is controlled by a general purpose measurement program "CASSY". Since this process we obtain the energy spectra from the different configurations of the phoswich.

5.2.1.4 Oscilloscope

In order to visualize signals from PMT and SiPM, we have used a digital oscilloscope, model *DS06104A* by Agilent. Its bandwidth is of 1 GHz, the sample rate can reach 4 GSa/s and the depth memory is 8 Mpts. Also, it accepts signals until ±75V and is able to use two values of input impedance 50Ω or 1MΩ. Furthermore, it provides some advantages like different types of filtering, several ways of digitization, and allows changing the trigger mode.

Digitizing the pulses and storing them in a PC allows us not only to corroborate the shape of the pulses and level of the baseline, but to reprocess every signal with different parameters (integration time, filtering, delay) what we expect to test. Also it is possible to check that there is no parasitic current, pile-up or electronic noise in the signal, in other words, this method allows us to assure the correct behavior of the electronic system and the shape of the pulses. Figure 5.3 shows the Agilent oscilloscope described.

Fig. 5.3: *Agilent Oscilloscope model DSO6104A. Left, front panel; Right, Rear panel.*

5.3. Sampling and Acquisition Modes

Sampling is the process of converting a portion of an input signal into a number of discrete values for the purpose of storage, processing, and/or display. The magnitude of each sampled point is equal to the amplitude of the input signal at the instant in time in which the signal is sampled [CAEN, 2011]. For digital oscilloscopes, an array of sampled points is reconstructed on a CRT, with the measured amplitude on the vertical axis and time on the horizontal axis (see Figure 5.4).

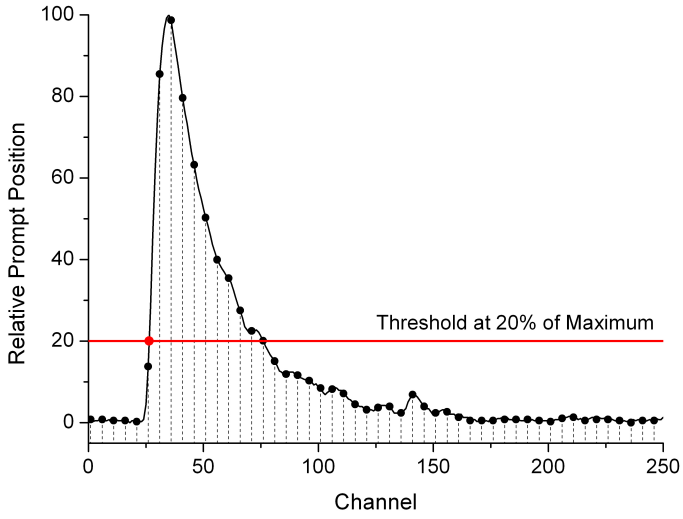

Fig. 5.4*: This positive pulse was digitized with 250 points. Here they are plotted only 50 points. The red line shows the threshold at 20% of the Maximum value. The amplitude is normalized to the Maximum. Sampling points or channels are connected by simple lines, there is no interpolation.*

Figure 5.1 shows a positive pulse acquired with our oscilloscope. This pulse was sampled through 250 points or samples. In the image we only plot 50 points in order to show the vertical separation of equitemporal samples. Both each prompt position and the threshold level were normalized to the maxima amplitude value. Also, the points were connected by a simple straight line.

In order to extract information about the behavior of the pulses and hence from the phoswich, we must optimized the sampling methods and the acquisition modes in our scope. Especially, we dealt with different parameters to improve the quality of the signal and to

digitize every pulse.

5.3.1. Sampling Modes

Our digital oscilloscope offers three basic sampling methods: Real Time sampling, Equivalent Time sampling and sampling through Segmented Memory. For our purpose we discard the equivalent time because we are not dealing with periodic pulses. Moreover, we discarded the Segmented Memory method because it did not provide any benefit in comparison with the Real Time sampling approach, even it could be more difficult to deal with it. For these reasons, all our measurements were done in Real Time Mode (*RTIMe*).

Sampling in Real Time mode captures an entire waveform of each trigger event. It is also called "single-shot" mode. A large number of data points are captured in one continuous record. The oscilloscope is acting like an extremely fast ADC in which the sample rate determines the sample spacing and the memory depth determines the number of points that will be displayed. In order to capture any waveform, the ADC sampling rate needs to be significantly faster than the frequency of the incoming waveform. In Real Time Sampling, the digitizer (or sampler) operates at maximum speed to acquire as many points as possible in one sweep. Therefore, real time sampling is intended for capturing single shot or transient events.

The real-time scope triggers when the amplitude of the incoming waveform reaches a certain threshold. It is at this point that the scope starts converting the analog waveform to digital data points at a rate asynchronous and very much unrelated to the input waveform's data rate. That conversion rate, known as the *sampling rate*, is typically derived from an internal clock signal. The scope samples the amplitude of the input waveform, stores that value in memory, and continues to the next sample. Thus the main task for the trigger is to provide a horizontal time reference point for the incoming data [CAEN, 2011].

Measurement systems such as our Agilent DSO6104A scope, with a sample rate of 4 GSa/s and bandwidths to 1 GHz, have been optimized for capturing very fast single shot and transient events. These systems have the ability to sample input signals as fast as once every 250 ps. For these reason we have chose this device as digitizer for our phoswich pulses.

5.3.2. Acquisition Modes

Although our oscilloscope has four acquisition modes: Normal, Average, Peak Detect and High Resolution, for these measurements we only will use the High Resolution mode (HRESolution).

The High Resolution mode is used to reduce noise and increase the effective resolution in bits of the ADC conversion, at slower sweep speeds where the digitizer samples faster than needed to fill memory for the displayed time range. For this reason is also known as smoothing mode. For instance, if the digitizer samples at 200 MSa/s, but the effective sample rate is 1 MSa/s (because of a slower sweep speed), only 1 out of every 200 samples needs to be stored. Instead of storing one sample (and throwing others away), the 200 samples are averaged together to provide the value for one display point [Agilent, 2012].

5.3.3. Acquisition Parameters

In order to optimize the data from digitalization, the acquisition parameters have to be optimized. In the next chart we list all the values of the parameters for both photosensors used: SiPM and PMT.

	Photosensor	
Parameter	**PMT**	**SiPM**
Number of samples used	250	
Time between consecutive samples	4 ns	
Sampling ratio	4 GSa/s	
Total pulses captured	40,000	
Trigger Mode	Normal	
Trigger Type	Edge Slope Negative	
Trigger Coupling	AC	
Channel Coupling	DC	
Pulse Polarity	Negative	
Inverted	No	
Impedance	50 Ω	
Amplitude scale: Y-scale value per division	50-75 mV/div	60-70 mV/div
Time scale: X-scale value per division	100 ns/div	
Bias Supply	-1800 V	-69.5 V

Table 5.4 *Acquisitions parameters values for both photosensors.*

In general almost all the values are similar to both photosensors. However, there are some differences in the amplitude scale and the bias supply. The height of the pulses depends on the yield provided from the phoswich, which in its turn depends of the position of the crystals. Hence, for the same PMT the Y-scale could be changed when the phoswich is coupled to the photodetector in inverse position.

5.3.4. Pyvisa: control program

In order to fix the parameters and send the commands to the oscilloscope, it is necessary to use a control program which permits us to link with the device gently. We have chosen a Python package called *Pyvisa* that binding to the "Virtual Instrument Software Architecture" VISA library to control measurements devices and test equipment via GPIB, RS232 or USB. In our case we connect the scope through USB-2 port to PC.

In this way, we use Python, a dynamic object-oriented programming language, with some extra libraries to set the parameters and modes of acquisition in the oscilloscope. After declaring the values for several settings, we have to define the digitization process itself. In the next chart the main lines of the code are highlighted.

```
agilent.write(":WAV:FORM WORD")
⋮
agilent.write(":WAV:DATA?")
datos = agilent.read_raw()
pulso = struct.unpack('<'+str(len(datos[10:510])/2)+'H',datos[10:510])
```

The "*WAVeform:FORMat*" sets the data transmission mode for waveform data points. This command controls how the data is formatted when sent from the oscilloscope to the PC. There are three different types of formats: Word, ASCII and Byte. We chose the Word format because it provides more precision without rounding and it is compact enough Data samples are transferred as two bytes [Agilent, 2012].

Finally, the output files of the pythons program contains the information of all the sampled pulses separated by a "-1".

5.4. Pulse Processing

After the pulses were digitized and transferred to the PC, they are stored as plain text ASCII files. The analysis of each pulse is performed by means a program written in fortran. This program, which we call "*pulse-processor.f*", integrates the pulses after removing the baseline and introducing trigger conditions. It also implements the Delayed Energy Method to separate pulse layer (See flowchart in figure 5.6).

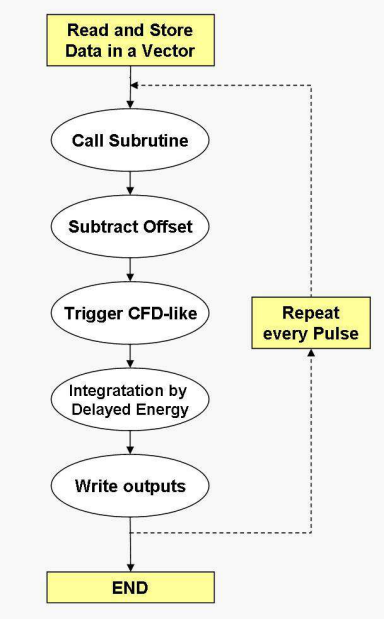

Fig. 5.5: *Flowchart of the code.*

The code integrates the pulses from their initial sample (established by the trigger conditions) or starting at a later sample. Separation of layers with different delays is examined and then the optimum delay is chosen. In other words, with this program we pretend to maximize the separation between pulses through the *Delayed Charge Integration Method* [Seidel, 1999].

The program takes each pulse and then calls a Subroutine to analyze it. First, it defines and subtracts the offset level (or baseline) obtained as the average of the first ten samples. Later, it sets the trigger point through a CFD-like procedure. In our case we fixed the threshold level around 20% of the maximum amplitude. Finally, the charge is integrated for each pulse at different delays: from 10 samples before the trigger point (total pulse integration) and delayed integrations starting at 10, 20, 30, 40, 50, 60, and 70 ns. The outputs are written in plain text files in order to allow us to analyze them with any plotting program.

5.5. Results

5.5.1. Configuration of the Phoswich

We have tried three different configurations for the crystals. The first one positioned one crystal next to the other (we called side-by-side) and provides the properties of the crystal separately. In the second configuration we set the LuAG:Pr close to the photosensor while the LYSO is in phoswich configuration, above the LuAG:Pr coupled by optical grease. The third configuration inverts the position of the crystal, now the LYSO is in contact to the photosensor and the other is far. Both phoswich configurations were tested with SiPM and

PMT read-outs. The configuration side-by-side can not be tested with SiPM because they do not have enough active area (see figure 5.6).

Fig. 5.6: *Configurations tested. Left, side-by-side configuration in the PMT. Middle, phoswich coupled to the PMT with a gamma point-like source. Right, the phoswich coupled to SiPM in a black box.*

In order to explore a wide range of energies, we have tested all configurations with three gamma point-like sources: ^{60}Co, ^{137}Cs and ^{22}Na. We obtain pulses for each source in two scenarios: when the source is close or far from layer one or with layer two. In the table 1.5 we show the different configurations tested.

	Photosensor	
Configuration	**PMT**	**SiPM**
Each individual crystal	Over LuAG:Pr crystal	Over LuAG:Pr crystal
	Over LYSO crystal	Over LYSO crystal
Side-by-Side	Close to LYSO	N-A
	Close to LuAG:Pr	
	On Top	
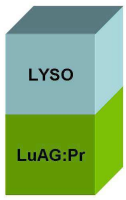	Close to LYSO	Close to LYSO
	Close to LuAG:Pr	Close to LuAG:Pr
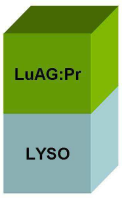	Close to LYSO	Close to LYSO
	Close to LuAG:Pr	Close to LuAG:Pr

Table 5.5: *Chart of configurations explored and the position of the sources.*

5.5.2. Energy spectra for the different configurations

The energy spectra were taken from the energy signal of the PMT (dynode terminal) and from the added signal of the four pixels of the SiPM. These signals were analyzed with a multipurpose MCA. The information provided by the spectra allows comparing the best configuration of the phoswich by means of a simple criterion: *Which is the configuration that minimizes the energy separation between similar peaks?*

5.5.2.1 Each Individual Crystal

In this section we present histograms of the individual crystal coupled to the photosensors.

a) LYSO crystal

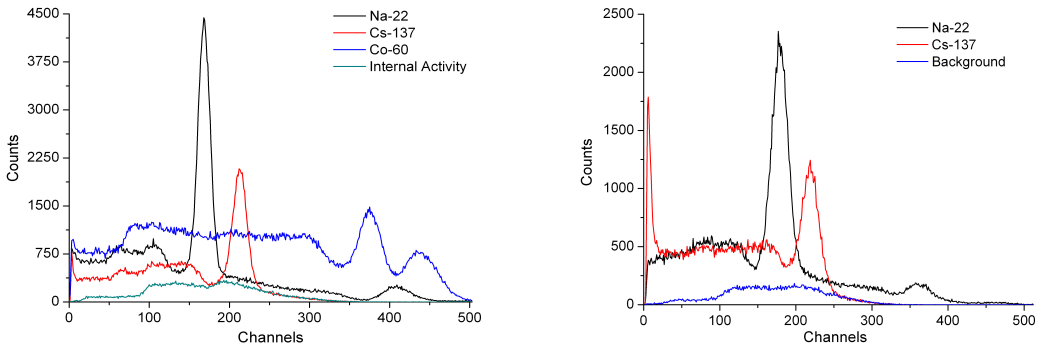

Fig. 5.7: *Histogram for a 1 cm^3-cube LYSO crystal coupled to PMT (left) and coupled to SiPM (Right).*

Three aspects have to be highlighted in these histograms (see figure 5.7): first, when the crystal was coupled to the SiPM the peaks from the ^{60}Co source can not be resolved, this is due to saturation in the SiPM for high photon energy. Second, the internal activity caused by the ^{176}Lu presents in the LYSO scintillator is clearly seen. Finally, spectra from PMT have better energy resolution. All the histograms were acquired for 100 seconds.

b) LuAG:Pr crystal

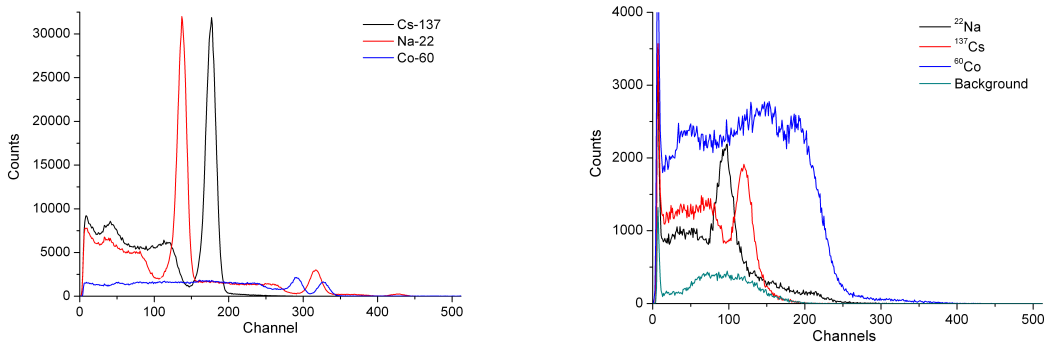

Fig. 5.8: *Histogram for a 1 cm^3-cube LuAG:Pr crystal coupled to PMT (left) and coupled to SiPM (Right).*

Three observations for the histograms plotted in figure 5.8: First, all were taken during 600 seconds. The resolution in the PMT is better than in the SiPM, and it was better in the PMT than the only of LYSO. And lastly we the internal activity (plus background) was widely treated in chapter three.

5.5.2.2 Side-by-side Configuration

In the figure 5.9 we show some pulses obtained from the side-by-side configuration. It can be seen how LYSO pulses are larger than LuAG:Pr ones, which is due to the major yield (photons/keV) of the LYSO. For the figure we have used a monoenergetic gamma source

(^{137}Cs).

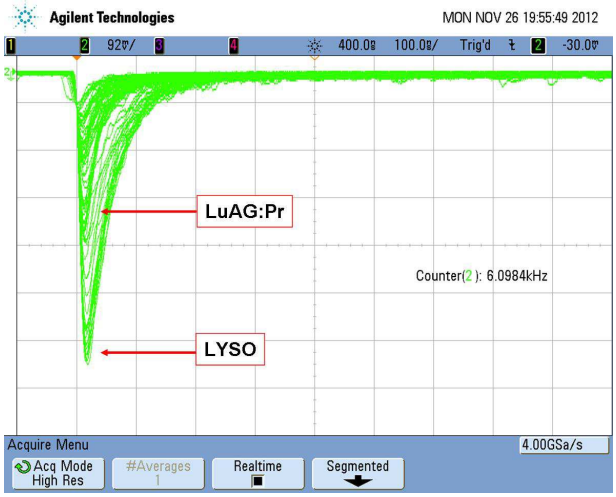

Fig. 5.9: *Pulses obtained from the PMT for the side-by-side configuration. LYSO provides a larger signal because have a larger yield (photons/keV) for the same fluence.*

In the next chart several histograms are presented for three different position of the radioactive source: top, with similar fluence for each, and close to each crystal. The histograms were recorded during 200 seconds from the dynode of the PMT.

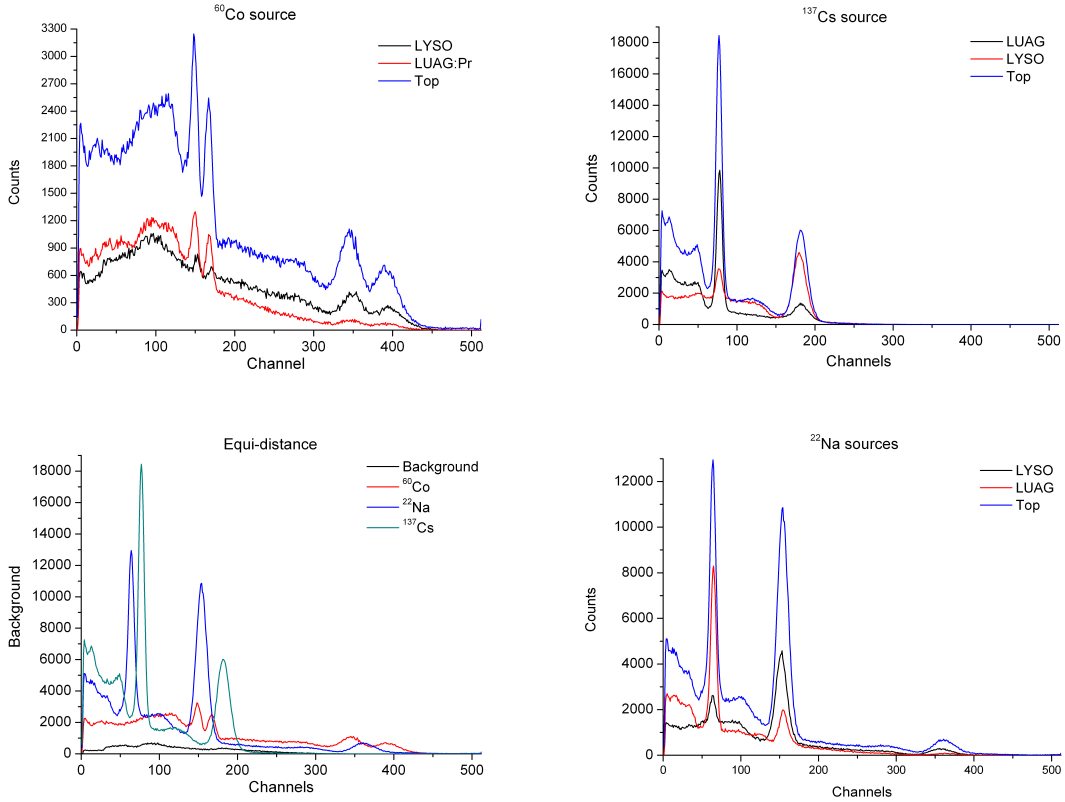

Fig. 5.10: *Histograms obtained from side-by-side configuration coupled to PMT and with different gamma point-like sources: top left, ^{60}Co, top right ^{137}Cs and bottom right, ^{22}Na. The equidistance histogram (bottom left) shows a shape approximately equal to the sum of all top histograms.*

In the previous histogram we can see how LYSO has a larger yield than LuAG:Pr through the position of the same energy peaks in the histogram.

5.5.2.3 Phoswich configuration with PMT

The next two figures provide the histograms for both configurations of the phoswich coupled to PMT. The first set of plots shows the results for the LuAG:Pr coupled directly to the photocathode window while the LYSO is coupled to the other crystal. All these were obtaining during 200 seconds (see figure 5.11).

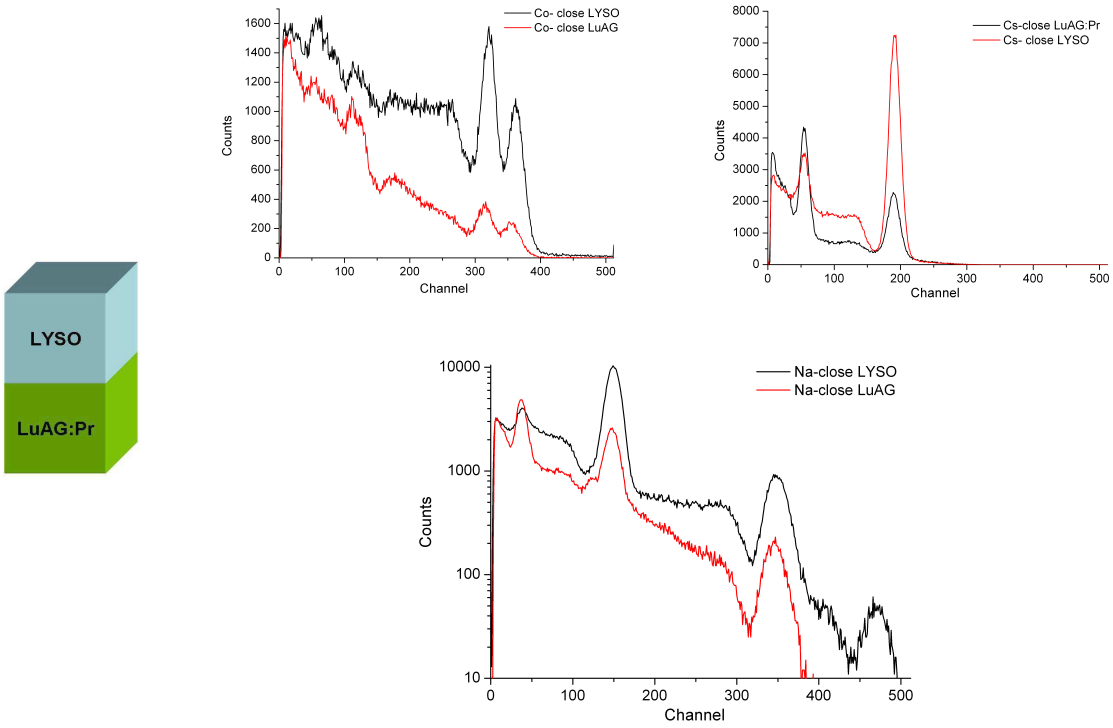

Fig. 5.11: *Histograms taken in the configuration (LuAG:Pr+LYSO) during 200 seconds mode with the MCA CassyLab.*

The second set of plots shows the result for phoswich configuration where LYSO is coupled directly to the PMT and the LuAG:Pr in the opposite side. All these histograms were obtaining during 200 seconds and background was subtracted from them (see figure 5.12).

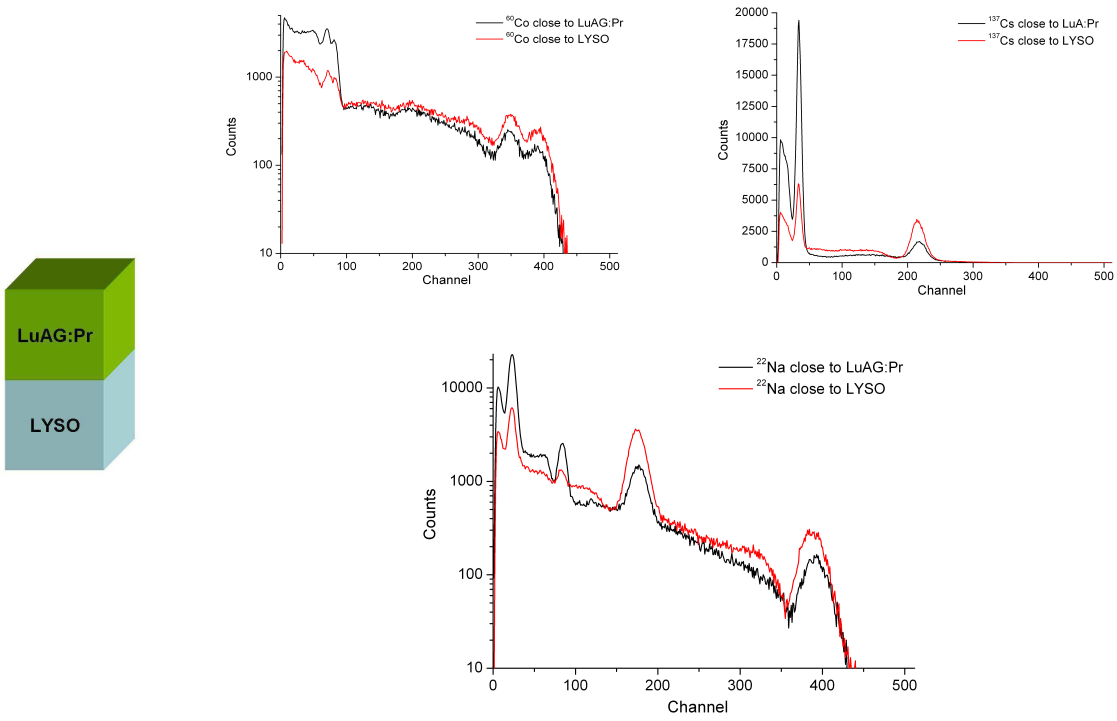

Fig. 5.12: *Histograms taken in the configuration (LYSO+LuAG:Pr).*

From the previous histograms we can see how, for the second phoswich configuration (LYSO+LuAG:Pr), the LuAG:Pr peaks are concentrated in the low energy channels, that is, with the larger difference in the amplitude produce by photons of the same energy, being absorbed in different layers. This presents a problem because it reduces the dynamic range and the ratio between peaks with the same energy is larger than the other situation. Conversely, the first phoswich configuration (LuAG:Pr+LYSO) provides a smaller ratio between the maximum amplitudes for similar peaks and the dynamic range needed in the system would be more amenable. For instance, if we compare the histograms in log-scale for the ^{22}Na source, we look how the 511 keV-LuAG:Pr peak is rounding the 50 channel and the 1274 keV peak is almost overlapping the 511 keV-LYSO peak, while for the other configuration the peak are more separated, even we can distinguished easily every peak. In this way, the first configuration is better because it would require smaller dynamic range.

1.5.2.2 Phoswich configuration with SiPM

The next two figures provide the histograms for both configurations of the phoswich coupled to SiPM. The first set of plots shows the results for the LuAG:Pr coupled directly to the active area while the LYSO is couple to the other crystal (see figure 5.13).

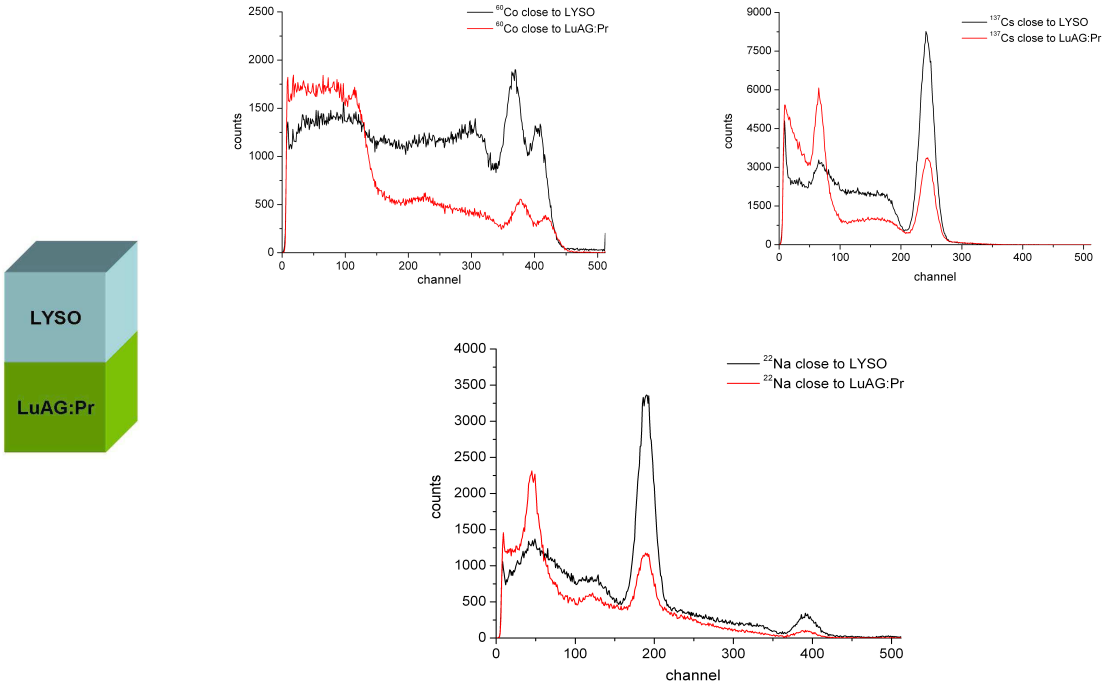

Fig. 5.13: *Histograms taken in the configuration (LuAG:Pr+LYSO).*

The second set of plots shows the results for phoswich configuration which set the LYSO coupled directly to the SiPM and the LuAG:Pr in the opposite side. All these histograms were obtaining during 200 seconds and the background was subtracted for each one (see figure 5.14).

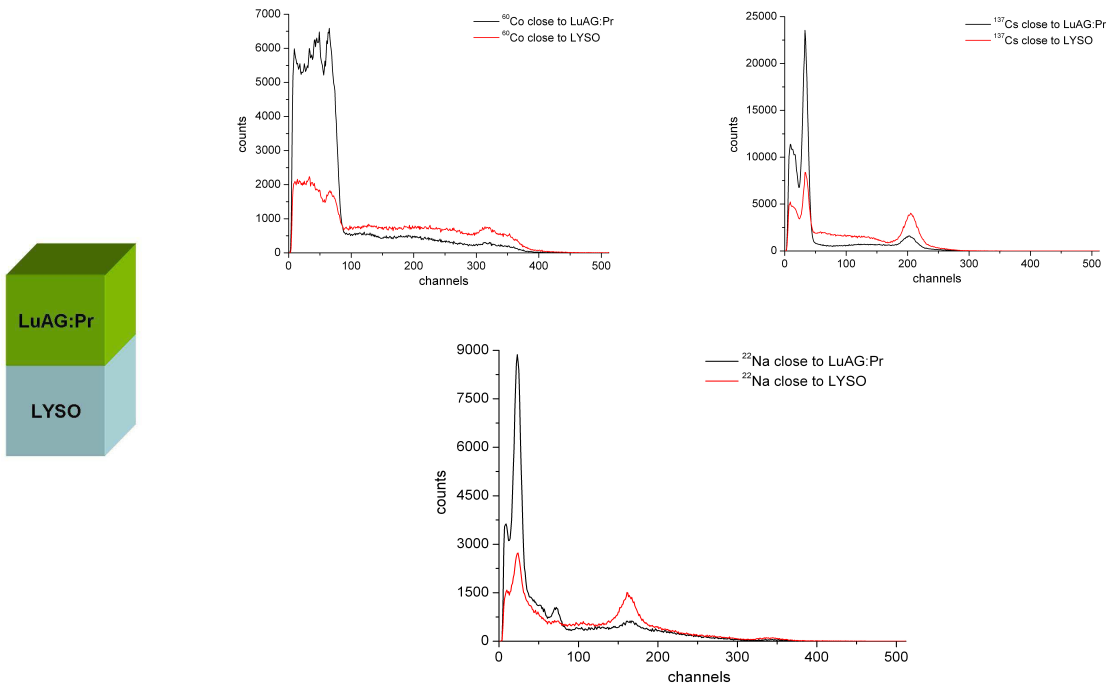

Fig. 5.14: *Histograms taken in the configuration (LYSO+LuAG:Pr)*

As we comment in the previous section, the best configuration is provided by the LuAG:Pr+LYSO phoswich.

5.5.3. Shape of the pulses

In order to explore the shape of the pulses provided by each crystal, an average of 20,000 normalized pulses was obtained. In figure 5.15 we plotted both spectra in logarithmic scale to show the slow component of the tails and to highlight the region where the pulses cross each other (around 90 ns).

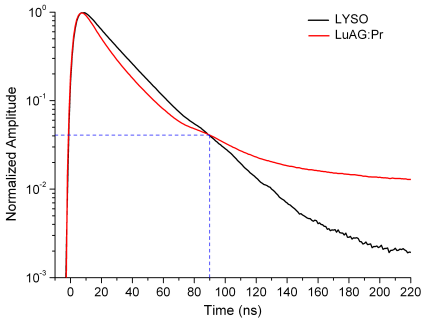

Fig. 5.15: *Average pulses for LYSO and LuAG:Pr crystals coupled to PMT.*

5.5.4. Phoswich Optimization

5.5.4.1 Results with PMT

Although we have tested several delays (from 0 to 75 ns), only four representative integration delays have been plotted in figure 5.16. The first two (top) delays prevent a separation of layers by a straight line, hence have been discarded. Bottom plots show a linearization of the layers. However the rightmost (40 ns) provides a blurred separation, while the remaining delay (30ns) allows setting a value to separate clearly two layers.

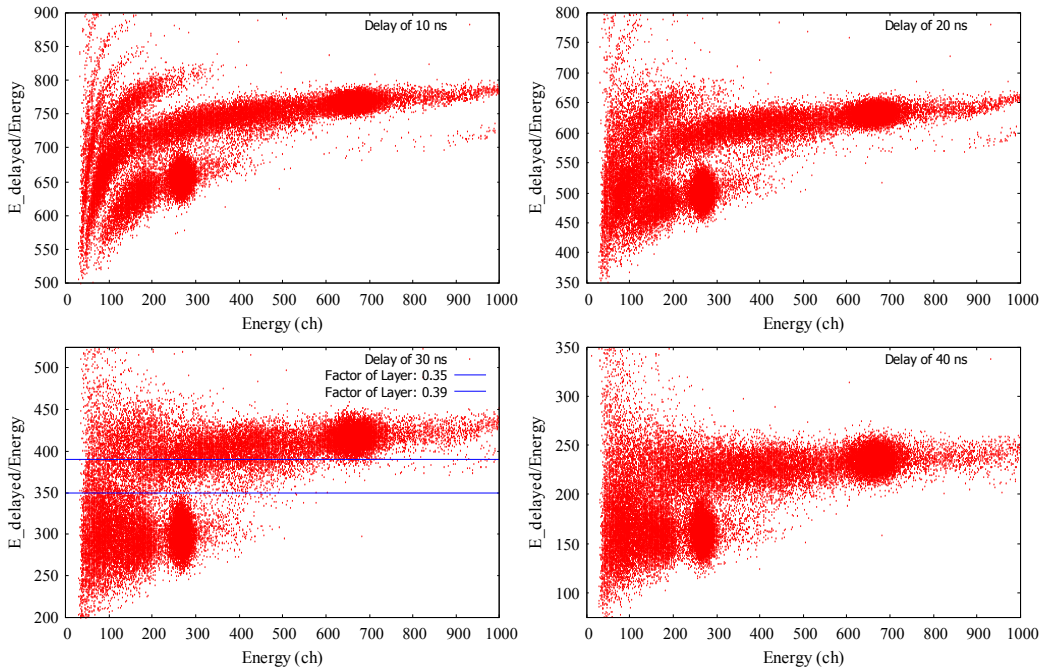

Fig. 5.16: *Phoswich diagrams for the LuAG:Pr+LYSO configuration coupled to the PMT.*

In the bottom-left plot in the figure 5.17 we have plotted the best delay value around 30 ns. We also drew two blue lines to depict the window of possible factors to separate the information which coming for each crystal. The optimum "Factor of Layer" or delayed integral to total integral ratio would be in the range from 0.35 to 0.39. Above it, LYSO interactions dominate. Below it, LuA:Pr are more abundant.

The next step is to use these factors to obtain energy spectra for separated layers. In our case we represent in the figures 5.18 and 5.19 the energy spectra of a monoenergetic source (662 keV-137Cs) from each crystal separated by different "Factors of Layer".

In the figure 5.18 are shown the results for a range of values as expected, the most reasonable set of separated spectra is obtained with a factor of 0.35.

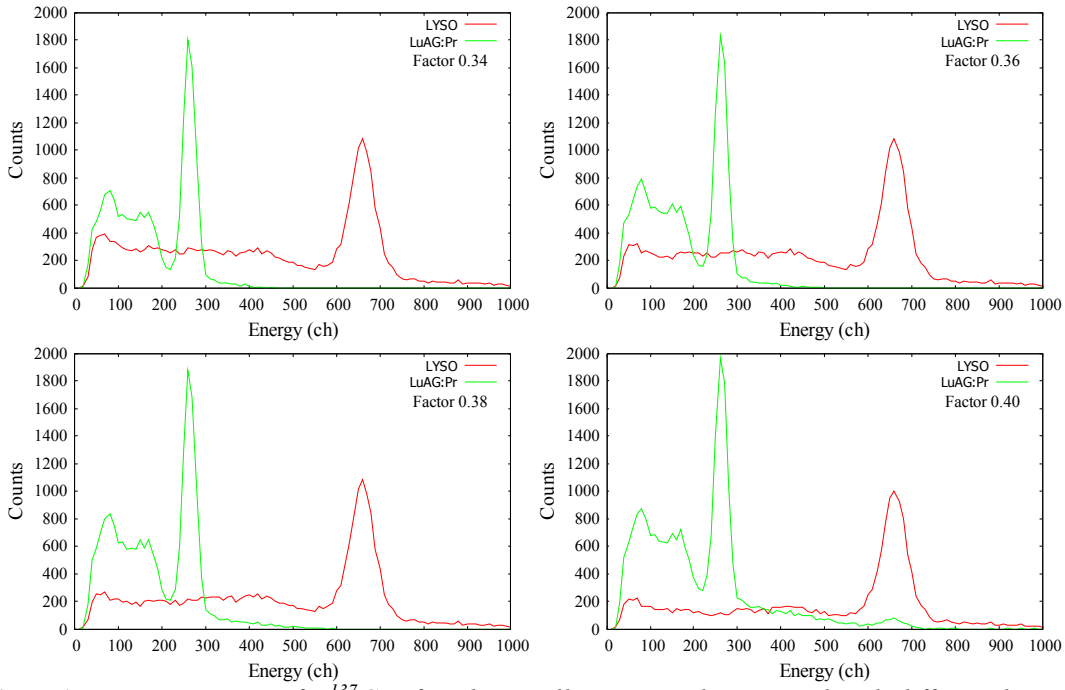

Fig. 5.17 *Energy spectra of a ^{137}Cs of each scintillator crystal separated with different limiting layer factors. The optimum separation is obtained at 0.35.*

1.5.4.1 Results for SiPM

In figure 5.18 some phoswich diagrams for four representative delay values are compared. As we mentioned before, the optimum delay has to provide two discernible layers, easily separable by a straight line. For the LuAG:Pr+LYSO configuration coupled to the SiPM, the best delay value is around 70 ns. Because these diagrams were re-scaled in order to stand out its distribution, the layer factors obtained have to be divided by 1000 (vertical scale factor). Hence, in the bottom-right plot we can see two blue lines which show the range of possible Factors of Layer: 0.055-0.075.

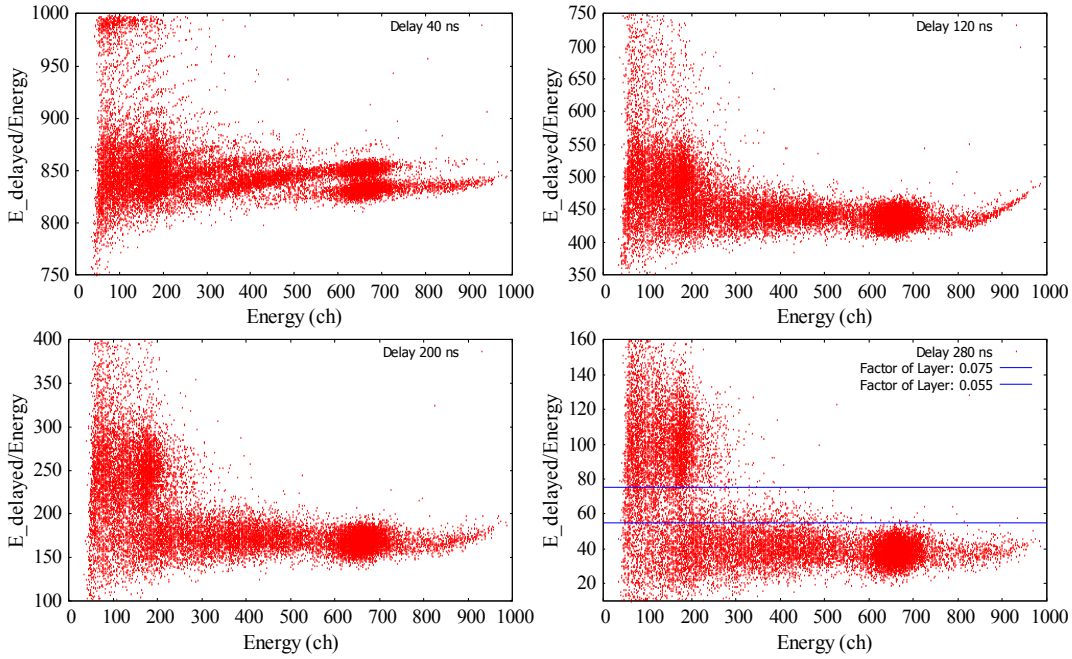

Fig. 5.18: *Phoswich diagrams for the LuAG:Pr+LYSO configuration coupled to the SiPM.*

Another possible representation to separate in layers the information provide by each crystal is to plot the Delay Integral (also called Charge Delayed Integral) in front of the Normal Integral (Total Charge of the pulse). For this type of graph, we have to optimize a angular separation between two oblique lines. Because we already know the best delay value (280 ns), we have plotted the diagram for these reference delay. In the figure 5.19 we have drew a straight line to show the two layers. The slope of this linear function is precisely the same what we have discovered by the previous representation.

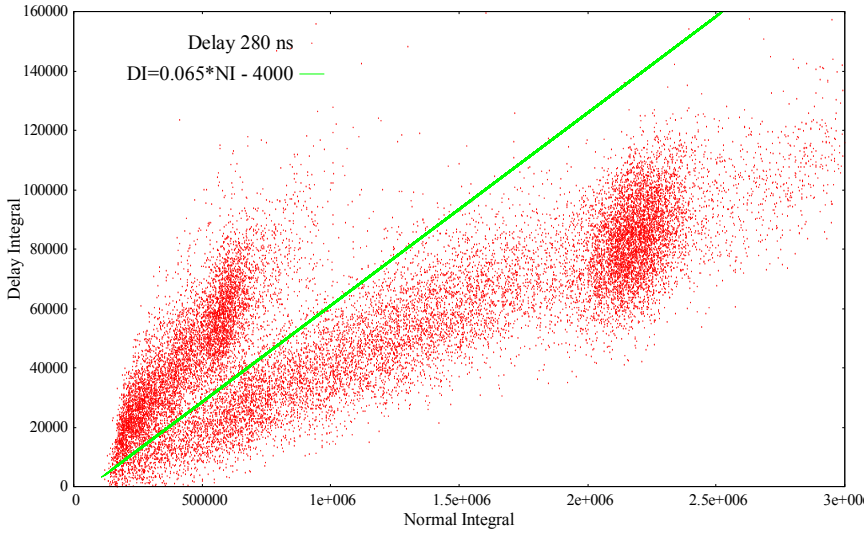

Fig. 5.19: *Phoswich diagrams for the LuAG:Pr+LYSO configuration coupled to the SiPM.*

In the figure 5.20 we have studied energy spectra for each layer, with different values of the limiting layer factor. One spectrum is provided by the LYSO (green) and the other for the LuAG:Pr (red). Besides we have explored several layer factors, the best delay have been obtained around of 0.065 (bottom-left plot).

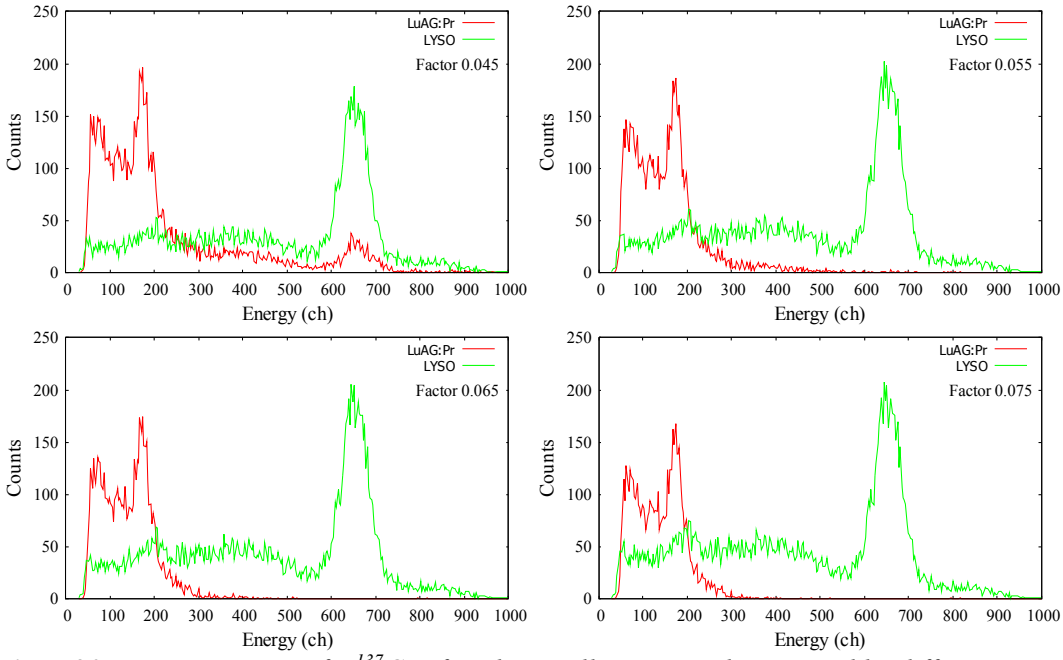

Fig. 5.20: *Energy spectra of a ^{137}Cs of each scintillator crystal separated by different Layer Factor. All the factors are in the range of 0.45 to 0.75. The optimum has to be around 0.065*

5.5.4.2 Summary of parameters

In the Table NN we summarize the parameters which allow us to separate the information from one crystal to the other for the LuAG:Pr+LYSO configuration.

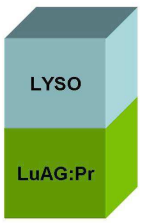

Photosensor	Delay (ns)	Limiting Layer Factor
PMT	30	0.35
SiPM	70	0.065

Table 5.6: *Summarize of the optimum parameters for the LuAG:Pr+LYSO phoswich configuration. These values were obtained through the Delayed Energy Method.*

Finally, we plot the separated and calibrated energy spectra for both scenarios: when the phoswich is coupled to the PMT (see figure 5.22) and to the SiPM (see figure 5.23). Also, we have normalized in order to have the main energy peaks with similar counts.

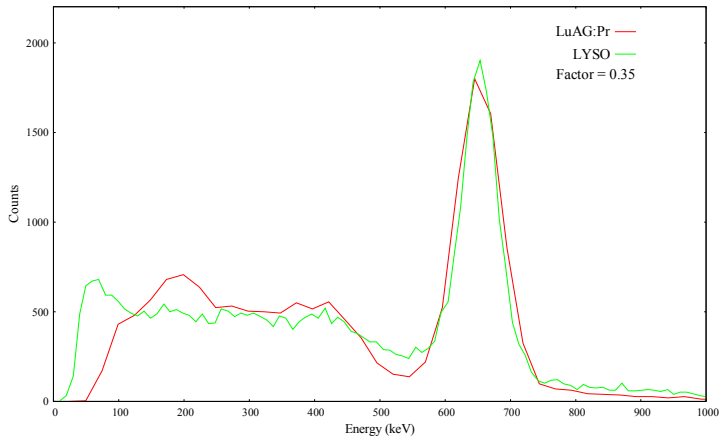

Fig. 5.21: *Separated and calibrated spectra for a LuAG:Pr+LYSO phoswich coupled to PMT.*

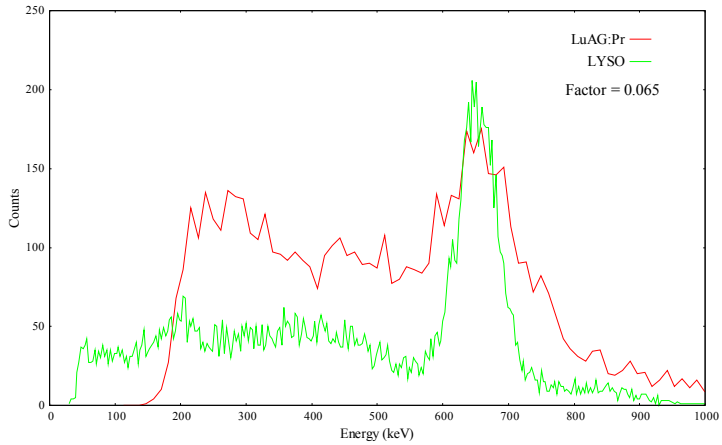

Fig. 5.22: *Separated and calibrated spectra for a LuAG:Pr+LYSO phoswich coupled to SiPM.*

5.6. Conclusions

We have characterized a new proposal of phoswich based on two high density scintillators crystals: LuAG:Pr and LYSO. Four configurations of the crystals were evaluated in order to set the best arrangement for a phoswich. The optimum configuration consists of the LuAG:Pr coupled directly to the photosensor, whether SiPM or PMT.

Furthermore, we have explored the energy response with some gamma point-like sources for the different configuration of the crystal: individually, side-by-side, LuAG:Pr+LYSO and LYSO+LuAG:Pr. By means of this energy spectra we have selected the configuration which requires the smaller dynamic range. In other words, we studied the configuration which provides the centroid ratio closer to unity for peaks with the same energy but coming from different crystals. In this case: Photodetector+LuAG:Pr+LYSO.

We have also written a program in Python which use Pyvisa libraries to control an Agilent oscilloscope and its functions as digitizer. After adjustment several acquisition parameters, we have digitized all the pulses at the same conditions (See table 5.1).

In addition, we have used the Delayed Charge Integration Method (or shortly Delayed

Energy Method) to estimate the optimum delay value of integration and the best limiting layer factor to separate pulses. Through the code that we have written in Fortran we found that when the phoswich is coupled to the PMT, the best separation of signal is reached with 40 ns of delay and 0.35 to distinguish between layers. And for the SiPM we estimate 70 ns of delays and 0.65 of factor.

Finally, after all these tests we have proven that this phoswich is viable. Although we only test a limited range of energy, the described properties become this phoswich in a promising tool for medical applications, for instance positron emission tomography (PET).

5.7. References

Agilent. 6000 Series Oscilloscopes Programmer's Reference. Version A.03.50.0000. URL: http://www.home.agilent.com/en/pd-565260-pn-DSO6104A/oscilloscope-1-ghz-4-channels?nid=-536902766.536905504&cc=US&lc=eng (2006).

Agilent. DSO6104A Oscilloscope. URL: http://www.home.agilent.com/en/pd-565260-pn-DSO6104A/oscilloscope-1-ghz-4-channels?nid=-536902766.536905504&cc=US&lc=eng (2012)

CAEN. Digital Pulse Processing in Nuclear Physics. 3th revision. Agust, 2011.

Chewpraditkul, W., Swiderski, L., Moszynski, M., Szczesniak, T., Syntfeld-Kazuch, A., Wanarak, C., Limsuwan, P. IEEE Transactions on Nuclear Science, 56 (6), Dec. (2009)

Derdzyan, M.V., Ovanesyan, K., Petrosyan, A., Belsky, A. Dujardin, C., Pedrini, C., Auffray, E., Lecoq, P., Lucchini, M., Pauwels, K. Journal of Crystal Growth 361 (2012) 212–216

Drozdowski, W., Dorenbos, P., Bos, A., Bizarri, G., Owens, A., Quarati, F., IEEE Transactions on Nuclear Science 55(3), 1391 (2008)

Fraile, L.M., Mach, H., Vedia, V., Olaizola, B., Picado, E., Paziy, V.,Udías, J.M., Nuclear Instruments and Methods in Physics Research A submitted (2012)

Haas, J.T.M., and Dorenbos, P. Advances in Yield Calibration of Scintillators. IEEE Trans Nucl Sci, 55:1086-1092, 2008.

Hamamatsu. MPPC. Multi-Pixel Photon Counter. September 2010.

Hamamatsu. Photomultiplier tube R5320. URL: http://www.hamamatsu.com/jp/en/R5320.html (2012)

Knoll, Glen. Radiation Detection and Measurement. Third Edition. New Jersey: John Wiley & Sons, Inc., 2000.

Leo, W.R. Techniques for Nuclear and Particles Physics Experiments. A How-to Approach. Second Revised Edition. Berlin: Springer-Verlag, 1994.

Lewellen, T.K., Physics in Medicine and Biology 53(17), R287 (2008). URL: http://stacks.iop.org/0031-9155/53/i=17/a=R01

Mares, J.A., Beitlerova, A., Nikl, M., Solovieva, N., D'Ambrosio, C., Blazek, K., Maly, P., Nejezchleb, K., de Notaristefani, F. Scintillation response of Ce-doped or intrinsic scintillating crystals in the range up to 1 MeV. Radiation Measurements, 38:353-357, 2004. (LuAG:Pr)

Novotny, R., Doring, W., Hejny, V., Kotulla, M., Krusche, B., Metag, V., Nold, M., Stroher, H., Wolf, M. A plastic-BaF2 phoswich telescope for charged/neutral particle and photon detection. Nuclear Science, IEEE Transactions on. Vol. 43, 3 (1996) DOI: 10.1109/23.506674

Yao, R., Ma, T., Shao, Y. IEEE Nuclear Science Symposium. 4497-4502. Nov. (2007)

6. General Conclusions

The detection of gamma photons is a technique in continuous evolution and with an ever growing range of applications. In this thesis we deal with state of the art detectors and techniques in gamma detection and explore a number of new technological solutions, either by the use of new scintillator materials, new photosensors or a combination of both. As mentioned in the introduction, the knowledge gained during this research will be applied in the development of FAMITA, a new fast timing gamma spectroscopy instrument, and in the design of improved detector modules for PET and ToF PET.

Specific conclusions of this PhD are:

6.1. For HPGe detector

The system developed to refill the Dewar of the HPGe with LN2 worked fine. Basically a boiling system was created in order to drive the LN2 from a portable-Dewar to Fix-Dewar where is located the HPGe. The system demonstrated itself as a cheap and efficient method of transfer LN2 with negligible losses. Optimal shaping and peaking times and resulting dead time of the electronics of the HPGe are determined. Shaping time was fixed at 1 μs in the amplifier and the Peaking Time was set at 5 μs for the MCA. The Dead Time was associated to a function to correct the results taken in Live Time mode.

The HPGe shows a very good linear response in energy in the range explored. The resolution and linearity presents a quite linear behaviour. Simple linear relationships for resolution and energy versus channel were enough for our HPGe detector.

We also determined that the Lead castle reduces the rate of counts from the background. However, in the other hand, if the sample emits gammas with enough energy to excite the Lead, then the shielding could release some X-rays. As consequence of this effect some extra peaks appears in the spectra. Thus to characterize samples in the range of 70-80 keV we have to be careful and consider this fluorescence effect from the shielding. Also, the backscatter from the lead castle would be considerable.

It was possible to obtain absolute efficiency for our HPGe. At low energy a quadratic curve was used to fit the data from 30 to 244.7 keV and for the High Energy interval we have used a linear fitting from 244.7 to 1408 keV. Both functions overlap reasonably in the overlapping energy region. Absolute calibrations with accuracy better than 10% were possible to obtain.

6.2. For LuAG:Pr detector

LuAG:Pr crystal was found as a good alternative to LSO and LYSO in PET, with an energy resolution of 5.1% and a time resolution of 238 ± 2 ps at 511 keV. For ^{60}Co energies the time resolution at -1940V was optimized in 147 ± 2 ps. The internal activity was found as much as compared to 215 ± 20 Bq/cm^3 estimated theoretically, including self-absorption. Our

empirical calculation provided a concentration of 215 ± 30 Bq/cm^3 of ^{176}Lu. The crystal, coupled to the PMT, shows a very good linear response to energy in the range of 122 to 1408 keV.

These results for the new formula would make LuAG:Pr a promising candidate for use as fast timing scintillator, but nonetheless its strong internal activity due to lutetium may hamper its use in low count rate experiments. However, for high activity scenarios like PET, this crystal would be useful not only as direct detector (to form arrays), but as phoswich constituent.

6.3. For $CeBr_3$ detector

$CeBr_3$ crystal provided excellent properties to substitute the conventional NaI:Tl in almost all enforcements scenarios. When a 1'x1' cylindrical crystal was coupled to the R9779 PMT at 1330V, we obtained the very good energy and time responses. For instance, at 511 keV the energy resolution was 5.5% and the time resolution (~$E^{-1/2}$) was 164 ± 2 ps. Also, we fit successfully the energy resolution to a polynomial expression and obtained the very first absolute efficiency fitting for this crystal in the range from 31.61 to 1408 keV at three distances.

The radiopurity of a CeBr3 crystal was studied in an underground facility. Our research was performed for a 30x30 mm cylindrical crystal and its housing. The main results evidence the presence of Radium and Thorium chains but not from Actinides chains. Also, we found contamination traces of ^{138}La due to chemical affinity but not neutron activation products as ^{82}Br or ^{139}Ce.

In conclusion we have proven that $CeBr_3$ is a very promising candidate for a range of applications. The energy resolution is among the best for inorganic scintillators, with 5% measured at 662 keV with fast PMTs. The efficiency is good and comparable to the $LaBr_3$:Ce. The time response is extremely good. Lastly, the radiopurity of the crystal makes it competitive for low counting requiring. Even, the radiopurity can be further improved by requiring radiopure aluminium housing.

6.4. For Phoswich detector

The new scintillators evaluated LuAG:Pr and $CeBr_3$BrCe exhibit interesting properties. $CeBr_3$ would be an alternative to $LaBr_3$:Ce for fast timing applications and for improved energy resolution gamma spectroscopy. LuAG:Pr would substitute with advantage LYSO and LSO in PET scanners, thanks to its improved energy resolution and shorter decay time properties, which would allow for faster count rates in PET scanners. It may be even considered as the scintillator of choice for Time of Flight PET scanners, thanks to its improved timing properties over LYSO. LuAG:Pr may be even be considered for fast-timing applications. The LYSO+LuAG:Pr combination has been shown to perform adequately, allowing for layer identification, when read both by PMTs and, more interestingly, by SiPM. New PET detectors are increasingly being made with SiPM read-out, owing to the PET-MRI multimodality scanners being developed. This dual layer combination outperforms phoswich arrangements being employed in commercial PET scanners. The Delayed Charge Integration Method (or shortly Delayed Energy Method) estimated optimum delay value of integration and the best limiting layer factor to separate pulses. When the phoswich is coupled to the

PMT, the best separation of layer is reached with 40 ns of delay and a 0.35 ratio to distinguish layers. And for the SiPM we estimate 70 ns of delay and 0.065 of ratio delayed/total energy. In the SiPM case, the shape of the pulse is dominated by the preamplifier and not by the intrinsic pulse shape.

7. Publications Derived from this Thesis

Papers Published in International Journals

L.M. Fraile, H. Mach, **E. Picado**, V. Vedia, J.M. Udías. Study of the time response of a LuAG(Pr) crystal for fast timing applications. NIM A 713, 27-32 (2013).

L.M. Fraile, H. Mach, V. Vedia, B. Olaizola, V. Paziy, **E. Picado**, J.M. Udías. Fast timing study of a $CeBr_3$ crystal: Time resolution below 120 ps at ^{60}Co energies. NIM A 701, 235-242 (2013).

Papers Submitted to International Journals

L.M. Fraile, J.M. Udías, P.M.G. Corzo, J. Cal-Gonzalez, S. España, J.L. Herraiz, E. Herranz, **E. Picado**, E. Vicente, A. Muñoz-Martín and J.J. Vaquero. PET imaging with gallium radioisotopes produced by a low energy proton beam. Submitted to *Journal of Instrumentation* (JINST). Received: 2013-03-07 02:08:01.0

Conference Proceedings

B. Olaizola, L.M. Fraile, H. Mach, J.A. Briz, J. Cal-Gonzalez, D. Ghita, U. Köster, W. Kurcewicz, S. Lesher, D. Pauwels, **E. Picado**, D. Radulov, G. Simpson, J.M. Udias. Fast timing study of n-rich Fe nuclei populated in the beta-decay of Mn-65. Oral presentation. 2nd European Nuclear Physics Conference (EuNPC2012) . La Rábida, Huelva, España. 17 al 21 Septiembre 2012.

B. Olaizola, L.M. Fraile, H. Mach, J.A. Briz, J. Cal-Gonzalez, D. Ghita, U. Köster, W. Kurcewicz, S. Lesher, D. Pauwels, **E. Picado**, D. Radulov, G. Simpson, J.M. Udias. Fast timing study of n-rich Fe nuclei populated in the beta-decay of Mn-65. Oral presentation. Congress: Encuentros de Física Nuclear 2012. La Rábida, Huelva, España. 14 al 16 Septiembre 2012.

L.M. Fraile, H., Mach, B., Olaizola, V., Paziy, **E. Picado**, J.J., Sanchez, J.M., Udías, J.J., Vaquero, V., Vedia in Nuclear Science Symposium Conference Record, 2011. NSS '11. IEEE (2011), pp. 72 -74

P.M.G. Corzo, J. Cal-Gonzalez, **E. Picado**, S. España, J.L. Herraiz, E. Herranz, E. Vicente, J.M. Udias, J.J. Vaquero, A. Munoz-Martin and L.M. Fraile. *Measurement of Activity Produced by Low Energy Proton Beam in Metals Using off-Line PET Imaging.* Conference: IEEE Nuclear Science Symposium & Medical Imaging Conference. Publication: IEEE NSS-MIC 2011 Conference Record. Valencia, Spain. October 2011.

E. Picado, L.M. Fraile, V. Paziy, B. Olaizola, J.J. Vaquero, J. M. Udías. Comparison of Time and Energy Responses using PMT and SIPM. XXXIII Bienal de Física. Publication: ISBN 978-84-86116-41-5. Santander, Spain, September 2011.

B. Olaizola, L.M. Fraile, H. Mach, J.A. Briz, J. Cal-Gonzalez, D. Ghita, W. Kurcewicz, S. Lesher, D. Pauwels, **E. Picado**, D. Radulov, J.M. Udias. Fast timing studies below Ni-78 . Oral Presentation. ARIS-2011. Leuven, Belgium. 29 Mayo al 3 Junio 2011.

P.M.G. Corzo, J. Cal-Gonzalez, **E. Picado**, S. España, J.L. Herraiz, E. Herranz, E. Vicente, J.M. Udias, J.J. Vaquero, A. Munoz-Martin and L.M. Fraile. Measurement of Activity Produced by Low Energy Proton Beam in Metals Using off-Line PET Imaging. XXXIII Bienal de Física. Publication: ISBN 978-84-86116-41-5. Santander, Spain, September 2011.

B. Olaizola, L.M. Fraile, H. Mach, J.A. Briz, J. Cal-Gonzalez, D. Ghita, W. Kurcewicz, S. Lesher, D. Pauwels, **E. Picado**, D. Radulov, J.M. Udias. Fast timing study of n-rich Fe nuclei populated in the beta-decay of Mn. Poster. Tenth Exotic Beam Summer School 2011. Michigan State University, East Lansing, E.E.U.U. 25 al 30 Julio 2011

Vaquero, E. Picado, S. España, J. Cal-González, L.M. Fraile, J.L. Herraiz, E. Vicente, M. Desco, J.M. Udías. Viavilidad del uso de fotodetectores SiPM en sistemas PET/IRM. Oral Presentation. Conference: CASEIB 2010. Madrid, Spain. November 2010.

B. Olaizola, L.M. Fraile, H. Mach, J.A. Briz, J. Cal-Gonzalez, D. Ghita, W. Kurcewicz, S. Lesher, D. Pauwels, **E. Picado**, D. Radulov, J.M. Udias. Fast-timing study of n-rich Fe nuclei populated in the beta-decay of Mn. Libro: XIII Reunión Bienal de la Real Sociedad Española de Física 2010 (ISBN: 978-84-86116-41-5)

S. España; J. Cal-González; L. M. Fraile; **E. Picado**; J. L. Herraiz; E. Vicente; J. M. Udías; M. Desco; J.J. Vaquero. Performance Evaluation of SiPM Photosensor in the Presence of Magnetic Fields. Clave: A. AIP Conference Proceedings. Apr. 2010. Vol. 1. (171-172)

P.M.G. Corzo, **E. Picado**, J. Cal-González, S. España, E. Vicente, E. Herranz, L.M. Fraile, J.J. Vaquero, J.M. Udías, A. Muñoz. Off-line PET Study of Proton Beam Activated Metals. Oral Presentation. Conference: International Workshop on bio-medical applications of micro-PET. Seville, Spain. September, 2010.

S. España; J. Cal-González; G. Tapias, L. M. Fraile; **E. Picado**; J. M. Udías; M. Desco; J.J. Vaquero. Caracterización de Fotomultiplicadores de silicio para su uso en Escáneres PET en presencia de campos magnéticos. Conference Proceedings in XXXII Bienal de Física. Jul. 2009. Vol. 1 (460-462)

S. España, J. Cal-González, G. Tapias, L.M. Fraile, **E. Picado**, J.L. Herraiz, J.M. Udías, M. Desco, J.J. Vaquero. Performance Evaluation of SiPM Photosensor in the Presence of Magnetic Fields. Oral Presentation. Conference: XXXII Bienal de Física. Publication: ISBN 978-84-692-4956-7. Ciudad Real, Spain. September, 2009.

S. España, J. Cal-González, G. Tapias, L.M. Fraile, **E. Picado**, J.L. Herraiz, J.M. Udías, M. Desco, J.J. Vaquero. Performance Evaluation of SiPM Photosensors for PET Imaging in

the Presence of Magnetic Fields. Oral Presentation. International Scientific Meeting on Nuclear Physics: La Rábida 09. Publication: ISBN 978-0-7354-0776-3. Huelva, Spain. July 2009.

8. Summary

8.1. Introduction

Gamma spectroscopy is a very useful tool, with an established tradition of decades, and with an increasing number of applications. It is based on gamma interaction with matter and the applications range from atomic, molecular, nuclear and high energy physics to medical physics, homeland security, material sciences, cultural heritage studies, geosciences, etc.

There are various materials that can be used to detect gamma to radiation, with specific dosimetric and spectroscopic properties. Some of these, particularly some very recently introduced in the market and that will be reviewed almost for the first time, will be studied in this PhD. work.

In this work we characterize three new gamma ray detectors in order to explore its properties and to try to define their viability as candidates for several measurements scenarios. In addition, we will characterize a standard HPGe and lead cage, which will be employed for low activity gamma measurements such as to estimate internal activity of scintillator crystals and also calibrated point-like gamma sources.

In this thesis we will study several devices employed for gamma spectroscopy. Beginning with an HPGe detector that will be used as energy reference, to measure internal activity and to compare efficiency, with the other detectors studied in this thesis. Further, two new inorganic materials recently introduced in the market, a high-Z lutetium based scintillator, and a halide one, CeBr3, similar to LaBr3:Ce, will be studied for efficiency, energy resolution and timing properties.

Finally, we would assess the possibility of combining two dissimilar scintillators optically coupled to a single photomultiplier, either SiPM or PMT, what is often called a phoswich detector. The crystals for the phoswich detectors are chosen to have different decay times so that the shape of the output pulse depends on the relative contribution of scintillation light from the two scintillators. Most applications involve the use of this pulse shape difference to distinguish events that have occurred in only one scintillator from those that occur in both, or events that take place in one layer against events that take place in another [Knoll, 2000].

8.2. Goals of this thesis

The Nuclear Physics Group of Complutense University (GFN-UCM) is actively engaged in the development of new gamma detectors, with improved energy resolution, timing properties, stopping power or all of them altogether. These are needed on one side due to the commitment of the group to the development of FATIMA (Fast Timing Array, (http://nuclear.fis.ucm.es/fasttiming), coordinated by Luis Mario Fraile and funded within NUPNET. The goal of FATIMA is to design a new modular high-efficiency FAst TIMing array designed for measurements with the ultra fast timing method using fast response

scintillation detectors, to measure level lifetimes in the range from a few picoseconds to several nanoseconds [Mach, H., *et al.*, 1989, Mach, H., *et al.*, 1991]. Thus a large part of the activity presented in this thesis are aimed toward the test of new scintillator and photodetectors that can be used for fast timing with improved in the existing ones, either in price, performance or both. To this end, the recently available $CeBr_3$ scintillator was tested and fully characterised [Fraile, L.M., *et al.*, 2013 (1), Fraile, L.M., *et al.*, 2013 (2), Fraile, L.M., *et al.*, 2011, Corzo, P.M.G., *et al.*, 2010, Vaquero, J.J., *et al.*, 2010]. Also related to the fast timing measurements agenda of the GFN-UCM were the characterization for timing, efficiency and energy resolution of the very newly introduced LuAG:Pr scintillator. Not only this scintillator has a high stopping power, similar to BGO, but its energy resolution is very interesting and, further and not so well established in the literature previous to our work, its timing properties make this scintillator a very promising alternative for fast timing measurements where the internal activity is not a drawback.

The GFN-UCM is also heavily involved in the development of new detectors for Positron Emission Tomography imaging [PhD thesis: Vicente, E., 2012; Abushap, K., 2012, España, S., 2009 and papers: Fraile, L.M., *et al.,* 2012, Corzo, P.M.G., *et al.*, 2010]. This includes the evaluation of new scintillators with improved timing capabilities for their use as PET detectors with time of flight capabilities, a technology which enables PET images of quality (spatial resolution, quantification properties, signal to noise ratio) not achievable in common PET scanners. For this application, the LuAG:Pr scintillator may prove very useful, depending on the results of its characterization. Thus, a second part of this thesis work pertains the evaluation of LuAG:Pr and to assess its suitability for PET applications, including its suitability to be mounted in phoswich arrangements.

8.3. Structure of the thesis

After a brief general introduction in the chapter 1, chapter 2 presents the characterization of an HPGe detector. An empirical expression for the full energy photo-peak efficiency in terms of gamma-ray energy (E) and the vertical distance from the detector surface (d) has been obtained for a high pure germanium detector (HPGe) using a 5% absolutely calibrated ^{152}Eu sources. Through this semiempirical formula the internal activity of scintillator crystals and point-like gamma sources was calibrated.

In chapter 3 we present a complete characterization of a novel LuAG:Pr crystal. Here we report measurements performed using a small crystal cube of 1 cm^3 coupled to a Hamamatsu R5320 photomultiplier tube. We study the energy resolution and linearity, together with the time response at ^{22}Na and ^{60}Co energies. In addition, we estimate the internal activity of ^{176}Lu by gamma ray spectrometry with an HPGe detector and from theoretical estimates.

Chapter 4 contains a complete characterization of a novel inorganic scintillator $CeBr_3$. Several measurements are performed using a $CeBr_3$ cylindrical crystal of 1-inch in height and 1-inch in diameter, at ^{22}Na and ^{60}Co photon energies for timing and ^{137}Cs, ^{152}Eu and ^{133}Ba sources for energy resolution and linearity. Moreover, we estimate the absolutely efficiency of the crystal with absolutely calibrated gamma sources positioned at 5, 15 and 25 cm in front of the entrance face of the detector. Furthermore, we study the radiopurity of the crystal in an ultra-low level underground facility located in LSC, Spanish Pyrenees.

In chapter 5 we study a new phoswich configuration based on two continuous high

density inorganic crystals: LYSO and LuAG:Pr. We explore the energy response and pulse shape for several crystal arrangements in order to identify the optimum configuration. We digitize the pulse with a high speed oscilloscope using a Python code developed in the group, with a large commitment from this PhD candidate. In addition, we search the best for Delayed Energy Method parameters to disentangle phoswich layers (delay and layer factors).

At the end of this manuscript we present the general conclusions of this thesis and the scientific communications derived from the work presented here.

8.4. General conclusions

The detection of gamma photons is a technique in continuous evolution and with an ever growing range of applications. In this thesis we deal with state of the art detectors and techniques in gamma detection and explore a number of new technological solutions, either by the use of new scintillator materials, new photosensors or a combination of both. As mentioned in the introduction, the knowledge gained during this research will be applied in the development of FAMITA, a new fast timing gamma spectroscopy instrument, and in the design of improved detector modules for PET and ToF PET.

Specific conclusions of this PhD are:

For HPGe detector – chapter 2:

The system developed to refill the Dewar of the HPGe with LN2 worked fine. Basically a boiling system was created in order to drive the LN2 from a portable-Dewar to Fix-Dewar where is located the HPGe. The system demonstrated itself as a cheap and efficient method of transfer LN2 with negligible losses. Optimal shaping and peaking times and resulting dead time of the electronics of the HPGe are determined. Shaping time was fixed at 1 μs in the amplifier and the Peaking Time was set at 5 μs seconds for the MCA. The Dead Time was associated to a function to correct the results taken in Live Time mode.

The HPGe shows a very good linear response in energy in the range explored. The resolution and linearity presents a quite linear behaviour. Simple linear relationships for resolution and energy versus channel were enough for our HPGe detector.

We also determined that the Lead castle reduces the rate of counts from the background. However, in the other hand, if the sample emits gammas with enough energy to excite the Lead, then the shielding could release some X-rays. As consequence of this effect some extra peaks appears in the spectra. Thus to characterize samples in the range of 70-80 keV we have to be careful and consider this fluorescence effect from the shielding. Also, the backscatter from the lead castle would be considerable.

It was possible to obtain absolute efficiency for our HPGe. At low energy a quadratic curve was used to fit the data from 30 to 244.7 keV and for the High Energy interval we have used a linear fitting from 244.7 to 1408 keV. Both functions overlap reasonably in the overlapping energy region. Absolute calibrations with accuracy better than 10% were possible to obtain.

For the LuAG:Pr detector – chapter 3:

LuAG:Pr crystal was found as a good alternative to LSO and LYSO in PET, with an energy resolution of 5.1% and a time resolution of 238 ± 2 ps at 511 keV. For ^{60}Co energies

the time resolution at -1940V was optimized in 147 ± 2 ps. The internal activity was found as much as compared to 215 ± 20 Bq/cm^3 estimated theoretically, including self-absorption. Our empirical calculation provided a concentration of 215 ± 30 Bq/cm^3 of ^{176}Lu. The crystal, coupled to the PMT, shows a very good linear response to energy in the range of 122 to 1408 keV.

These results for the new formula would make LuAG:Pr a promising candidate for use as fast timing scintillator, but nonetheless its strong internal activity due to lutetium may hamper its use in low count rate experiments. However, for high activity scenarios like PET, this crystal would be useful not only as direct detector (to form arrays), but as phoswich constituent.

For the $CeBr_3$ detector – chapter 4:

$CeBr_3$ crystal provided excellent properties to substitute the conventional NaI:Tl in almost all enforcements scenarios. When a 1'x1' cylindrical crystal was coupled to the R9779 PMT at 1330V, we obtained the very good energy and time responses. For instance, at 511 keV the energy resolution was 5.5% and the time resolution (~$E^{-1/2}$) was 164 ± 2 ps. Also, we fit successfully the energy resolution to a polynomial expression and obtained the very first absolute efficiency fitting for this crystal in the range from 31.61 to 1408 keV at three distances.

The radiopurity of a CeBr3 crystal was studied in an underground facility. Our research was performed for a 30x30 mm cylindrical crystal and its housing. The main results evidence the presence of Radium and Thorium chains but not from Actinides chains. Also, we found contamination traces of ^{138}La due to chemical affinity but not neutron activation products as ^{82}Br or ^{139}Ce.

In conclusion we have proven that $CeBr_3$ is a very promising candidate for a range of applications. The energy resolution is among the best for inorganic scintillators, with 5% measured at 662 keV with fast PMTs. The efficiency is good and comparable to the $LaBr_3$:Ce. The time response is extremely good. Lastly, the radiopurity of the crystal makes it competitive for low counting requiring. Even, the radiopurity can be further improved by requiring radiopure aluminium housing.

For the Phoswich detector – chapter 5:

The new scintillators evaluated LuAG:Pr and $CeBr_3$BrCe exhibit interesting properties. $CeBr_3$ would be an alternative to $LaBr_3$:Ce for fast timing applications and for improved energy resolution gamma spectroscopy. LuAG:Pr would substitute with advantage LYSO and LSO in PET scanners, thanks to its improved energy resolution and shorter decay time properties, which would allow for faster count rates in PET scanners. It may be even considered as the scintillator of choice for Time of Flight PET scanners, thanks to its improved timing properties over LYSO. LuAG:Pr may be even be considered for fast-timing applications. The LYSO+LuAG:Pr combination has been shown to perform adequately, allowing for layer identification, when read both by PMTs and, more interestingly, by SiPM. New PET detectors are increasingly being made with SiPM read-out, owing to the PET-MRI multimodality scanners being developed. This dual layer combination outperforms phoswich arrangements being employed in commercial PET scanners. The Delayed Charge Integration Method (or shortly Delayed Energy Method) estimated optimum delay value of integration and the best limiting layer factor to separate pulses. When the phoswich is coupled to the PMT, the best separation of layer is reached with 40 ns of delay and a 0.35 ratio to distinguish layers. And for the SiPM we estimate 70 ns of delay and 0.065 of ratio

delayed/total energy. In the SiPM case, the shape of the pulse is dominated by the preamplifier and not by the intrinsic pulse shape.

References

Abushab, Khaled. (2012). Simulation and Image Reconstruction of Clinical TOF-PET Scanners. (PhD thesis) Departamento de Física Atómica, Molecular y Nuclear. Universidad Complutense.

Attix, F. Introduction to Radiological Physics and Radiation Dosimetry. United States of America: John Wiley & Sons, Inc, 2004.

Cooper, P.N: Introduction to Nuclear Radiation Detectors. Cambridge: Cambridge University Press, 2011.

Corzo, P.M.G., Cal-González, J., Picado, E., España, S., Vicente, E., Herranz, E. Fraile, L.M., Vaquero, J.J., Udías, J.M., Muñoz, A. Off-line PET Study of Proton Beam Activated Metals. Oral Presentation. International Workshop on bio-medical applications of micro-PET. (2010) Seville, Spain.

Corzo, P.M.G., Cal-Gonzalez, J., Picado, E., España, S., Herraiz, J.L., Herranz, E., Vicente, E., Udias, J.M., Vaquero, J.J.. Munoz-Martin A., Fraile, L.M. Measurement of Activity Produced by Low Energy Proton Beam in Metals Using off-Line PET Imaging. IEEE Nuclear Science Symposium & Medical Imaging Conference. IEEE NSS-MIC (2011) Conference Record, Valencia, Spain.

España, S. (2009). Simulaciones avanzadas aplicadas al diseño de escáneres y mejora de la calidad de imagen en tomografía por emisión de positrones. (PhD thesis) Departamento de Física Atómica, Molecular y Nuclear. Universidad Complutense.

Fraile, L.M., Mach, H., Vedia, V., Olaizola, B., Picado, E., Paziy, V.,Udías, J.M., Nuclear Instruments and Methods in Physics Research A (701), 235-242 (2013) DOI: 10.1016/j.nima.2012.11.009

Fraile, L.M., Mach, H., Picado, E., Vedia, V., Udías, J.M. in Nuclear Instruments and Methods in Physics Research A (713), 27-32 (2013) DOI: 10.1016/j.nima.2013.02.015

Fraile, L.M., Mach, H., Olaizola, B., Paziy, V., Picado, E., Sanchez, J.J., Udías, J.M., Vaquero, J.J., Vedia, V., in Nuclear Science Symposium Conference Record, 2011. NSS '11. IEEE (2011), pp. 72 -74. DOI: 10.1109/NSSMIC.2011.6154403

Knoll, Glen. Radiation Detection and Measurement. Third Edition. New Jersey: John Wiley & Sons, Inc., 2000.

Leo, W.R. Techniques for Nuclear and Particles Physics Experiments. A How-to Approach. Second Revised Edition. Berlin: Springer-Verlag, 1994.

Mach, H., Gill, R.L., Moszynski, M., Nuclear Instruments and Methods in Physics Research A 280, 49 (1989)

Mach, H., Wohn, F., Molnar, G., Sistemich, K., Hill, J.C., Moszynski, M., Gill, R., Krips, W., Brenner, D. Nuclear Physics A 523, 197 (1991)

Shah, K.S., Glodo, J., Higgins, W., Van Loef, E.V., Moses, W.W., Derenzo, S.E., Weber, M.J., IEEE Transactions on Nuclear Science 52(6), 3157 (2005)

Vaquero, J.J., España, S., Picado, E., Cal-González, J., Fraile, L.M., Herraiz, J.L., Vicente, E., Desco, M., Udías, J.M. Viavilidad del uso de fotodetectores SiPM en sistemas PET/IRM. Oral Presentation. CASEIB (2010) Madrid, Spain.

Vicente Torrico, E. (2012). Caracterización, Mejora y Diseño de Escáneres PET Preclínicos. (PhD thesis) Departamento de Física Atómica, Molecular y Nuclear. Universidad Complutense.

9. Resumen en Castellano

9.1. Introducción

La espectrometría gamma es una herramienta bastante útil desde hace varias décadas cuyo rango de aplicaciones sigue en crecimiento. Se basa en la interacción de rayos gamma con la materia y sus aplicaciones van desde física atómica, molecular, nuclear y altas energías hasta física médica, seguridad nacional, ciencia de materiales, ciencias del patrimonio, geociencias, etc.

Existen varios materiales con propiedades dosimétricas y espectroscópicas adecuadas que pueden ser usados para detectar la radiación gamma. Algunos de ellos son de muy reciente aparición en el mercado. En este trabajo vamos a caracterizar tres nuevos detectores gamma con el fin de explorar sus propiedades y tratar de definir su viabilidad como candidatos en distintos escenarios de medición. Además, vamos a caracterizar un detector hyperpuro de Germanio (HPGe) así como su blindaje.

En particular vamos a caracterizar tres cristales centelladores inorgánicos: CeBr3, LuAG:Pr y un arreglo phoswich de LYSO+LuAG:Pr. Todos van a ser sometidos a pruebas mientras están acoplados a dos tipos de fotosensores: tubos fotomultiplicadores (PMT) y fotomultiplicadores de Silicio (SiPM).

9.1.1. Objetivos de esta tesis

El Grupo de Física Nuclear de la Universidad Complutense (GFN-UCM) participa activamente en el desarrollo de nuevos detectores de radiación con mayores prestaciones, es especial que tengan mejores respuesta temporal y energética. La búsqueda de estas mejoras en los detectores actualmente disponibles se debe, por un lado, al compromiso del grupo para el desarrollo de FATIMA (FAst TIMing Array, http://nuclear.fis.ucm.es/fasttiming), coordinado por Luis Mario Fraile y financiado dentro NUPNET. El objetivo de FATIMA es el diseño de un nuevo sistema modular de medición con alta eficiencia para medidas de "*Ultra Fast Timing Method*" usando detectores de centelleo de rápida respuesta temporal. Este instrumento servirá para medir vida media de niveles nucleares en el rango de unos pocos picosegundos hasta varios nanosegundos [Mach, H., *et al.*, 1989, Mach, H., *et al.*, 1991].

De esta forma gran parte de la actividad presentada en esta tesis podrá ser incorporada en el proyecto FATIMA con el fin de mejorar la actual arquitectura. Para este fin, el recientemente disponible centellador de $CeBr_3$ fue probado y totalmente caracterizado [Fraile, L.M., *et al.*, 2013 (1), Fraile, L.M., *et al.*, 2013 (2), Fraile, L.M., *et al.*, 2011, Corzo, P.M.G., *et al.*, 2010, Vaquero, J.J., *et al.*, 2010].

También relacionado con la agenda de medidas de Fast Timing del GFN-UCM se ha

caracterizado la respuesta temporal, eficiencia y resolución en energía de un cristal recientemente introducido al mercado: LuAG:Pr. Este cristal no sólo ofrece un alto poder de frenado, similar al BGO, sino que tiene una respuesta temporal y energética bastante atractiva tanto para Fast timing como otros ámbitos de aplicación, por ejemplo, imagen médica, en particular para PET. Bajo estos escenarios la actividad interna del cristal no resulta ser un inconveniente. Además, muchas de las propiedades reportadas en esta tesis no han sido estudiadas antes de este trabajo.

El GFN-UCM está fuertemente involucrado en el desarrollo de nuevos detectores para Tomografía por Emisión de Positrones (PET) [PhD thesis: Vicente, E., 2012; Abushap, K., 2012, España, S., 2009 and papers: Fraile, L.M., *et al.,* 2012, Corzo, P.M.G., *et al.*, 2010]. Una de las tareas es evaluar nuevos centelladores con respuesta temporal y energética mejoradas para uso en detectores PET con capacidad para Tiempo de Vuelo (ToF). Dicha tecnología permite al equipo PET ganar en calidad (mayor resolución espacial, mejor cuantificación de propiedades, optimización relación señal-ruido), algo no factible en escáneres PET convencionales. Para esta última aplicación el centellador LuAG:Pr puede resultar muy útil, en función de los resultados de su caracterización. Por lo tanto, una segunda parte de este trabajo de tesis se refiere a la evaluación de LuAG:Pr y para evaluar su idoneidad para aplicaciones de PET, incluyendo su idoneidad para ser montado en arreglos phoswich.

9.2. Desarrollo

La tesis está dividida en 5 capítulos, el primero es una breve introducción y contextualización, el segundo versa sobre el HPGe, los siguientes dos sobre un par de cristales inorgánicos individuales y el último sobre una configuración phoswich. En cada uno de ellos se hace una caracterización de las principales propiedades espectrométricas y dosimétricas necesarias para explorar posibles escenarios de aplicación.

9.2.1. Detector HPGe

En este capítulo se realizó una caracterización de un detector semiconductor de germanio hyperpuro (HPGe) modelo LOAX 60450-30P-CW de ORTEC con el fin de determinar su eficiencia absoluta en funció de la energía y la distancia. En primer lugar, se ha hecho una optimización de los parámetros asociados al procesamiento de la señal, tales como voltaje, tiempo de conformado (shapping time), tiempo hasta el pico (peaking time) y tiempo muerto (Dead Time). En la figura R.1 se aprecian los resultados de esta optimización.

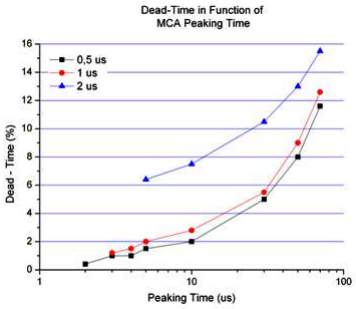

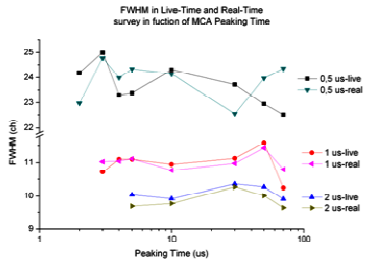

Fig. R.1: Izquierda, Tiempo Muerto en función del Peaking Time en el MCA a diferentes tiempos de conformado (shapping time). Derecha, FWHM del pico de 662 keV en función del peaking time y del tiempo de conformado.

Los detectores de HPGe ofrecen la mejor resolución en energía en espectrometría gamma debido a su bajo valor de gap enérgetico entre capas. La única restricción que pone este valor es que el detector debe estar muy frío para operar adecuadamente. En este trabajo hemos construido un sistema de transvaso de nitrógeno líquido (LN2) para rellenar el depósito del Dewar que acompaña al HPGe a partir de un Dewar porátil. En la figure R.2 se muestra cómo funciona el sistema de trasvasado. La estrategia seguida consiste en evaporar parte del LN2 de tal forma que este vapor ejerza presión sobre el líquido y lo obligue a desplazarse a través de un bastón de aluminio y luego por un manguera hasta llegar al otro depósito Dewar. Cuando el proceso de trasvaso ha terminado, simplemente se permite salir al gas de LN2 de modo que la presión disminuye y se detiene el traspaso. Este proceso ha demostrado ser barato y eficiencia en comparación a otros sistemas de rellenado.

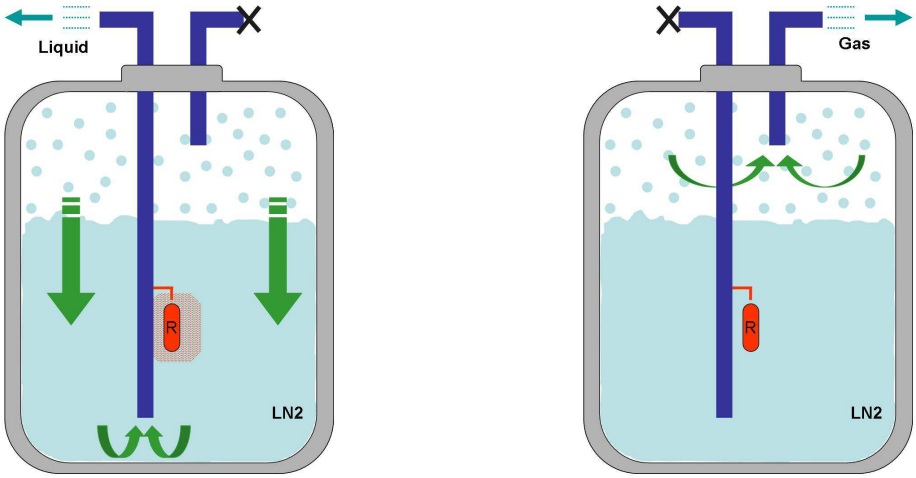

Fig R.2: *Izquierda, el Ni2 gaseoso empuja el LN2 para que este vaya hacia el otro depósito. Derecha, se abre un orificio para que la presión del gas disminuya y así se detenga el proceso de trasvaso de LN2.*

Luego de optimizar los espectros se procedió a caracterizar tanto el fondo de radiación como el blindaje de plomo. En la figura R.3 mostramos un espectro de radiación gamma con el HPGe fuera y dentro del castillo de plomo. Asimismo exploramos el efecto del castillo

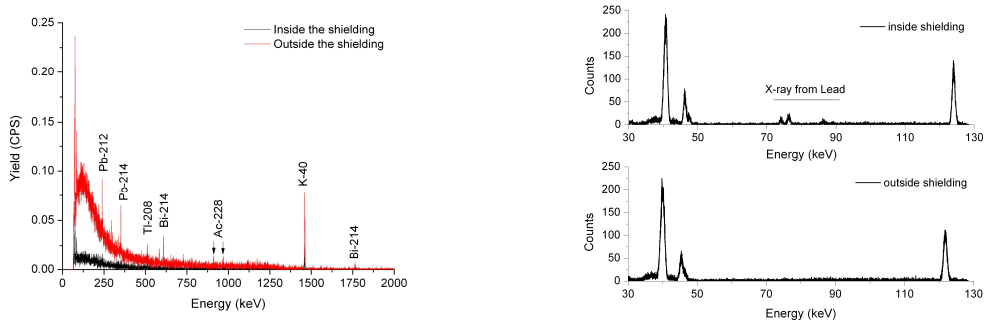

Fig. R.3: *Espectro gamma del fondo de radiación en el laboratorio medido para dos escenarios: dentro y fuera del castillo de plomo. Derecha, efecto de los rayos X del Pb presente en el blindaje para el rango de bajas energías.*

Con los parámetros de medida optimizados, procedimos a realizar medidas espectrales mediante una fuente de ^{152}Eu absolutamente calibrada al 5%. Posicionamos la fuente en distintos de modo que pudimos estimar la eficiencia absoluta del HPGe para distintas energías y distancias. Los resultados se presentan en la siguiente figura (Fig. R.4).

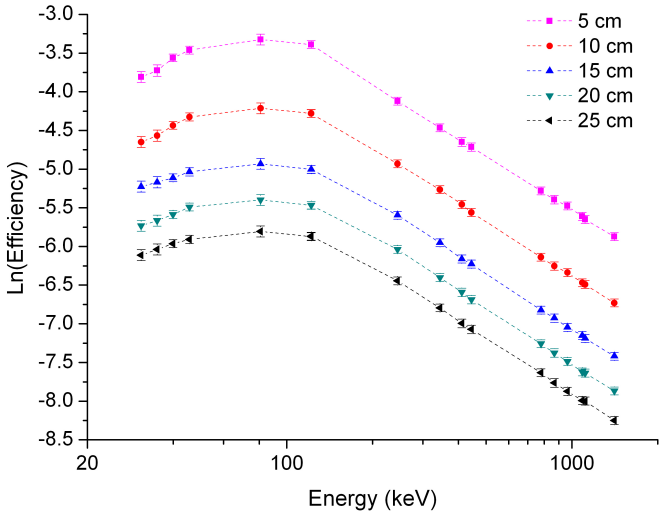

R.4: *Eficiencia Absolute del HPGe en función de la energía y la distancia. Los valores obtenidos tienen errores inferiores al 6%.*

También realizamos ajustes cuadráticos a estos resultados con el fin de poder interpolar valores de eficiencia y así poder calibrar otras fuentes de radiación o determinar la actividad interna de un cristal centellador que contiene 176Lu. (Ver siguiente sección). En la figura R.5 se muestra el ajuste que hemos realizado para estas curvas. En general, hemos divido todo el rango de energía en dos intervalos, el de baja energía (30-244.7 keV) que lo ajustamos con una función cuadrática y el alta energía (244.7-1408 keV) que lo aproximamos con una línea recta. Recordando que todos se realiza en escala doblemente logarítmica.

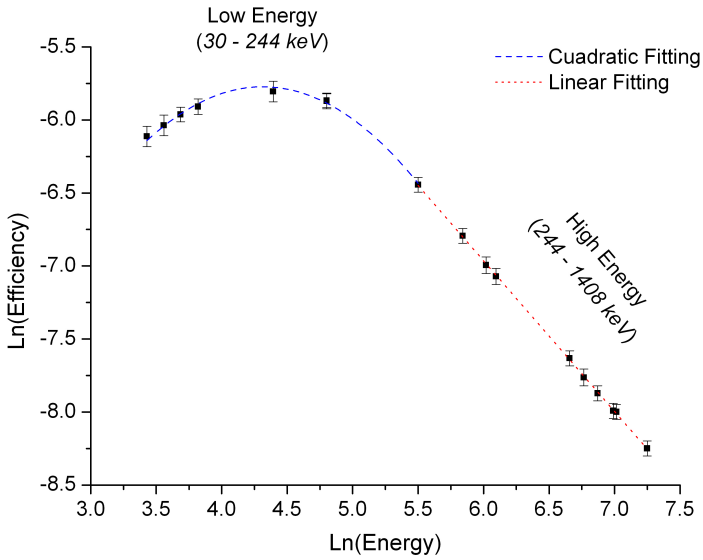

Fig. R.5: *Ajuste de los valores de eficiencia absoluta obtenida para el HPGe. El rango de energías se divide en dos intervalos para así aplicar una ajuste sencillo y adecuado para cada uno.*

9.2.2. Detector LuAG:Pr

En el capítulo 3 caracterizamos un cristal centellador cúbico (1-cm^3) acoplado a un tubo fotomultiplicador (PMT) modelo R5320 de Hamamatsu. En la figura R.6 se adjunta una imagen de ambos objetos.

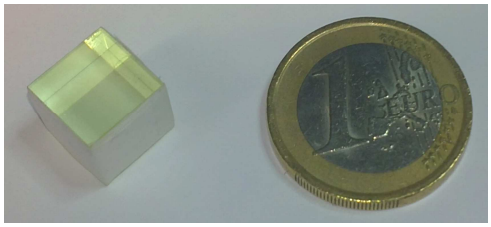

Fig. R.6: *Izquierda, cristal cúbico de LuAG:Pr al lado de un moneda de un euro. Derecha, fotografía del R5320 fuera del encapsulado magnético.*

Primeramente, se ha realizado pruebas para optimizar los parámetros de adquisición y procesamiento de las señales: se ha estudiado la resolución en función del voltaje, se ha fijado el mejor tiempo de retardo externo, y se ha realizado medidas de espectrometría gamma con distintas fuentes gammas para tener información sobre su respuesta temporal y energética. En general, se han caracterizado la respuesta temporal y energética, se ha medido la linealidad y la actividad interna del cristal. En la figura R.7 se muestra un espectro de ^{137}Cs y la curva de linealidad.

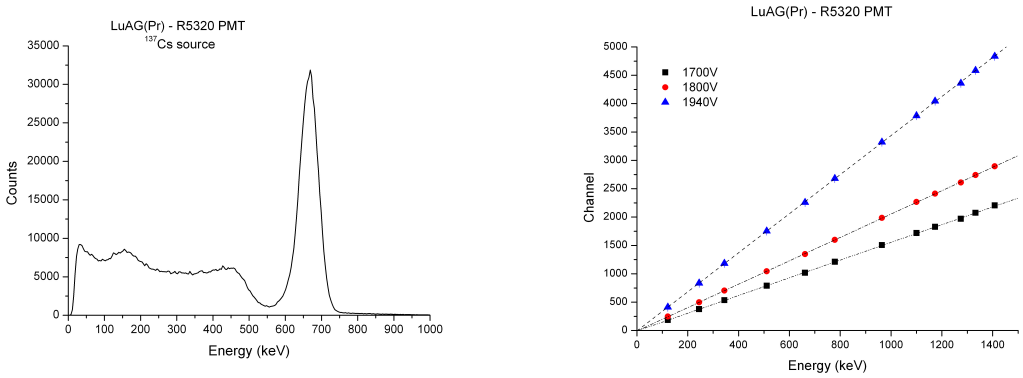

Fig. R.7: *Izquierda, espectro de energía de una fuente de 137Cs. Derecha, curvas de linealidad del PMT ante varios voltees.*

Para las medidas temporales hemos usado un método de coincidencias por tiempo de retardo, en el cual tomamos un cristal centellador de referencia, en nuestro caso un BaF_2, y procedemos a realizar medidas con nuestro cristal de prueba. Luego, los picos obtenidos en un espectro de tiempo lo deconvolucionamos para obtener la contribución característica, o resolución temporal, de nuestro cristal centellador. En la figura R.8 se presentan dos imágenes, una del banco de pruebas (donde se acoplan los PMT+cristales) y la electrónica utilizada para el procesamiento de la señal.

Fig. R.8: *Izquierda, banco de trabajo, se aprecian los dos cristales acoplados a sus PMT y geometría frontal para optimizar la eficiencia geométrica. Derecha, módulos NIM y el montaje que se utilizó para realizar las medidas.*

El cristal de LuAG:Pr está constituido por lutecio. Una fracción pequeña, pero considerable de este elemento, son isótopos de ^{176}Lu, el cual introduce una actividad interna que debe ser caracterizada y tomada en cuenta según los escenarios en donde se quiera utilizar este cristal. Nosotros hemos utilizado el HPGe absolutamente calibrado para determinar la concentración de ^{176}Lu en el cristal.

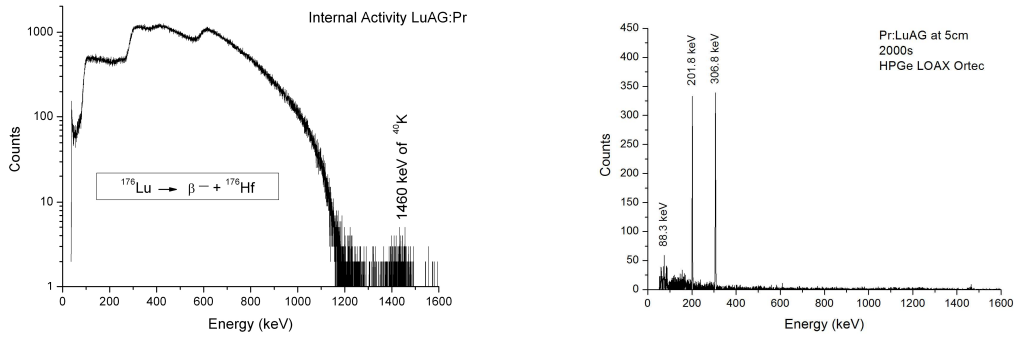

Fig. R.9: *Espectro del fondo de radiación más la contribución beta del ^{176}Lu presente en el cristal centellador. El cristal estaba acoplado al PMT antes citado. Derecha, espectro de energía de las emisiones gammas propias del cristal obtenidas con el HPGe. El cristal se colocó a 5cm del detector durante 2000 segundos.*

Los espectros de tiempo obtenidos por el método de coincidencias retardas a las energías de ^{22}Na y ^{60}Co. Estos valores se han deconvolucionado con el valor del cristal de referencia para estas mismas energías. En la figura R.10 se muestran los espectros temporales óptimos para la energía de 511 keV y los dos picos del ^{60}Co.

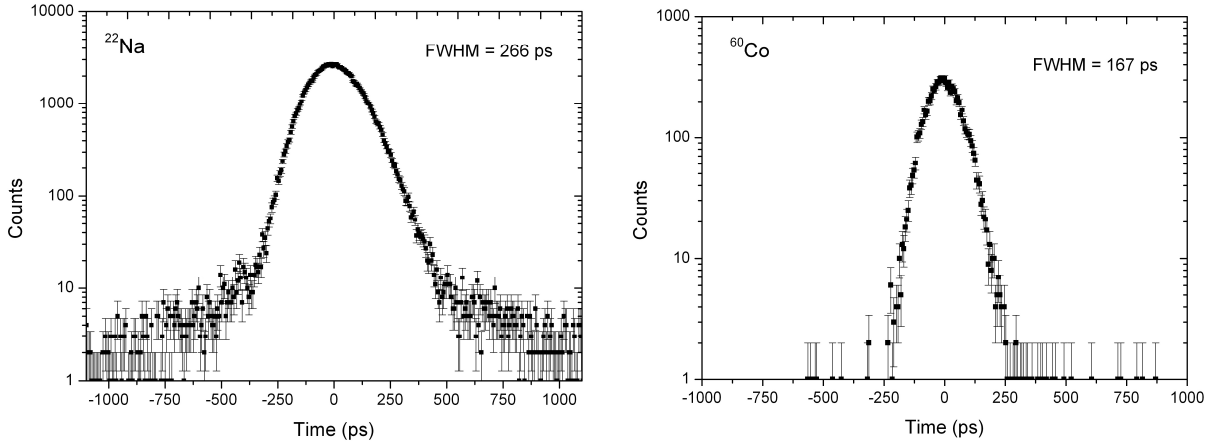

Fig. R.10: *Espectros temporales del LuAG:Pr + BaF_2. Izquierda, el pico de 266 ps obtenido para el 511 keV del ^{22}Na. Derecha, espectro temporal para las enegías del ^{60}Co.*

9.2.3. Detector $CeBr_3$

En el capítulo 4 hacemos una caracterización completa de un cristal inorgánico con propiedades realmente prometedoras. En este trabajo investigamos las propiedades de un cristal cilíndrico de CeBr3 acoplado a dos PMT (uno de Hamamatsu y otro Photonis). En la figura R.11 se muestra el cristal y un esquema de las dimensiones del mismo.

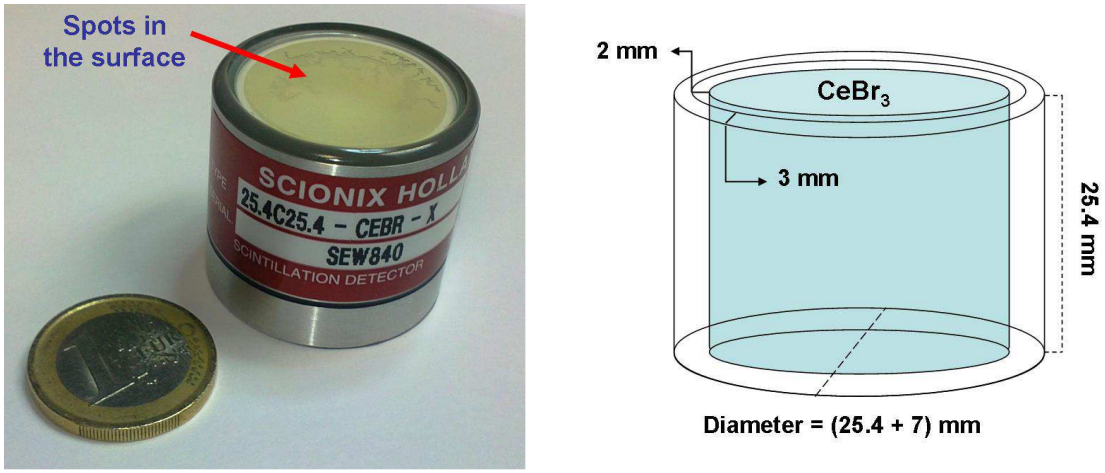

Fig. R.11: *Izquierda, cristal de $CeBr_3$ utilizado para las medidas. Derecha, un esquema con las medidas del cristal.*

Después de optimar los parámetros de medición, se han estudiado la respuesta energética del cristal mediante linealidad y la resolución en energía. En la figura R.12 mostramos los resultados del cristal acoplado a los PMT. De estos gráficos se nota cómo el PMT de Hamamatsu (R9779) presenta mayor linealidad que el de Photonis (XP20D0).

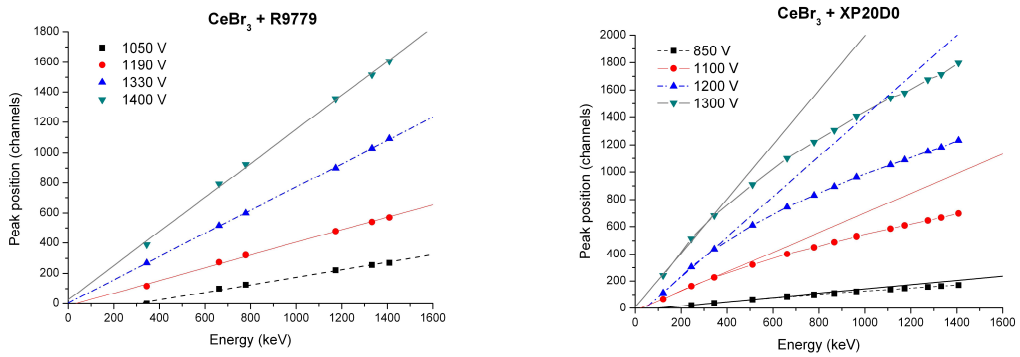

Fig. R.12: *Linealidad del $CeBr_3$ acoplado a los dos tubos fotomultiplicadores. Izquierda, con el PMT de Hamamatsu. Derecha, con el PMT de Photonis. Cada uno fue testado a diferentes voltajes.*

Mediante un método similar al expuesto en la sección anterior, hicimos una caracterización de la respuesta temporal de este cristal centellador. En la figura R.13 mostramos los resultados de los espectros temporales para las energías de 511 keV del ^{22}Na y las energías del ^{60}Co.

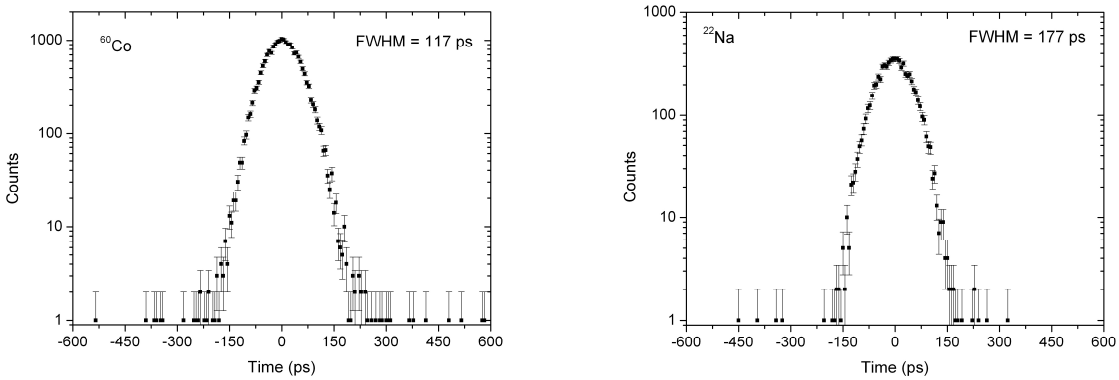

Fig. R.13: *Espectros temporales del $CeBr_3$ acoplado al PMT de Hamamatsu. Los espectros fueron tomados a las energías del ^{60}Co (izquierda) y ^{22}Na (derecha).*

En la siguiente tabla se presentan los resultados obtenidos luego de optimizar:

Detector	**^{60}Co** *(1173/1332 keV)*	**^{22}Na** *(511 keV)*
$CeBr_3$ – XP20D0	146 ± 2 ps	210 ± 2 ps
$CeBr_3$ – R9779	119 ± 2 ps	164 ± 2 ps

Tabla: *Resumen de resultados de resolución temporal para $CeBr_3$ acoplado a los dos PMT.*

Además de las medidas antes descritas, se realizó un estudio de radiopureza del cristal en el Laboratorio Subterráneo de Canfranc. Las medidas se realizaron con detectores de HPGe dentro de un castillo de plomo y con un sistema de circulación de aire para reducir la contribución por isótopos en suspensión.

Fig. R.14: *Izquierda, entrada secundaria al laboratorio. Derecha, sistema de adquisición basado en HPGe. Se aprecia el castillo de plomo y el encapsulado.*

Primero se obtuvo un fondo de 55 días, y luego se realizó una medida continua durante 34.6 días del cristal. En la figura R.15 se muestran ambos espectros superpuestos. Antes fueron normalizados en tiempo y calibrados para poder subtraer el fondo y así obtener la contribución neta del cristal y su encapsulado.

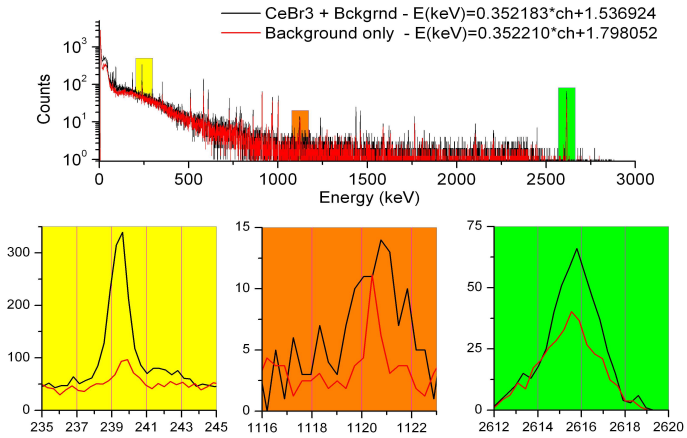

Fig. R.15: *Espectros superpuestos, y normalizados en tiempo, del fondo (rojo) y del $CeBr_3$ (negro)*

A continuación se muestra una tabla con los isótopos encontrados y su concentración estimada por día y kilogramo. Dado que el CeBr3 es higroscópico, no pudidmos separar el cristal de su encapsulado. En la siguente tabla puede aparecer cualquier de ellos.

Energy Peak (*keV*)	**Radionuclide**	**Chain**	**Intensity (*counts per day*)**	**Yield (*counts per day per kg*)**
46.54	^{210}Pb	^{238}U	17.4 ± 2.6	160.9 ± 24
63.29	^{234}Th	^{238}U	10.1 ± 1.6	93.4 ± 14.8
92.59	^{234}Th	^{238}U	17.6 ± 1.8	162.7 ± 16.6
186.21	^{226}Ra	^{238}U	9.1 ± 1.4	84.1 ± 12.9
238.63	^{212}Pb	^{232}Th	21.2 ± 1.7	196 ± 15.7
241.99	^{214}Pb	^{238}U	1.5 ± 1.2	13.9 ± 11.1
295.22	^{214}Pb	^{238}U	2.1 ± 1.2	19.4 ± 11.1
300.09	^{212}Pb	^{232}Th	1.4 ± 1.1	12.9 ± 10.2
351.93	^{214}Pb	^{238}U	7.7 ± 1.1	71.2 ± 10.2
510.77	^{208}Tl	^{232}Th	3.8 ± 1.0	35.1 ± 9.2
583.19	^{208}Tl	^{232}Th	10.3 ± 1	95.2 ± 9.2
609.32	^{214}Bi	^{238}U	6.7 ± 0.8	62 ± 7.4
727.33	^{212}Bi	^{232}Th	1.7 ± 0.6	15.7 ± 5.5
768.36	^{214}Bi	^{238}U	1.0 ± 0.6	9.2 ± 5.5
788.74	^{138}La	Ce affinity	2.0 ± 0.5	18.5 ± 4.6
860.56	^{208}Tl	^{232}Th	1.5 ± 0.4	13.9 ± 3.7
1001.03	^{234m}Pa	^{238}U	1.8 ± 0.6	16.6 ± 5.5
1238.12	^{214}Bi	^{238}U	0.6 ± 0.3	5.5 ± 2.8
1435.8	^{138}La	Ce affinity	3.3 ± 0.4	30.5 ± 3.7
1460.82	^{40}K	-	2.1 ± 0.4	19.4 ± 3.7
1620.5	^{212}Bi	^{232}Th	0.3 ± 0.2	2.8 ± 1.8
2614.51	^{208}Tl	^{232}Th	4.6 ± 0.8	42.5 ± 7.4

Table R.1: *Picos obtenidos provenientes del $CeBr_3$ y su encapsulado.*

Finalmente, hemos realizado la primera medición de eficiencia absoluta para el cristal de $CeBr_3$ mediante una fuente calibrada de ^{152}Eu y otras fuentes calibradas (^{133}Ba, ^{137}Cs, ^{60}Co, ^{22}Na), tal como fue descrito en el capítulo del HPGe. Las medidas se realizaron a tres distancias diferentes. En la figura R.15 se muestran los resultados obtenidos.

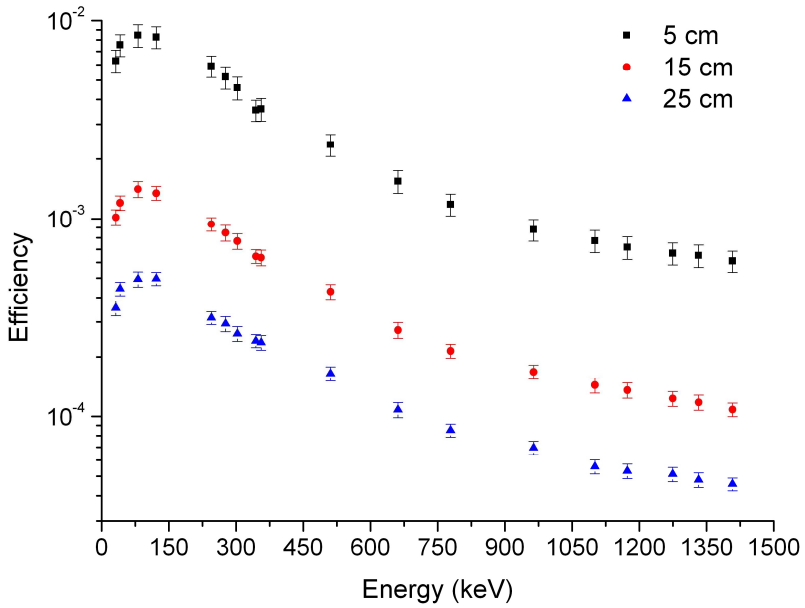

Fig. R.15: *Eficiencia Absoluta para el cristal de CeBr3 acoplado al XP20D0 a3 distancias.*

9.2.4. Detector Phoswich: LYSO+LuAG:Pr

EN el capítulo 5 exploramos una configuración phoswich conformada por dos cristales inorgánicos de alta densidad: LYSO y LuAG:Pr. En la figura R.16 mostramos estos cristales y algunas de las configuraciones que se investigaron. Se realizaron pruebas con dos fotosensores distintos: SiPM y PMT.

Fig. R.16. *Distintas configuraciones de phoswich que fueron testadas, el cual fue acoplado tanto al PMT como a un SiPM.*

Para esta configuración hemos explorado la respuesta energética y la forma del pulso para distintas configuraciones de phoswich con tal de hallar la configuración óptimca de los cristales y de los parámetros de medición.

Los pulsos fueron digitalizados mediante un osciloscopio de alta sampleo y controlado por un código de python escrito por nosotros. Asimismo realizamos un análisis off-line de los pulsos mediante el Método de Energías Retardadas dentro de un código escrito por nosotros en fortran.

En la figura R.17 se enlistan las configuraciones que fueron exploradas del phoswich así como las posiciones de la fuente gamma que se utilizó para las medidas (en este caso fueron ^{22}Na y ^{137}Cs).

Configuration	Photosensor	
	PMT	SiPM
Each individual crystal	Over LuAG:Pr crystal	Over LuAG:Pr crystal
	Over LYSO crystal	Over LYSO crystal
Side-by-Side	Close to LYSO	N-A
	Close to LuAG:Pr	
	On Top	
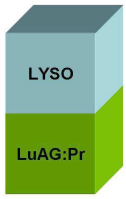	Close to LYSO	Close to LYSO
	Close to LuAG:Pr	Close to LuAG:Pr
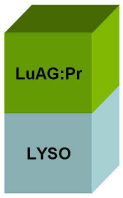	Close to LYSO	Close to LYSO
	Close to LuAG:Pr	Close to LuAG:Pr

Debido a la mejor resolución en energía y la cercanía de los picos de provenientes de cada cristal, escogimos la configuración que pone al LuAG:Pr en contacto directo con el fotosensor y al LYSO un poco más alejado.

Después buscamos el mejor retraso de integración para separar en capas la información de los pulsos. Para el caso del PMT hemos encontrado que el óptimo retraso está en 30 ns. En la figura R.17 mostramos gráficos de energía retarda/energía versus energía. Los valores de retardo óptimos deberán permitir separar la información de los puntos en capas diferenciables por una línea recta.

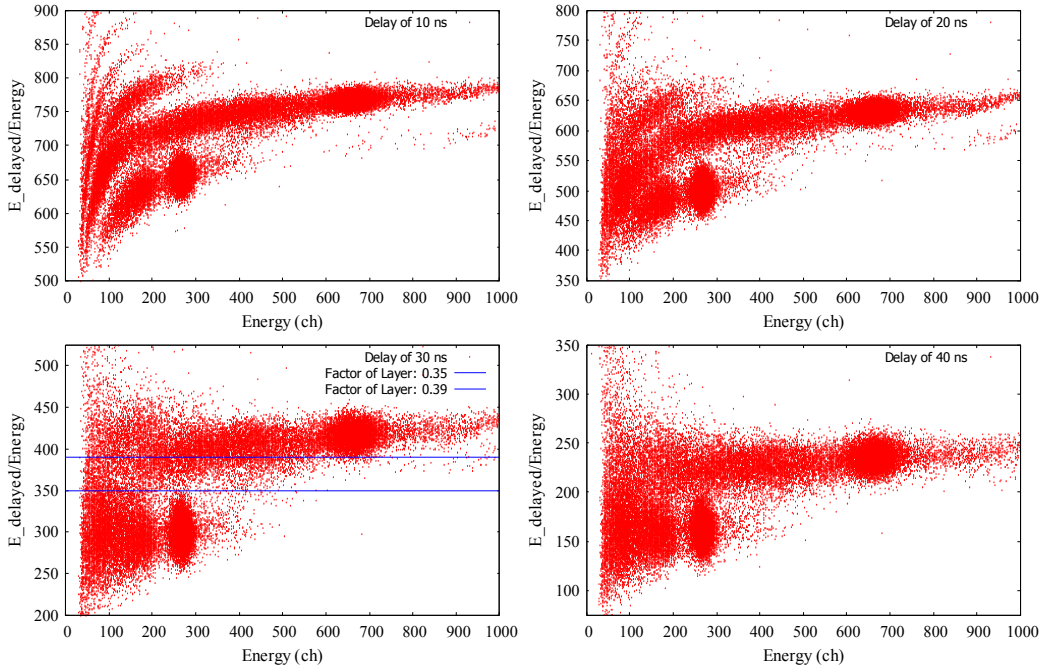

Fig. 5.16: *Phoswich diagrams for the LuAG:Pr+LYSO configuration coupled to the PMT.*

Mediante un proceso análogo se obtuvieron los valores para el SiPM. EN la siguiente tabla resumimos los resultados obtenido para el retraso y factor de capa necesarios para resolver los pulsos que provienen de un cristal o del otro.

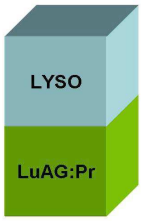

Photosensor	Delay (ns)	Limiting Layer Factor
PMT	30	0.35
SiPM	70	0.065

9.3. Conclusiones

Ahora, expondremos las principales conclusiones de cada capítulo:

9.3.1. Detector HPGe

El sistema desarrollado para rellenar el Dewar del HPGe con nitrógeno líquido funciona bien. Básicamente un sistema de ebullición fue creado para llevar LN2 desde un Dewar portátil a uno fijo en donde se encuentra el HPGe. El sistema se ha demostrado barato y ser un método eficiencia para transferir el LN2 con pérdidas despreciables.

Además, se han optimizado el tiempo de conformado (shapping time) y tiempo de subida (peaking time) y resultando tiempo muerto de la electrónica del HPGe fueron determinado. Se determinó el valor óptimo para parámetros temporales como…

El shapping time se fijó en 1 μs en el amplificador y el peaking time se fijó en 5 μs en el MCA. El tiempo muerto está asociado a una función para corregir los resultados tomados en modo tiempo vivo (Live Time).

El HPGe muestra una respuesta bastante linear ante la energia en el rango explorado. La resolución y linearidad presents un comportamiento bastante lineal. Simples relaciones líneas para la esolucióin y energía contra canales fueron suficiente for our HPGe detector.

También deteminamos que el castillo de plomo reduce el número de cuenta provienetes del fondo radiactivo. Sin embargo, por otro lado, si la muestra emite gammas con suficiente energía para excitar el plommo, entonces el blindaje podría liberar algunos rayos-X. Como consecuencia de este efecto algunos picos adicionales pueden aparecer en el espectro. De esta forma para caracterizar muestras en el rango de 70-80 keV debemos ser cuidadadosos y considerar este efecto de fluorescencia desde el blindaje. Asimimso, la radiación de retroceso (backscatter) desde el castillo de Pb podría ser considerable en funete de la actividad de muestra.

Fue posible obtener una eficiencia absoluta para nuestra detector. A bajas energía una curva cuadrática fue usada para ajustar los datos entre 30 y 244.7 keV y para el intervalo de altas energías usamos una ajuste linear de 244.7 a 1408 keV. Ambas funciones se superponen razonablemente bien en la zona de superposición explorada. También calibraciones absolutas con incertidumbre mejor al 10% fueron posibles de obtener.

9.3.2. Detector LuAG:Pr

El cristal de LuAG:Pr ha mostrado ser una buena alternativa para LSO o LYSO para PET, con una resolución del 5.1% y una resolución temporal de 238 ± 2 ps en 511 keV. Para las energías del ^{60}Co la resolución temporal fue optimizada en 147 ± 2 ps. La actividad interna proveniente del ^{176}Lu se encuentra alrededor de los 215 ± 20 Bq/cm^3. El cristal acoplado al PMT mostró una muy buena linealidad en el rango de 122 a 1408 keV.

Esto lo convierte en un buen candidato para ser usado en Fast timgin y en ámbitos clínicos donde halla alta fluencia.

9.3.3. Detector $CeBr_3$

Los cristales $CeBr_3$ poseen excelentes propiedades temporales que pueden llegar a substituir al convencional NaI:Tl en casi todas las aplicaciones. En un cristal cilíndrico 1'x1' acoplado a un R9779 PMT, se obtuvieron muy buenas respuestas temporales y energéticas a 1330 V. Por ejemplo, a 511 keV la resolución en energía fue del 5.5% mientras que la resolución temporal ($\sim E^{-1/2}$) fue de 164 ± 2 ps. Por primera vez medimos la eficiencia absoluta de este cristal en un rango de energías desde 31.61 hasta 1408 keV a tres distancias distintas. Los resultados se ajustaron a un expresión polinómica.

La posibilidad de contaminantes radiactivoes en el $CeBr_3$ se midió en el laboratorio subterráneo de Canfranc. Nuestro estudio se llevó a cabo para un cristal cilíndrico de 30x30 mm y su encapsulado. Las principales conclusiones evidencian la presencia de las cadenas de desintegración del Radio y el Torio, pero no de la cadena de los Actínidos. También encontramos trazas del ^{138}La debido a su afinidad química con el Ce, pero no se observaron productos de activaciones neutrónicas, como el ^{82}Br o ^{139}Ce.

En conclusión, hemos demostrado que el cristal de $CeBr_3$ es un prometedor candidato para varias aplicaciones. Su resolución en energía está entre las mejores para centelaldores inorgánicos, con un 5% medido a 662 keV con un PMT rápido. La eficiencia de detección es buena y comparable a la del $LaBr_3$:Ce. La respuesta temporal es extremadamente buena. Por último, la radiopureza del cristal lo hace competitivo para medidas de bajo fondo. Es más, esta radiopureza puede mejorarse aún más usando un encapsulado de aluminio radiopuro.

9.3.4. Detector Phoswich: LYSO+LuAG:Pr

El phoswich formado por LuAG:Pr y LYSO tiene propiedades interesantes. La combinación de ambos permite una identificación por capas, esto es, que la señal de los cristales se puede separar, sea que estén acoplados a PMT o SiPM. Esta propiedad resulta atractiva para la nueva generación de sistema PET que incorporan ToF. De esta forma, permite una buena resolución energética y temporal a la vez que permite aumentar la resolución espacial. Cuando el phoswich estuvo acoplado al PMT se obtuvieron buena separación de capa con los 40 ns de retraso y 0.35 de factor de capa. Para el SiPM los valores fueron 70 ns de retraso y 0.0065 de factor de capa. Por otro lado, los parámetros de resolución en energía y linealidad son bastante buenos.

9.4. Referencias

Abushab, Khaled. (2012). Simulation and Image Reconstruction of Clinical TOF-PET Scanners. (PhD thesis) Departamento de Física Atómica, Molecular y Nuclear. Universidad Complutense.

Attix, F. Introduction to Radiological Physics and Radiation Dosimetry. United States of America: John Wiley & Sons, Inc, 2004.

Cooper, P.N: Introduction to Nuclear Radiation Detectors. Cambridge: Cambridge University Press, 2011.

Corzo, P.M.G., Cal-González, J., Picado, E., España, S., Vicente, E., Herranz, E. Fraile, L.M., Vaquero, J.J., Udías, J.M., Muñoz, A. Off-line PET Study of Proton Beam Activated Metals. Oral Presentation. International Workshop on bio-medical applications of micro-PET. (2010) Seville, Spain.

Corzo, P.M.G., Cal-Gonzalez, J., Picado, E., España, S., Herraiz, J.L., Herranz, E., Vicente, E., Udias, J.M., Vaquero, J.J.. Munoz-Martin A., Fraile, L.M. Measurement of Activity Produced by Low Energy Proton Beam in Metals Using off-Line PET Imaging. IEEE Nuclear Science Symposium & Medical Imaging Conference. IEEE NSS-MIC (2011) Conference Record, Valencia, Spain.

España, S. (2009). Simulaciones avanzadas aplicadas al diseño de escáneres y mejora de la calidad de imagen en tomografía por emisión de positrones. (PhD thesis) Departamento de Física Atómica, Molecular y Nuclear. Universidad Complutense.

Fraile, L.M., Mach, H., Vedia, V., Olaizola, B., Picado, E., Paziy, V.,Udías, J.M., Nuclear Instruments and Methods in Physics Research A (701), 235-242 (2013) DOI: 10.1016/j.nima.2012.11.009

Fraile, L.M., Mach, H., Picado, E., Vedia, V., Udías, J.M. in Nuclear Instruments and Methods in Physics Research A (713), 27-32 (2013) DOI: 10.1016/j.nima.2013.02.015

Fraile, L.M., Mach, H., Olaizola, B., Paziy, V., Picado, E., Sanchez, J.J., Udías, J.M., Vaquero, J.J., Vedia, V., in Nuclear Science Symposium Conference Record, 2011. NSS '11. IEEE (2011), pp. 72 -74. DOI: 10.1109/NSSMIC.2011.6154403

Knoll, Glen. Radiation Detection and Measurement. Third Edition. New Jersey: John Wiley & Sons, Inc., 2000.

Leo, W.R. Techniques for Nuclear and Particles Physics Experiments. A How-to Approach. Second Revised Edition. Berlin: Springer-Verlag, 1994.

Mach, H., Gill, R.L., Moszynski, M., Nuclear Instruments and Methods in Physics Research A 280, 49 (1989)

Mach, H., Wohn, F., Molnar, G., Sistemich, K., Hill, J.C., Moszynski, M., Gill, R., Krips, W., Brenner, D. Nuclear Physics A 523, 197 (1991)

Shah, K.S., Glodo, J., Higgins, W., Van Loef, E.V., Moses, W.W., Derenzo, S.E., Weber, M.J., IEEE Transactions on Nuclear Science 52(6), 3157 (2005)

Vaquero, J.J., España, S., Picado, E., Cal-González, J., Fraile, L.M., Herraiz, J.L., Vicente, E., Desco, M., Udías, J.M. Viavilidad del uso de fotodetectores SiPM en sistemas PET/IRM. Oral Presentation. CASEIB (2010) Madrid, Spain.

Vicente Torrico, E. (2012). Caracterización, Mejora y Diseño de Escáneres PET Preclínicos. (PhD thesis) Departamento de Física Atómica, Molecular y Nuclear. Universidad Complutense.